Ocean-atmosphere interaction under tropical cyclones in the north Indian Ocean

A Thesis submitted to Goa University for the award of the Degree of

DOCTOR OF PHILOSOPHY

in

MARINE SCIENCES

By

S. Neetu

Goa University,
Taleigao, Goa
2017

Ocean-atmosphere interaction under tropical cyclones in the north Indian Ocean

A Thesis submitted to Goa University for the award of the Degree of

DOCTOR OF PHILOSOPHY

in

MARINE SCIENCES

By

S. Neetu

Goa University,
Taleigao, Goa
2017

Ocean-atmosphere interaction under tropical cyclones in the north Indian Ocean

Table of Contents

Statement

As required under the University ordinance OB-9.9 (v-vi), I hereby state that the present thesis entitled **"Ocean-atmosphere interaction under tropical cyclones in the north Indian Ocean"** is my original contribution and it has not been submitted on any previous occasion.

The literature related to the problem investigated has been cited. Due acknowledgements have been made wherever facilities and suggestions have been availed of.

S. Neetu
CSIR-National Institute of Oceanography, Goa

Place: Dona Paula
Date:

Certificate

This is to certify that the thesis entitled **"Ocean-atmosphere interaction under tropical cyclones in the north Indian Ocean"**, submitted by S. Neetu to the Goa University for the degree of Doctor of Philosophy, is based on her original studies carried out under my supervision. The thesis or any part thereof has not been previously submitted for any other degree or diploma in any university or institution.

Prof. H. B. Menon
Department of Marine Science
Goa University, Goa.

Acknowledgements

I express my sincere gratitude to Prof. H. B. Menon for agreeing to be my guide and for the continuous support and guidance rendered by him during my Ph.D. I am also indebted to Dr. M. M. Ali for introducing me to my guide and for guiding me as well throughout my Ph.D. work. I am thankful to the V. C. nominee Dr. P. Vethamony for his valuable suggestions that have been very helpful in my work. I also thank my FRC committee members, Prof. Janarthanan, Prof. C.U. Rivonkar and Prof. G. N. Nayak for their helpful comments on my work and for their encouragement. I also thank the librarian at Goa University, Dr. Gopakumar, for carrying out the plagiarisms checks on my thesis.

I acknowledge the support received from Dr. S.W.A. Naqvi, Ex Director, CSIR-NIO in terms of providing the necessary facilities to accomplish my thesis work. I sincerely thank Dr. T. Pankajakshan, Dr. M. R. Rameshkumar and Dr. P. M. Muraleedharan for their valuable advices and discussions on my work.

The results of this thesis would not have been obtained without a strong collaboration with LOCEAN/IRD, Paris, France. I owe a great appreciation and gratitude to Dr. Matthieu Lengaigne with whom I started this work. My heartfelt thanks to him for his invaluable guidance, sharing his immense knowledge, providing support and encouragement throughout my research work, and that too during the most difficult phase in my career. I am highly thankful to Dr. Jérôme Vialard for guiding me in my work with his great expertise. I also thank Dr. Emmanuel Vincent, Dr. Guillaume

Samson, Dr. Julie, Dr. Christophe Menkes, Dr. Morgan Mangeas, Dr. Marina Levy and Dr. Fabien Durand for all their help in my work.

This work forms a part of an Indo-French Collaborative project funded by CEFIPRA, New Delhi through Grant No. 4907-1. I sincerely acknowledge CEFIPRA for supporting my research on Tropical Cyclones.

My friends, Cathrine, Mani Murali, Siby, Ravindran, Soniya and the entire DS group, have long been with me since the time I joined CSIR-NIO. I am grateful to them for offering me valuable help, warm company and moral support. I also appreciate the students in our lab, including Akhil and Keerthi, for their help.

I would like to specially thank my loving sister, brother, and father for all their support. I won't be able to express my gratitude in words to my mother for her unconditional love, care and reminding me of my strengths during the low phases of my life. A bouquet of thanks to my little son Siddhant for his cute, loving smile that makes me happy all the times.

Finally, I would like to express my heartfelt thanks to my husband Suresh for all his support, encouragement and patience, especially during the initial stages of this Ph.D. and without him, I would not have had the courage to restart my journey towards Ph.D. He not only provided me the confidence, but also helped me throughout the process.

S. Neetu

List of Figures

	pre-monsoon (b) post-monsoon season in the BOB (Sengupta et al., 2008).	
1.26	Average lead time TC intensity forecast errors for TCs over AS, BoB and NIO (Mohapatra et al., 2013).	51
1.27	Average official intensity forecast errors for strong and weak TCs over a period of 2009-11 in NIO (Mohapatra et al., 2013).	52
2.1	(Left panel) Average TC-induced cooling in the model in the BoB, as a function of the WPi (a proxy of the TC-energy input to the upper ocean) (9 bins of 0.3) and CI (a proxy of the inhibition of the cooling by the ocean stratification) (9 bins of 3) (Right panel) Best fit of the model cooling using degree 2 polynomial.	65
2.2	Climatological SSS (in psu; color) and BLT (in meters, grey contours) for pre-monsoon (left panels) and post-monsoon (middle panels) seasons and their difference (right panels) derived from observed SSS climatology of Chatterjee et al. [2011] and BLT climatology of de Boyer-Montegut et al.[2004] (upper panels) and model (lower panels). The thick contour delineates the region where 80% of TCs occur in the northern Indian Ocean (i.e., where TCs density is larger than 0.4 TCs per year in 2° by 2° bins). Dashed colored boxes on panel (c) highlight the regions of the BoB discussed in Table 1 (Red : North-East BoB, Green : East Indian Coast, Blue : Southwest BoB). The black dashed line indicate the temperature and salinity section at 90°E shown on Figure 2.4.	66
2.3	Climatological depth at which the ocean temperature is 2°C below the surface temperature (in meters) for pre-monsoon (left panels) and post-monsoon (middle panels) seasons, and their difference (right panels) derived from de Boyer-Montegut et al. (2004) climatology (upper panels) and the model (lower panels). The thick contour delineates the region where 80% of TCs occur in the northern Indian Ocean (i.e., where TCs density is larger than 0.4 TCs per year in 2° by 2° bins) while dashed colored boxes on panel (a) highlight the regions of the BoB discussed in Table 1 (Red : North-East BoB, Green : East Indian Coast, Blue : Southwest BoB). The black dashed line indicate the temperature and salinity section at 90°E shown on Figure 2.4.	68
2.4	Latitude-depth section (at 90°E) of observed climatological salinity (in psu; color) and temperature (in °C; contour) in BoB during (a) pre-monsoon and (b) post-monsoon seasons. (c) Observed temperature (red) and salinity (blue) profiles averaged in the BoB north of 15°N for pre-monsoon (plain line) and post-monsoon (dashed line) seasons. (d-f) Same for model outputs.	69
2.5	Climatological cooling inhibition index (CI; in $(J.m^{-2})^{-1/3}$) for pre-monsoon (left column) and post-monsoon	70

List of Tables

List of Acronyms

Acronym	Full Form
AMSR	Advanced microwave scanning radiometer
ANN	Artificial Neural Networks
AS	Arabian Sea
ATL	North Atlantic
BL/BLT	Barrier layer/ Barrier layer thickness
BMJ	Betts-Miller-Janjic
BoB	Bay of Bengal
CI	Cooling inhibition index
CI_{S0}	CI calculated with a constant salinity profile
CISK	Conditional instability of second kind
CPL	Coupled oceanic-atmospheric simulation
E925	925 hpa Equivalent potential temperature
ECMWF	European centre for medium range weather forecast
ENSO	El Niño/Southern Oscillation
FOR	Uncoupled (Forced) atmospheric simulation
GFDL	Geophysical Fluid Dynamics Model
GFS	Global Forecast System
GPI	Genesis Potential Index
HWRF	Hurricane Weather Research and Forecasting
IBTrACS	International Best Track Archive for Climate Stewardship
IO	Indian Ocean
IOD	Indian Ocean dipole
ITCZ	Inter-tropical convergence zone
JMA	Japan Meteorological Agency
JTWC	Joint Typhoon Warning Center
KF	Kain-Fritsch
LGEM	Logistic growth equation model
ML/MLD	Mixed layer/Mixed layer depth
MLR	Multiple linear regression
MPI	Potential intensity/Maximum potential intensity
NEMO	Nucleus of European model of the Ocean

NEP	North Eastern Pacific
NHC	National Hurricane Center
NIO	North Indian Ocean
NOW	NEMO-OASIS3-WRF
NWP	North Western Pacific
OGCM	Ocean general circulation model
OHC	Ocean heat content
PDO	Pacific decadal oscillation
PER	Intensity change during previous 12 hour
RHHI	500 to 300 hpa Average relative humidity
SH-STIPS	Southern Hemisphere Statistical Typhoon Intensity Prediction Scheme
SHIPS	Statistical hurricane intensity prediction schemes
SHRD	200 to 850 hpa Wind shear magnitude
SIO	Southern Indian Ocean
SSS	Sea Surface Salinity
SST	Sea surface temperature
STIPS	Statistical typhoon intensity prediction scheme
SVM	Support Vector Machines
SWP	South Western Pacific
T200	200 hpa Temperature
TC	Tropical cyclone
TCHP	Tropical cyclone heat potential
TMI	TRMM Microwave Imager
TRMM	Tropical Rainfall Measuring Mission
USHR	200 to 850 hpa Zonal wind shear magnitude
VMAX	Initial intensity
WISHE	Wind-induced surface heat exchange
WPi	Wind power index
WRF	Weather research and forecasting model
YGP	Yearly genesis parameter
Z850	850 hpa Vorticity

Chapter 1 General Introduction

Tropical cyclones (TCs) are one of the most powerful and destructive phenomenon of the earth's atmosphere. TCs develop over the warm oceans (more specifically above surface temperatures in excess of 26°C) and are characterized by a low-pressure area surrounded by strong rotating winds and heavy rainfall. Figure 1.1 displays a satellite derived image of TC Phailin over the Bay of Bengal (BoB) on the 11th April 2013,

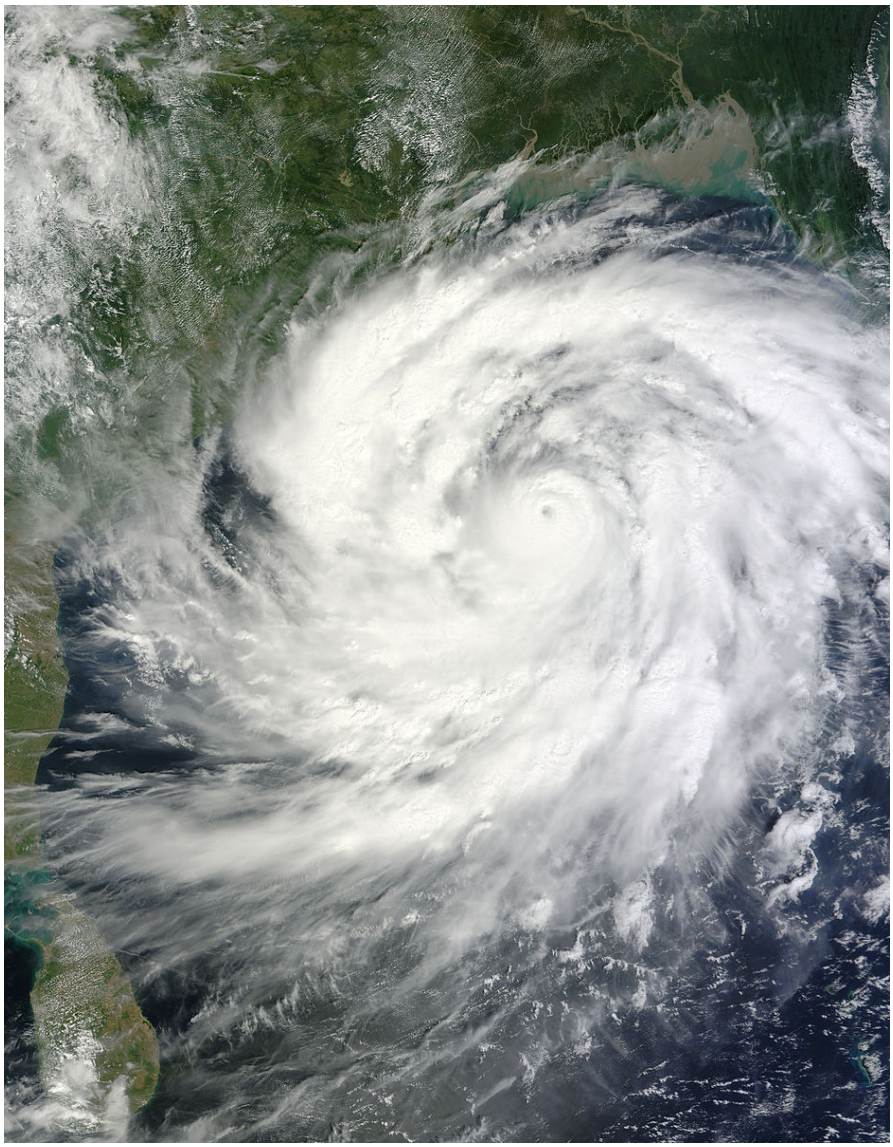

Figure 1.1: Satellite (MODIS/NASA) derived image of cyclone Phailin in the Bay of Bengal on 11 April 2013.

while the major features of a typical mature tropical cyclone are schematized in Figure 1.2. The TC appears as a dense mass of cloudy spirals spreading over a 200-1000 km area and rolling up around a central point referred as the eye of the cyclone (Figure 1.1 and 1.2). These cloudy spirals, characterized by ascending airflow, have a typical width of 5 to 40 km and alternate with clearer sky spirals where the airflow is subsident. The wind and cloud patterns have counter-clockwise (resp. clockwise) rotation in northern (resp. southern) hemisphere. The central point of the system, i.e. the TC eye, is a calm and cloud-free region with warm subsiding air (Figure 1.2). The main region of deep convection, of about 15 km height, occurs in the area surrounding the eye and is called the eyewall (Figure 1.2). This is the region where strongest winds and heaviest rainfall occur. Usually, the radius of the eye varies between 20 km to 50 km and the width of eyewall is about 10 to 50 km.

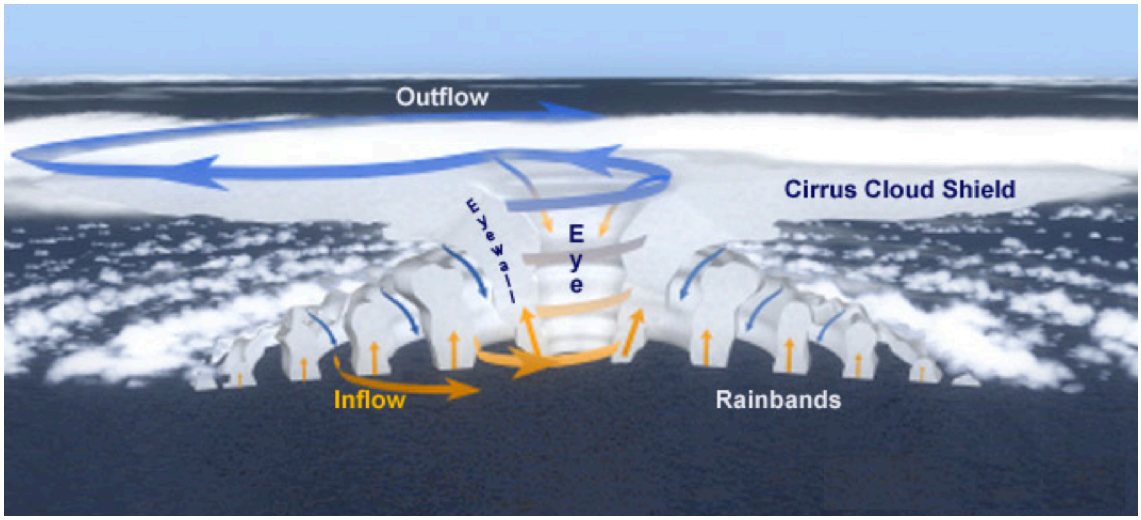

Figure 1.2: Schematic vertical cross-section of a tropical cyclone showing its main features (Gray and Emanuel, 2010).

1.1 Main characteristics of tropical cyclones (TCs)

1.1.1 Thermodynamic properties

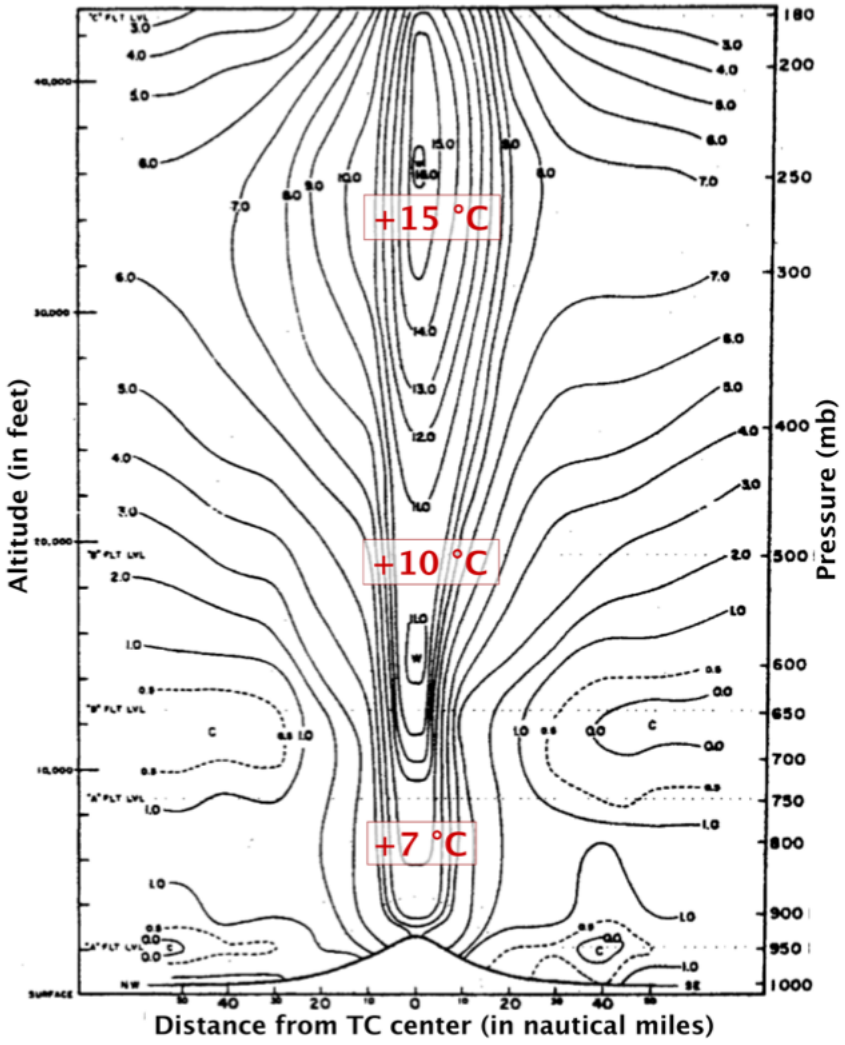

Figure 1.3: Vertical cross-section of temperature anomalies for a tropical cyclone (Hawkins and Imbembo, 1976).

The latent heat released by the deep atmospheric convection acts to warm the air within the eyewall. This warm core extend up to the upper troposphere with maximum upper level temperature anomalies relative to the environment reaching up to ~10-15^{o} C (Figure 1.3). This warm core reduces the density of the atmospheric column and results

in a very low surface pressure at the center. The pressure difference between the center and the surrounding regions generate intense winds blowing towards the TC eye and rolling up cyclonically around it under the effect of the Coriolis force.

1.1.2. Wind structure

General description. The flow in the core of a TC is approximately axisymmetric. The tangential wind speed increases rapidly away from the storm center, reaching a maximum value (~20 to 85 $m.s^{-1}$) in the eyewall (distance knows as radius of maximum winds, ranging from 50 to 100km), and then decreases gradually away from the center of the storm (Figure 1.4). This tangential wind increases is maximum around 500m height. Wind spirals inwards cyclonically at the lower levels, rises in the deep convection center, and outflows anti-cyclonically in the upper troposphere (Figure 1.2). The convergence at the lower level and divergence at the upper level results in rising motion at the inner-core and descending motion away from the core region. The tangential winds rotating around the center and the circulation in radial-vertical direction are referred as primary and secondary circulations, respectively. The rotational primary circulation is the dominant motion of a TC and is much stronger than the overturning secondary circulation. TCs are generally classified based on the maximum wind speeds associated with their primary circulation. The primary circulation is approximated by gradient wind equation, which results from the balance of centripetal, Coriolis and pressure gradient forces. The secondary circulation is driven by the conversion of heat energy (released as latent heat) to mechanical energy and is approximated by the Carnot heat engine.

Parametric representation of wind fields. There are various methods that allow parameterizing the TC surface wind field as a function of its main characteristics. These parametric models reconstruct the TC wind radial structure from a few parameters. These reconstructions are useful not only for TC operational forecasting but also for forcing various ocean models such as wave models, storm surge models and general circulation models, as we will see in the next chapter of this thesis. Holland (1980) used a three-parameter model to approximate the radial wind structure, including the maximum wind, the radius of maximum winds, and a parameter to control the shape of the wind profile. Willougby et al. (2004) pointed out the systematic errors associated with Holland method relative to available observations, including an overestimation of the width of maximum winds, an underestimation of the winds close to the eye and too rapid decrease of the winds on either side of radius of maximum winds (Figure 1.4). Willoughby et al. (2006) proposed an alternate radially continuous wind profile based on a statistical fit to airborne observations of 500 TCs. This double exponential wind profile fits the observed wind profiles (Figure 1.4) better and allows overcoming the shortcomings of Holland method at the expense of a larger number of parameters:

$$V(r) = \begin{cases} V_{\text{in}} = V_{\max}\,(r/r_m)^n & r \leqslant R_1 \\ V_{\text{out}} = V_{\max}\left((1-A)\exp\left(-\left(\frac{r-r_m}{X_1}\right)\right) + A\exp\left(-\left(\frac{r-r_m}{X_2}\right)\right)\right) & r \geqslant R_2 \\ V_{\text{wall}} = (1-w)\,V_{\text{out}} + w\,V_{\text{in}} & R_1 \leqslant r \leqslant R_2 \end{cases}$$

Here V_{in} is the tangential wind component within the eye, V_{out} is the tangential wind component outside the eye and V_{wall} is the transitional component over the region that lies between the two i.e. $r \leq R_1$ and $r \geq R_2$. $V_{\max}$ and r_{m} denote maximum wind and its radius. The X_1, X_2 and A parameters define the e-folding lengths and proportion of the two exponential functions. w is the parameter that allows a smooth connection between

the winds within and outside the eye. This parametric method for reconstructing TCs wind profile will be used in chapter 2.

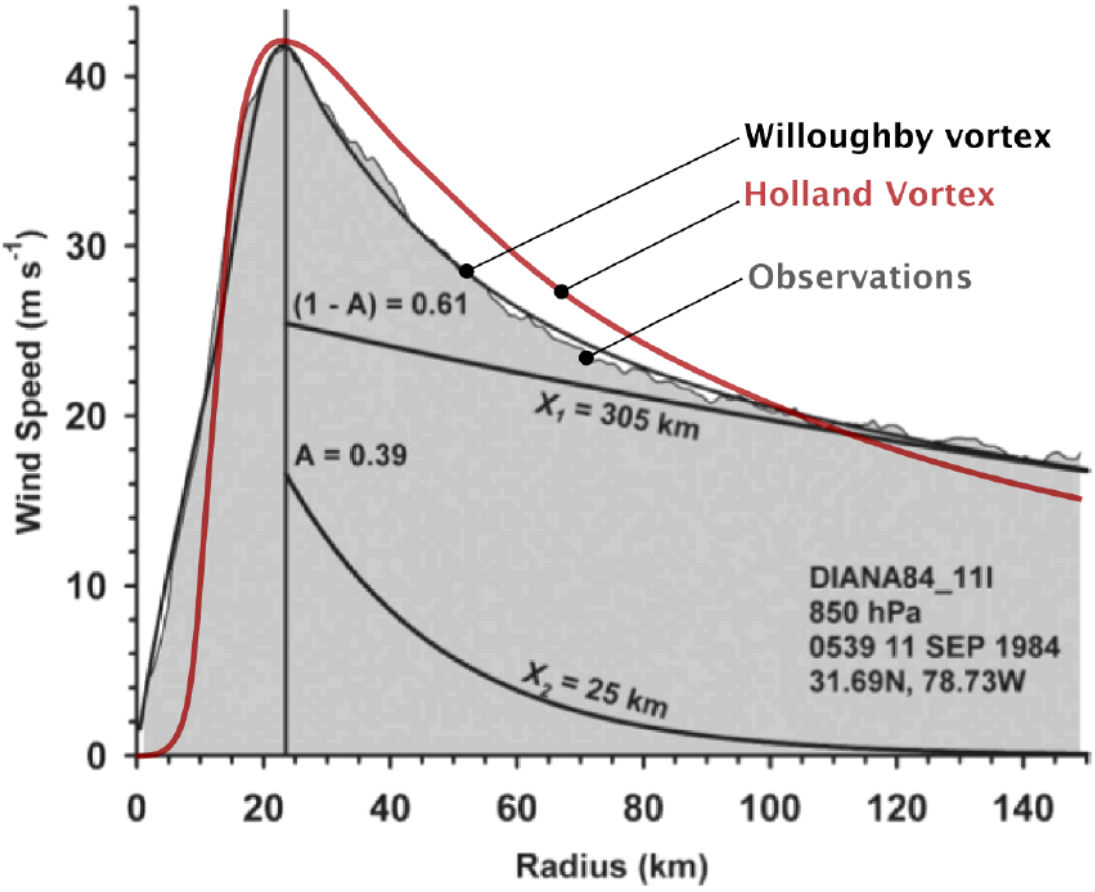

Figure 1.4: A parametric wind profile of a tropical cyclone based on Willoughby et al. (2006; dark curve) and Holland et al. (1980; red curve) compared to observed TCs winds (shading) (Willoughby et al., 2006).

1.1.3 Life cycle

The averaged lifetime of a TC is about one week. Its development stages, from genesis to decay, are described below and illustrated by Figure 1.5 for the Orissa super cyclone in October 1999.

Genesis. TC genesis occurs in areas of pre-existing synoptic-scale disturbances or cloud clusters with maximum surface winds reaching 15 m/s when the system has the

potential to intensify by utilizing the heat acquired at the surface. The TC genesis is defined as the transformation of this disorganised disturbance into an organised convection with a cyclonic wind circulation. This TC initial stage is known as tropical disturbance (winds >15 $m.s^{-1}$). Only a very small percentage of such disturbances develop into TCs. There are several processes that can initiate the formation of a self-sustained warm core vortex, including westward-propagating equatorial Rossby and mixed Rossby gravity waves, interaction of easterly waves with tropical disturbances (in the Atlantic ocean), merging of several weaker convective systems with cyclonic vorticities. The monsoon trough or inter-tropical convergence zones (ITCZ) are also identified as cyclogenesis regions, as they allow intense convection. These systems need favourable atmospheric conditions to intensify further.

Intensification. Given favourable environmental conditions, this initial tropical disturbance strengthens and evolves into a tropical storm. Convection becomes more organised and the storm intensifies. At this stage, energy gained by evaporation at the ocean surface caused by its own winds (> 18 $m.s^{-1}$) becomes the primary driving mechanism of the storm intensification and favorable environmental conditions are no longer a necessary condition for the intensification of the cyclone. The tropical storm can then evolve into a TC with surface winds exceeding 33 $m.s^{-1}$. The tropical surface pressure drops rapidly and wind starts spiralling around the centre. The cyclonic structure becomes more organised and symmetric, with circularly arranged clouds and a visible distinct eye (Figure 1.5). At this stage TC stops intensifying further, remains at its maximum intensity with lowest central pressure and maximum surface winds. TCs usually do not last long in this stage (approximately a day) and starts decaying thereafter.

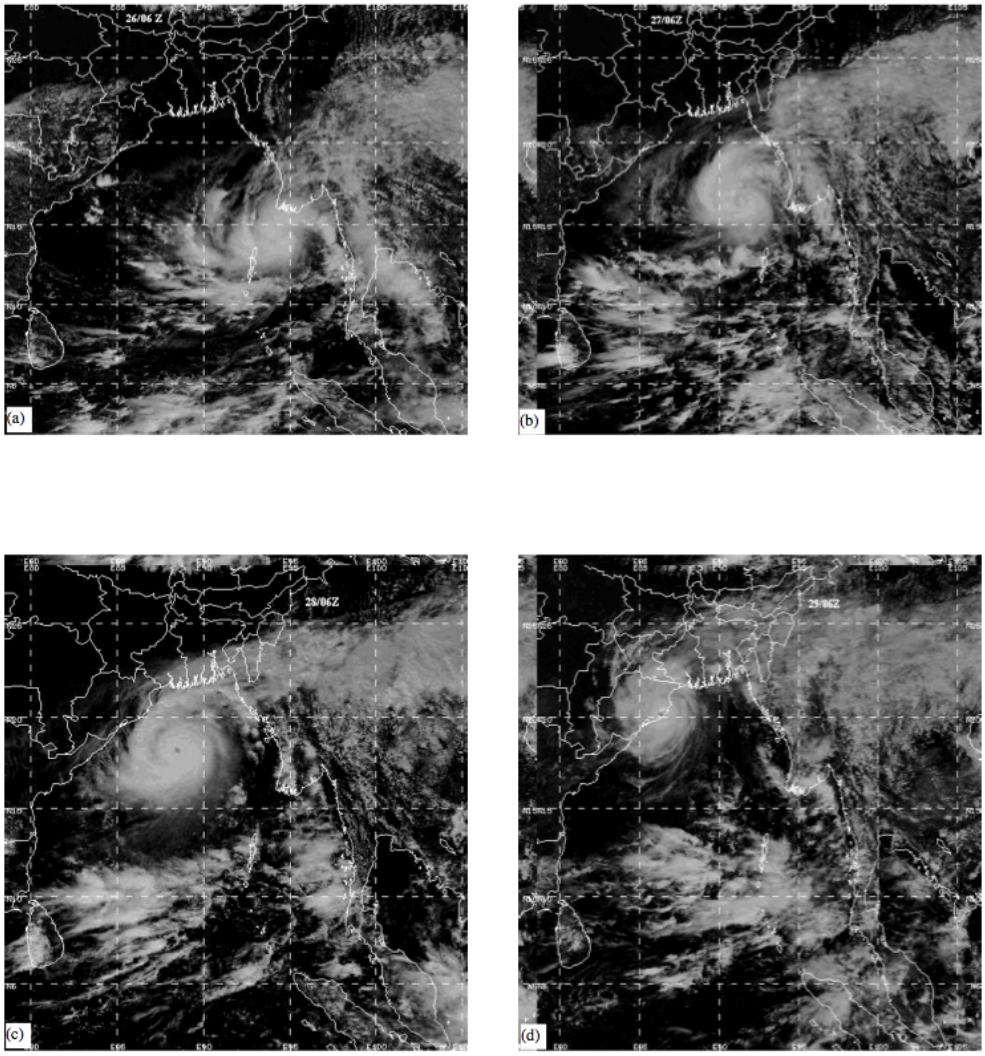

Figure 1.5: Life cycle of Orissa super cyclone, October 1999 (Kalsi, Mausam, 2006).

Trajectory. TCs generally move westward and poleward. The large-scale environmental circulation and Coriolis effect mainly control the trajectory of a TC. The westward movement is imparted by the tropospheric winds, which are westward in tropical regions. The Coriolis effect due to earth's rotation induces a poleward drift. Because of the TC translation speed, TC wind speed are generally larger on the right side (same direction of TC winds and TC motion) as compared to the left side (opposite direction of TC winds and TC motion).

Decay. TCs start decaying when environmental conditions become unfavourable. There are many ways by which a TC can dissipate. If a TC hits the land, its oceanic source of energy disappears and the TC weakens (Figure 1.5). These TCs cause great destruction in the coastal areas due to heavy rains, winds and storm surges associated with them. If a TC moves over a region where environmental conditions are unfavorable, like a strong vertical wind shear (see section 1.2), it can rapidly destroy the TC circulation.

1.1.4 TC Observations

The extreme weather conditions during TCs and its relatively small size relative to the near-surface wind and pressure observational network pose major hurdles to build reliable a TCs database based on *in-situ* observations. Since 1970s, the satellites orbiting the earth have hence been used to detect and classify TCs. These satellite-based observations rapidly became the main source that feeds existing TC databases. The frequency of the orbiting satellite pass however resulted for long in a poor temporal resolution of the order of the day, and it was only in the late 1980s that TCs hourly observation became available globally thanks to geostationary satellites. Although radiometers such as QuikSCAT provide information on TCs surface winds, they do not provide a reliable measure of the most intense winds and have an observational frequency of the order of the day. The observations in the visible and infrared (from geostationary satellites) are hence preferred to determine TCs intensity. The technique of Dvorak (1975) is used to estimate the intensity of a cyclone from satellite images of its cloud structure. The errors in the estimated maximum surface winds are at least 10% (i.e. 5-10 $m.s^{-1}$ for maximum winds of ~ 50 $m.s^{-1}$). In addition to the existing microwave satellites and coastal radars, accurate *in-situ* observations about the structure and intensity of TCs are now available from airborne measurements derived from wind

sensors (GPS drop wind sensors) deployed inside the TC (Powell et al., 2003). Routine reconnaissance flights are however only undertaken in the Atlantic. Before the satellite era, TCs trajectories included in the databases were mainly based on ship observations at sea or in coastal areas (Vecchi and Knutson, 2008). These data, collected before the satellite era, are hence very fragmented since the TCs were only observed over a limited part of their trajectories. Many TCs before 1970s are absent from this database. The variability of the TC activity at global scale can be studied from direct observational data over a period of ~ 40 years (1970- 2012). In this thesis, IBTrACS database (International Best Track Archive for Climate Stewardship) have been used that aggregate global TCs paths and intensities estimated every 6 hours by the various operational forecasts centers.

Tropical Cyclone Classifications (all winds are 10-minute averages)										
Beaufort scale[20]	10-minute sustained winds			N Indian Ocean (IMD)	SW Indian Ocean (MFR)	Australia (BoM)	SW Pacific (FMS)	NW Pacific (JMA)	NW Pacific (JTWC)	NE Pacific & N Atlantic (NHC, CHC, & CPHC)
	knots	km/h	mph							
0–6	<28	<52	<32	Depression	Tropical Disturbance	Tropical Low	Tropical Depression	Tropical Depression	Tropical Depression	Tropical Depression
7	28-29	52-56	32-35	Deep Depression	Tropical Depression					
	30-33	56-63	35-39							
8–9	34–47	63-89	39-55	Cyclonic Storm	Moderate Tropical Storm	Tropical Cyclone (1)	Tropical Cyclone (1)	Tropical Storm	Tropical Storm	Tropical Storm
10	48–55	89-104	55-64	Severe Cyclonic Storm	Severe Tropical Storm	Tropical Cyclone (2)	Tropical Cyclone (2)	Severe Tropical Storm		
11	56–63	104-119	64-74							
12	64–72	119-135	74-84	Very Severe Cyclonic Storm	Tropical Cyclone	Severe Tropical Cyclone (3)	Severe Tropical Cyclone (3)	Typhoon	Typhoon	Hurricane (1)
13	73–85	135-159	84-99							Hurricane (2)
14	86–89	159-167	99-104			Severe Tropical Cyclone (4)	Severe Tropical Cyclone (4)			Major Hurricane (3)
15	90–99	167-185	104-115		Intense Tropical Cyclone					
16	100–106	185-198	115-123							Major Hurricane (4)
17	107-114	198-213	123-132			Severe Tropical Cyclone (5)	Severe Tropical Cyclone (5)			
	115–119	213-222	132-138		Very Intense Tropical Cyclone				Super Typhoon	
	>120	>222	>138	Super Cyclonic Storm						Major Hurricane (5)

Table 1.1: Tropical cyclone classification in different basins.

TCs are classified differently in each basin based on their maximum sustained surface wind speeds or surface pressure drop at their centres. Table 1.1 lists the various TC classification scales. The objective of these scales was originally to provide simple and

representative information of potential damage to alert people living in the coastal areas. However, it is now widely recognized that the damage caused by a TC is not simply related to the maximum wind speed, but also to the size of the cyclone, its duration of exposure (hence the translational speed of TC), the extent of rainfall, as well as the sea state generated by the TC. The use of the scales listed in Table 1.1 are therefore questionable and call for the development of more relevant TC scales. It has for example been proposed to classify TCs based on the integral of the amount of energy lost through friction (Emanuel, 2005) or on the kinetic energy of the wind (Powell and Reinhold, 2007).

1.1.5 Energetics

The maximum intensity of a TC is defined in terms of maximum wind speed or minimum surface pressure. There are two widely discussed theories that explain the TC intensity and describe its energy cycle.

Classical theory: Conditional instability of second kind (CISK): Prior to CISK theory, Miller (1958) proposed a theory to explain the minimum central pressure of a TC. In this theory, the vertical temperature profile of eye was estimated by using surface temperature and humidity and the central surface pressure drop giving the strength of a TC was then calculated using hydrostatic equation. Later, Charney and Eliassen (1964) developed the CISK theory for TC intensity, consistent with Miller (1958)'s one. The CISK model assumes that the initial pressure disturbance causing low-level convergence is required for the TC formation. The moist air rises in this low-pressure area and develops deep cumulonimbus convection. The pressure is further reduced by the convective latent heat release at the upper levels, which strengthens the

initial instability. According to this theory, frictional convergence of the moist and warm air within the boundary layer causes vertical motion and release of latent heat in the vertical motion converted to mechanical energy drives the TC secondary circulation. In this theory, TC will intensify if the mechanical energy due to latent heat release exceeds the energy loss due to surface frictional dissipation.

The Carnot cycle theory: Wind-induced surface heat exchange (WISHE). TC can grow even in a convectively neutral atmosphere because of air-sea coupling. Emanuel et al. (1994) hence proposed an alternate WISHE theory by considering the air-sea interaction process as the driving mechanism of TC intensification. Here, the instability is provided by the evaporation from the ocean surface, which increases with increasing wind speed and surface temperature. This theory of TC intensification has similarities with the Carnot cycle where the net heat gain is in balance with the work done by the system. Heat is provided to the TC through the wind-induced heat transfer from the ocean surface and removed through radiative cooling in the outflow region. Figure 1.6 shows the idealized representation of Carnot cycle for TCs that can be explained in four parts.

i. Isothermal expansion: From A to B air flows towards the low-pressure area approaching the eye of a TC at a nearly constant temperature. The air gains energy and entropy from the ocean through latent heat transfer due to evaporation of ocean surface water and also due to isothermal expansion. The rate at which heat is added to the system depends on the surface wind speed and temperature.

ii. Adiabatic expansion: As the air reaches eyewall, it starts ascending and flows outwards near the tropopause from point B to C (Figure 1.6). This ascent is very rapid and therefore nearly adiabatic. No entropy change occurs from B to C.

iii. Isothermal compression: Air flows out at tropopause from C to D and losses heat/entropy isothermally due to infrared radiation to space.

iv. Adiabatic compression: Finally adiabatic compression/warming takes place from point D to A and completes the Carnot cycle.

The energy cycle is closed in this idealized theory but in reality this energy cycle is not completely closed because in the outflow region air interacts with the environmental flow.

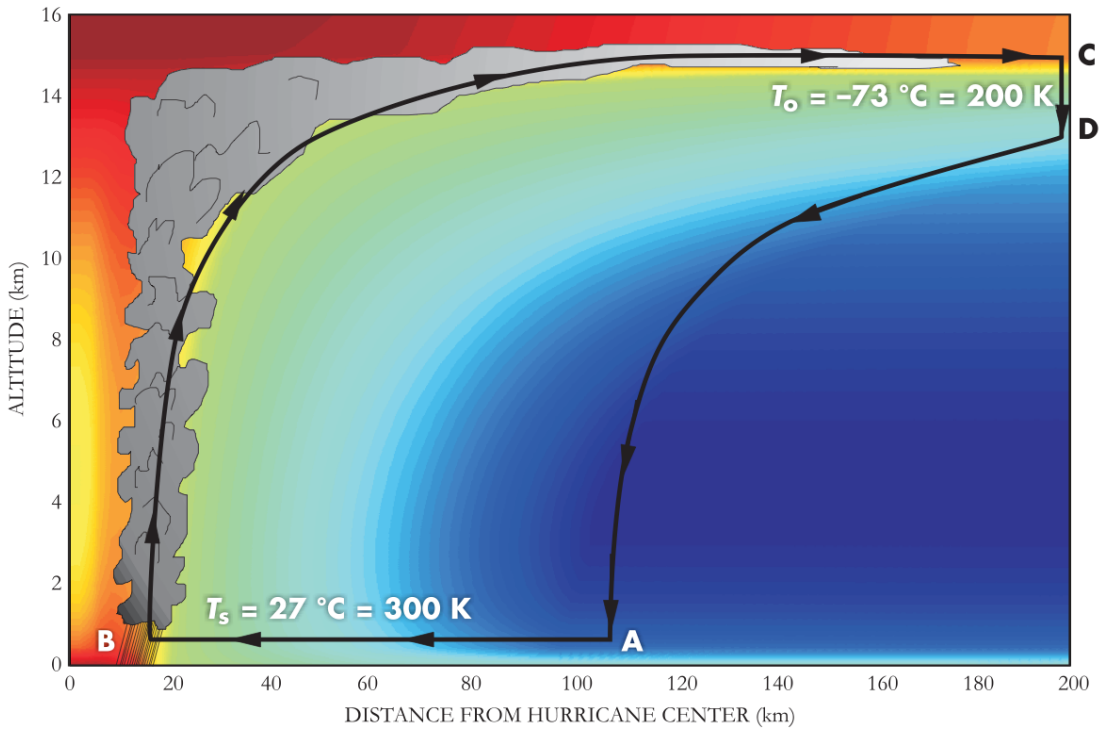

Figure 1.6: Carnot heat engine representation of tropical cyclone. Color fill is for entropy, which increases from blue to red (Emanuel, 2006).

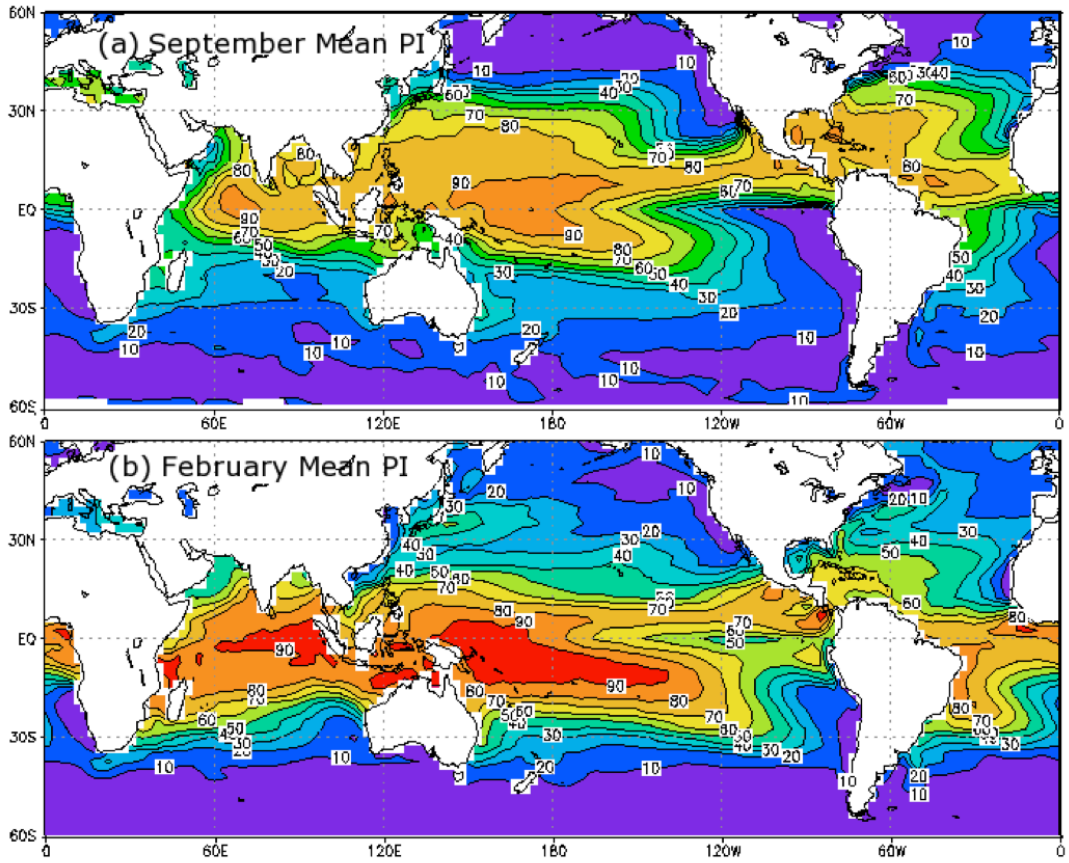

Figure 1.7: Potential intensity for the months of September (peak of TC season in northern hemisphere) and February (peak of TC season in southern hemisphere). Here maximum winds are given in m/s averaged over 1-minute period. (http://wind.mit.edu/~emanuel/pcmin/climo.html)

Potential Intensity. Using the Carnot cycle theory, Emanual (1986, 1995) estimated the maximum possible surface winds that a TC could attain and called it Potential intensity. TCs are driven by the contrast between warm tropical ocean and the cold tropopause. The maximum TC wind speed is given by

$$|V_{\max}|^2 \approx \frac{C_k}{C_D}\frac{T_s - T_0}{T_0}(k_0^* - k).$$

where T_s is the sea surface temperature and T_0 is the temperature near the tropopause (top of the TC). C_k and C_D are transfer coefficients of momentum and enthalpy. k_0* and k are the specific enthalpies of ocean surface and air near the surface. Those values are

estimated at the eyewall where winds are maximum. To calculate the maximum wind speed using this formulation, the C_k/C_D ratio is generally assumed to be 1 due to lack of measured values. This theory relates the SST to the efficiency of energy conversion from ocean to the atmosphere; increased SSTs would result in stronger TCs. Large-scale SST plays an important role in establishing a favourable environment for TCs. High SSTs are associated with particular areas of low-level convergence and cyclonic vorticity and determine the potential intensity over large areas, as shown in Figure 1.7. High SSTs also favour strong latent heat fluxes at the air-sea interface through the Clausius-Clapeyrion relation. The maximum intensity that a TC can reach is hence an increasing function of SST. Most TCs never reach the potential intensity as TCs often make landfall or face unfavourable atmospheric and oceanic conditions before that.

1.2 Influence of large-scale atmospheric environment on TCs

1.2.1 Large-scale environmental parameters influencing the TC

Although there is no theory describing the cyclogenesis, large-scale environmental conditions necessary for tropical cyclogenesis are known from empirical studies since several decades. Following Gray (1968), these conditions are the following:

1. Warm ocean with temperature (> 26^o C) in the upper 60 m of the ocean: SST plays a key role in controlling the air-sea heat exchange. Since the heat and moisture content of the surface air are closely related to the temperature of underlying water surface, warm SST is necessary for the development of mature TCs, and SSTs set the maximum intensity that can be reached by a TC given otherwise favourable atmospheric conditions (Merrill, 1988; DeMaria and Kaplan, 1994; Webster et al., 2005; Kotal et al., 2008). The amplitude of the heat exchange, the primary energy source of the cyclone, is strongly associated with high winds and is particularly high in

a 200-km radius around the centre of the TC, latent heat fluxes reaching an amplitude of the order of 1000 $W.m^{-2}$. The sensible heat flux is generally lower, around 100 $W.m^{-2}$. These surface enthalpy fluxes have an essential role in intensifying and maintaining TCs (Emmanuel, 1999).

2. Low vertical wind shear: Vertical wind shear between the low levels (850 mb) and the top of the troposphere (200 mb) is a crucial parameter affecting TCs formation, intensification and decay. In the presence of favourable conditions, TC induce a cyclonic flow, and the TC core structure remains vertically aligned in the absence of wind shear. The presence of wind shear distorts its shape and TC vortex becomes tilted in the vertical. These tilted vortex systems are not very efficient in acquiring heat and moisture from the ocean, which inhibits the TC development. A large wind shear also increases ventilation by bringing cold and dry air from the mid-troposphere into the TC. Ventilation removes the heat away from the TC and weakens the system. Empirical studies have shown that the wind shear zonal component wind shear is found to be more important than the meridional component for inhibiting TCs.

3. High mid-tropospheric moisture: High moisture content between 300 mb to 500 mb levels is also a favourable to TC generation and intensification, as it allows rapid air saturation and latent heat release through water condensation. The entrainment of dry air at mid-levels has hence been shown to weaken TCs (Dunion and Velden, 2004) and relatively humid environments are preferred for intensification.

4. Relative vorticity at low-levels: The converging winds of a TC cannot rotate in the absence of absolute vorticity. In presence of positive absolute vorticity, the converging winds of a TC produce positive relative vorticity. Surface friction in presence of low-level positive relative vorticity produces upward motion, increased cumulus convection and thus strengthens the TC intensity.

5. Away from the equator: In order to have the required vorticity ,the Coriolis parameter ($f = 2\Omega \sin\phi$, where ϕ is the latitude and Ω is the angular velocity of Earth) should exceed a certain value. No cyclones form in the immediate vicinity of equator.

6. Conditional instability: the atmospheric column should not be too stable, in order to allow moist convection.

These conditions are necessary but not sufficient for cyclogenesis and do not help predicting the development of a TC. There is a broad consensus on these necessary conditions, with the exception of mid-tropospheric high humidity content (item 3) because the convection is possible even in a near-neutral atmospheric profile (Emanuel, 1986). These conditions are generally met in Inter Tropical Convergence Zones (ITCZ). The rate of change in TC intensity is also affected by several other atmospheric parameters, in addition to above, such as potential intensity (MPI), equivalent potential temperature and upper-level air temperature (Merril, 1998; De Maria, 1996; De Maria et al., 2005; Emanuel et al., 2004; Emanuel, 2007; Frank and Ritchie, 1999, 2001; Kaplan and De Maria, 2003; Knaff et al., 2005).

1.2.2 Cyclogenesis indices

Given the list of favourable large-scale environment described above, Gray (1975; 1979) proposed an empirical cyclogenesis index referred to as the Yearly Genesis Parameter (YGP). This first index was followed by the construction of two other well-known cyclogenesis indices: the Modified Yearly Convective Genesis Potential Index developed by Royer et al. (1998) which is a variant of the YGP, and the Genesis Potential Index (GPI) developed by Emanuel and Nolan (2004). The advantage of these

indices is that they can inherently reveal the main large-scale factors influencing cyclogenesis on mean, seasonal (Menkes et al., 2012) or other timescales, such as El Niño/Southern Oscillation (ENSO) at interannual timescales (e.g. Vincent et al., 2009) or during the Madden Julian Oscillation at intraseasonal timescales (Camargo et al., 2009). The formulations of these indices are fitted empirically onto a global and seasonal scale.

We will detail the GPI formulation in the following as this index is used in chapter 3 of this thesis. The GPI monthly index is constructed as in Camargo et al. (2007a, b) and Emanuel and Nolan (2004) :

$$\mathrm{GPI} = \underbrace{\left|10^5\eta\right|^{3/2}(1+0.1V_{\mathrm{shear}})^{-2}}_{\text{dynamic}}\underbrace{\left(\frac{H}{50}\right)^3\left(\frac{V_{\mathrm{pot}}}{70}\right)^3}_{\text{thermal}}$$

with η is the absolute vorticity at 850 hPa in s^{-1}, H is the relative humidity at 600 hPa, V_{pot} is the potential intensity, V_{shear} is the magnitude of the vertical wind shear between 850 and 200 hPa in ms^{-1}. Consistently, with the previous subsection, this index increases with background vorticity, mid tropospheric humidity, potential intensity and decreases with vertical shear.

1.2.3 Global TC climatology

About 100 TCs form globally each year. The main regions of TCs formation are shown on Figure 1.8. TCs form over warm ocean water (SST > 27°C) usually between 5°-20° latitude bands. Besides ocean temperature, cyclogenesis in certain areas can be favoured by a combination of several variables. Cyclogenesis indices are used to qualitatively describe these areas as shown in Figure 1.8. There are six major tropical cyclogenesis areas in the world. The western North Pacific is the most active cyclone region (~31%

of the total number of TCs at global scale) followed by North Atlantic (~22%), Eastern North Pacific (~17%), Southern Indian Ocean (~13%) and Southern Pacific (~10%) (Figure 1.8). North Indian Ocean (NIO) is least active cyclone region (~6%) but most impacted and vulnerable basin: 14 of the 20 deadliest TCs in the world history have developed over the BoB (Longshore, 2008). Southern hemisphere TCs are relatively weaker than in the northern hemisphere. In the Western North Pacific and North Atlantic, TCs are more frequent, intense and have long life span, and their tracks can extend to very high latitude. There is a strong seasonality associated with the cyclogenesis. TCs generally occur in boreal summer (June-October) and austral summer (November-April) for northern and southern hemisphere respectively (Figure 1.9). NIO

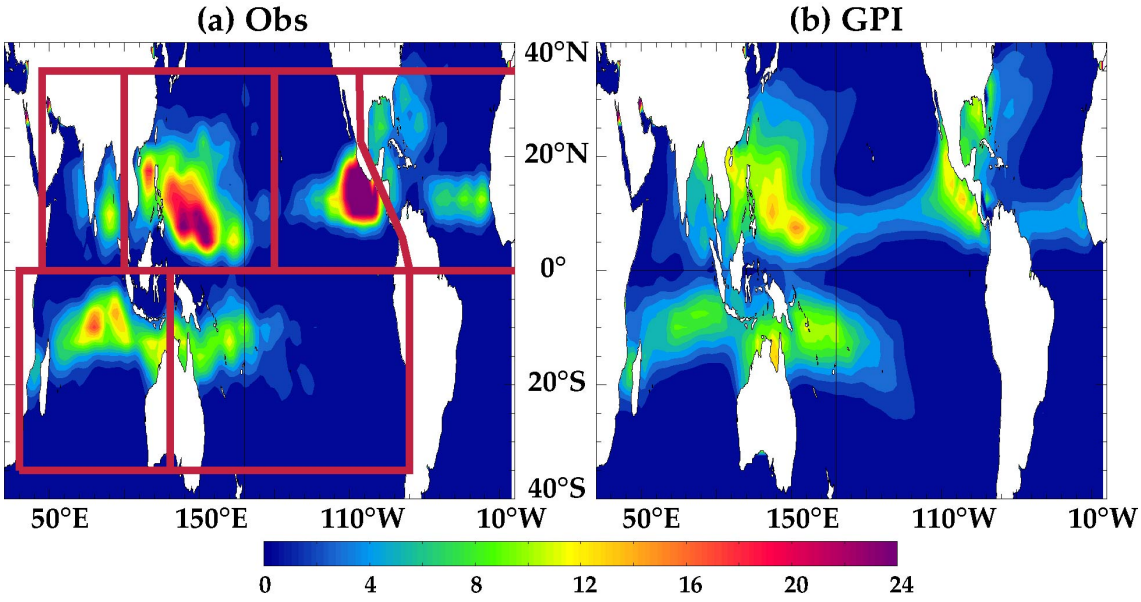

Figure 1.8: Mean cyclogenesis density per 5° box and per 20 years for the observations (left) and GPI index (right). The six red frames indicate the TCs region (NWP: Western North Pacific, NEP: Eastern North Pacific, SWP: Southern Pacific, NA: North Atlantic, SIO: Southern Indian Ocean, NIO: Northern Indian Ocean).

TCs have distinct behaviour, which will be discussed later in section 1.4. The Southeast tropical Pacific and South tropical Atlantic basins are characterized by an absence of

cyclogenesis related to anticyclonic relative vorticity, high wind shear and very stable atmosphere.

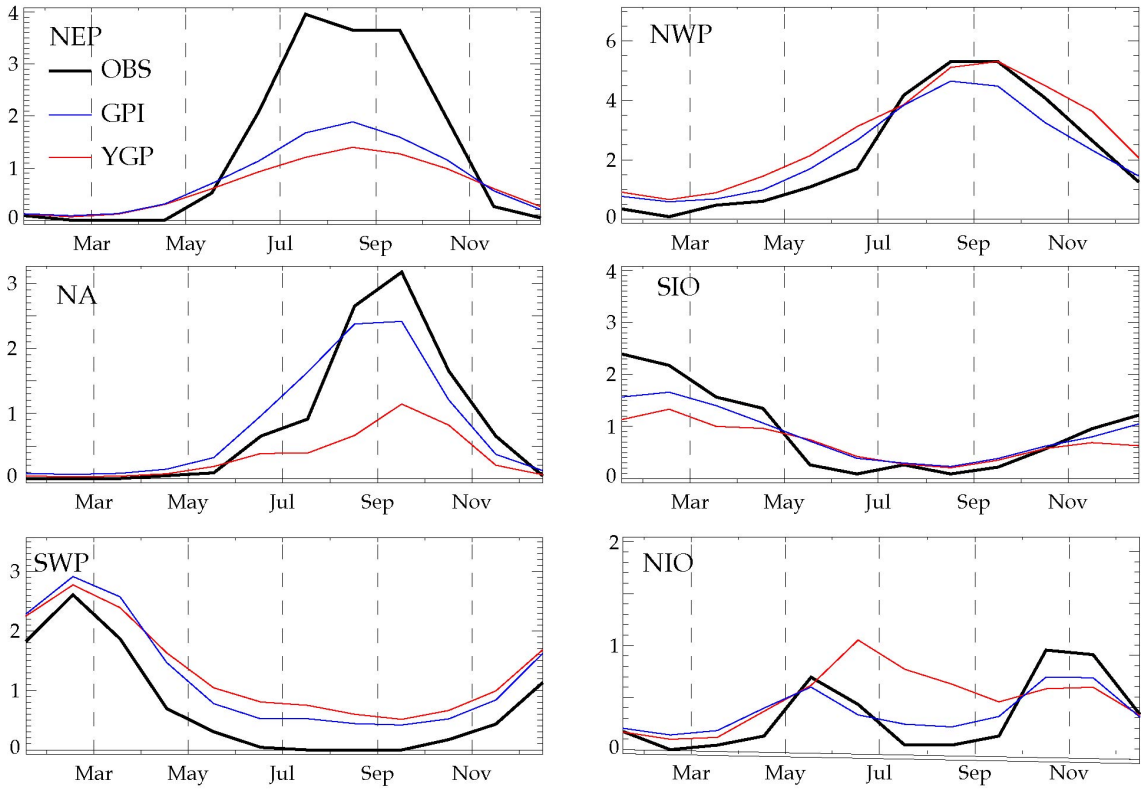

Figure 1.9: Seasonal variations of observed cyclogenesis (black), GPI and YGP indices in all regions framed on Fig. 1.8.

1.2.4 TCs intensity forecasts

Due to their tremendous societal impacts, accurate forecasts of TCs track and intensity are a very important pre-requisite for a proper risk management. The TC track is mainly governed by the environmental conditions rather than the TC's own characteristics, and is hence more predictable than its intensity. TCs tracks forecasts have dramatically improved during the last decade for both short and long lead times, while intensity forecasts have only modestly improved for long lead time, the improvement rates being only one third of the tracks improvement rates (De Maria et al., 2014). The TCs

intensity forecast errors are indeed large, reaching ~10 kt at 12 hr lead time and ~20-25 kt for 120 hr lead time (Figure 1.10; Cangialosi and Franklin, 2014; De Maria et al., 2014). Dynamical and statistical models are used for storm intensity predictions, but both of these models have large errors in predicting rapidly-intensifying TCs.

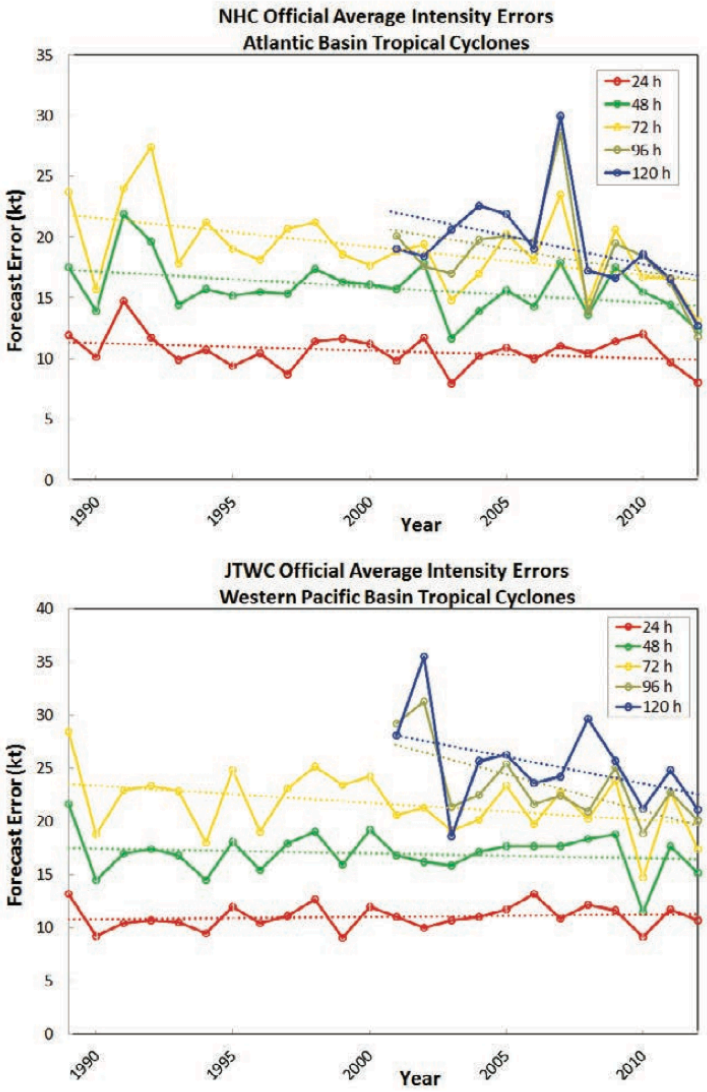

Figure 1.10: Time-series of mean absolute error in operation TC intensity forecast for Atlantic (from NHC; top) and Western Pacific (from JTWC; bottom) regions at different forecast lead-times. Dashed line indicates the linear trend (De Maria et al., 2014).

Dynamical forecast. Dynamical TCs intensity forecasts utilizes three-dimensional global or regional Numerical Weather Prediction (NWP). Dynamical models used for intensity prediction include Hurricane Weather Research and Forecasting Model (HWRF), NCEP Global Forecast System (GFS), Geophysical Fluid Dynamics Model (GFDL) Hurricane Model, European Centre for Medium range Weather forecast (ECMWF) model and Japan Meteorological Agency (JMA) model (Bao et al., 2000; Bender et al., 2007; Bender and Ginis, 2000; Hong et al., 2000; Kurihara et al., 1998; Tallapragada et al., 2014; Zhu and Zhang, 2006). The coarse horizontal resolution (~100 km) of global atmospheric general circulation models cannot resolve the storm's core structure and they are hence not very useful for intensity prediction. High-resolution regional or nested models can represent the TC core structure well but intensity prediction is still limited by the ability to initialize these models from existing observations, and by the realism of the representation of key physical processes such as deep convection, microphysics, radiative transfer. Realistic coupled ocean-atmosphere regional models developed for Atlantic and Pacific basins have been mainly used for case studies on a few storms or coarse resolution climate studies.

Statistical forecast. Statistical models are also routinely used for predicting TC tracks and intensity, along with dynamical models. These models are based on the statistical relationship of TC intensity change with the parameters known to affect the TC intensity such as the TCs characteristics at the initial time and large-scale atmospheric fields along its track, as described in section 1.2.2. The track is usually obtained from a separate dynamical model forecast, and large scale atmospheric fields along this track by weather forecasts. A part of the dataset is used in training or developing the statistical model, while the remaining independent dataset is used for testing during

hindcasts over the historical period. Intensity forecasts are generally provided from 12 hours up to 5 days lead times, at 12 hours intervals. Separate statistical models are built for each forecast hour. Multiple linear regression (MLR) techniques are generally used in developing these statistical models. These models will be described in more details in chapters 4 and 5.

Performance. Statistical model TCs intensity forecasts are competitive with dynamical models and often more skilful in predicting the TC intensity changes (Kucas, 2010). Their low computational cost and quick run-time is another added advantage for operational use. Operational statistical intensity forecast models generally predict TC intensity change for the next five days. Different operational MLR-based statistical prediction schemes have been developed for each basin: the statistical typhoon intensity prediction scheme (STIPS; Knaff et al., 2005) for the Northwest Pacific region, the southern hemisphere statistical typhoon intensity prediction scheme (SH-STIPS; Knaff and Sampson, 2009) for the southern hemisphere (gathering the Southwest Pacific and Southern Indian Ocean regions), and the statistical hurricane intensity prediction schemes (SHIPS; DeMaria et al., 1994, 1999, 2005) for the Atlantic basin. A logistic growth equation model (LGEM; DeMaria et al., 2009) with the same inputs as SHIPS is also being used for Atlantic and Northeast Pacific since 2006. A model based on STIPS (Kotal et al., 2008) has also been developed for the NIO. Very few studies attempted to compare the predictive skill of statistical-dynamical forecast models across different TC-prone regions. A recent study (DeMaria et al., 2014) provided such a comparison of the intensity error of various dynamical and statistical models as a function of the basin. (Figure 1.11). Their results indicate that these errors are generally larger in the Northwest Pacific and southern hemisphere TCs (~12kt at 24h lead-time and ~25kt at

120h lead-time) than for Atlantic and Northeast Pacific TCs (~10kt at 24h lead-time and ~15kt at 120h lead-time). The reasons behind this basin-wise skill dependency are however currently unknown. They could have several distinct origins. First, these differences may be related to the different TCs intensity distribution in each of the basin: more intense TCs in the Northwest Pacific may for instance explain the larger errors in this basin. It may however well be that the differences in the predictors and in datasets used in each of regional statistical schemes could contribute to this basin-wise skill dependency. Finally, this dependency could also simply be explained by differences in intrinsic TC intensity predictability in each basin.

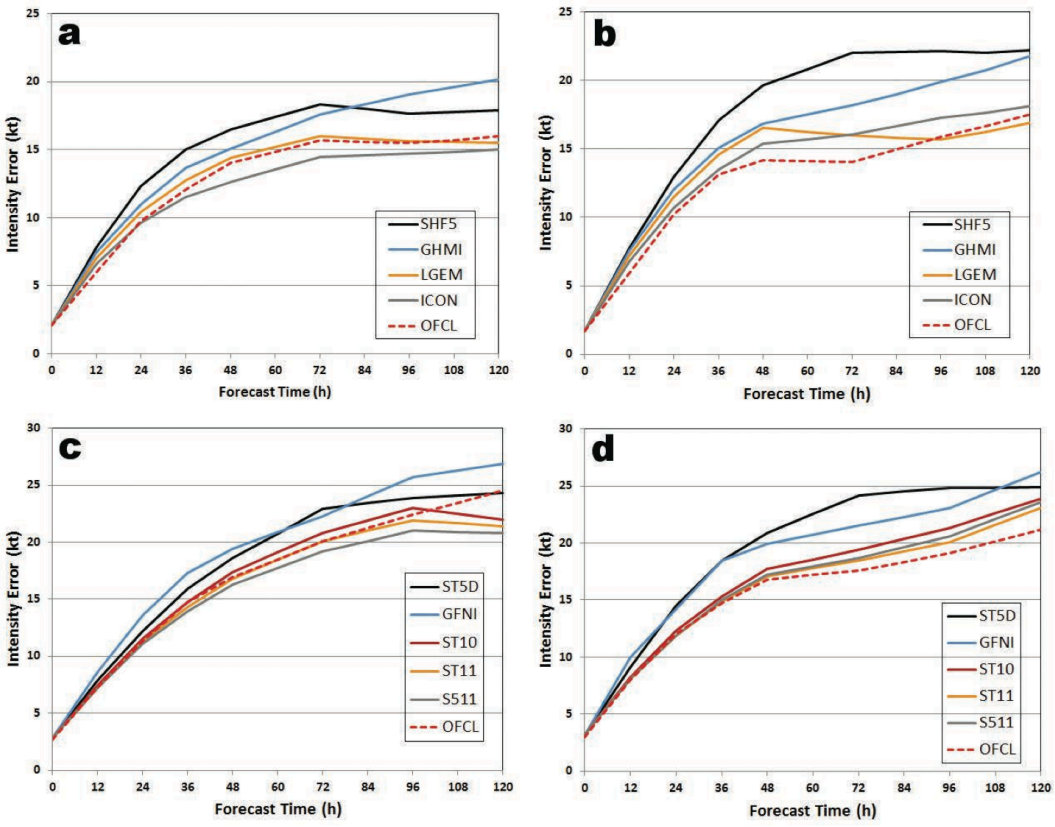

Figure 1.11: Mean absolute errors in TC intensity forecast from various models as a function forecast lead time for (a) Atlantic (b) Eastern Pacific (c) Western Pacific averaged over 2009-2012 period and (d) Southern hemisphere averaged over 2010-2012 period (De Maria et al., 2014).

1.3 Ocean response to TCs

1.3.1 Importance of vertical mixing

Mixing vs other processes. The strong cyclonic winds associated with TC affects the ocean by altering the surface wave activity, near surface currents and upper ocean heat content. Figure 1.12 summarizes the major upper-ocean processes under the passage of storm. Friction at the air-sea boundary layer supplies kinetic energy to the ocean that drives strong currents near the ocean surface. This resulting vertical shear causes vertical mixing, which brings deep and cold water into the mixed layer, and conversely warms deeper ocean layer. Energetically, this corresponds to a conversion of kinetic energy into potential energy (vertical mixing lifts the centre of mass of the water column). Vertical mixing is by far the main process that controls the surface cooling observed in the TC wake (Price et al., 1994; Jacob et al., 2000; Vincent et al., 2012a). In contrast, enhanced air-sea heat fluxes and the advection processes play a smaller role. In the following, I summarize the major processes controlling vertical mixing under TCs.

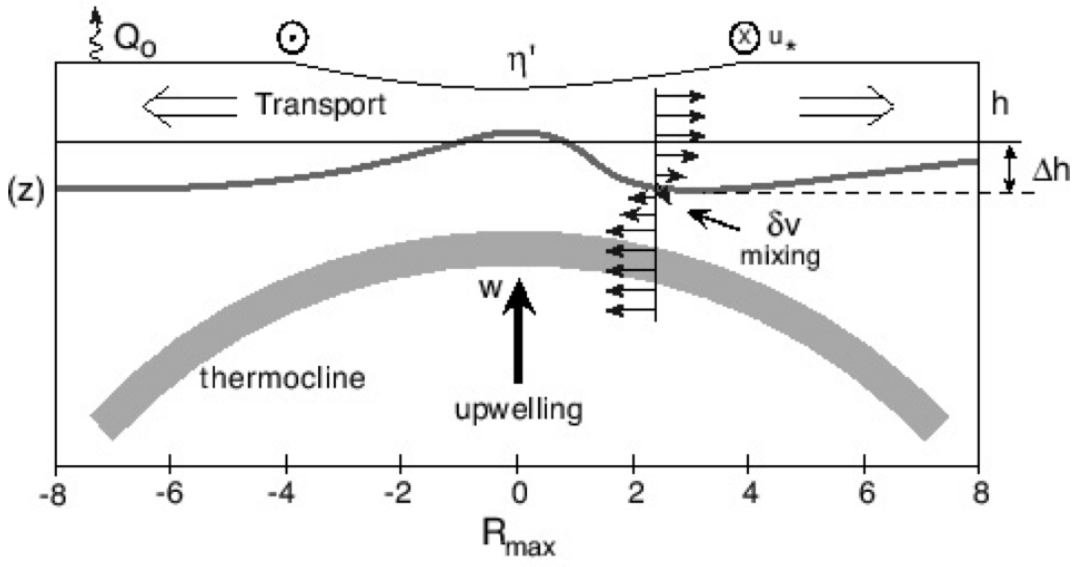

Figure 1.12: Schematic of physical processes contributing to SST cooling induced by TC winds. Q_o and Δh represents the surface heat flux and change in the mixed layer depth. R_{max} is the radius of maximum winds (Shay, 2010).

Ekman pumping. When wind blows over the ocean surface, it forms an oceanic boundary layer called the Ekman layer, whose thickness increases with the increasing wind intensity. Under the effect of the Coriolis force, the average transport in this layer (a.k.a. the Ekman transport) is at righ angle to the wind forcing (to the right in the Northern hemisphere and to the left in the Southern hemisphere). Ekman transport flows in the perpendicular direction and toward the outside of the eyewall. As a result, there is a net upwelling (i.e. Ekman pumping) within the radius of maximum winds region and net downwelling outside (Fig. 1.12).

Inertial currents. Since the timescale of change of TC wind field is comparable to the inertial period ($2\pi/f$, f being the coriolis parameter), TC wind forcing also excites near-inertial oscillations in the ocean (Sanford et al., 2007). These inertial currents are free oscillations under the influence of the Coriolis force and gravity. These currents rotate clockwise in northern hemisphere and anti-clockwise in southern hemisphere. When the vertical shear due to these oscillations is large enough as compared to the stability of the water column, it results in vertical mixing. These oscillations generally start at the surface and then propagate downwards into the thermocline region (e.g. Cuypers et al. 2013). The upper ocean currents are asymmetric in the TC wake, with larger magnitude on the right side of TC track in the northern hemisphere (Price, 1981). This asymmetry arises mainly due to two factors: (1) the translation speed and the rotational winds fields add together on the right side in the northern hemisphere and have opposite direction on the left side of the TC track and (2) the resonance between wind and inertial currents (Samson et al., 2009). Indeed, in the northern hemisphere, the TCs wind vector rotate clockwise on the right side of the track, in the same direction as the rotation of ocean

current vectors due to the inertial oscillation. On the other hand, they rotate anti-clockwise on the left of the track, and hence in the opposite direction of ocean currents. As a result, the work of wind on ocean currents (i.e. the energy transfer from the atmosphere to the ocean) is maximized to the left (right) of the TC track in the Southern (Northern) hemisphere. This resonant coupling between inertial currents and the TC wind-field generates a larger vertical mixing and hence a larger cooling to the left (right) of the TC track in the Southern (Northern) hemisphere (Price, 1981; Dickey and Simpson, 1983).

Thermal stratification. The surface cooling depends crucially on the thermal stratification of the ocean below the storm. Vertical mixing will hardly cool the surface if the thermocline is very deep. On the other hand if there is a strong subsurface thermal stratification at shallow depth, it makes the entrainment of cold water into the mixed layer and hence the surface cooling larger. As a result, for given TC properties, the cold wake is more pronounced over a region of shallow mixed layer and sharp temperature stratification (Vincent et al., 2012a).

1.3.2 Controls of the SST cooling

Amplitude of observed cooling. The TC-induced vertical mixing results in a SST cooling during the TC passage, resulting in a cold wake left behind, as captured by both satellite and in situ measurements. Before the era of satellite microwave SST, the measurements (using ship measurements, bathythermograph and buoy arrays) of SST cooling were limited to few TC case studies (Cione et al., 2000; D'Asaro, 2003; Leipper, 1967; Shay et al., 1992). Microwave Satellite measurements allowed to monitor a large number of surface oceanic response induced by TCs, allowing a more detailed

description of the SST cold wake (Chiang et al., 2011; Lin et al., 2005; Lloyd and Vecchi, 2011). Using these satellite data, Lloyd and Vecchi (2011) for instance documented the SST cooling under TCs, globally over the 1998-2007 period. The amplitude of the SST cooling ranges from 0°C to to 10° C (Chiang et al., 2011; Cione et al., 2000; Chinthalu et al., 2001; Gopalakrishna et al., 1993; Lin et al., 2003; Price, 1981; Price et al., 2008; Rao, 1987; Sengupta et al., 2008; Shay et al., 1991; Subrahmanyam et al., 2005; Walker et al., 2005). The SST cooling (~2°-3° C) associated with TC Nargis (2008) in the BoB is illustrated on Figure 1.13.

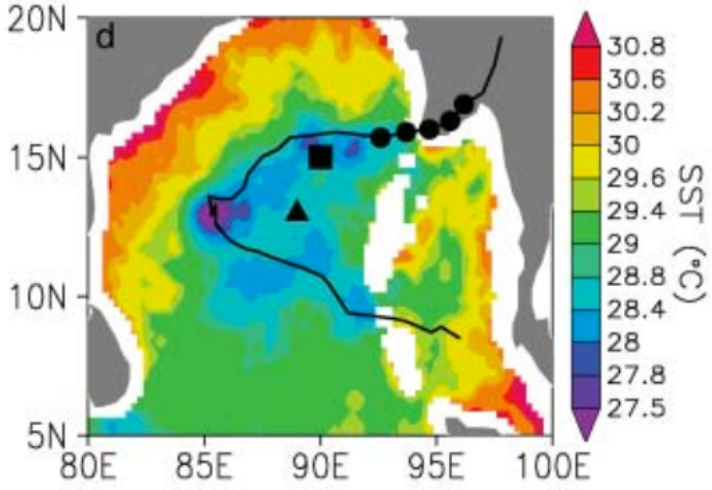

Figure 1.13: TMI/AMSR-E observed Sea Surface temperature on 2 May 2008. Black line is the track of TC Nargis and black dots indicate 6 hourly position of the eye on 2 May. (McPhaden et al., 2009).

Control by TC characteristics. TC characteristics such as the translation speed, intensity and cyclone size strongly affect the amplitude of TC-induced SST cooling (Schade and Emanuel, 1999). A slow-moving storm can produce larger SST cooling than a fast-moving storm (Price, 1981; Mei and Pasquero, 2013) as slow-moving TCs have more time to transfer momentum into the ocean, hence magnifying the vertical mixing (Mei et al., 2012). Dare and McBride (2011) quantified the amplitude of SST

cooling for slow and fast moving TCs globally. SST cooling of 1.1°C was found for TCs with low translation speed (< 8 km.h^{-1}) and 0.75°C for faster moving TCs. Lloyd and Vecchi (2011) further showed that the cooling amplitude increases linearly with TC wind intensity up to Category 2 but that saturates for Cat-3 TCs and above. Vincent et al. (2012a) attributed this peculiar behaviour to the influence of the TC translation speed that is not accounted for in the Saffir-Simpson scale. They hence developed a new dimensionless quantity, the Wind Power index (WPi), to account for the strength of TC forcing. This quantity WPi integrates many parameters that are known to influence the cold wake amplitude like size of a storm, maximum surface winds and TC translation speed in a single measure. The WPi develops on the power dissipated (*PD*) by friction at the ocean-atmosphere boundary (Emanuel, 2005), is an index that estimates the kinetic energy transferred by the TC winds to the ocean currents (Vincent et al., 2012b). The *PD* is calculated for every location of cyclone track as:

$$PD = \int_{t_o}^{t_c} \rho\, C_D |\mathbf{V}|^3 \, dt$$

and the WPi is calculated as follows:

$$WPi = \left[PD / PD_0 \right]^{1/3}$$

where ρ is the air density at the surface, C_D the surface drag coefficient (dimensionless), $|\mathbf{V}|$ the local magnitude of TC surface wind, t_o the time when a storm's influence is first felt at a given point and t_c the present time. $PD_0 = \int_{t_o}^{t_c} \rho\, C_D |\mathbf{V}_0|^3 \, dt$ is a constant used for normalization and is corresponding to a weak TC with a maximum wind speed of 15 m.s^{-1} and with a translational speed of 7 m.s^{-1} (the wind speed of 15 m.s^{-1} is associated with a very weak classified cyclonic system i.e. Tropical Depression). t_o is taken to 3 days before a cyclone reaches a considered ocean point, while t_c is set as 3 days after the cyclone passage. WPi is a proxy of the kinetic energy available for upper-ocean mixing

underneath the storm. As surface cooling largely results from mixing caused by vertical shear of ocean currents (Price, 1981; Vincent et al., 2012a), WPi is hence a relevant variable to describe it. Vincent et al. (2012a) have shown that WPi is a better predictor of the SST cooling than more classical parameters such as the TC maximum wind speed. They show that the mean cooling underneath a TC increases with wind intensity only up to the category 2 TCs as illustrated by Lloyd and Vecchi (2011), whereas it increases nearly linearly with WPi beyond the category 2 cyclones up to the largest wind power (Figure 1.14). This index will be used in later chapters of the thesis.

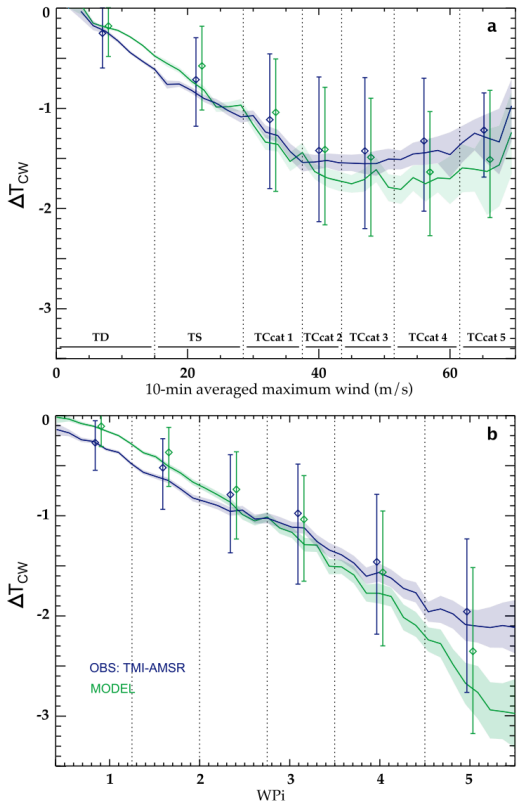

Figure 1.14: TMI/AMSR-E observed and NEMO ocean model simulated Sea Surface temperature cooling with respect to (a) 10-m averaged maximum wind speed and (b) Wind Power Index (WPi) for the TCs during 1998-2007 period. 95% confidence level, median, lower and upper quartiles for the SST are indicated by shading, triangles and vertical bars respectively (Vincent et al., 2012a).

Control by ocean stratification. As explained earlier, the vertical mixing and resulting TC cold wake not only depends on the winds but also on the upper ocean stratification

(Cione and Uhlhorn, 2003; Jacob and Shay, 2003; Shay and Brewster, 2010). Recent studies have shown that pre-storm sub-surface oceanic conditions have significant impact on the amplitude of SST cooling (Lloyd and vecchi, 2011; Vincent et al., 2012b). Shallow mixed layer and highly stratified upper ocean temperature profile favor a strong SST cooling due to efficient mixing under TCs. Deeper mixed layer associated with mesoscale features like warm core rings also significantly reduce the SST cooling under the TCs which results in its intensification (Ali et al., 2007; Hong et al., 2000; Jacob and Shay, 2003; Shay et al., 2000). The upper ocean heat content (OHC), defined as heat content of the ocean from the surface down to the 26^{o}C isotherm, is the most commonly used parameter in TCs air-sea interaction studies (Lin et al. 2008, Mainelli et al., 2008). Recently, Vincent et al. (2012a,b) showed that the control of the amplitude of the TC-induced cooling by the ocean stratification is better captured by the Cooling Inhibition index (CI). This index is based on the main physical mechanism responsible for surface cooling under TC i.e. the conversion of kinetic energy into potential energy through heat-conserving vertical mixing. Vincent et al. (2012b) showed that the amplitude of TC-induced SST cooling is proportional to the cube root of the potential energy change. Therefore CI is defined as the cube root of the necessary potential energy needed to induce a given (2°C) surface cooling through vertical mixing:

$$CI = [\Delta E_p(-2°C)]^{1/3} \quad \text{with} \quad \Delta E_p(\Delta T) = \int_{h_m}^{0} \left(\rho_f - \rho_i(z)\right) g\, z\, dz$$

where g is the acceleration of gravity, z the ocean depth, ρ_i the pre-cyclone density profile, ρ_f and h_m respectively the homogeneous final density profile and mixing depth to achieve a 2°C surface cooling through vertical mixing. The CI can easily be computed from any available temperature and salinity profiles before the cyclone passage (by assuming that mixing results in a perfectly homogeneous temperature and

salinity profile down to h_m). It captures the inhibition of mixing-generated surface cooling by the ocean background conditions. The cold wake amplitude as function of both WPi and CI is shown on Figure 1.15. Using a very simple statistical model, Vincent et al. (2012b) showed that cold wake amplitude hindcasts are more accurate with the CI than with the OHC metric.

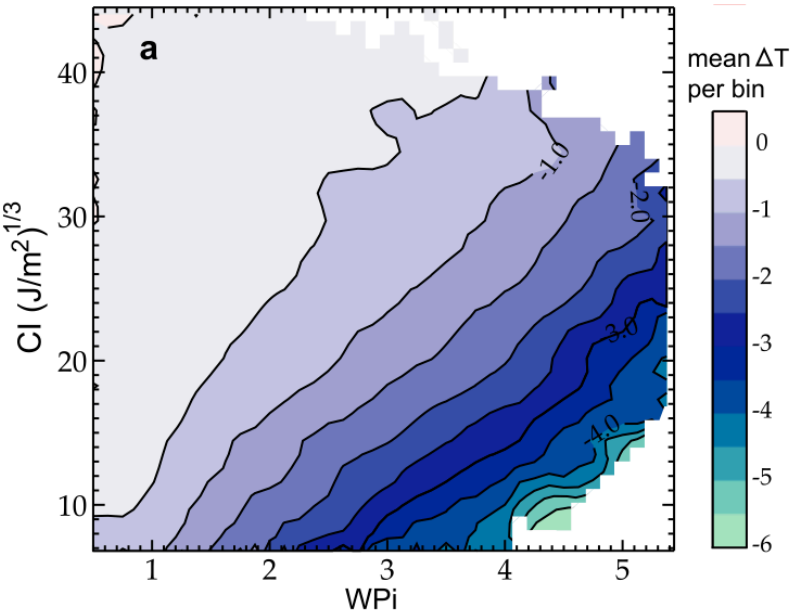

Figure 1.15: Average SST cooling as function of WPi and CI for global ocean with 40 equally spaced bins of WPI and CI each (Vincent et al., 2012b).

1.4 Air-sea coupling under TCs

1.4.1 Observational results

Theoretical considerations. The heat energy transfer from the ocean to atmosphere is a fundamental process driving the TC intensification. The SST cooling under the TC track reduces the surface evaporation due to the Clausius-Clapeyron relation. This in turn limits the upward enthalpy flux that feeds the TC. Thus, the SST cooling under TC can negatively feedback on the cyclone intensity. Thermodynamic arguments (Holland,

1997; Schade, 2000) suggest a large negative SST feedback on storm intensity, reducing the cyclone's maximum potential intensity (MPI) by 21–45 hPa.°C^{-1}. This sensitivity is much higher than that of storm intensity to the ambient (large-scale) SST estimated from thermodynamic theory (Emanuel 1988: 10 hPa °C^{-1}).

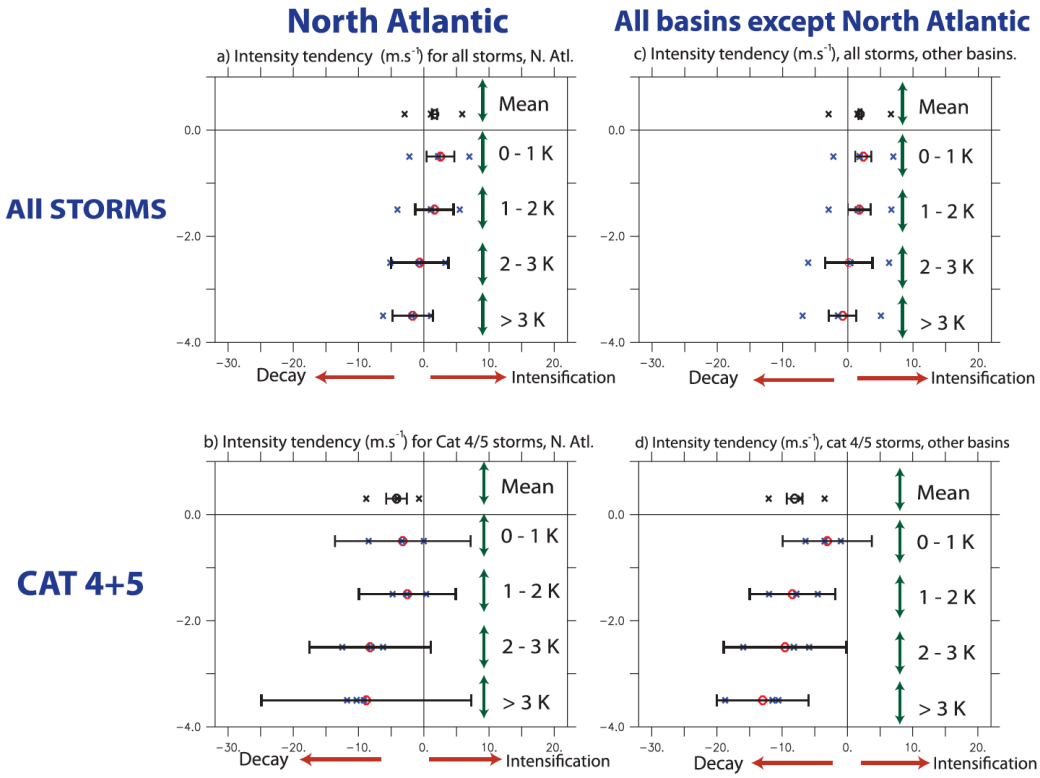

Figure 1.16: Intensification tendency for different amplitudes of SST cooling. Mean intensification tendency and 95% confidence limit are indicated by red circles and bars (Lloyd and Vecchi, 2011).

Observations. There are several observation-based studies, which have attempted to assess the impact of air-sea coupling on TCs. The theoretical estimate of the impact of air-sea coupling on TC intensity (Emanuel, 1988) was found to be in agreement with the observational study of DeMaria and Kaplan (1994a). A large number of observational case studies indeed reported that TCs passing over cold and warm oceanic eddies generally experience a rapid change of their intensification rate (e.g. Shay et al., 2000;

Lin et al., 2005; Jaimes and Shay, 2009; Zheng et al., 2010; Walker et al. 2014). A statistical analysis based on in-situ observations of 23 TCs in the Atlantic further suggested that TCs inducing large SST cooling generally experience a weaker upward surface enthalpy flux fuelling the TC (up to 40% reduction for a ~1°C cooling), and are hence less likely to intensify (Cione and Ulhorn, 2003). Lloyd and Vecchi (2011) showed that the amplitude of the TC-induced cooling is statistically related to the TC intensification rate in their observational sample (Figure 1.16). Lloyd and Vecchi (2011) further interpreted the leveling-off of the TC-induced cooling with increasing TC intensity (from Cat-2) as an evidence of the negative ocean feedback onto TC intensification. They also illustrated the influence of the upper-ocean stratification on the TC intensity: weaker stratification for stronger TCs. Emanuel (1999) showed that a 2.5°C cooling is sufficient to completely cut down the heat supply to the cyclone. The strength of the negative feedback on TCs intensity was also found to be related to TC translation speed (Figure 1.17, Lin et al., 2009; Mei et al., 2012). TCs with slow translation speed (<1.5 m/s) can weaken rapidly (Walker et al., 2014) as TCs slow translational speed contributes to increase the cold wake amplitude (Price, 1981; Price et al., 1994; Lin et al., 2009). Lin et al. (2014) also showed that fast travelling speed and warm sub-surface water caused rapid intensification of a strong TC. Zeng et al. (2007, 2008) found that fast TC translational speed and strong vertical wind shear negatively feedback the TC intensification and lifetime peak intensity. Cione (2015) showed that, along oceanic factors, near surface air temperature and moisture are dominant factors in maintaining the TC. Recent studies have shown that upper ocean warming increases the average TC intensity (Mei et al., 2015) and strong TCs frequency (Wu and Zhao, 2012). A study by Jin et al. (2014) found a strong correlation between the El Niño/Southern Oscillation (ENSO) and TC activity in the Eastern North Pacific, which they related to a

modulation of subsurface oceanic conditions and hence TC-induced cooling. Finally, the inclusion of an upper ocean parameter in statistical intensity forecasting improves TCs intensity forecast, (DeMaria et al., 2005; Mainelli et al., 2008), reducing the errors by ~5% on average.

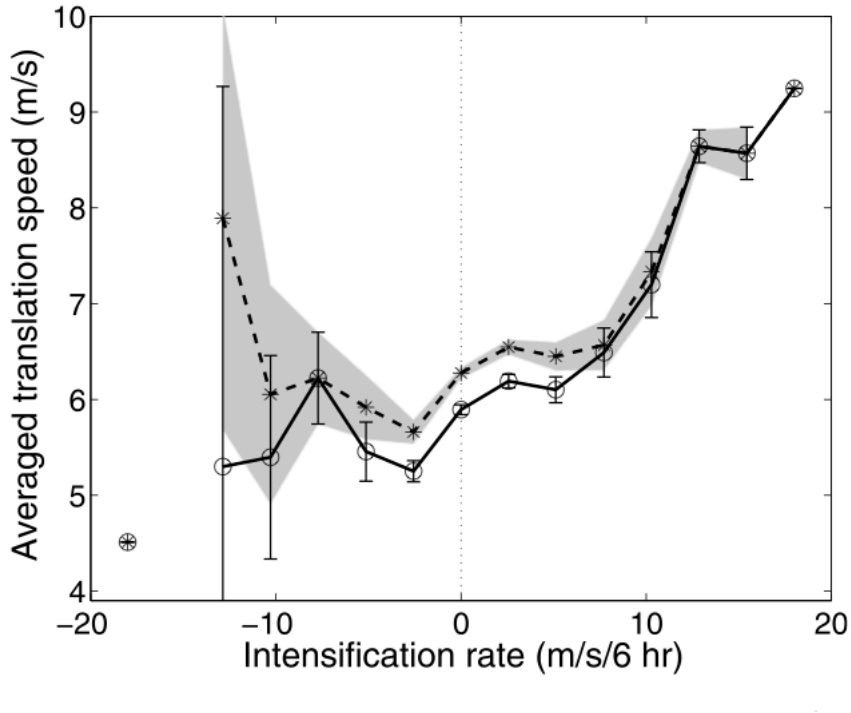

Figure 1.17: TC translation speed vs TC intensification rate in North Atlantic. Dashed and solid lines are for all translational speed data and for translational speed less than 10 m/s. Shading and bars indicate the corresponding standard errors (Mei et al., 2012).

1.4.2 Results from dynamical models

The first numerical assessment of the negative ocean feedback onto TC intensification were conducted using a very simple coupled models (Chang and Anthes, 1979; Sutyrin and Khain, 1979, 1984). Recent studies using three-dimensional atmosphere–ocean coupled models further demonstrated that forecasts of TC intensity in the North Atlantic and Pacific basins could be significantly improved when the TC-induced ocean

feedback was accounted for by imposing a limitation on the over-intensifying TCs (e.g. Bender and Ginis, 2000; Hong et al., 2000; Lin et al., 2005; Chen et al., 2010; Sandery et al., 2010; Kim et al., 2014; Ito et al., 2015; Wu et al., 2016). Other idealized modelling studies further confirmed that the TC-induced cooling limits TC intensification (Bender et al., 1993; Schade and Emmanuel, 1999; Zhu et al., 2004; Wu et al., 2007; Chen et al., 2010; Liu et al., 2011; Ma et al., 2013; Halliwell et al., 2015) but also demonstrated an impact of this ocean feedback on the TC size (Chen et al., 2010; Ma et al., 2013) and TCs asymmetrical structures (Zhu et al., 2004; Chen et al., 2010). An example of impact of SST cooling on TC intensification using idealized model experiments is provided on Figure 1.18 (Ma et al., 2013): the model including

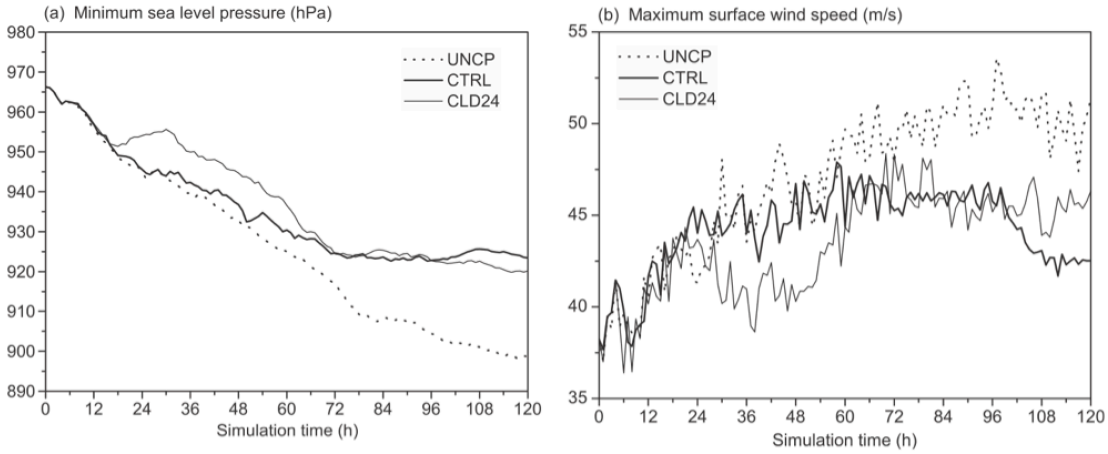

Figure 1.18: Time series of TC intensities in terms of (a) minimum sea level pressure (hPa) and (b) maximum surface wind speed (m/s) for three model experiments: Coupled ocean-atmosphere model (CTRL), idealized cold core eddy inclusion in the coupled model (CLD24) and atmospheric model with fixed SST of 29oC(UNCP))(Ma et al., 2013).

the interaction between a TC and an warm-core eddy reproduces the intensification better. In contrast, most the aforementioned studies did not find TC tracks to be sensitive to the TC-induced cooling (Zhu et al., 2004; Chen et al., 2010; Liu et al.,

2011). Finally, over the past decade, it has become increasingly clear that the oceanic component of these models needs to include three-dimensional processes to correctly simulate the TC-induced upper ocean response, especially for slow-moving TCs (Yablonsky and Ginis, 2009; Halliwell et al., 2011; Wu et al., 2016). The impact of air-sea coupling on TC characteristics has been generally assessed from realistic or idealized case studies using short-term coupled model integrations. Only a couple of studies did investigate the ocean feedback onto TCs statistics by comparing long-term (~20 years) coupled model integrations in coupled and uncoupled modes for the Northwest Pacific (Ogata et al., 2015) and Southwest Pacific (Jullien et al., 2014). Ogata et al. (2015) suggested that air-sea coupling acts to shift the location of the most intense TCs equatorward, improving the climatological distribution. They attributed the decrease in the numbers of intense TCs in the subtropical region (north of 20°N) to the shallow mixed layers and thermocline there that promote intense TC-induced cooling, hence limiting TCs intensification. Jullien et al. (2014) also suggested a more realistic cyclogenesis pattern in the coupled simulation, with reduced cyclogenesis compared to the forced run in the Coral Sea, where mixed layers are particularly shallow. Jullien et al. (2014) further demonstrated that accounting for air-sea coupling generally results in a 10% decrease in the number of TCs, with a stronger reduction for strongest TCs (Figure 1.19). In these simulations, air-sea coupling reduces the enthalpy flux (up to 30 $W.m^{-2}$ for a 1°C), resulting in a 15 $hPa.°C^{-1}$ reduction for strongest TCs. Because of the computational cost of performing long-term experiments, these study rely on relatively coarse atmospheric models that prevent simulating the strongest TCs (Cat-4 and more).

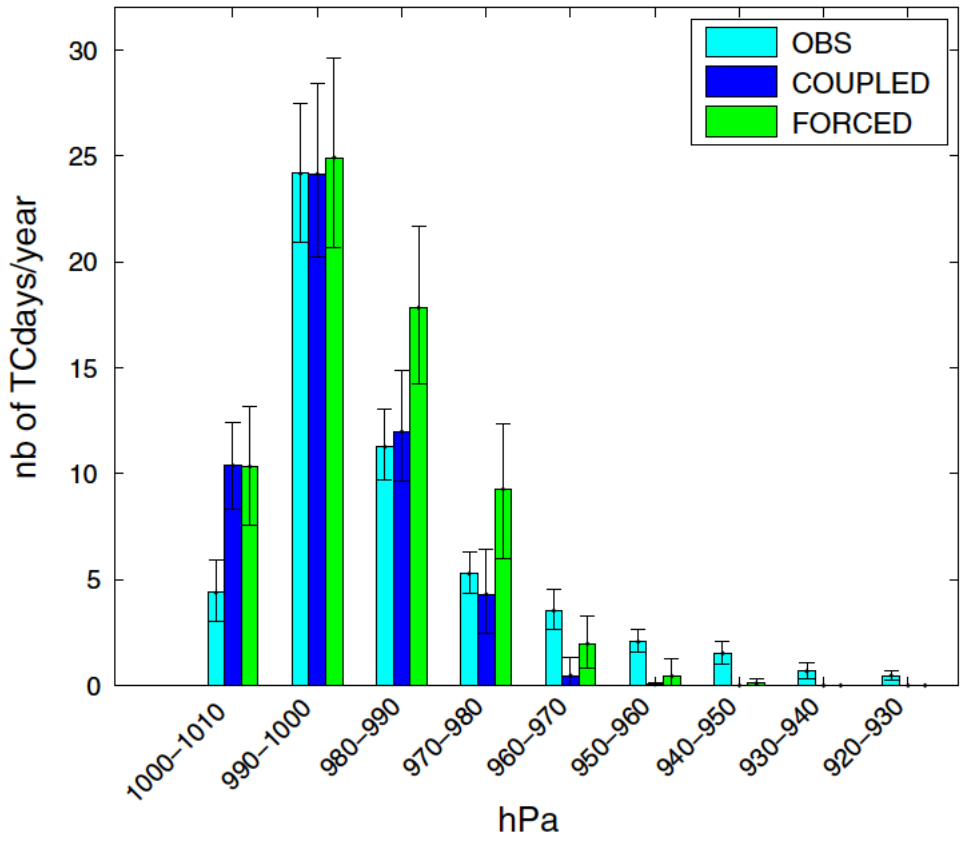

Figure 1.19: TC occurrence (number of TC days per year) as function of TC intensity (central pressure in hPa) for observation, coupled ocean-atmosphere model and forced atmospheric model (Jullien et al., 2014).

1.4.3 Results from statistical models

Feedback from the ocean is one of the under-represented mechanisms controlling the statistical TC intensity forecast (Marks and Shay, 1998). A better understanding of TC-ocean interaction is therefore likely to improve the operational predictions of their intensity. For statistical models, it is necessary to identify the mechanisms by which the ocean influences the intensity of a TC and to integrate relevant variables as additional predictors. Oceanic heat content (OHC) is the most commonly used index accounting for ocean subsurface information. It is computed as the integral of ocean temperature from surface to the depth 26^{o}C isotherm (Leipper and Vogenau, 1972):

$$OHC = c_p \rho \int_0^{D26} \Delta T(z) dz,$$

where ρ, C_p and T are respectively density, specific heat capacity and the temperature of sea water and D26 is depth of 26°C isotherm. Statistical TC intensity forecast were modestly improved by inclusion of OHC as one of the predictors (De Maria et al., 2005; Lin et al., 2013; Mainelli et al., 2008). The OHC inclusion in SHIPS slightly improves (~5%) the intensity prediction in the Atlantic, but this improvement is much larger for intense TCs (Figure 1.20, Mainelli et al., 2008). Goni et al. (2009) advocated to include improved oceanic metrics of TC-ocean interactions other than OHC in forecast models. One such metric is the depth-averaged temperature from surface up to 100m of depth (T100; D'Asaro et al., 2007). T100 represents the typical mixed layer depth under a strong TC (Price, 2009). Other alternatives suggested in the literature are the Interacting tropical cyclone heat content (ITCHC, Buarque et al., 2009) defined as the heat content of the mixed layer and depth of upper 10m average temperature minus 2°C (denoted by h_2 hereafter, Lloyd and Vecchi, 2011). As already mentioned before, Vincent et al. (2012ab) finally suggested another metric named as cooling inhibition index (CI),. Lin et al (2013) have modified the SST-based potential intensity index by incorporating the subsurface temperature information. Shay et al. (2010) have introduced equivalent OHC metric (OHC_E), which better correlates with TC intensity change and is given by

$$OHC_E = OHC\sqrt{N_{max}}/N_o,$$

where N_{max} and N_o are the maximum buoyancy frequency at the base of mixed layer and reference buoyancy frequency for a particular reference density. The inclusion of these improved ocean-atmosphere coupling metrics has the potential to improve

statistical TC intensity forecasts but none of these metrics have been tested and compared in statistical forecast models so far.

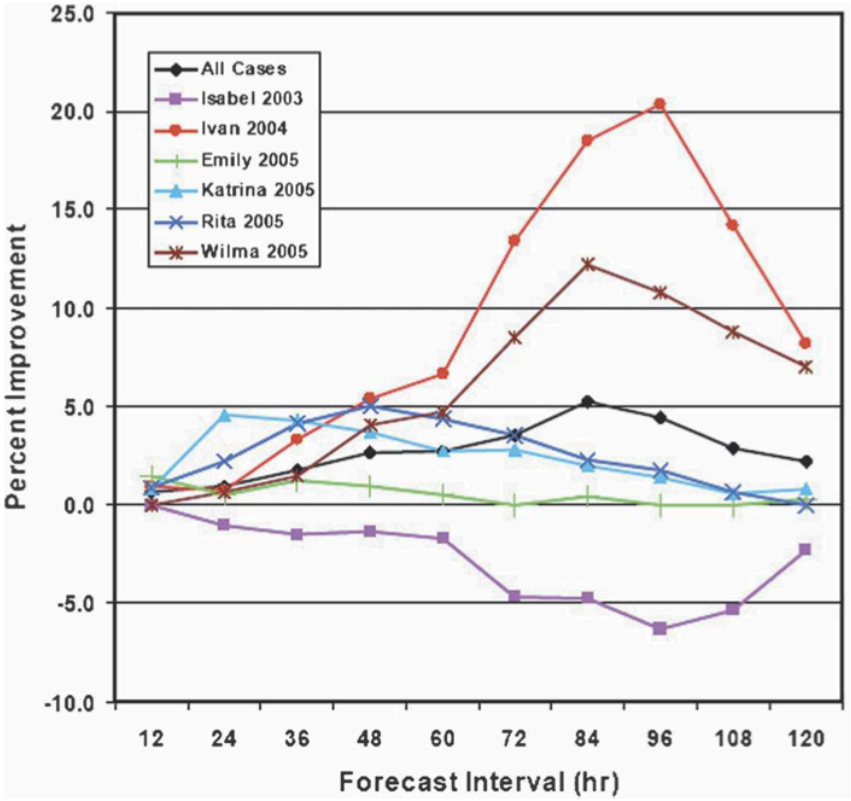

Figure 1.20: Improvement in SHIPS model forecast by inclusion of OHC for six Atlantic TCs separately and collectively (Mainelli et al., 2008).

1.5 The specific case of the North Indian Ocean TCs

1.5.1 TCs activity over the Northern Indian Ocean

TCs societal implications. Due to its unique geography and climatic conditions, the Indian subcontinent experiences a variety of weather systems like thunderstorms or monsoons depressions. But the most severe weather systems that affect the Indian coastline are undoubtedly TCs. The BoB is home to about 4 named TCs each year, which accounts for ~5% of the total annual TC numbers worldwide (Alam et al., 2003; Anwar, 1999; Neumann, 1993). There are fewer TCs (~1-2 per year) in the Arabian Sea (AS) than in the BoB and very few of them intensify to reach highTCs categories (Evan

and Camargo, 2011). These few TCs may not be the most intense but have catastrophic impacts. Of the top 20 deadliest TCs in the world history, 14 were generated in the BoB (Islam and Peterson, 2008; Longshore, 2008). The high population density distributed along low-lying coastal areas and poor disaster management strategies largely explain the very strong vulnerability of countries around the Bay (India, Sri Lanka, Bangladesh, Myanmar) to natural disasters. For instance, TC Nargis, which occurred in 2008, reached Category 4 strength and caused the worst natural disaster in Myanmar with more than 140,000 lives lost, one million homeless people, and over $10 billion in economic losses (Webster, 2008; McPhaden et al., 2009). It is therefore of utter practical importance to identify the key factors that control TC intensity in this region.

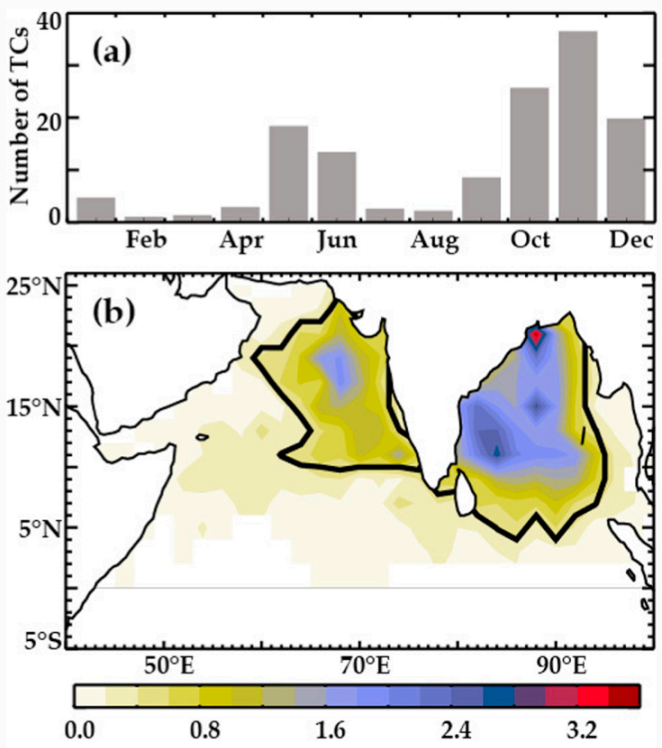

Figure 1.21: (a) Seasonal evolution of the number of TCs north of the equator in the Indian Ocean over the 1978– 2007 period. (b) Number of TCs per year in 2^{o} by 2^{o} bins over the 1978–2007 period. The thick line delineates a region where 80% of TCs occur in the northern Indian Ocean. Data set used is IBTrACS (Neetu et al., 2012).

Seasonal characteristics. In the BoB, TCs generally originate from the southern part of the bay and usually travel westward, northwestward, or northward before hitting the

east coast of India or Bangladesh, resulting in cyclone density confined towards the western and central part of the basin (Figure 1.21). In contrast to the single peak TC seasonal distribution in other basins, BoB TCs exhibits a very peculiar bimodal seasonal distribution (Girishkumar and Ravichandran, 2012; Li et al., 2013; Singh et al., 2000), with TCs primarily occurring before and after the monsoon (Figure 1.21). Li et al. (2013) examined the large-scale environmental parameters responsible for cyclogenesis and concluded that major factors responsible for TC activity are the increase in relative humidity in pre-monsoon period and the decrease in wind-shear in post-monsoon period. The absence of TC activity during the summer monsoon results from the combined unfavourable wind shear, absolute vorticity and potential intensity, which overcome the favourable increase in relative humidity (Li et al., 2013). According to Yanase et al. (2012), the reason for bimodal distribution of TCs in BoB is mainly attributable to vertical wind shear whereas Xing and Huang (2013) underline potential intensity followed by vertical wind shear. The difference in the TC frequency between the two seasons is related to the relative humidity difference between these seasons (Xing and Huang, 2013). The TCs in the AS generally originate close to the west coast of India or central AS and move towards north or northwest direction. TCs in the AS also have bimodal seasonal distribution with peak activity during pre and post-monsoon season. Changes in the large-scale environmental features like relative vorticity, low level winds and vertical wind shear together favour the TC development in both the seasons in the AS (Gray, 1968; Evan and Camargo, 2011).

Interannual variations. Besides this peculiar annual cycle, the BoB TCs also undergo significant interannual variations. The TCs characteristics over the northern Indian Ocean have been suggested to be influenced by two dominant modes of interannual

variability on the Indian Ocean climate, namely the Indian Ocean Dipole (IOD) and the El Niño Southern Oscillation (ENSO) through their atmospheric teleconnections over this region (Girishkumar and Ravichandran, 2012; Ng and Chan, 2012; Clifford et al., 2013; Sumesh and Ramesh Kumar, 2013; Mahala et al., 2015). The ENSO-induced stratification meridional dipole in BoB may indeed contribute to the interannual modulations of pre-monsoon TC intensity (Balaguru et al., 2016) . The relationship between ENSO and BoB TCs may also be modulated by the Pacific decadal oscillation (PDO, Girishkumar et al., 2015). The IOD however potentially exerts a larger control than ENSO on the BoB TCs occurrence frequency, its peak being in phase with the post-monsoon season (Yuan and Cao, 2013). More (resp. less) frequent BoB TC genesis occurs in post-monsoon season during negative (resp. positive) IOD. The main contributor to the IOD-related TC frequency fluctuations appears to be relative humidity (Li et al., 2016).

Long-term variations. Analysis of TC long-term trends over the BoB have been more limited. The intensity of major TCs has however been suggested to increase during the post-monsoon period (Elsner et al., 2008; Singh et al., 2001; Balaguru et al., 2014) due to warmer SSTs, enhanced upper ocean heat content and convective instability during the recent decades (Balaguru et al., 2014). The BoB warming may also be responsible for the increasing TC intensification rate during the pre-monsoon period (Wang et al., 2013). The intensification of pre-monsoon TCs after 1997 in the AS has further been attributed to reduced vertical wind shear forced by increased anthopogenic aerosols (Evan et al., 2011) or to an earlier onset of Indian summer monsoon due to increased land-ocean thermal contrast (Wang et al., 2012). Most of the future projections do not show an increase in the northern Indian Ocean basin-wise TC frequency (Knutson et al.,

2010). A recent study (Murakami et al., 2012) however projected an increase in the future TC frequency over the AS (~46%) and a decrease over the BoB (~31%).

1.5.2. Specific oceanic features of the northern Indian Ocean and related impacts

AS and BoB contrasts. The Northern Indian Ocean experiences intense forcing by the monsoonal winds, which are strong southwesterlies during boreal summer (June–September; Figure 1.22) and relatively weaker northeasterlies during boreal winter (November – March). Although the AS and BoB are located in the same latitudinal belt, they exhibit very different characteristics (Prasad, 2004). Winds are stronger over the AS and blow parallel to the coast in the western AS (Figure 1.22), favouring a strong upwelling signal along the coasts of Oman and Somalia maximum in summer (e.g. Schott and McCreary, 2001). In contrast, the BoB winds are weaker and have a weaker alongshore component (Figure 1.22) which does not lead to any major coastal upwelling in BoB. This keeps the summer SST warmer there as compared to the AS. The alternating monsoon winds drive seasonally reversing coastal currents along the eastern rim of BoB, popularly known as the East India Coastal Current (EICC), which flows poleward (equatorward) before (after) the summer monsoon (e.g., Shankar et al., 1996; McCreary et al., 1996). Earlier studies have recognized the role of EICC in the exchange of water masses between BoB and AS (e.g., Shetye et al., 1996; Durand et al., 2009).

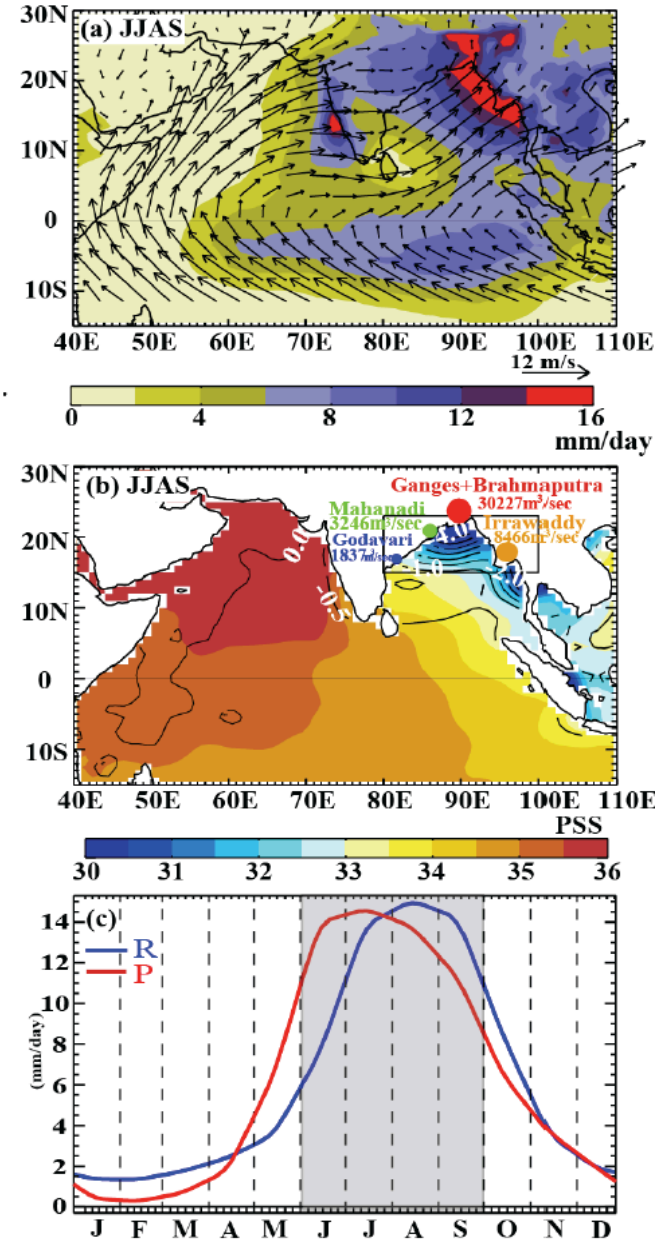

Figure 1.22: Summer climatology of (a) rainfall and surface winds (b) sea surface salinity (SSS), SSS minus salinity at 50 m depth (in contour) and (c) seasonal rainfall and river runoff in BoB north of 15°N (Akhil et al., 2014).

Contrasted freshwater forcing. In addition to those dynamical differences linked to the wind intensity, the AS and BoB also display striking difference in hydrological cycles. The Arabian Sea is an evaporation basin, while the BoB is in general a dilution basin (Shenoi et al., 2002). The BoB is also characterized by large seasonal freshwater influx, which occurs primarily during or right after the summer monsoon (Shenoi et al.,

2002). This freshwater flux occurs from rivers as well as excess precipitation over evaporation, both of which, showing nearly equal contributions (e.g. Chaitanya et al., 2014). The riverine flux into the BoB is mainly due to the Ganga-Brahmaputra river system in the head Bay and the Irrawaddy river on the eastern rim, with an average discharge of ~8.7 10^4 m^3s^{-1} and ~3.4 10^4 m^3s^{-1} respectively during July-September (Papa et al., 2012; Dai and Trenberth, 2002; Akhil et al., 2014; Chaitanya et al., 2014; Sengupta et al., 2006).

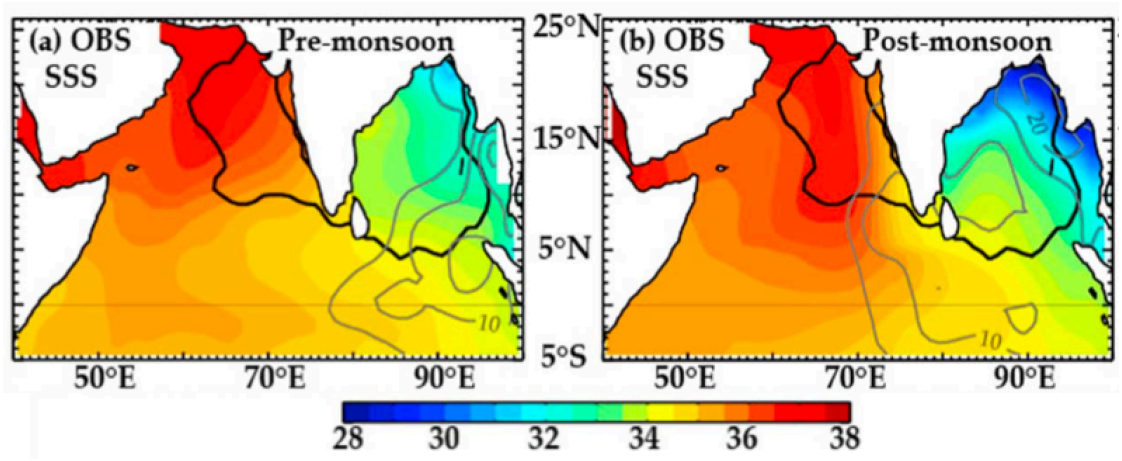

Figure 1.23: Observed SSS (in psu, color) and BLT (in meter, gray contour, 5m contour interval) during (a) pre-monsoon (b) post-monsoon seasons. Black thick line gives the region where 80% of the of TCs occur in NIO (Neetu et al., 2012).

Specific BoB SSS distribution. This seasonal freshwater influx leads to a very peculiar salinity distribution over the NIO (Rao and Sivakumar, 2003). The Arabian Sea is characterized by very salty surface waters (Figure 1.23), due to the excess of evaporation over precipitation (Rao and Sivakumar, 2003) and proximity to two high-salinity seas, namely the Red Sea and the Persian Gulf. On the other hand, the huge river runoff and excess precipitation over evaporation during summer monsoon leads to a strong near-surface halocline in the BoB. The salinity is especially low salinity (< 28 pss) in the northeastern BoB after the monsoon (Figure 1.23b), 3 psu fresher than during the pre-monsoon season (Figure 1.23a). The northern BoB freshwaters are advected

southward by the EICC in the post-monsoon season along the west coast of India into the southern BoB (Vinayachandran et al., 2005; Chaitanya et al. 2014; Akhil et al. 2014) and eastern Arabian Sea. This results in a very strong near-surface halocline along the rim of the BoB during the post-monsoon season, which affects density stratification and the depth of wind-induced vertical mixing (Vinayachandran et al., 2002). As a consequence, the mixed layer is usually shallow there and controlled by salinity stratification. This often results in the formation of a barrier layer (BL) (Lukas and Lindstrom, 1991; Sprintall and Tomczak, 1992), the salinity-stratified layer between the base of the mixed layer and the top of the thermocline (Figure 1.24). The BL that forms during summer monsoon in the northern bay exists throughout the post-monsoon season but is much thinner during the pre-monsoon season (contours on Figure 1.23; Thadathil et al., 2007).

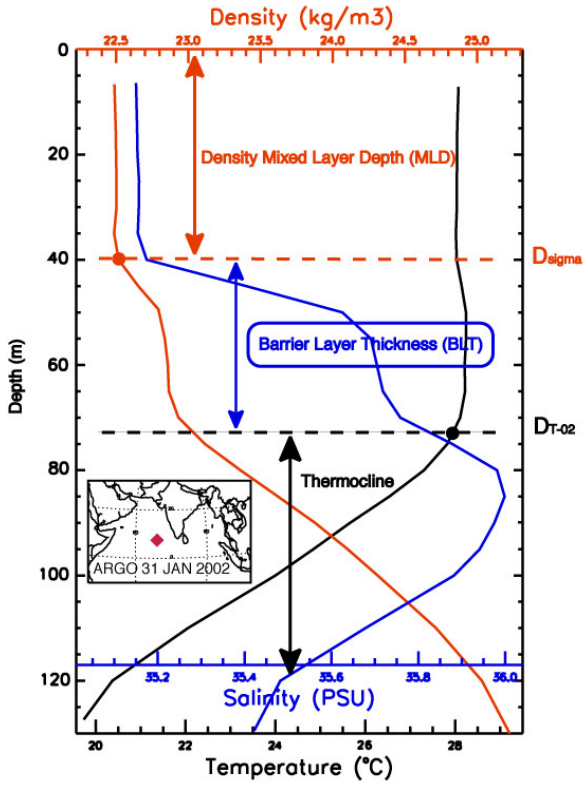

Figure 1.24: Barrier layer depiction (ARGO observed barrier layer in the Arabian Sea) (De Boyer Montégut et al. 2007a).

Climatic impacts. This presence of strong near-surface stratification and the associated BL in the BoB prevents the vertical exchanges of heat between the upper mixed layer and the thermocline. This in turn inhibits entrainment cooling of the mixed layer (de Boyer Montégut et al. 2007a), resulting BoB sea surface temperature (SST) above 28.5°C, a necessary condition to maintain deep atmospheric convection and rainfall (Gadgil et al. 1984). Thus there is a positive feedback loop between strong vertical salinity stratification, high SST, and strong rainfall (Shenoi et al., 2002), which has the potential to impact the regional climate of the north Indian Ocean. Further, this salinity stratification also influences the intra-seasonal variability (Vinayachandran et al., 2012) and biological productivity (Prasanna Kumar et al., 2002). It may likewise inhibit vertical mixing below BoB TCs and favour their intensification, as we will detail in the following section.

1.5.3 Oceanic response to TCs in the BoB

Effect of BoB stratification on TCs cold wake. Cold wakes of the order ~1-2.5^{o}C have been reported for both BoB and AS TCs (Byju and Prasanna Kumar, 2011; Murty et al., 1983; Rao et al., 2010). As in other basins, vertical mixing is the dominant process controlling the SST cooling under TCs (Girishkumar et al., 2014). Several studies also suggested that the BoB seasonal stratification changes could modulate the amplitude of TC-induced surface cooling. Indeed, case studies based on XBT profiles, ship observations, moored buoy data or satellite observations suggest that SST cooling underneath TCs is larger during the pre-monsoon (~2–3^{o}C) (Gopalakrishna et al., 1993; Rao, 1987; McPhaden et al., 2009; Sengupta et al., 2008) than during the post-monsoon (~0.5^{o}–1^{o}C) in the BoB (Figure 1.25, Chinthalu et al., 2001; Sengupta et al., 2008; Subrahmanyam et al., 2005; Smita et al., 2006). Oceanic observations for individual

case studies (Figure 1.25) suggested that the weaker observed surface cooling during the post-monsoon season results from the presence of the BL that prevents entrainment of cold water into the mixed layer (Sengupta et al., 2008; Vissa et al., 2013a). These findings led to speculate that freshwater from monsoon rain and river runoff may influence TC intensity in the BoB (Sengupta et al., 2008). Moderate (low) SST cooling under TCs were indeed observed in the areas of weak (strong) stratification (Vissa et al., 2013a; 2013b).

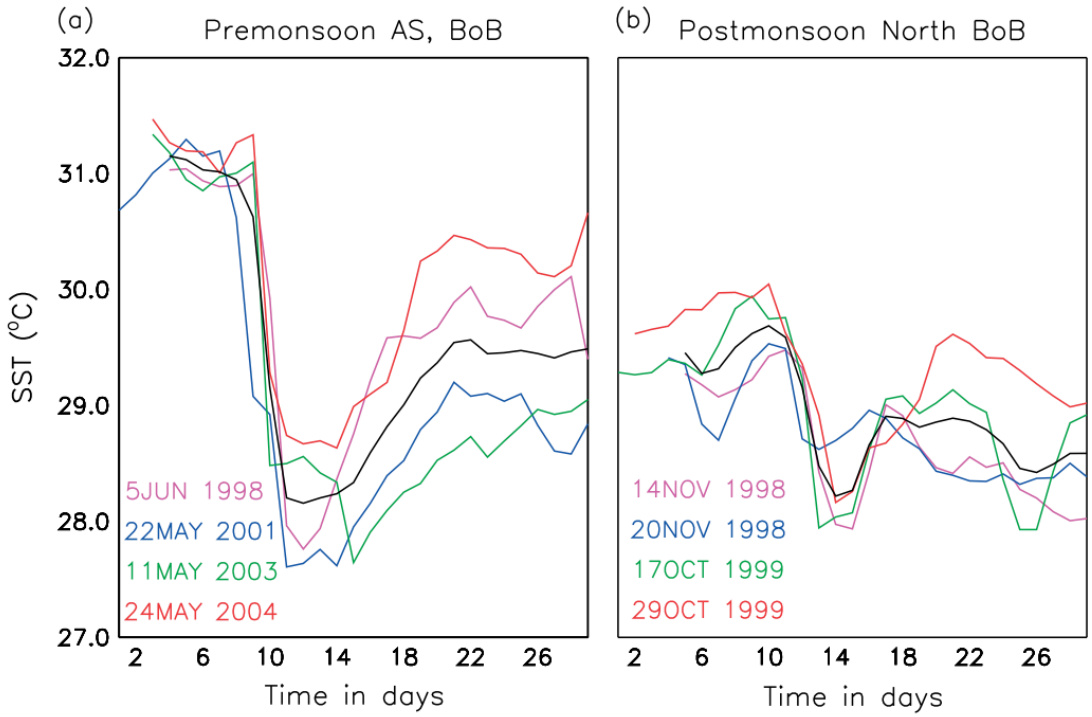

Figure 1.25: TRMM/TMI observed SST cooling under TCs during (a) pre-monsoon (b) post-monsoon season in the BOB (Sengupta et al., 2008).

Impact on TCs. Several idealized and realistic modelling case studies have also discussed the ocean response to a limited number of TCs in the BoB. The response of a 1.5 layer reduced gravity ocean model to idealized TC forcing did simulate the rightward bias in the current response (Behera et al., 1998, Deo et al., 2006). The pre-

storm vertical temperature gradient was also found to strongly modulate the TC oceanic response (Deo et al., 2006a, 2006b, 2012). The southward heat transport and reduced downward net heat flux associated to two consecutives TCs have also been shown to contribute to the OHC reduction within the BoB (Wang et al., 2012a, 2012b). Wang et al (2014) used the same OGCM to simulate the SST cooling under the two TC cases in the BoB and studied the individual ocean response to TCs forcing. Case studies of the ocean response to TCs in an OGCM suggest that turbulent mixing and upwelling were the main drivers of the heat content redistribution and temperature cooling over the upper ocean. The use of more realistic TC wind forcing in an OGCM also considerably improves the SST cooling simulated by OGCMs (Das et al., 2014). Conclusion from the above-mentioned studies largely rely on the analysis of the modelled oceanic response to a limited number of TCs. The conclusions drawn from these studies may hence not be representative of all BoB TCs.

1.5.4 Influence of air-sea coupling on NIO TCs

Observations. Only a few studies attempted to quantify the impact of air-coupling on TCs characteristics in the northern Indian Ocean from observations. Based on the analysis of satellite measurements of three TCs, (Subrahmanyam, 2005) suggested that BoB salinity stratification and AS thermal stratification could affect TC tracks. Observations further suggest that northern Indian Ocean barrier layer could considerably affect the TC intensification rate (Balaguru et al., 2012), with a ~50% increase in the TC intensification rate over regions where barrier layers were present. High SST and OHC combined with strong stratification also appears to strongly contribute to the intensification of strong TCs in the western BoB (Venkatesan et al., 2014). As in other regions of the world, satellite analysis suggest that warm core eddies

could promote TC intensification in the BoB (Ali et al., 2007, Sadhuram et al., 2012). Despite these observational suggestions that air-sea coupling may strongly influence TCs characteristics in the BoB, there is to date no specific study quantifying this influence using dynamical models.

1.5.5 TCs forecasts

The India Meteorological Department (IMD) is the agency responsible for official TC track and intensity forecasts for the northern Indian Ocean. TC intensity forecasts are issued by analysing the numerical weather predictions from different international agencies and statistical models (Kotal et al., 2008) implemented at IMD (Mohapatra et al., 2013). A review of the intensity forecast for the TCs that occurred during 2005-2011 period in northern Indian Ocean show that the average absolute intensity errors (with respect to persistence) were about 11, 14 and 20 knots for 24, 48 and 72 hours forecast lead times respectively (Figure 1.26), which amounts to predictive skill of 44%, 60% and 60% at these forecast lead hours. Errors are relatively larger for stronger category TCs (Figure 1.27), probably because the models inability to predicting rapidly intensifying TCs.

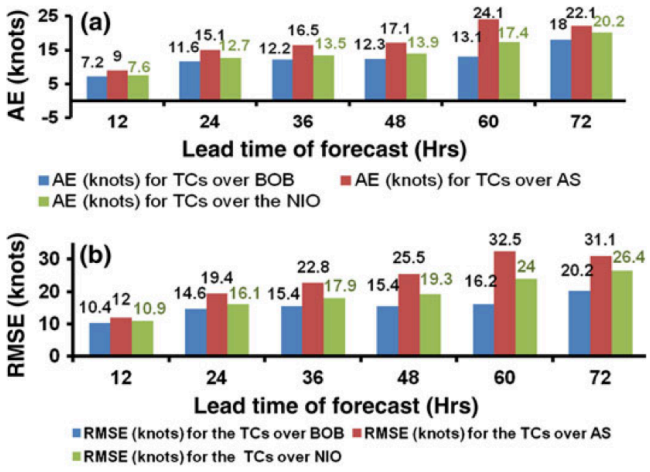

Figure 1.26: Average lead time TC intensity forecast errors for TCs over AS, BoB and NIO (Mohapatra et al., 2013).

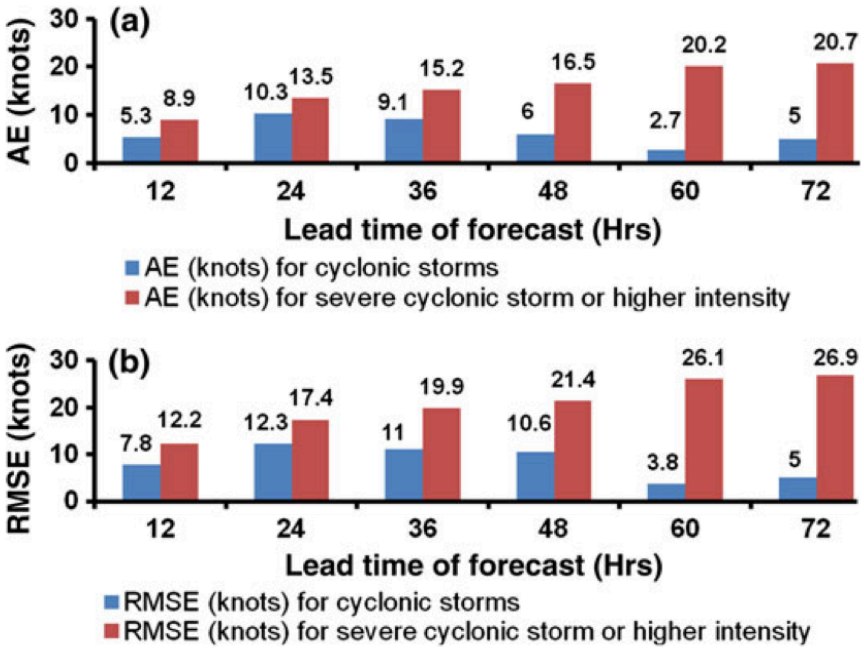

Figure 1.27: Average official intensity forecast errors for strong and weak TCs over a period of 2009-11 in NIO (Mohapatra et al., 2013).

1.6 Aim and objectives of the thesis

While several statistical (e.g. Mainelli et al., 2008) and coupled model-based (e.g. Jullien et al., 2014) studies have already addressed the influence of ocean-atmosphere coupling on TCs characteristics in the Atlantic and Pacific, this topic has not been much investigated in the northern IO. The tremendous human and socio-economical consequences of these extreme events as well as the specificity of the hydrography of the BoB, which leads to a very strong salinity stratification in the post-monsoon season, urge to an in-depth investigation of the influence of ocean-atmosphere coupling on TCs characteristics in this region, through the use of both statistical and dynamical modelling.

More precisely, this research focusses on the following three major objectives:

- **Identifying the specific impact of the haline stratification on oceanic TC-induced response in the Bay using a forced ocean model:** Only a few observationally based case studies have addressed interactions between tropical cyclones and the upper ocean in the Bay of Bengal (e.g. Sengupta et al., 2008, Vinayachadran and Mathew, 2003). Based on the case study of eight TCs, Sengupta et al. (2008) suggest that the weak observed surface cooling after the monsoon in the BoB is due to haline stratification. This small sample prevented a quantitative estimate of the respective influence of haline and thermal stratification and TCs winds intensity on the amplitude of the surface ocean response to TCs. This first objective of this PhD is hence to analyze a much larger sample derived from an ocean simulation forced by a realistic TCs wind forcing over the 1978-2007 period. This simulation hence provides a relatively large sample consisting of the simulated oceanic response to 135 TCs over a 30 years period.

- **Quantifying and understanding the feedback of this TC-induced cooling on the IO TCs characteristics by using a regional high resolution coupled model:** The investigation of the role of air-sea coupling on TCs using long three-dimensional coupled ocean-atmosphere model simulations has only be performed in the Atlantic and Pacific basins to date (e.g. Bender and Ginis, 2000; Jullien et al., 2014; Ogata et al., 2015). The second objective of this PhD is hence to investigating the role of ocean-atmosphere interactions on TCs

characteristics in this basin. I will benefit from the recent development of a 25-km resolution regional coupled ocean-atmosphere model for the IO, which is able to reasonably reproduce the cyclonic activity and its related ocean-atmosphere interactions. To isolate the role of the oceanic feedback onto TCs characteristics, I will compare TCs statistics from two twenty year-long experiments (a reference coupled experiment and forced atmospheric experiment with no air-sea coupling) to provide a reliable statistical assessment of the air-sea coupling impact on IO TCs.

- **Quantifying the influence of air-sea coupling on TCs characteristics in the Bay of Bengal using statistical TC intensity forecast models:** A commonly used metric of the TC sensitivity to the ocean subsurface structure is the TC heat potential, a measure of the heat content between the sea surface and the depth of the 26°C isotherm (e.g. Goni and Trinanes, 2003). The inclusion of this heat potential as an additional predictor in the widely used linear statistical prediction models of TCs intensity in Atlantic and Pacific oceans only resulted in a very modest skill improvement (DeMaria et al., 2005; Mainelli et al., 2008). This prompted several authors to propose better-suited metrics of air-sea interactions under TCs, such as the physically based cooling inhibition index proposed by Vincent et al. (2012b). While a linear statistical TC intensity forecast model has been developed for the Bay of Bengal (Kotal et al., 2008), the improvement brought by including subsurface oceanic information has not yet been quantified. Owing to the non-linear nature of the relationship between oceanic parameters and TC intensification rate, the last objectives of this PhD are hence to assess the additional skill yielded 1) by using non-linear statistical schemes (artificial

neural network or support vector machine) instead of the commonly used linear regression models and 2) by including physically-based oceanic subsurface information in the model predictors, with a particular focus on the northern IO.

Chapter 2 Sea Surface temperature response to tropical cyclones in the Bay of Bengal

2.1 Introduction

Previous studies suggest that the seasonal stratification changes modulate the amplitude of TC-induced surface cooling in BoB. Indeed, SST cooling underneath TCs is larger during pre-monsoon (~2-3°C; Gopalakrishna et al., 1993; Rao, 1987; Sengupta et al., 2008) than during post-monsoon season in the BoB (~0.5°C-1°C; Chinthalu el al., 2001; Sengupta et al., 2008; Subrahmanyam et al., 2005). From oceanic observations for individual case studies, Sengupta et al. (2008) suggested that the weaker observed surface cooling during the post-monsoon season results from the presence of the barrier layer (BL) that prevents entrainment of cold water into the mixed layer. These findings led the authors to speculate that freshwater from monsoon rain and river runoff may influence TCs intensity in the BoB.

The aforementioned study relies on a restricted number of TCs (eight) and CTD data over a short period (October 2003), which prevented the authors to provide a quantitative estimate of the respective influences of the seasonal changes in haline and thermal stratification on the differences in TC-induced cooling amplitude between the two seasons. In the present study, we address this issue using a much larger sample. This is made possible by the use of Vincent at al. (2012a) global ocean simulation which includes TC wind forcing prescribed from an analytical vortex fitted to observed TC tracks and intensities over the 1978-2007 period. This simulation captures reasonably well the main characteristics of TC-induced surface cooling at the global scale (Vincent et al., 2012a). Our approach hence provides a relatively large sample consisting of the simulated oceanic response to 135 TCs over a 30-year period in the

BoB. While Vincent et al. (2012b) discusses the sensitivity of TC-induced cooling amplitude to the pre-cyclone stratification at global scale, it neither discusses regional aspects nor the potential salinity contribution to the upper-ocean stratification. The present study hence allows investigating TCs surface response in a region where salinity stratification is known to be particularly strong and has hence been suggested to influence to TC-induced cooling amplitude.

The chapter is organized as follows. Section 2.2 briefly describes the observational datasets as well as numerical strategy. Section 2.3 validates the model climatology and cold wake characteristics for the pre-monsoon and post-monsoon seasons. We then analyze and relate differences in TC-induced cooling between the two seasons to the thermohaline stratification in Section 2.4 and further quantify the respective contribution of temperature and salinity stratification to the TC-induced cooling amplitude. The final section provides a summary of the results and a discussion of their implications.

2.2 Data and methods

2.2.1 Observed datasets

The observed datasets used in the present study are listed in Table 2.1. We use the temperature and salinity of the North Indian Ocean Atlas (NIOA; Chatterjee et al., 2012) to validate the model (discussed in section 2.2.2) climatological thermohaline structure in the BoB. This monthly climatology of 1° x 1° spatial resolution uses all the data accounted for in the World Ocean Atlas 2009 (Locarnini et al., 2010; Antonov et al., 2010), but adds a considerable amount of data from Indian sources, especially within the Indian Exclusive Economic Zone. This addition improves considerably the climatology in the BoB compared to the WOA, especially along its western boundary

(Chatterjee et al., 2012). We also validate the simulated mixed layer depth (MLD) and BL thickness (BLT) to the updated MLD climatology and BLT climatology of de Boyer Montégut et al. (2004, 2007b), which now includes ARGO profiles until September 2008.

The 0.25° x 0.25° spatial resolution daily SST derived from the blended Tropical Rainfall Measuring Mission (TRMM) Microwave Imager (TMI) and Advanced Microwave Scanning Radiometer (AMSR-E) (downloaded from http://www.ssmi.com/sst/microwave_oi_sst_data_description.html) is used in the analysis. This dataset is used to describe the SST response to TCs over the period of 1998-2007 in the observations and for the validation of model simulated SST response to TCs. Though TMI/AMSR-E is unable to retrieve SST under heavy rainfall conditions, it is still advantageous to use this data due to its insensitivity to atmospheric water vapor (Wentz et al., 2000). It provides the accurate SST observations below the clouds, a few days before and after the storm passage. The inner-core cooling (i.e. cooling underneath the eye) cannot be assessed confidently with TMI-AMSR-E, since data are most of the time missing within 400 km of the current TC position. This dataset provides a consistently good estimate of SST cooling under the tracks of TCs, generally data being available just one or two days after the cyclone passage.

Observed TC location and maximun wind intensity are derived from the International Best Track Archive for Climate Stewardship (IBTrACS; Knapp et al., 2010). Here, we focus on global satellite coverage period 1978-2007, over which the location and estimated magnitude of wind speed is available at six hourly basis for more than three thousand TCs. worldwide (135 in the BoB). To define the pre-monsoon and the post-monsoon seasons, we consider the months when at least five TCs occurred during the 1978-2007 period. May-June will then be considered as the pre-monsoon season and

September-October-November-December as the post-monsoon season. It should however be noted we defined those periods based on cyclonic seasons rather than traditional monsoon (the months of June and September being usually encompassed within the monsoon period (Wang et al., 2009)).

S. No.	Parameter	Description
1	SST	Blended TRMM/TMI and AMSR-E daily SST
2	Temperature and Salinity climatology	North Indian Ocean Atlas (NIOA; Chatterjee et al., 2012)
3	Mixed Layer Depth and Barrier Layer Thickness climatology	de Boyer Montégut et al. (2004, 2007b),
4	Tropical cyclone position and intensity	IBTrACS dataset (Knapp et al., 2010).

Table 2.1: Data used in the study.

2.2.2 Model description and setup

The model configuration and strategy to include TC forcing have been previously described in Vincent et al. (2012a). The following section provides a short summary of this modeling framework.

Global ½° ocean model configuration (known as ORCA05, Biastoch et al., 2008) built from the NEMO (Nucleus of European Model of the Ocean, version 3.2; Madec, 2008), with 46 vertical levels (higher resulotion in the upper layers; upper 100 m depth with 10 vertical levels and 250 m resolution at deeper depths) is used in the present study. This configuration includes the latest version of mixed layer dynamics: a Turbulent Kinetic Energy (TKE) closure scheme (Blanke and Delecluse, 1993) improved by including the effect of Langmuir cells and incorporating surface wave breaking parameterization

(Axell, 2002; Mellor and Blumberg, 2004). This scheme also uses energetically consistent time and space discretization (Burchard, 2002; Marsaleix et al., 2008). This configuration successfully reproduces Indo-Pacific ocean variability from intra-seasonal to decadal time scales (Penduff et al., 2010; Lengaigne et al., 2012, Keerthi et al., 2013; Nidheesh et al., 2013) as well as the local SST response to TC winds forcing (Vincent et al., 2012a).

In this model, the MLD is defined as the depth where the vertical density increases by 0.01 kg.m^{-3} as compared to water density at the surface. The various terms, which contribute to the heat budget of the mixed layer (ML), are calculated online in the model. In the model, the ML temperature evolution equation reads:

$$\partial_t T = -\underbrace{\left\langle u\partial_x T + v\partial_y T + w\partial_z T \right\rangle}_{a} + \underbrace{\left\langle D_l(T) \right\rangle}_{b} - \frac{1}{h}\underbrace{\frac{\partial h}{\partial t}\left(T - T(z=h)\right)}_{c} + \underbrace{\frac{\left(k\partial_z T\right)(z=h)}{h}}_{d} + \underbrace{\frac{Q^* + Q_s\left(1 - F(z=h)\right)}{\rho_0 C_p h}}_{e}$$

where T is the model simulated temperature in the ML and h is the time varying MLD. Ocean currents in (x, y, z) directions are denoted by (u, v, w). $D_l(T)$ and k are the lateral diffusion parameter and the vertical diffusivity coefficient respectively. Brackets denote the vertical average over the mixed layer h. The term (a) is the advection term and is denoted as ADV. The term (b) the lateral diffusion term and is neglected in the cold wake of TCs. The terms (c) and (d) are the entrainment/detrainment and the vertical diffusion flux at the mixed layer base respectively. The terms (c) and (d) are combined together and denoted as vertical processes term MIX. The term (e) denotes the heat flux stored in the mixed layer. In this term, Q_s represents the solar heat flux, Q^*, the non-solar heat fluxes, which include sensible, latent, radiative heat fluxes, and F(z=h), the fraction of solar irradiance that penetrates below the mixed layer. The term (e) is the

surface forcing term and is denoted as FOR. As in Vincent et al. (2012a), this heat budget calculation will be used to quantify the contribution of various processes to the TC-induced cooling amplitude. To quantify the relative contribution of all processes to the cooling magnitude, each term of the ML heat budget is integrated starting 10 days prior to TC passage.

The CORE II forcing dataset developed under "coordinated ocean-ice reference experiments (COREs)" program is used as surface boundary conditions for the model simulations (Griffies et al., 2009). This atmospheric datasets and formulations presented by Large and Yeager (2009) are based on NCEP/NCAR reanalysis for near surface wind, temperature, specific humidity and density, combined with a variety of satellite datasets for radiation, SST, sea-ice concentration and precipitation. Turbulent fluxes are computed from bulk formulae as a function of the prescribed near surface atmospheric state and the simulated ocean surface state (SST and surface currents). Data are provided at six-hourly (wind speed, humidity and atmospheric temperature), daily (short- and long-wave radiation) and monthly (precipitation) resolution, with interannual variability over the 1978–2007 period except for river runoff that remains climatological (Fekete et al., 1999). The sea surface salinity is restored to monthly climatology with a times-cale of 300 days (for a 50m-thick mixed layer) to avoid the model drift (Griffies et al., 2009). The large nudging timescale compared to the typical response time to a TC allows simulating a realistic climatological haline stratification, a key feature to study the TCs ocean response in the Bay, without significantly affecting the salinity stratification at the timescale of TCs (a few days). The model is initialised at rest with World Ocean Atlas 2005 temperature and salinity data (Locarnini et al., 2006; Antonov et al., 2006). It is then integrated for a 30-year period for spin-up using the COREII bulk formulae and interannual forcing dataset (1948-1977) (Large and Yeager,

2009; Griffies et al., 2009). The final state is then used to start the simulations described below (which are run over 1978-2007).

The NCEP/NCAR reanalysis used as wind forcing in the original COREII dataset has a coarse horizontal resolution (~ 2°), insufficient to resolve the spatial scale of TCs that typically display radius of maximum wind of ~50km (Kikuchi et al., 2009). This dataset hence only contains weak TC-like vortices and cannot directly be used to investigate the model response to TCs, as shown by Vincent et al. (2012a). To include a more realistic TC wind forcing, a cyclone-free forcing is first prepared from the original interannual CORE forcing by filtering these weak TC wind signatures. These weak TC vortices are removed by applying a 11-day running mean (the maximum time of influence of a TC at a given point) to the original wind forcing components, within 600km around each cyclone track position. Then winds were linealy interpolated from filtered to unfiltered winds between 600km and 1200km (the maximum radius of influence for TCs winds) for smooth transition. Then realistic TC-wind signatures superimposed on the filtered forcing were used to force the model. The 6-hourly cyclone position and magnitude from IBTrACS database (Knapp et al., 2010) are linearly interpolated to the model timestep (i.e. every 36 minutes). This information is used to reconstruct the 10-m wind vector from an idealized TC wind vortex fitted to observations (Willoughby et al., 2006; see their Figure 2 for resulting analytical wind profile). This procedure results in a simulation where TC wind magnitude and structure is more realistic than in the COREII original forcing (see Figure 1 in Vincent et al., 2012a). A more detailed description of this forcing strategy can be found in Vincent et al. (2012a), together with a model validation at global scale. Vincent et al. (2012c) further showed that the ½° resolution is a good compromise between accuracy and numerical cost for a realistic global simulation of the ocean response to TCs: compared to a 1/12° grid, a ½° resolution

provides very similar results in terms of TC power dissipation, a good proxy for TC-induced vertical mixing, while slightly underestimating the TC wind-driven upwelling.

2.2.3 Methodology to monitor the ocean response

To characterize the ocean response to TCs, the mean SST seasonal cycle is first subtracted from model and TMI-AMSR-E observations. This mean seasonal cycle is calculated over the 1998-2007 when comparing model results to observations (Figures 2.6 and 2.7) and over 1978-2007 when model results are extended over the entire available period (Figure 2.8 onwards). TC track postions are then used to extract the ocean response to TCs. To characterize the cooling amplitude, average SST anomalies within a radius of 200 km around each TC track locations are used. This radius has been choosen corresponding to the area where SST has an influence on TC intensity (Cione and Uhlhorn, 2003; Schade, 2000).

Following the approach of Vincent et al. (2012ab), the reference unperturbed pre-storm SST condition (SST_0) is defined as the 1 week average SST before the storm passage (i.e. from -10 to -3 days) and the SST in the wake of the storm (SST_{CW}) is defined as the 3-day average starting 1 day after the storm passage (i.e. from 1 to 3 days). The SST cooling amplitude in the cold wake ($\Delta T_{CW} = SST_{CW} - SST_0$) describes the amplitude of SST response. We will see in section 2.3 and specifically from Figure 2.6 that these choices for temporal averaging are justified by our observational and modelling results.

As in Vincent et al. (2012b), we use two variables to examine the TC wind forcing magnitude and the impact of pre-storm subsurface oceanic conditions. WPi denotes the strength of the TC wind forcing and is discussed is section 1.3.2. WPi represents the amount of kinetic energy available for mixing under the TC (Vincent et al., 2012b). As surface cooling largely results from mixing caused by vertical shear of oceanic currents

(Price, 1981; Vincent et al., 2012a), WPi is hence a pertinent variable to describe it. Vincent et al. (2012b) have shown that the mean cooling underneath a TC increases nearly linearly with WPi but demonstrated that the cooling magnitude also depends on ocean background conditions. In addition to this atmospheric variable, hence an oceanic variable, the CI, discussed in section 1.3.2, which characterizes the ocean background conditions control of the cooling amplitude, has been used. The CI is computed from both temperature and salinity profiles and therefore accounts for the intensity of the haline stratification, including BL effect in its calculation.

Vincent et al. (2012b) earlier showed that SST variations under TCs in our simulation are largely a function of WPi and CI, with CI modulating the cooling amplitude by up to an order of magnitude for a given WPi. The dependence of the cooling amplitude on both WPi and CI for the specific case of the BoB is further illustrated on Figure 2.1a where the average cooling amplitude underneath TCs conditions in the Bay is binned as a function of WPi and CI. The average cooling increases as a function of WPi and decreases as a function of CI. Large cooling (>2°C) only occurs in the BoB when powerful TCs (WPi>2.5) travel over favourable oceanic conditions (CI<20). As shown on Figure 2.1b, this dependence of the cooling amplitude on CI and WPi can be reasonably well approximated by a 2^{nd} order polynomial least-square function. This least-square fit will be used in Section 2.4 to hindcast the simulated cooling in the BoB and assess the respective contribution of thermal and haline stratification to TC-induced cooling amplitude.

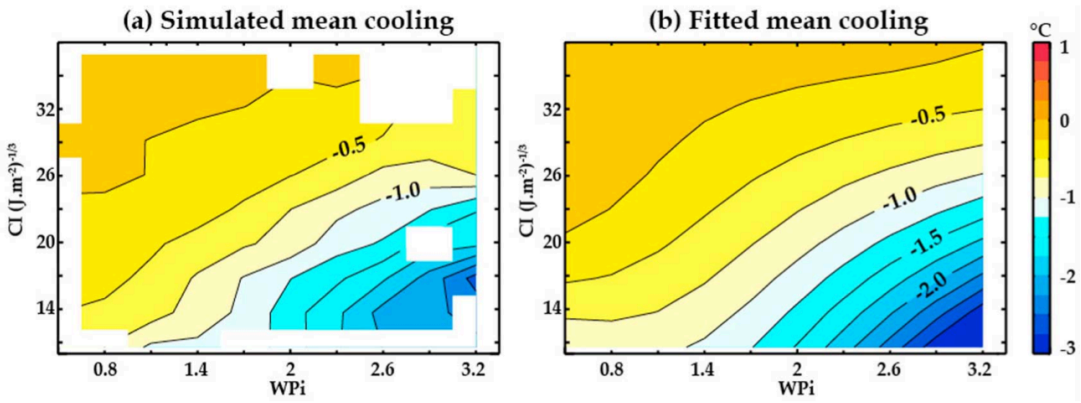

Figure 2.1: (Left panel) Average TC-induced cooling in the model in the BoB, as a function of the WPi (a proxy of the TC-energy input to the upper ocean) (9 bins of 0.3) and CI (a proxy of the inhibition of the cooling by the ocean stratification) (9 bins of 3) (Right panel) Best fit of the model cooling using degree 2 polynomial.

2.3. Model validation

Figure 2.2 compares the model climatological sea surface salinity (SSS) with observational SSS for pre-monsoon and post-monsoon seasons in the Northern Indian Ocean. In observations, high salinities characterize the Arabian Sea, due to the excess of evaporation over precipitation (Rao and Sivakumar, *2002*) and proximity to two high-salinity seas, namely the Red Sea and the Persian Gulf. On the other hand, the BoB exhibits a large excess of precipitation over evaporation (Harenduprakash and Mitra, 1988; Prasad, 1997). Low salinity water fills the entire bay throughout the year, with freshest water along the coast adjacent to the major river mouths (Ganga, Brahmaputra, and Irrawadi). This results in a very large meridional salinity gradient, with very low salinity in the northern and eastern BoB and higher salinity in the southwestern BoB. Huge river runoff and excess precipitation over evaporation during summer monsoon lead to a post-monsoon near-surface salinity minimum of less than 28 psu in the

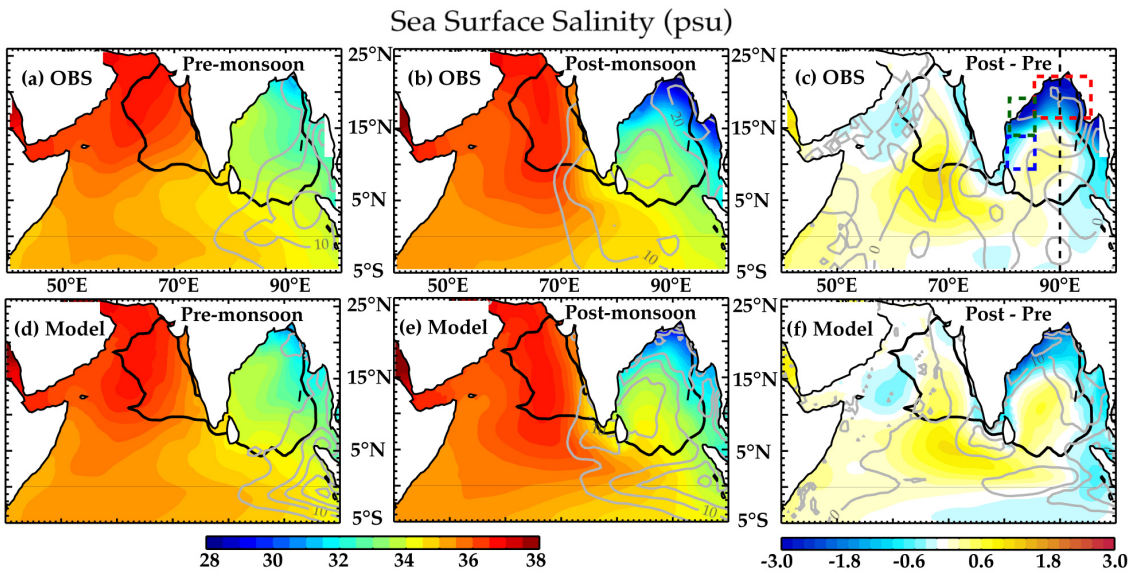

Figure 2.2: Climatological SSS (in psu; color) and BLT (in meters, grey contours) for pre-monsoon (left panels) and post-monsoon (middle panels) seasons and their difference (right panels) derived from observed SSS climatology of *Chatterjee et al.* [2011] and BLT climatology of *de Boyer-Montegut et al.*[2004] (upper panels) and model (lower panels). The thick contour delineates the region where 80% of TCs occur in the northern Indian Ocean (i.e., where TCs density is larger than 0.4 TCs per year in 2° by 2° bins). Dashed colored boxes on panel (c) highlight the regions of the BoB discussed in Table 2.2 (Red : North-East BoB, Green : East Indian Coast, Blue : Southwest BoB). The black dashed line indicate the temperature and salinity section at 90°E shown on Figure 2.4.

northern part of the Bay (Figure 2.2b), 3 psu fresher than during the pre-monsoon season (Figure 2.2a). These regional patterns and seasonal features are reasonably well reproduced by the model (Figure 2.2de). The freshening of the Northern Bay may however be underestimated away from the coast during the post-monsoon season by ~1 psu (Figure 2.2cf, Table 2.2), although observational estimates in this region may not be reliable due to the scarcity of available observations. If real, this underestimation may arise from inaccurate runoffs and precipitation forcing or from the rather coarse ½° resolution of the model that may not allow exporting enough coastal freshwater offshore.

Regions	ΔSSS (psu)		ΔH_{SST-2^oC} (m)		ΔBLT (m)		ΔCI $(J/m^2)^{1/3}$	
	OBS	MOD	OBS	MOD	OBS	MOD	OBS	MOD
North-East BoB	-2.2	-1.3	13.0	15.6	14.3	11.9	8.4	9.0
South-West BoB	-0.2	0.0	-6.6	-1.8	6.3	2.4	-1.4	-0.9
East Indian Coast	-1.5	-1.0	4.0	14.0	9.8	8.8	3.6	5.0

Table 2.2: Average observed and modeled differences between post-monsoon and pre-monsoon seasons for SSS, $H_{SST-2°C}$, BLT and CI in the regions displayed as colored dashed squares on Figures 3, 4 and 6: North-East (85°E-95°E, 16°N-22°N), South-West (81°E-85°E, 9°N-14°N) and East Indian Coast (81°E-85°E, 14°N-20°N).

These low SSS in the BoB during post-monsoon season are associated with the development of a BL along the northern rim of the Bay, especially in the eastern part of the basin and along the eastern coast of India (Figure 2.2ab; contour), in agreement with the observational analysis of Thadathil et al. (2007). These BL are almost absent during the pre-monsoon season, except in the eastern part of the Bay where TCs hardly occur (thick contour on Figure 2.2). The model is also able to represent this seasonal contrast albeit with an underestimation of the BL spatial extent in the central and southwestern part of the Bay during post-monsoon season (Figure 2.2def, Table 2.2).

The near surface thermal stratification is diagnosed in the model and observations by calculating the depth at which ocean temperature is 2°C below the surface temperature ($H_{SST-2°C}$), a measure first proposed by Lloyd and Vecchi (2011). The larger this depth the more difficult it is for a given TC to cool the ocean surface: it is thus an appropriate measure to validate the ocean thermal stratification in relation to TC response. Figure 2.3 compares the model climatological $H_{SST-2°C}$ with observational estimates for pre-monsoon and post-monsoon seasons in the Northern Indian Ocean, as well as the difference between the two seasons. Observations indicate that $H_{SST-2°C}$ is relatively homogeneous in the Bay during the pre-monsoon season (Figure 2.3a), but displays a

clear east/west contrast during the post-monsoon season (Figure 2.3b). The upper-ocean stratification deepens by 20 to 30m in the northeastern part of the Bay as well as by ~10m along the eastern coast of India (Figure 2.3c; Table 2.2). In contrast, the upper-ocean stratification shoals by ~5-10m in the southwestern part of the Bay. Seasonal $H_{SST-2°C}$ changes generally agree between model and observations (Figure 2.3c and 2.3f; Table 2.2). The model however underestimates the depth of the upper-ocean stratification in the BoB during both seasons (Figure 2.3de).

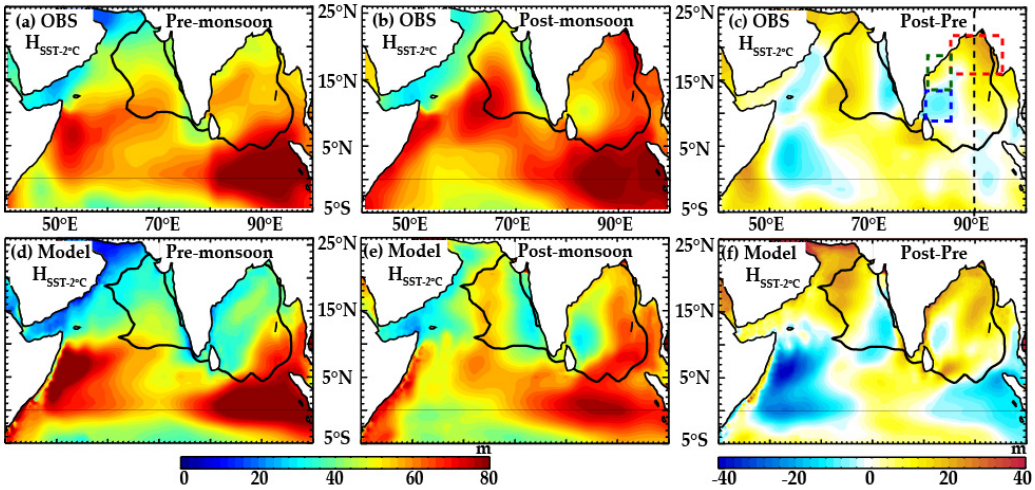

Figure 2.3: Climatological depth at which the ocean temperature is 2°C below the surface temperature (in meters) for pre-monsoon (left panels) and post-monsoon (middle panels) seasons, and their difference (right panels) derived from de Boyer-Montegut et al. (2004) climatology (upper panels) and the model (lower panels). The thick contour delineates the region where 80% of TCs occur in the northern Indian Ocean (i.e., where TCs density is larger than 0.4 TCs per year in 2° by 2° bins) while dashed colored boxes on panel (a) highlight the regions of the BoB discussed in Table 2.2 (Red : North-East BoB, Green : East Indian Coast, Blue : Southwest BoB). The black dashed line indicate the temperature and salinity section at 90°E shown on Figure 2.4.

Longitudinal sections in the Bay (Figure 2.4ab) and vertical profile of climatological salinity and temperature north of 15°N (Figure 2.4c) further allow contrasting the thermohaline structure during pre-monsoon and post-monsoon seasons. Compared to pre-monsoon season, post-monsoon season displays much larger salinity stratification in the northern part of the Bay in the upper 40 m (~0.1 $psu.m^{-1}$ against ~0.03 $psu.m^{-1}$

before the monsoon). While the SST during the pre-monsoon season is higher than 29°C, the SST drops by ~1°C during the post-monsoon season, explaining the deeper MLD and upper-ocean thermal stratification discussed on Figure 2.2 and 2.3. Once again, the model simulates the contrast between these two seasons reasonably well, both in terms of temperature and salinity stratification (Figure 2.4def).

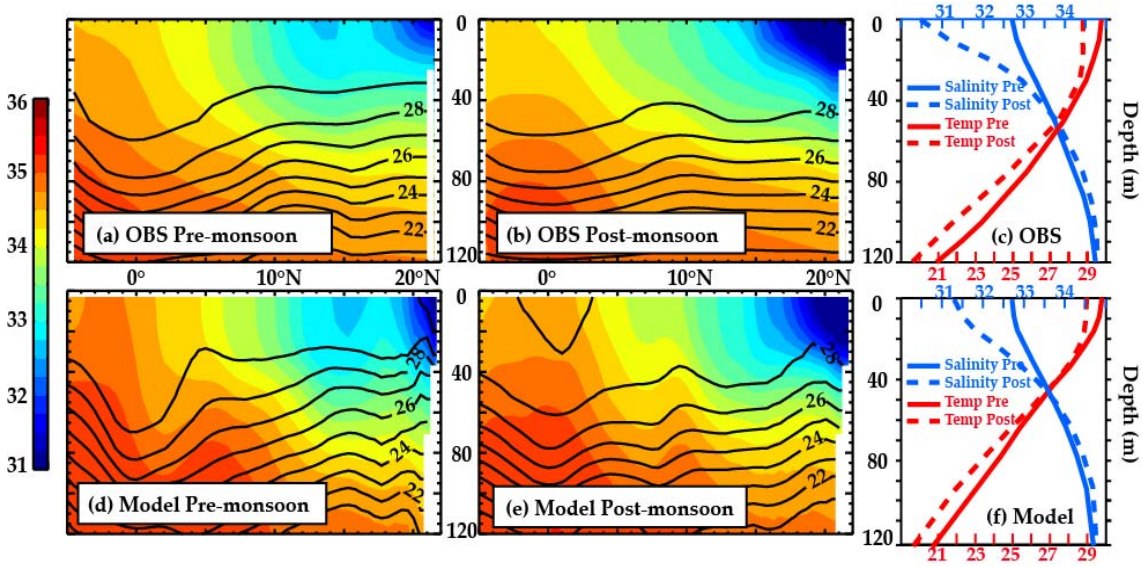

Figure 2.4: Latitude-depth section (at 90°E) of observed climatological salinity (in psu; color) and temperature (in °C; contour) in BoB during (a) pre-monsoon and (b) post-monsoon seasons. (c) Observed temperature (red) and salinity (blue) profiles averaged in the BoB north of 15°N for pre-monsoon (plain line) and post-monsoon (dashed line) seasons. (d-f) Same for model outputs.

Figure 2.5 shows the CI calculated from model and observations during pre-monsoon and post-monsoon seasons, as well as the difference between the two seasons. This measure also allows validating the relevant ocean stratification for the response to TCs (Vincent et al., 2012b), which (contrary to $H_{SST\text{-}2°C}$) integrates the effect of salinity stratification. Observations indicate that the CI index is relatively homogeneous during the pre-monsoon season in the Bay (Figure 2.5a), but displays a very strong northeast/southwest contrast during the post-monsoon season (Figure 2.5b). The

northern and eastern part of the Bay as well as the eastern coast of India display the largest CI changes (Figure 2.5c, Table 2.2), corresponding to a ~20 to 30% CI increase (Figure 2.5). In contrast, the southwestern part of the Bay exhibits opposite seasonal changes, with a ~10% CI reduction off shore of Tamil Nadu and north of Sri Lanka.

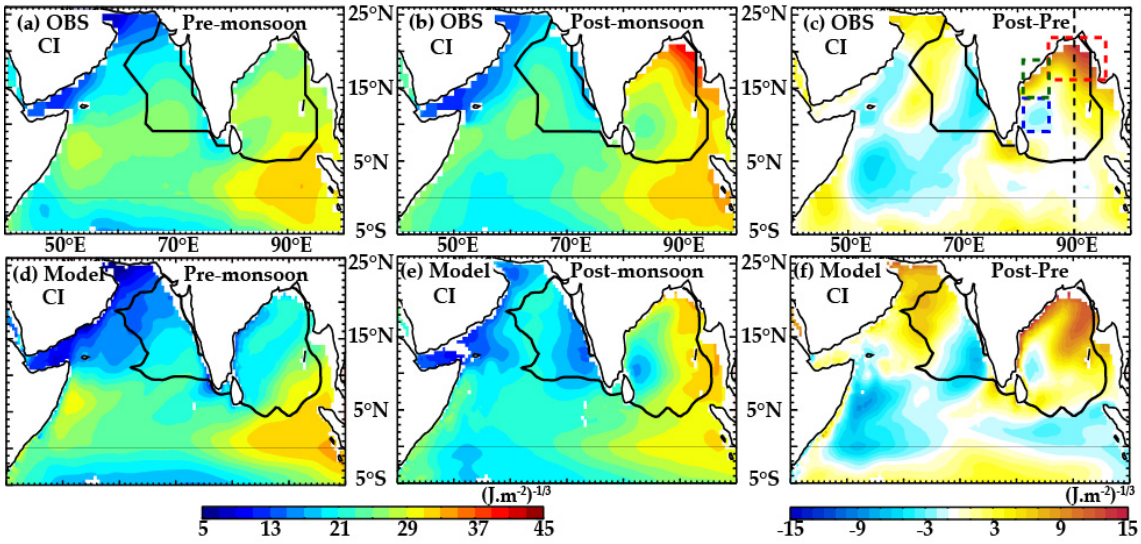

Figure 2.5: Climatological cooling inhibition index (CI; in $(J.m^{-2})^{-1/3}$) for pre-monsoon (left column) and post-monsoon (middle column) seasons, and their difference (right column) using observations (upper panels) and the model (lower panels). The thick contour delineates the region where 80% of TCs occur in the northern Indian Ocean (i.e., where TCs density is larger than 0.4 TCs per year in 2° by 2° bins) while dashed colored boxes on panel (a) highlight the regions of the BoB discussed in Table 2.2 (Red : North-East BoB, Green : East Indian Coast, Blue : Southwest BoB). The black dashed line indicate the temperature and salinity section at 90°E shown on Figure 2.4.

Seasonal CI changes estimated from model outputs generally agree qualitatively with those inferred from the observed climatology (Figure 2.5c and f, Table 2.2). The physical meaning of this pattern follows: the deeper thermal stratification (Figures 2.3 and 2.4) resulting from the cooler SST and strong near surface salinity gradient in the northern part of the Bay (Figures 2.2 and 2.4) result in a stronger oceanic inhibition of vertical mixing-driven cooling during the post-monsoon season, compared to the pre-

monsoon season. A given TC is hence likely to induce a weaker cooling during the post-monsoon season, especially in the northeastern part of the Bay and along the eastern Indian coastline. The model underestimates the CI in the BoB during both seasons (Figure 2.5de) but displays similar seasonal change (Figure 2.5f and Table 2.2).

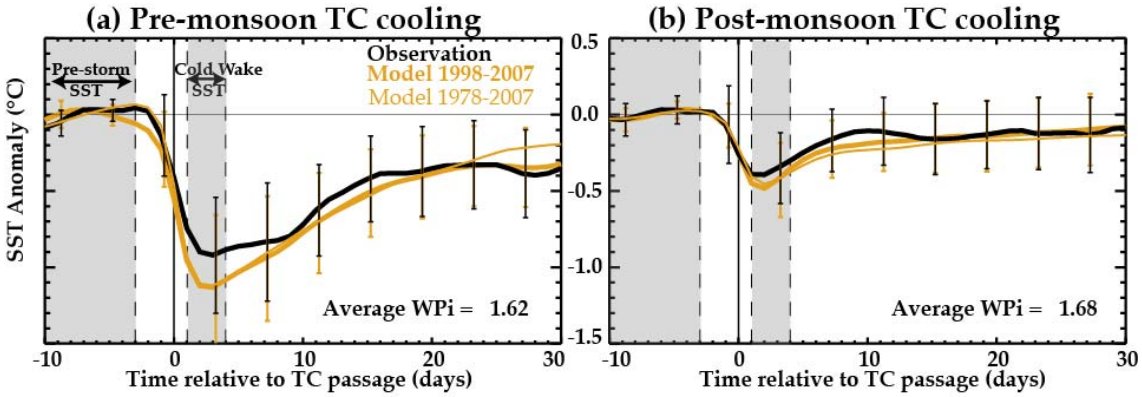

Figure 2.6: Composite evolution of TC-induced SST cooling within 200 km of TC-tracks in the BoB (in °C) during pre-monsoon (left) and post-monsoon (right) seasons for observations (black line) and the model over the 1998-2007 (thick orange line) and the model over the 1978-2007 periods (thin orange line). The upper and lower quartiles are shown as vertical bars (black for the observations and orange for the model). These quartiles are not shown for the model results over the 1978-2007 period for clarity.

Figure 2.6 provides a first illustration of the potential impact of this seasonal change in stratification on TC-induced cooling. The composite TC-induced surface cooling amplitude derived from satellite observations over the 1998-2007 period is larger during pre-monsoon (~ 0.9°C; Figure 2.6a) than during post-monsoon (~ 0.4°C; Figure 2.6b) season in the BoB. Largest cooling usually occurs ~2-3 days after the cyclone passage and recedes within ~20 days. However, after the passage of storm the average SST remains 0.1-0.4°C colder than SSTs before the passage of storm. Lloyd and Vecchi (2011) earlier noticed this phenomenon. The model accurately reproduces both the amplitude and timing of the TC induced SST cooling, before and after the monsoon,

although with a slightly overestimated cooling (Figure 2.6). The above results agree well with previous observations underneath individual TCs in the BoB, with larger cooling during pre-monsoon season (Gopalakrishna et al., 1993; Rao 1987; Sengupta et al., 2008) than during post-monsoon season (Chinthalu et al., 2001; Sengupta et al., 2008; Subrahmanyam et al., 2005). The mean wind power over the cyclone tracks does not differ much between the pre-monsoon and post-monsoon seasons (WPi: 1.62 against 1.68; Figure 2.6). The distribution of WPi for both

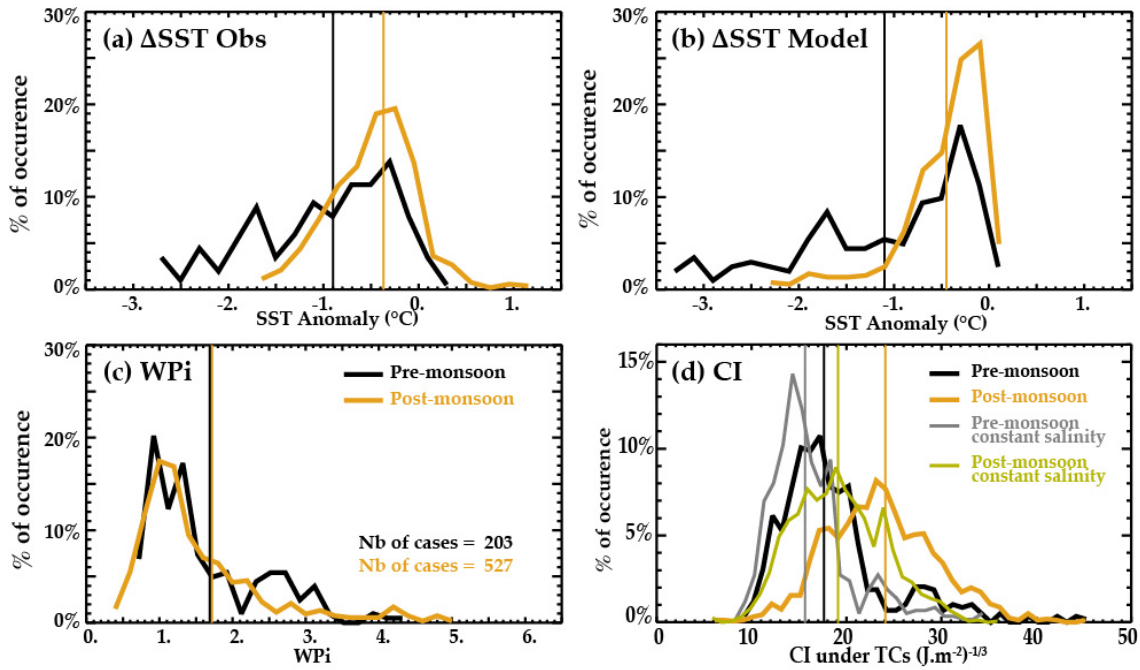

Figure 2.7: Probability density function in the BoB for pre-monsoon (black line) and post-monsoon seasons (orange line) of the TC-related distributions of (a) observed TC-induced SST cooling (bin size: 0.2°C), (b) modeled TC-induced SST cooling (bin size: 0.2°C), (c) WPi (bin size: 0.2) and (d) CI (bin size: 1) over the 1998-2007 period. The number of cases on panel (c) represents the number of cooling locations, sampled every six hours along the TCs tracks. The grey (resp. green) line on panel (d) indicate the pre monsoon (resp. post monsoon) CI calculated with a constant salinity profile (CI_{S0}) of 33.85 psu (averaged salinity in the BoB in post-monsoon season within the upper 200 m). Vertical lines on each panel indicate the mean value for pre-monsoon (black lines) and post-monsoon season (orange lines). The grey (green) vertical lines on panel (d) indicate the mean value for pre-monsoon (post-monsoon) CI_{S0}.

seasons is further displayed on Figure 2.7c: the two distributions are very much alike with mean values (vertical lines) having very similar values in the two cases. In contrast, the TC-induced cooling distributions are significantly different with a weaker mean during the post-monsoon seasons and most intense observed cooling (up to -2.5°C-3°C) occurring only during the pre-monsoon season for observations (Figure 2.7a). The modelled cooling exhibits a similar behaviour (Figure 2.7b), although the mean for the pre-monsoon season is overestimated by 10 to 20% as compared to observations. This overestimation is likely related to the underestimation of the climatological CI (see Figure 2.5). The weak differences in WPi (i.e. in TC mechanical energy transfer to the ocean) between the two seasons are a first indication that ocean stratification is the main responsible for differences in cooling amplitude.

2.4 Processes controlling differences in pre-monsoon and post-monsoon TC cooling

In the previous section, we only used model results from the satellite period (1998-2007) to allow a fair comparison with observations. The results discussed in the previous section remain true over the full 1978-2007 model simulation period: a weaker cooling is simulated during the post-monsoon compared to the pre-monsoon season over the 1978-2007 period, while the wind power remains very similar. In this section, we hence analyse the model response to 135 TCs in the BoB over the 1978-2007 period, in order to obtain a larger sample and a higher statistical significance.

Figure 2.8 exhibits the probability density functions of TC-induced SST cooling as a function of WPi for the pre-monsoon and post-monsoon seasons. These two distributions are strikingly different: the slope of the median cooling amplitude against WPi is about three times smaller during the post-monsoon season than during the pre-

monsoon season (0.28°C against 0.80°C). This result demonstrates that, for a given wind power input, the resulting cooling is on average 3 times smaller during the post-monsoon season. Differences in oceanic stratification underneath TCs between the two seasons are further demonstrated by displaying histograms of the CI (Figure 2.7d). The

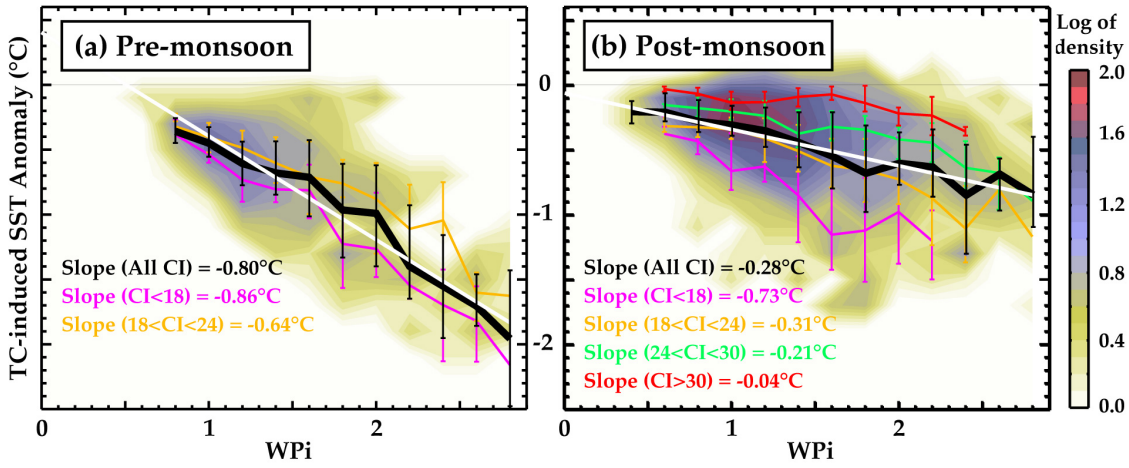

Figure 2.8: Two-dimensional distribution of TC-induced SST cooling (in °C) versus WPi in the model over the entire period (1978-2007) for (a) pre-monsoon and (b) post-monsoon seasons. The thick black line indicates the average of the cooling distribution for a given WPi, the white line is a linear fit of the black line, and the vertical black bars indicate the upper and lower quartile of the cooling distribution for a given WPi. The slope of the linear fit is also reported on each panel. The average cooling (in °C) as a function of WPi for different CI (in $(J.m^{-2})^{-1/3}$) ranges (CI<18, 18<CI<24, 24<CI<30, CI>30) during (a) pre-monsoon and (b) post-monsoon seasons is indicated with colored lines. Results for the two upper CI ranges (24<CI<30 and CI>30) are not displayed during pre-monsoon season due to the lack of oceanic profiles with such CIs at this time of the year. Vertical color bars indicate the upper and lower quartiles of the cooling distribution for a given WPi, for each range of CI. The slope of the linear fit of each curve is reported on each panel.

CI distribution is remarkably different between the two seasons, with stronger near-surface haline stratification and deeper thermal stratification (i.e. stronger CI) during the post-monsoon season. The range of CI values under which TCs occur is also larger during post-monsoon than during pre-monsoon season. While CI values above 22 are hardly found underneath TCs before the monsoon, half of CI values exceed this

threshold during the months following the monsoon. The influence of oceanic stratification on TC-induced cooling amplitude is further demonstrated by the coloured curves on Figure 2.8 that display the average cooling as a function of WPi for four different ranges of CI (less than 18, between 18 and 24, between 24 and 30 and greater than 30). The influence of CI allows explaining the wide range of possible TC-induced cooling amplitudes for a given wind power input and hence the dispersion of TC-induced cooling during the post-monsoon season seen on Figure 2.8b. When TCs transit over waters displaying large CI (greater than 30, i.e. strongly stratified) during the post-monsoon season, the resulting cooling amplitudes are very weak (regression slope of 0.04°C). In contrast, cooling amplitudes for TCs that transit over waters with lowest CI (less than 18; i.e. weakly stratified) are larger (~0.73°C) and match those simulated during pre-monsoon season (slope of 0.86°C) This demonstrates that oceanic stratification is a major factor controlling the amplitude of the SST response to a TC in the BoB.

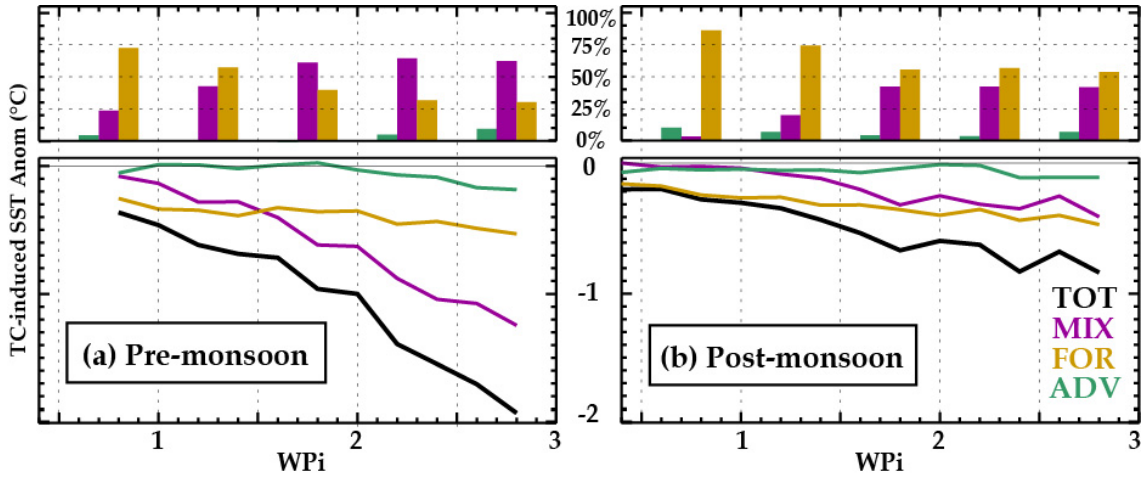

Figure 2.9: TC-induced mean cooling amplitude (TOT) and the contribution of heat fluxes (FOR), vertical mixing (MIX), and advection (ADV) to the total cooling amplitude as a function of the WPi for pre-monsoon (left panels) and post-monsoon seasons (right panels). Absolute values (resp. relative contribution) of each process to the total cooling are shown on the lower (resp. upper) panels.

An analysis of the physical processes responsible for the simulated TC-induced cooling (Figure 2.9) derived from the online tendency terms equation of the ML temperature described in section 2.2.2 provides further evidence on the role of upper-ocean stratification in the cooling amplitude difference between the two seasons. The TC-cooling induced by heat flux (mainly latent) is indeed very similar between the two seasons and does not exceed -0.5°C for the strongest TC forcing (WPi>2.5, compare the orange curves in Figures 2.9a and b). Advective processes are of secondary importance and only slightly contribute to TC-induced cooling for the strongest WPi (i.e. strongest cyclones). In contrast, the amplitude of mixing-induced cooling strongly differs between the two seasons. During pre-monsoon, mixing-induced cooling rapidly increases with WPi, explaining more than 60% of the TC-induced cooling for WPi larger than 1.5. In contrast, mixing-induced cooling is three to four times weaker during the post-monsoon season for a given wind power input and never exceeds the amplitude of the cooling induced by heat fluxes. This reduced cooling by vertical mixing is largely responsible for the reduced TC-induced cooling amplitude for the post-monsoon season compared to pre-monsoon season. This tendency terms analysis demonstrates that cooling by mixing is weaker during the post monsoon season. This is because the stronger upper-ocean stratification opposes a stronger resistance to mixing, hence resulting in a lesser entrainment of colder subsurface water. This is one more indication that changes in ocean stratification explains most differences in TC-induced cooling between the two seasons.

The oceanic stratification depends on both temperature and salinity. Using the CI, it is possible to infer their respective contribution to the total stratification and relate them to TC-induced surface cooling differences between the two seasons. Figure 2.7d compares the distribution of the CI underneath TCs for the two seasons calculated with a constant

salinity profile of 33.85 psu (i.e. the CI recomputed using a fixed salinity of 33.85 psu: the average upper 200 m BoB value in post-monsoon season; hereafter CI_{S0}; results are not very sensitive to the salinity value used to perform this calculation). This index therefore only accounts for thermal stratification effects. The overall CI_{S0} distribution is shifted toward lower values compared to CI (Figure 2.7d); i.e. salinity stratification inhibits vertical mixing in the BoB. This is an expected result as salinity strongly contributes to upper ocean static stability in the upper BoB (Figure 2.4). The impact of salinity on stratification is twice larger during the post-monsoon than during the pre-monsoon season in the BoB (CI - CI_{S0} ~2 on average during pre-monsoon season and ~5 during post-monsoon season). This simple diagnostic illustrates the key role of salinity in density stratification of the BoB, especially during the post-monsoon season.

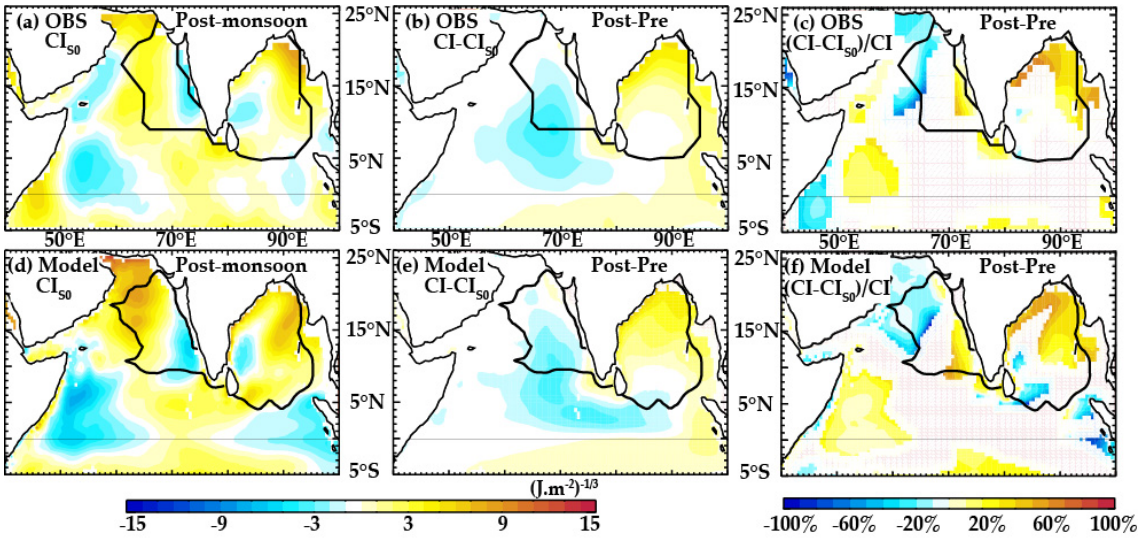

Figure 2.10: Post-monsoon minus pre-monsoon Cooling Inhibition index calculated with constant salinity profile CI_{S0} (left column), CI-CI_{S0} (middle column) and percentage of CI seasonal change due to salinity (CI-CI_{S0})/CI (right column) using observations (upper panels) and model outputs (lower panels). The middle column indicates the salinity propensity to inhibit cooling underneath TCs (i.e. the right column has yellow shading where salinity contributes to diminish TC-induced cooling during the post-monsoon season, relative to the pre-monsoon season). The right panels only display the salinity contribution for absolute CI seasonal changes larger than $2(J.m^{-2})^{-1/3}$.

Figure 2.10 further illustrates the regional distribution of salinity impact on the BoB stratification (i.e. differences between CI and CI_{S0}). As displayed on Figure 2.10c, salinity seasonal changes mainly affect the CI distribution along the northern rim of the BoB, where strongest seasonal changes in haline stratification (Figure 2.2 and 2.4) and BLT (Figure 2.2) are observed. Salinity accounts for about half of the seasonal cooling inhibition changes in the northeastern part of the Bay along the coast of Myanmar and Bangladesh and for a large part of CI increase along the eastern coast of India, offshore the state of Andhra Pradesh. On the other hand, temperature changes explain all of CI seasonal changes in the southwestern part of the Bay. The model generally reproduces these features (Figure 2.10d-f), although it slightly underestimates the relative role of haline stratification in the CI changes along the eastern Indian coastline.

While these results clearly demonstrate the important role played by salinity (ranging from less than 0% to more than 80% depending on the considered region), observational estimates and model results both indicate a strong contribution from the seasonal evolution of the thermal structure to the pre-monsoon and post-monsoon CI contrasts. The deepening of the upper thermocline related to the seasonal surface cooling in the northern and western part of the BoB (Figures 2.2 and 2.4) acts to increase the CI in these regions during post-monsoon season (Figure 2.10be) and contributes up to 80% of the seasonal stratification changes (Figure 2.10cf). Typically, because of the surface cooling taking place during the monsoon, vertical mixing has to penetrate deeper (down to ~50 m) during the post-monsoon season, as compared to the pre-monsoon season (down to ~35 m), in order to cool the mixed layer by 2°C (Figure 2.3). While salinity and temperature changes act in concert to increase CI after the monsoon along the northern rim of the BoB, they oppose each other in the southwestern part. The

freshening acts to increase CI while both the SST drop and the modest shoaling of the thermal stratification act to decrease CI in this latter region (Figure 2.10).

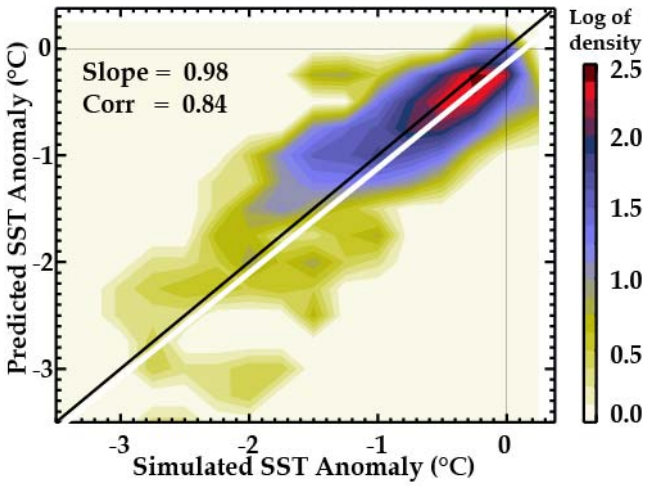

Figure 2.11: Two-dimensional distribution of predicted SST cooling versus simulated SST cooling in the BoB over the period 1978-2007. Regression slope and correlation between the two datasets is also indicated.

Our results clearly indicate that seasonal changes in the vertical haline and thermal structure are consistent with differences in TC-induced cooling amplitude between the pre-monsoon and post-monsoon seasons. A more quantitative estimate of their respective roles can further be obtained by using the least-square fit of the cooling amplitude as a function of WPi and CI discussed in Section 2.2.3 to hindcast the simulated cooling in the BoB. This approach performs very well, with a 0.84 correlation and a 0.98 regression between the amplitudes of the cooling simulated by the model and the cooling hindcasted using the least square fit (Figure 2.11). The probability density functions of the hindcasted SST cooling as a function of WPi (Figure 2.12a-b) also shows a very similar behavior to the SST cooling actually simulated by the model (Figure 2.8). The slope of the predicted cooling amplitude against WPi is indeed larger during the pre-monsoon season (-0.62°C, compared to -0.70°C for the simulated cooling,

Figure 2.8a) than during the post monsoon season (~ -0.28°C for both predicted and simulated cooling). The influence of salinity on the cooling amplitude can then be assessed from a cooling prediction using CI_{S0}. The cooling slope as a function of WPi only increases by ~10% when neglecting haline stratification for pre-monsoon season (Figure 2.12a and 2.12c). This suggests a relatively modest role of salinity on the amplitude of TC-induced cooling in the pre-monsoon season. In contrast, using CI_{S0} for

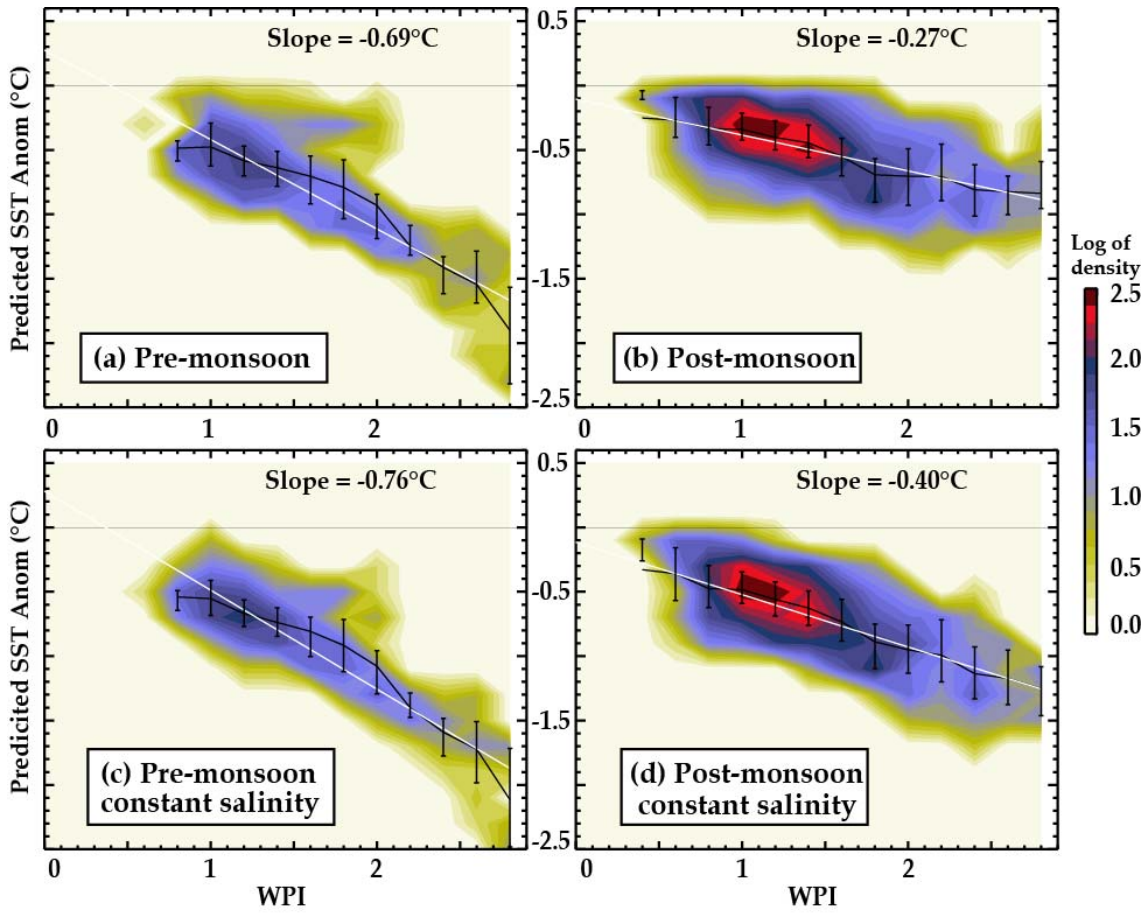

Figure 2.12: Two-dimensional distribution of predicted SST cooling with actual T,S profiles (top panels) and with constant salinity profile (lower panels) versus WPi during pre-monsoon (left column) and post-monsoon seasons (right column) in the BoB. For each panel, the thick black line indicates the median of the cooling distribution for a given WPi, the vertical bars indicate the upper and lower quartiles of the cooling distribution for a given WPi and the white line is linear fit of black line. The slope of the linear fit is reported on each panel.

the post-monsoon period results in a 50% increase of the slope from -0.28°C to -0.41°C, and hence in a ~50% increase of the hindcasted mean cooling amplitude (Figure 2.12b and 2.12d). In addition, the very weak predicted and simulated TC-induced cooling (-0.3°C<SST<0.0°C) for moderate WPi (1<WPi<2) do not appear anymore when salinity is not accounted for. However, the change of slope due to haline stratification during the post-monsoon season (from -0.28°C to -0.41°C; Figure 12bd) only explains 40% of the change of slope between post-monsoon and pre-monsoon seasons (from -0.28°C to -0.62°C; Figure 2.12ab). This indicates that changes in haline stratification are responsible on average for ~40% of the cooling reduction between pre-monsoon and the post-monsoon seasons, with changes in the thermal stratification explaining the remaining 60%. In other words, salinity effects reduce TC-induced cooling by 30% during the post-monsoon season.

2.5 Summary and conclusions

In this study, processes responsible for the smaller amplitude TC-induced surface cooling in the BoB during the post-monsoon compared to the pre-monsoon season have been investigated. Because detailed observations underneath TCs are scarce, we analyze a global ocean model simulation forced by realistic TC winds derived from an analytic shape adjusted to observed TC tracks and magnitude over the 1978-2007 period. Our approach samples the ocean response to 135 TCs in the BoB over this 30-year period. The model exhibits TC-induced SST cooling that is about 3 times larger during the pre-monsoon than during post-monsoon season, in agreement with observations.

As discussed by Vincent et al. (2012b), the amplitude of TC cooling is to a large extent explained by two parameters: the wind power input of the TC atmospheric forcing and the cooling inhibition from background oceanic conditions. TC wind power input does

not significantly change between the pre-monsoon and post-monsoon seasons, suggesting that seasonal changes in oceanic structure are responsible for larger TC-induced cooling amplitude during pre-monsoon season. The heavy precipitation and river discharge during and following the monsoon, resulting in a very intense upper-ocean freshening and the formation of a thick BL. Thermal structure also undergoes marked changes between pre-monsoon and post-monsoon seasons, with a cooler mixed layer over most of the BoB following the monsoon resulting in a deeper upper thermal stratification. These thermal and haline stratification changes reduce the entrainment of cooler thermocline waters into the mixed layer and consequently reduce TC-induced cooling during the post-monsoon season. Our analysis indeed reveals that stronger cooling inhibition by oceanic stratification is responsible for a cooling amplitude reduction by a factor of three during the post-monsoon season.

We then assess the respective contributions of seasonal changes in thermal and haline stratification to the reduction of TC-induced cooling. To that end, we use a simple bivariate statistical model that allows accurately predicting the amplitude of TC-induced cooling from wind power (WPi) and CI indices. This allows demonstrating that the strong near-surface salinity stratification during the post-monsoon season is responsible for ~40% of cooling decrease, with SST changes explaining the remaining 60%. The respective contributions of thermal and haline stratification however strongly vary spatially within the Bay: haline stratification explains most of the TC-induced cooling inhibition off shore of the eastern coast of India (~80%), where salinity seasonal changes are strongest while thermal stratification explains all the TC-induced cooling inhibition in the southwestern part of the BoB.

Our modeling study confirms previous case studies. Observations indeed suggest that TC-induced surface cooling is larger during the pre-monsoon (Gopalakrishna et al., 1993; Rao, 1987; Sengupta et al., 2008) than during the post-monsoon season in the BoB (Chinthalu el al., 2001; Sengupta et al., 2008; Subrahmanyam et al., 2005). Sengupta et al. (2008) suggest that weaker surface cooling during the post-monsoon season largely results from the presence of salinity and BL changes through individual case studies analysis. Our results, however, suggest that thermal changes are a major contributor to the difference in TC-induced cooling amplitude between the two seasons, although the effects of the changes in haline stratification also significantly contribute the seasonal TC-induced cooling changes, especially around the rim of the northern BoB.

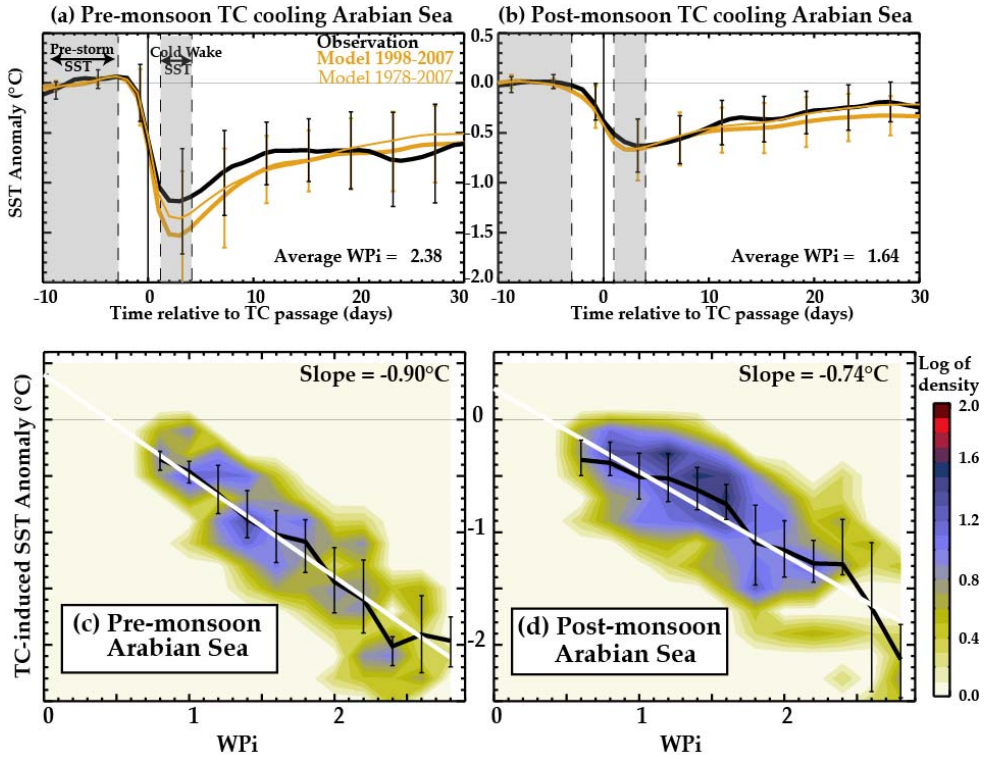

Figure 2.13: (a-b) Same as Figure 2.6ab but for the Arabian Sea. (c-d) Same as Figure 2.8 (but without the binning into CI), for Arabian Sea.

Satellite observations show that the amplitude of TC-induced surface cooling is also larger during the pre-monsoon (~1.2°C) than during post-monsoon (~0.6°C) season in

the Arabian Sea (Figure 2.13ab). Our model simulation (38 Arabian Sea TCs over the 1978-2007 period) reproduces these pre-monsoon/post-monsoon TC-induced surface cooling contrasts in the Arabian Sea (Figure 2.13ab). Figure 2.13cd shows the probability density function of TC-induced cooling as a function of WPi for pre-monsoon and post-monsoon seasons for the Arabian Sea. Unlike the BoB, there is a stronger wind power input before the monsoon than after (average WPi of ~2.4 against ~1.6). The regression slope of the TC-induced cooling to WPi does not change much between the pre-monsoon and post-monsoon seasons in the Arabian Sea (0.90°C / 0.74°C, against 0.80°C / 0.28°C in the BoB), and is similar to the 0.79°C slope during pre-monsoon season in the BoB. The stronger cooling during pre-monsoon season hence mostly results from changes in TC wind power input. Due to a less salinity-stratified upper ocean (e.g., Shenoi et al., 2002), the CI is lower in the Arabian Sea than in the BoB (Figure 2.5) and haline stratification has a weaker influence (Figure 2.10). During the post-monsoon season, salinity stratification acts to decrease the CI in the central part of the Arabian Sea (Figures 2.10e-f) due to lower salinity at depth (not shown). This hence partly compensates the CI increase due to changes in the thermal structure, resulting in a relatively small influence of the oceanic stratification on the cooling in the Arabian Sea, compared to the BoB.

This influence of salinity on TC-induced cooling calls for a better description and understanding of salinity variations within the Bay. Previous studies have already shown that the seasonal salinity evolution is largely determined by the fresh water sources/sinks and the redistribution of the resulting low/high-salinity water by ocean currents (e.g., Rao and Sivakumar, 2002; Vinayachandran et al., 2005; Sengupta et al., 2006). However, the paucity of observations in coastal regions does not yet allow

providing a robust and precise estimate of the intensity and extent of the BoB freshening. In addition, little is known about the interannual variability of SSS in the BoB. Although a limited amount of repeated observations along shipping lanes suggest that salinity variability is high in the tropical Indian Ocean (Delcroix et al., 2005; Rao and Sivakumar, 2002), details of basin-wide spatio-temporal structure of salinity interannual variations in the BoB and their mechanisms are still lacking.

This major influence of salinity also advocates for the use of an adequate oceanic index in statistical TCs intensity prediction schemes. As shown by Yu and McPhaden (2011), buoyancy content in the BoB upper layer has a higher correlation with salinity content than with heat content. A commonly used metric of TC sensitivity to the ocean is the Tropical Cyclone Heat Potential (TCHP), a measure of the heat content between the sea surface and the depth of the 26°C isotherm, computed from altimeter-derived vertical temperature profile estimates (Shay et al., 2000; Goni and Trinanes, 2003). This index is useful for identifying warm anticyclonic features, where hurricanes often undergo sudden intensification in the western Atlantic (e.g., Shay et al., 2000) and Northwestern Pacific (e.g., Lin et al., 2005). Using TCHP allows improving statistical intensity forecasts in these regions (DeMaria et al., 2005; Mainelli et al., 2008), where sea level variability is closely related to changes in the depth of the main thermocline, and salinity plays a lesser role. The present study advocates for the use of a different TC oceanic metric that accounts for the effect of salinity, as already suggested by Vincent et al. (2012b) and Yu et al. (2011). The CI proposed by Vincent et al. (2012b) is a relevant option, since it accounts for the effect of salinity stratification on TC-induced cooling inhibition. This metric can be derived from currently available operational oceanography products constrained by oceanic observations (e.g., Drévillon et al., 2008)

or directly from Argo data; and tested in cyclone intensity forecast schemes in place of the currently used TCHP, in particular in the BoB.

Chapter 3 Influence of air-sea coupling under Bay of Bengal tropical cyclones: A regional dynamical approach

3.1 Introduction

Tropical cyclones (TCs) tracks prediction has dramatically improved over the last decades, yet intensity forecasts improvements are limited (DeMaria et al., 2014). The internal dynamics, environmental forcing, and ocean features are generally identified as important elements affecting TCs intensity evolution (Wang and Wu, 2004). Various atmospheric large-scale atmospheric conditions inhibit TCs intensification: strong vertical wind shear that increases inner-core static stability due to the vortex tilting (DeMaria, 1996), ventilation of the warm core at upper levels (Frank and Ritchie, 2001) or the entrainment of dry air at mid-to-lower levels (Tang and Emanuel, 2010). As TCs primarily draw their energy from evaporation at the surface of the ocean (e.g. Riehl, 1950; Emmanuel, 1986), the enthalpy fluxes at the air–sea interface also have an essential role in intensifying and maintaining TCs (e.g. Malkus and Riehl, 1960; Emmanuel, 1999). While the ocean provides the necessary thermal energy for TCs through moist surface enthalpy flux, the TC intensity is also sensitive the Sea Surface Temperature (SST) evolution under the storm eye (Schade, 2000). The kinetic energy dissipated by friction at the air-sea interface (Emanuel, 2003) results in a significant SST cooling under the TC, largely through vertical mixing (Price, 1981; Cione and Uhlhorn, 2003; Vincent et al., 2012a), which can limit the TC intensification. The fundamental role of the air-sea heat exchanges in the TCs intensification paradigms hence emphasizes the need for quantifying and understanding of the feedback of this TC-induced cooling on TCs characteristics.

A large number of observational case studies indeed reported that TCs passing over cold and warm oceanic eddies generally experience a rapid change of their intensification rate (Shay et al., 2000; Lin et al., 2005; Jaimes and Shay, 2009; Zheng et al., 2010; Walker et al., 2014). The statistical analysis of Cione and Ulhorn (2003) based on in-situ observations of 23 TCs in the Atlantic further suggested that TCs inducing large SST cooling generally experience a weaker upward surface enthalpy flux (up to 40% reduction for a ~1°C change) and are hence less likely to intensify. They further show that the amplitude of the TC-induced cooling is statistically related to the TC intensification rate in their limited observational sample. The statistical analysis of Lloyd and Vecchi (2011) further revealed a levelling-off the TC-induced cooling with increasing TC intensity (from Cat-2) and they interpreted this behaviour as an evidence of the negative ocean feedback onto TC intensification. Mei et al. (2012) were also able to relate TCs intensity with TC translation speed and interpreted this behaviour as an indirect evidence of the impact of air-sea coupling on TCs intensification (slower cyclones cool the ocean more and are hence more likely to be influenced). Finally, the simple inclusion of an upper ocean parameter in statistical intensity forecasting improves TCs intensity forecast (DeMaria et al., 2005; Mainelli et al., 2008), reducing errors by ~5% on average.

The first numerical assessment of the negative ocean feedback onto TC intensification were conducted using very simple coupled models (Chang and Anthes, 1979; Sutyrin and Khain, 1979, 1984). Recent studies using three-dimensional atmosphere–ocean coupled models further demonstrated that North Atlantic and Pacific TCs intensity forecasts were significantly improved when the TC-induced ocean feedback was accounted for (some cyclones were otherwise over-intensifying, Bender and Ginis,

2000; Hong et al., 2000; Lin et al., 2005; Sandery et al., 2010; Ito et al., 2015; Wu et al., 2016). Other idealized modelling studies confirmed that the TC-induced cooling limit TCs intensification (Bender et al., 1993; Schade and Emmanuel, 1999; Zhu et al., 2004; Wu et al., 2007; Chen et al., 2010; Liu et al., 2011; Ma et al., 2013; Halliwell et al., 2015) but could also impact the TC size (Chen et al., 2010; Ma et al., 2013) and asymmetrical structures (Zhu et al., 2004; Chen et al., 2010). Most the aforementioned studies did not find TCs tracks to be sensitive to the TC-induced cooling (Zhu et al., 2004; Chen et al., 2010; Liu et al., 2011). Finally, it has become increasingly clear over the past decade that the oceanic component of these models needs to include three-dimensional processes to correctly simulate the TC-induced upper ocean response, especially for slow-moving TCs (Yablonsky and Ginis, 2009; Halliwell et al., 2011; Wu et al., 2016).

As discussed above, the impact of air-sea coupling on TC characteristics has been generally assessed from realistic or idealized case studies using short-term coupled model integrations. Only a couple of studies did investigate the oceanic feedback onto TCs statistics by comparing long-term (~20 years) coupled model integrations in coupled and uncoupled modes for the Northwest Pacific (Ogata et al., 2015) and Southwest Pacific (Jullien et al., 2014). Ogata et al. (2015) suggested that air-sea coupling acts to shift the location of the most intense TCs equatorward, improving the climatological distribution. They attributed the decrease in the numbers of intense TCs in the subtropical region (north of 20°N) to the shallow mixed layers and thermocline there that promote intense TC-induced cooling, hence limiting TCs intensification. Jullien et al. (2014) also suggested a more realistic cyclogenesis pattern in the coupled simulation, with reduced cyclogenesis compared to the forced run in the Coral Sea,

where mixed layers are particularly shallow. They further demonstrated that accounting for air-sea coupling processes generally results in a 10% decrease of TC counts, with a stronger reduction for strongest TCs. In these simulations, air-sea coupling reduces enthalpy flux (up to 30 $W.m^{-2}$ for a 1°C), resulting in a 15 $hPa.°C^{-1}$ reduction for strongest TCs. Because of the computational cost of performing long-term experiments, these study rely on relatively coarse atmospheric models (~35 to 60 km horizontal resolution) that prevented simulating strongest TCs (above Cat-3).

All the short-term and long-term coupled modelling studies discussed above have been performed in either the Atlantic or Pacific. The Indian Ocean (IO) is however home to about 25% of the global TC activity. TCs in the northern IO mainly occur in the western and central part of the BoB and exhibit a bimodal seasonal distribution, preferentially occur during the pre- and post-monsoon (Li et al., 2013). Although northern IO just accounts for 5% of TCs worldwide, those TCs have catastrophic impacts, with 14 of the 20 deadliest TCs in recent history having occurred in that region (Longshore, 2008). TCs in the southern IO occur over an elongated band centered around 15°S from November to April, with more frequent TCs occurrence over the Southwestern IO around the islands of Mauritius, La Reunion and Madagascar (Mavume et al., 2009). Few studies also reported an upper ocean cooling in response to TCs passage in both the northern (Subrahmanyam et al., 2005; Sengupta et al., 2008; McPhaden et al., 2009; Neetu et al., 2012; Girishkumar et al., 2014) and southern IO (Vialard et al., 2009). Even fewer observationally-based studies discussed the potential feedback of this oceanic response on IO TCs intensification, and only for the case of the BoB (Ali et al., 2007; Lin et al., 2009; Yu and McPhaden, 2011). From two case studies, Ali et al. (2007) discussed how eddies influence TCs intensification over the Bay of Bengal. The

observational analysis of Lin et al. (2009) and Sadhuram et al. (2012) showed that a pre-existing high oceanic heat content before the TC passage can act to reduce the TC-induced cooling and the resulting negative TC intensity feedback, favouring the TC intensification. The specificity of upper ocean thermohaline structure in IO TCs-prone regions may result in a different sensitivity of TCs to ocean-atmosphere coupling compared to other basins. The BoB is indeed characterized by a strong haline stratification that may limit the amplitude of the TC-induced cooling and promote TC intensification (Sengupta et al., 2008; Neetu et al., 2012; Maneesha et al., 2015). In stark contrast, the cyclogenesis region in the southwestern IO is one of the rare oceanic regions where warm SSTs (above the threshold for TC formation) coexist with a shallow thermocline ridge, hence potentially favouring enhanced cooling below the storm and a strengthened negative oceanic feedback onto the storm intensification (Xie et al., 2002). There is to date no single study that quantifies the influence of air-sea coupling on TC characteristics in the IO using a coupled model run over a long period.

In the BoB, the TC-induced oceanic cooling is three times larger during the pre-monsoon than during the post-monsoon (Gopalakrishna et al., 1993; Neetu et al. 2012; Sengupta et al., 2008). This difference is essentially related to seasonal changes in oceanic stratification, rather than in TCs strength (Neetu et al., 2012). This seasonal stratification change is related to both temperature and salinity. The post-monsoon indeed both displays a stronger haline stratification (due to the large freshwater flux into the Bay during and shortly after the monsoon) and a deeper thermocline along the BoB rim (in response to coastal Kelvin waves originating from the equatorial region; McCreary et al., 1996; Durand et al., 2009) than the pre-monsoon,. As quantified by Neetu et al. (2012), 60% of of the TCs cold wake reduction during the post-monsoon is

due to thermal stratification changes, while haline stratification accounts for the remaining 40%. As speculated by Sengupta et al. (2008), it is possible that the basin-scale dynamics, as well as freshwater from monsoon rain and river runoff, favours intense post-monsoon TCs in the BoB, by reducing TC-induced cooling and therefore the negative feedback on TCs amplitude during that season.

Main objective of the chapter and structure. We will hence use a regional IO, mesoscale coupled ocean-atmosphere model (Samson et al., 2014) to assess the negative oceanic feedback on TCs amplitude in this basin. This model simulates realistic spatial and seasonal distributions of IO tropical cyclones, as well as their interannual variations. It however fails reproducing strongest observed cyclones (category 3 and more) as for similar studies in other oceanic basins (Jullien et al., 2014; Ogata et al., 2015). We will compare TC statistics from two twenty year-long experiments (a reference coupled experiment and forced atmospheric experiment, i.e. with no air-sea coupling) to provide a reliable statistical assessment of the air-sea coupling impact on IO TCs. This approach has already been successfully used to study the effect of air-sea coupling on the South Pacific TCs climatology (Jullien et al., 2014). The rest of the chapter is organised as follows. Section 3.2 describes the observed datasets and the modelling framework. In section 3.3, we assess the strong impact of air-sea coupling on IO TC characteristics. Section 3.4 will discuss the related mechanisms. Section 3.5 addresses more specifically how the strong increase in ocean stability due to monsoon freshwater inputs affects air-sea coupling under BoB TCs. Section 3.6 discusses the robustness of results in the previous sections to the convective parameterization. The final section provides a summary and a discussion of the results.

3.2 Datasets and methods

3.2.1. The NOW regional coupled model

In this study, we use an IO configuration of the NOW (NEMO-OASIS3-WRF) regional coupled model. NOW couples the NEMO (Nucleus for European Modeling of the Ocean) ocean component (Madec et al., 2008) to the WRF (Weather Research and Forecasting Model) atmospheric component (Skamarock and Klemp, 2008) through the OASIS3 coupler (Valcke, 2013). This configuration has been extensively described and validated in Samson et al. (2014). A brief summary of this configuration is given in the following.

The turbulent kinetic energy scheme (Blanke and Delecluse, 1993) is used for model vertical mixing parameterizations, and subgrid-scale parameterizations include a bi-Laplacian viscosity and an iso-neutral Laplacian diffusivity (Lengaigne et al., 2003). Atmospheric model physics include the WRF single-moment six-class microphysics scheme (Hong and Lim, 2006), the Goddard shortwave radiation scheme (Chou and Suarez, 1999), the Rapid Radiation Transfer Model for longwave radiation (Mlawer et al., 1997), the Yonsei University planetary boundary layer (Noh et al., 2003) and the four-layer Noah land surface model (Chen et al., 1996). It also includes the updated Kain-Fritsch (KF) atmospheric convective scheme (Kain, 2004), a mass-flux convergence scheme that allows shallow convection, includes a minimum entrainment rate to suppress widespread convection in marginally unstable, relatively dry environments, and has changes in the downdraft formulation. This scheme indeed provides the best simulations for TC intensity and track prediction in the northern IO (Srinivas et al., 2013b), with higher convective warming with stronger vertical motions relative to the other tested cumulus schemes. As discussed in Samson et al. (2014), the

KF scheme allows simulating strong TCs (up to 55m.s^{-1}) compared to Betts-Miller-Janjic (BMJ) moist convective adjustment scheme (Janjic, 1994) but leads to a large overestimation of the number of IO TCs. As seen in chapter 1, deep convection is an essential mechanism for TCs, and the results presented here may be sensitive to the convective scheme. The sensitivity of our results to the choice of convective scheme will thus be addressed in the discussion section by comparing results obtained using KF with those obtained using the BMJ convective scheme. The drag parameterization over the ocean is based on the work of Donelan et al. (2004).

This model is applied to the Indian Ocean region [25.5°E-142.5°E, 34.5°S-26°N], with the oceanic and atmospheric component sharing the same 1/4^{o} horizontal grid. The ocean component has 46 vertical levels, with an enhanced 5 m resolution in the upper ocean. The atmospheric component has 28 sigma vertical levels, with a higher resolution of 30 m near the surface. Lateral boundary conditions of NEMO are supplied from a 1/4^{o} resolution global ocean model forced by Drakkar forcing dataset (Brodeau et al., 2010). Those of WRF are taken from 6 hourly ERA-Interim reanalysis (Dee et al., 2011). The initial condition on the 1st of January 1989 is provided from ERA-Interim reanalysis for the atmosphere and from the ¼° DRAKKAR simulation described above for the ocean. A 21 year coupled simulation is performed with this setup using 1989–2009 lateral boundary conditions, and will be referred to as KF-CPL (for Kain-Fritsch coupled). The first year of this experiment is discarded, and this simulation is hence analysed over a 20-years period.

Samson et al. (2014) demonstrated that this configuration is able to capture the main features of the Indian Ocean climate. At seasonal timescales, it reproduces the seasonal

rainfall distribution and the northward seasonal migration of monsoon rainfall over the Indian subcontinent. It also captures the observed interannual variability associated with the Indian Ocean Dipole and the El Niño Southern Oscillation. More importantly for our study, its relatively high horizontal resolution allows to explicitly simulate TCs, with realistic cyclogenesis, track density patterns and a realistic seasonal cycle, including the observed bimodal distribution in the northern IO. The seasonal evolution of the large-scale atmospheric parameters involved in the TCs genesis is also properly captured. The main discrepancy lies in the inability of this configuration to simulate strongest TCs, with maximum modelled TCs winds reaching ~55 m s^{-1}, in contrast to 70 m s^{-1} in observations.

3.2.2 Sensitivity experiments

Experiment design. To isolate the effect of air-sea coupling on TCs, a similar strategy to that of Jullien et al. (2014) is followed. We perform a twin uncoupled atmospheric simulation (referred to as KF-FOR) using the same WRF atmospheric configuration and SST fields from the KF-CPL simulation, from which TC-induced cold wakes have been suppressed. Cold wake signals are removed by masking the coupled model SST along all the TCs tracks, within a 3° radius and from 1 day before to 30 days after the TC passage. Masked regions are then filled using bi-linear interpolation from neighbouring regions. As a result, these forced simulations do not account for any ocean feedback. Comparing TCs in the coupled and forced simulations will therefore allow us to infer the impact of air-sea coupling on TCs characteristics in the IO. An illustration of the strategy employed to remove the SST signature of TCs in the forced experiment is provided on Figure 3.1: as can be seen on that particular example, the cold wake is efficiently suppressed from the KF-FOR surface boundary condition.

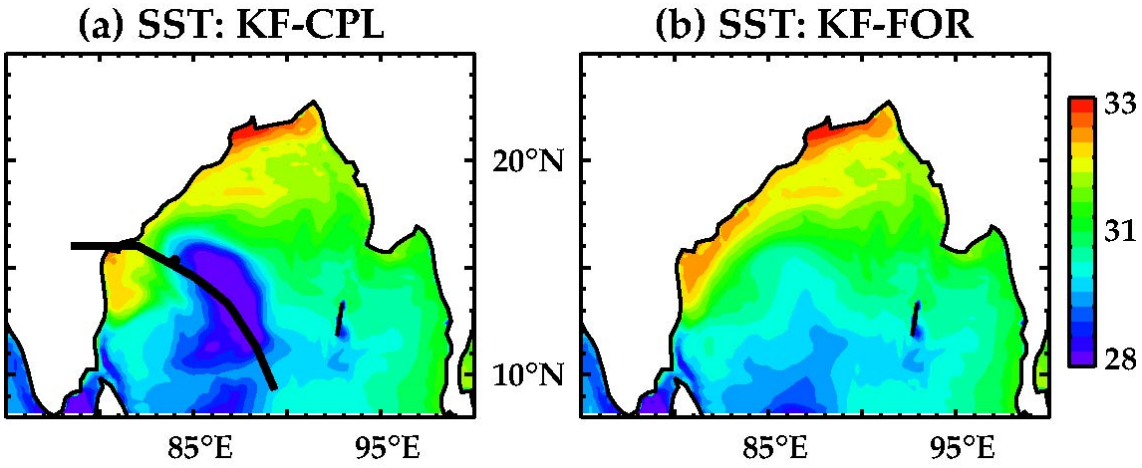

Figure 3.1: Sea surface temperature (^{o}C) snapshot for the (a) KF-CPL and (b) KF-FOR simulations. The SST boundary condition of the KF-FOR simulation is obtained after filtering the TC cold wake from the SST field shown in (a). The corresponding TC track from the KF-CPL simulation is denoted by black line on panel (a).

Analysis of the two experiments. It must however be kept in mind that the small perturbations induced by the cold wake removal are sufficient to change the courses of TCs between the forced and coupled simulations, due to the chaotic nature of the atmosphere. Genesis time and trajectories of simulated TCs in the forced and coupled experiments will therefore be different and TCs in these two simulations cannot be compared individually. Comparing the statistics of the simulated TCs in the forced and coupled experiments will however allow us to infer the influence of air-sea coupling on IO TCs characteristics. A similar strategy was successfully used by Jullien et al. (2014) to assess the impact of air-sea feedback under South Pacific TCs.

3.2.3 Tracking methodology and cyclogenesis indices

TCs from both simulations are tracked using the same methodology as in Samson et al. (2014). The following criteria are used to distinguish tropical cyclones from intense mid-latitude systems at each time step:

- 10 m wind > 17.5 $m.s^{-1}$ associated with a local sea level pressure minimum
- 850 hPa vorticity > $3*10^{-4}$ s^{-1}
- 700–300 hPa mean temperature anomaly > 1°K

TCs temperature anomalies are calculated with respect to their large-scale environment: the TC region is defined as 3 radii of maximum wind around the TC centre while the environmental temperature is averaged between 6 and 9 radii. Trajectories are then constructed by recursively detecting the closest neighbouring grid points that meet all above criteria. If no matching point is identified, all criteria are relaxed except vorticity. This relaxation technique allows following TCs over land and avoids counting the same TC twice. Tracks shorter than 1 day are eliminated. The vorticity and temperature thresholds are similar to those considered in previous studies (Jourdain et al., 2011; Jullien et al., 2014; Samson et al., 2014). In the rest of the chapter, we will refer to all storms verifying the above criteria as TCs. Each TC-prone basin uses a different TCs definition, rendering comparison between basins difficult. For instance, a TC is defined as a tropical system with sustained 10-m winds of at least 17 $m.s^{-1}$ in the west Australian and the northern IO basins, while this threshold is 33 $m.s^{-1}$ for the southwestern IO. For a fair comparison, we hence define TCs using a 17.$m\text{-}s^{-1}$ on the sustained 10-m winds and follow the Saffir-Simpson scale to define TC categories as: tropical storm (Cat-0 TC for 17 $m.s^{-1}<V_{max}<33$ $m.s^{-1}$), Category 1 TC (Cat-1 TC for 33 $m.s^{-1}<V_{max}<43$ $m.s^{-1}$), Category 2 TC (Cat-2 TC for 43 $m.s^{-1}<V_{max}<50$ $m.s^{-1}$), Category 3 TC (Cat-3 TC for 50 $m.s^{-1}<V_{max}<59$ $m.s^{-1}$), Category 4 TC (Cat-4 TCs for 59 $m.s^{-1}<V_{max}<70$ $m.s^{-1}$) and Category 5 TC (Cat-5 TC for $V_{max}>70$ $m.s^{-1}$).

Following Emmanuel and Nolan (2004), we use the Genesis Potential Index (GPI) to better understand the influence of large-large environmental parameters on the

cyclogenesis. The GPI monthly index is constructed as in Camargo et al. (2007) and Emanuel and Nolan (2004) as

$$\mathrm{GPI} = \underbrace{|10^5\eta|^{3/2}(1+0.1V_{\mathrm{shear}})^{-2}}_{\text{dynamic}}\underbrace{\left(\frac{H}{50}\right)^3\left(\frac{V_{\mathrm{pot}}}{70}\right)^3}_{\text{thermal}}$$

where η is the absolute vorticity at 850 hPa in s^{-1}, H is the relative humidity at 600 hPa, V_{pot} is the potential intensity calculated using a routine provided by K Emanuel (http:// wind.mit.edu/~emanuel/home.html) and V_{shear} is the magnitude of vertical wind shear between 850 and 200 hPa in $m.s^{-1}$.

3.2.4 Validation datasets

The observed datasets used in the present study are listed in Table 3.1. Observed TCs locations and wind magnitudes are derived from IBTrACS dataset (Knapp et al., 2010), that merges TC tracks and intensities data from various operational meteorological forecast centres. The maximum sustained wind speed value denoting the strength of a TC is taken as 10 meters wind speed averaged over a period 10 minutes. Observed SST response under TCs is characterized by using a blend of TRMM/TMI and AMSR-E SST data (http://www.ssmi.com/sst/microwave_oi_sst_data_description.html), which is available from 1998 onwards. It is advantageous to use this data due to its insensitivity to atmospheric water vapor (Wentz et al., 2000). It provides the accurate SST observations below the clouds, a few days before and after the storm passage. The atmospheric parameters that control the TCs intensification (vertical wind shear and mid-tropospheric humidity and maximum potential intensity) are extracted from the ERA-Interim atmospheric reanalysis (Dee et al., 2011).

S. No.	Parameter	Description
1	SST	Blended TRMM/TMI and AMSR-E daily SST
2	Atmospheric parameters (Wind, shear, Relative Humidity, Maximum Potential Intensity)	ERA-Interim atmospheric reanalysis (Dee et al., 2011).
3	Tropical cyclone position and intensity	IBTrACS dataset (Knapp et al., 2010).

Table 3.1: Data used in the study.

3.3 Influence of air-sea coupling in IO TCs climatology

Figure 3.2 compares the spatial distribution of IO TCs for observations (Figure 3.2a), KF-CPL and KF-FOR simulations (Figure 3.2bc). In the northern Indian Ocean, cyclogenesis is maximum in the southern part of the Bay of Bengal and Arabian Sea (around 5°N), although cyclogenesis also occurs further north in the Bay (Figure 3.2a). In this basin, most observed TCs travel northward and/or westward (not shown). Maximum TCs density is consequently found northwestward of the maximum cyclogenesis between 5°N and 20°N in the western half of the BoB. While weakening over the Indian peninsula, some storms are able to re-intensify when reaching the Arabian Sea and pursue their trajectory further westward (not shown). Tropical storms form less frequently over the Arabian Sea, with three times less TCs as compared to the Bay of Bengal. In the southern IO, cyclogenesis occurs mostly between 5°S and 25°S with a maximum located in the central part of the basin (around 80°E), and a weaker, secondary maximum Northwest of Australia. Maximum TCs density exhibits a poleward-shifted distribution relative to cyclogenesis. In this region, TCs usually travel southwestward between 10°S to 15°S to then deviate and travel in a southeastward

direction between 20°S and 30°S, being advected by climatological tropospheric winds (not shown). The KF-CPL simulation successfully captures these spatial patterns for both the northern and southern IO (Figure 3.2b). The modelled cyclogenesis exhibits a poleward bias in the BoB and a slight equatorward bias in the southern hemisphere. The maximum simulated TCs density is shifted eastward in the southern IO and the model does not reproduce the gap in TCs density around 100°E, offshore the West Australian coast. The major bias in the KF-CPL simulation is however to produce three times more TCs than in observations (Figure 3.2d). Compared to other basins (Jullien et al., 2014; Ogata et al., 2015), air-sea coupling does not significantly impact the spatial patterns of cyclogenesis and TC tracks in the IO (Figure 3.2bc). The only apparent change is a 20° eastward shift of the maximum TC density region in the southern IO from 85°E to 65°E, which is not statistically significant (not shown). The most robust impact of the oceanic feedback is a considerable decrease (~20%) in the numbers of storm reaching the 17 $m.s^{-1}$ threshold (Figure 3.2d), in both hemispheres.

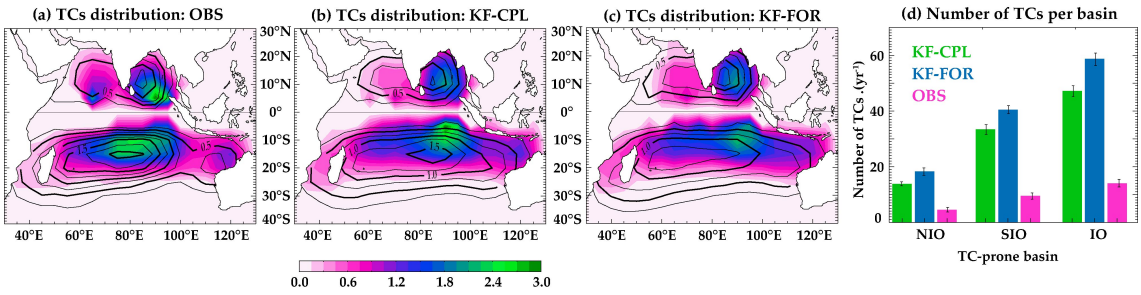

Figure 3.2: Climatological distribution of normalised cyclogenesis (colour) and TC density (contour) for **(a)** observations, **(b)** KF-CPL and **(c)** KF-FOR simulations. The climatological annual number of NIO and SIO TCs are ondicated on each panel. **(d)** Histograms of the number of TCs-days in the IO basin for each dataset (whiskers indicate the 90% confidence interval based on a student t-test).

In the southern IO, TCs preferentially occur in austral summer, i.e. from November to April, with very few cyclones forming during boreal winter (Figure 3.3a). This seasonal

cycle is reasonably well captured by the observed GPI (Figure 3.3a): in this region, high mid-tropospheric relative humidity, low vertical shear and high maximum potential intensity combine to favour cyclogenesis during austral summer in the southern IO (Figure 3.4b-e), when the Intertropical Convergence Zone is well established in the southern hemisphere (e.g. Menkes et al., 2012). The seasonal evolution of southern IO TCs statistics is generally well captured by KF-CPL, with a maximum TC activity (Figure 3.3b) and related large-scale favourable environmental conditions during austral summer (Figure 3.4a-e). The vorticity is however overestimated in the model (the MPI and wind shear also exhibit slight biases, being respectively slightly overestimated / underestimated). In the northern IO, the observed seasonal TC distribution exhibits a very peculiar bimodal distribution (Figure 3.3e): they indeed preferentially occur during the pre-monsoon (April–June) and post-monsoon (September–December), with much fewer TCs in June–July and almost no TCs in January-March. This bimodal distribution has been attributed to the combined effect of increased vertical wind shear, decreased maximum potential intensity and vorticity that overcome the increased relative humidity during the summer monsoon (Figures 3.4f–j), preventing the formation of tropical storms during that season (Tippett et al., 2011; Menkes et al., 2012; Li et al., 2013). The KF-CPL simulation captures this specific bimodal cyclogenesis distribution reasonably well (Figure 3.3f), although it overestimates the proportion of TCs occurring during the core of the summer monsoon (July-August). It must however be noticed that only Cat-0 TCs (with Vmax<33 $m.s^{-1}$) develop in KF-CPL (and observations) during this period (not shown). The seasonal evolution of the large-scale atmospheric drivers of the modelled TCs is also generally

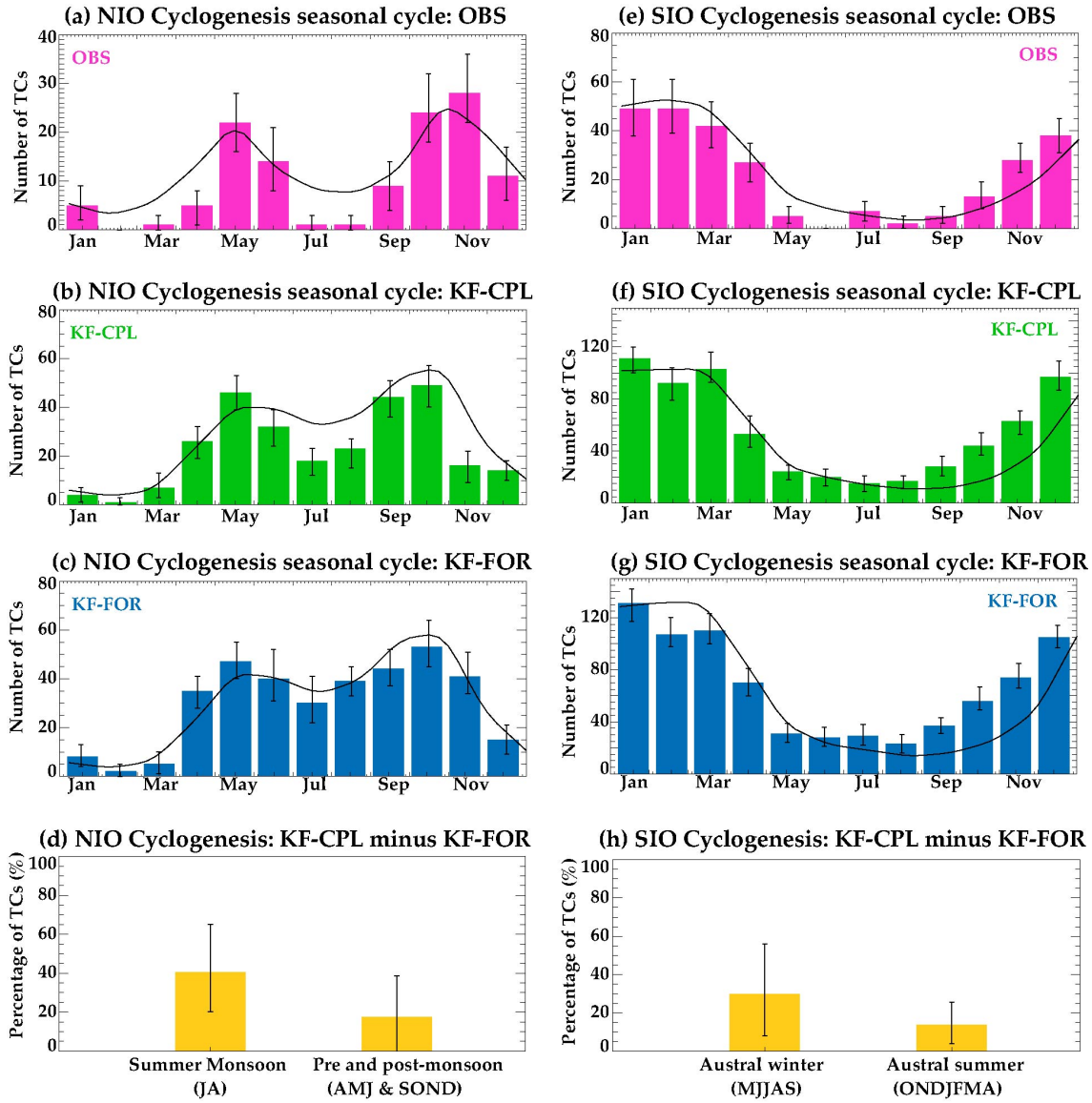

Figure 3.3: Histogram of the percentage of TCs occurring each calendar month in the (left) southern and (right) northern IO for **(a,e)** observations, **(b,f)** KF-CPL and **(c,g)** KF-FOR simulations. The monthly climatological evolution of the corresponding GPI index (northern IO: 40°E-100°E; 0°-25°N and southern IO: 30°E-130°E; 0°-25°S) is overlaid. Percentage of TC number decrease in KF-CPL relative to KF-FOR for cyclonic and non-cyclonic season for **(d)** southern and **(h)** northern IO. On all panels, the whiskers display the 90% confidence interval based on a student t-test.

well captured (Figures 3.4f–j). As in observations, the large increase of vertical shear during the monsoon results in a GPI minimum. This minimum is less marked than in observations, probably because of a more favourable vorticity, which is consistent with the overestimated number of TCs during the monsoon (Figure 3.3f). Another noticeable

mismatch is the tendency for the post-monsoon TC-prone season to occur one month earlier (September-October) than in observations (October-November). This bias can be tracked back to a similar bias in seasonal GPI (Figure 3.4f), most likely related to an earlier post-monsoon humidity decrease in the model (Figure 3.4h). The oceanic feedback reduces the number of TCs throughout the year (Figure 3.2d and Figure 3.3bf). Its impact is however largest during non-cyclonic seasons, i.e. when the large-scale environmental conditions are less favourable to TC development (Figure 3.3bc and 3.3fg). TCs are indeed ~20% less numerous in coupled simulations during the TC-prone seasons of both hemisphere, but this decrease reaches 30 % during boreal winter in the southern hemisphere (Figure 3.3d) and 40% during the summer monsoon in the northern IO (Figure 3.3h). This results in a more marked reduction in TC numbers during the summer monsoon in the coupled model, more in line with observations (Figure 3.3efg).

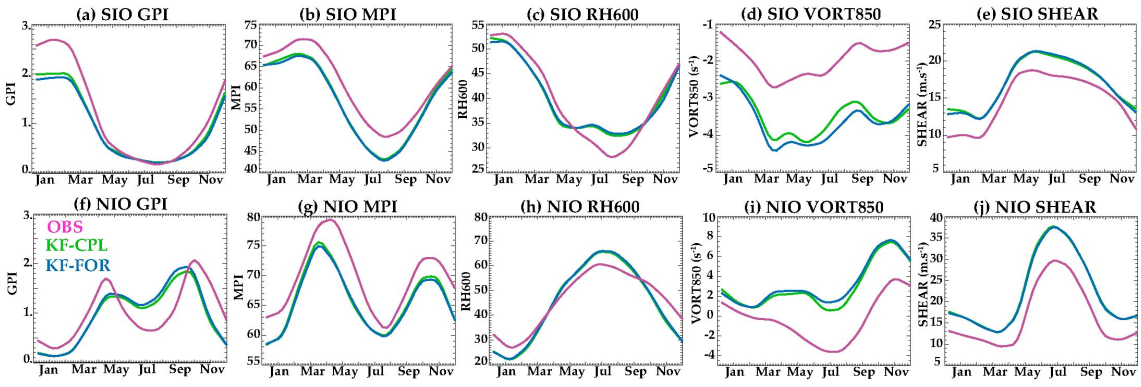

Figure 3.4: Seasonal evolution of the **(a)** Genesis Potential Index (GPI), **(b)** Maximum potential Intensity (MPI), **(c)** relative humidity at 600hPa, **(d)** vorticity at 850hPa and **(e)** vertical wind shear in the southern IO for observations, KF-FOR and KF-CPL. **(f-j)** Same for the northern IO.

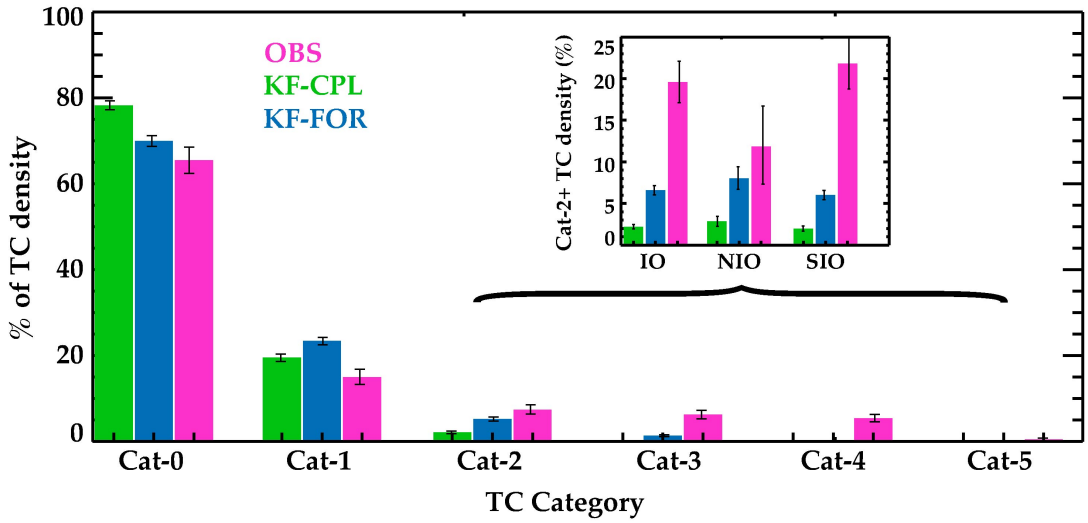

Figure 3.5: Histogram of the percentage of Indian Ocean TC occurrence as a function of TC intensity, based on maximum TC wind for observations, KF-CPL and KF-FOR simulations. The inner frame indicates the percentage of intense TCs (category 2 or more). The whiskers display the 90% confidence interval, computed using a Student's t-test.

Figure 3.5 summarizes the simulated and observed IO TCs intensity distribution. In observations, 9% of the storms exceed Cat-2 in the northern IO and 18% in the southern IO respectively (see inset in Figure 3.5), with maximum TCs wind that can exceed 70 $m.s^{-1}$. For both hemispheres, the KF-CPL experiment is able to simulate TCs with winds of up to 50 $m.s^{-1}$ but never exceed Cat-2. This results in a general tendency for KF-CPL to considerably underestimate the percentage of intense TCs (Cat-2 and more), with only 2-3% of the storms exceeding Cat-2 TCs (see inset in Figure 3.5). Symmetrically, KF-CPL overestimates the percentage of Cat-0 TCs by ~10% (Figure 3.5). As in Ogata et al. (2015) and Jullien et al. (2014), our rather coarse 25-km model resolution indeed does not allow to accurately simulate the sharp eyewall structure of tangential winds for strongest TCs. The radius of maximum wind speed are indeed overestimated in KF-CPL (75 km) relative to observations (50 km; not shown), as expected from a ¼° resolution (Gentry and Lackmann, 2010). The oceanic feedback has a considerable impact on the TCs intensity distribution: there is a four-fold decrease of strong (Cat-2

and above) TCs in the KF-CPL simulation (2%) relative to KF-FOR (8%). As a consequence, the proportion of tropical storms (Cat-0) is 10% larger in the coupled than in the forced experiment. Ogata et al. (2015) found that the region of maximum intense TCs shifts equatorward in the northwest Pacific when air-sea coupling is accounted for. In contrast, we do not find any significant change in the distribution of strongest TCs, neither in the northern or southern IO (not shown).

We also checked that the decrease in tropical cyclogenesis and the weaker TCs intensity in KF-CPL compared to KF-FOR cannot be attributed to changes in large-scale environmental parameters that remain virtually the same in the two simulations (Figure 3.4). These changes in the TC characteristics can hence confidently be attributed to the direct local oceanic feedback onto storm formation rather in an indirect large-scale change in the atmosphere. The mechanisms of this TC intensity reduction in presence of air-sea coupling are further investigated in the next section.

3.4 Mechanisms of air-sea coupling under TCs

The oceanic feedback onto TC characteristics operates through the SST changes induced by TCs. TCs are known to cool the ocean surface along their track, mainly through vertical mixing and upwelling (e.g. Price et al., 1981; Jullien et al., 2012; Vincent et al., 2012ab). In this study, the cooling under TCs is computed in a similar way to Vincent et al., 2012ab. To characterize the ocean response to TCs, we first subtract the mean SST seasonal cycle. TC track positions are then used to extract the oceanic response to TCs. The average SST anomalies are computed within a fixed 200

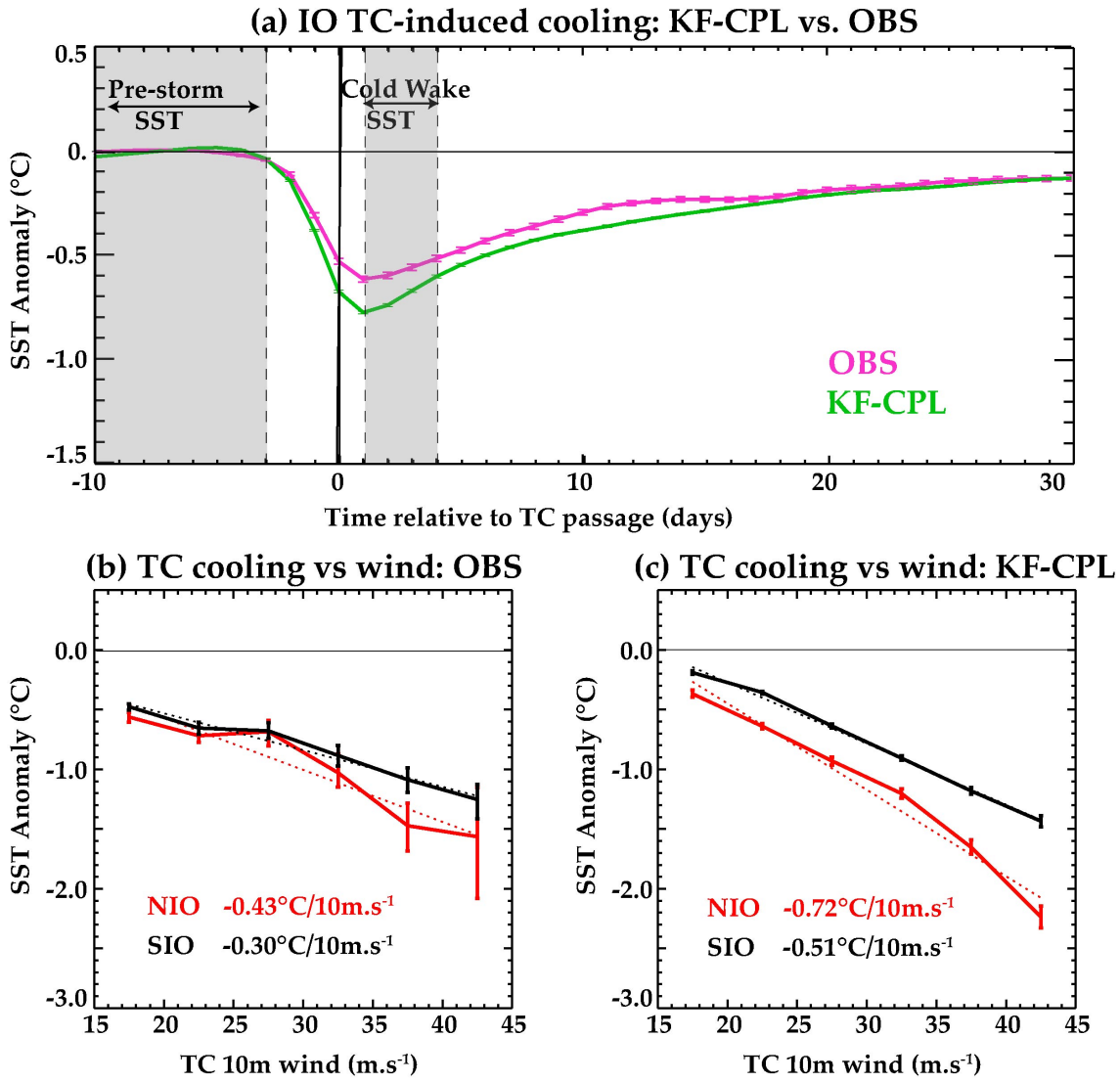

Figure 3.6: (a) Composite evolution of TC-induced SST cooling within 200 km of all TC-tracks in the IO (in °C) for observations (black) and the KF-CPL experiment (green). Northern and southern IO mean TC-induced cooling as a function of 10-min averaged maximum wind speed for **(b)** observations and **(c)** KF-CPL. Whiskers indicate the 90% confidence level from a bootstrap. The slope of the linear fit is also indicated.

km radius around each TC track position, from 10 days before to 30 days after the TC passage. This radius has been chosen because it corresponds to the area where SST has an influence on TC intensity (Cione and Uhlhorn, 2003; Schade, 2000). The observed and modelled composite evolution of TC-induced SST cooling is shown in Figure 3.6a. The model simulates the composite temporal evolution and amplitude of the TC-

induced cooling acurately. For both model and observations, decrease in SST is evident a few days before the storm reaches a given point and largest cooling usually occurs 1 day after the cyclone passage (Figure 3.6a). The decay timescale is much slower and it it takes about 30 days for the SST to recede. However, after the passage of storm the average SST remains 0.2°C colder than SSTs before the passage of storm. Lloyd and Vecchi (2011) and Vincent et al. (2012a) earlier noticed this phenomenon. The temporal evolutions of the composite SST cooling under TCs are very similar for the southern and northern IO for both model and observations (not shown). The amplitude of the cooling as a function of the TC maximum wind however differs between the two hemispheres (Figure 3.6bc). Although the observed cooling magnitude monotonically increases with wind intensity in both hemispheres, this increase is ~50% larger for the northern IO (-0.43°C per 10 $m.s^{-1}$) than for the southern IO (-0.30°C per 10 $m.s^{-1}$). There is hence a tendency for TCs to induce a larger oceanic cooling for a given TC wind intensity in the northern than in the southern IO. This behaviour is reasonably well captured by the model, despite an overestimated slope (0.72 and 0.51°C per $10.m.s^{-1}$ for the Northern and Southern hemisphere, respectively).

Two different reasons may explain this larger cooling in the northern hemisphere. First, differences in TC translation speeds can affect the amplitude of the TC-induced cooling (Zedler, 2009; Mei et al., 2012): slower-moving TCs indeed result in a larger TC-induced cooling for a given TC wind intensity, as they spend a longer time over any given oceanic point and hence input more momentum into the ocean, which eventually leads to enhanced vertical mixing. Figure 3.7a reveals that the translation speed distribution does not differ much between the two hemispheres (4.60 $m.s^{-1}$ average over the northern IO compared to 4.77 $m.s^{-1}$ average in the southern IO), suggesting that

differences in the TCs translation speed cannot explain the differences in the TC-induced cooling amplitude between the two hemispheres.

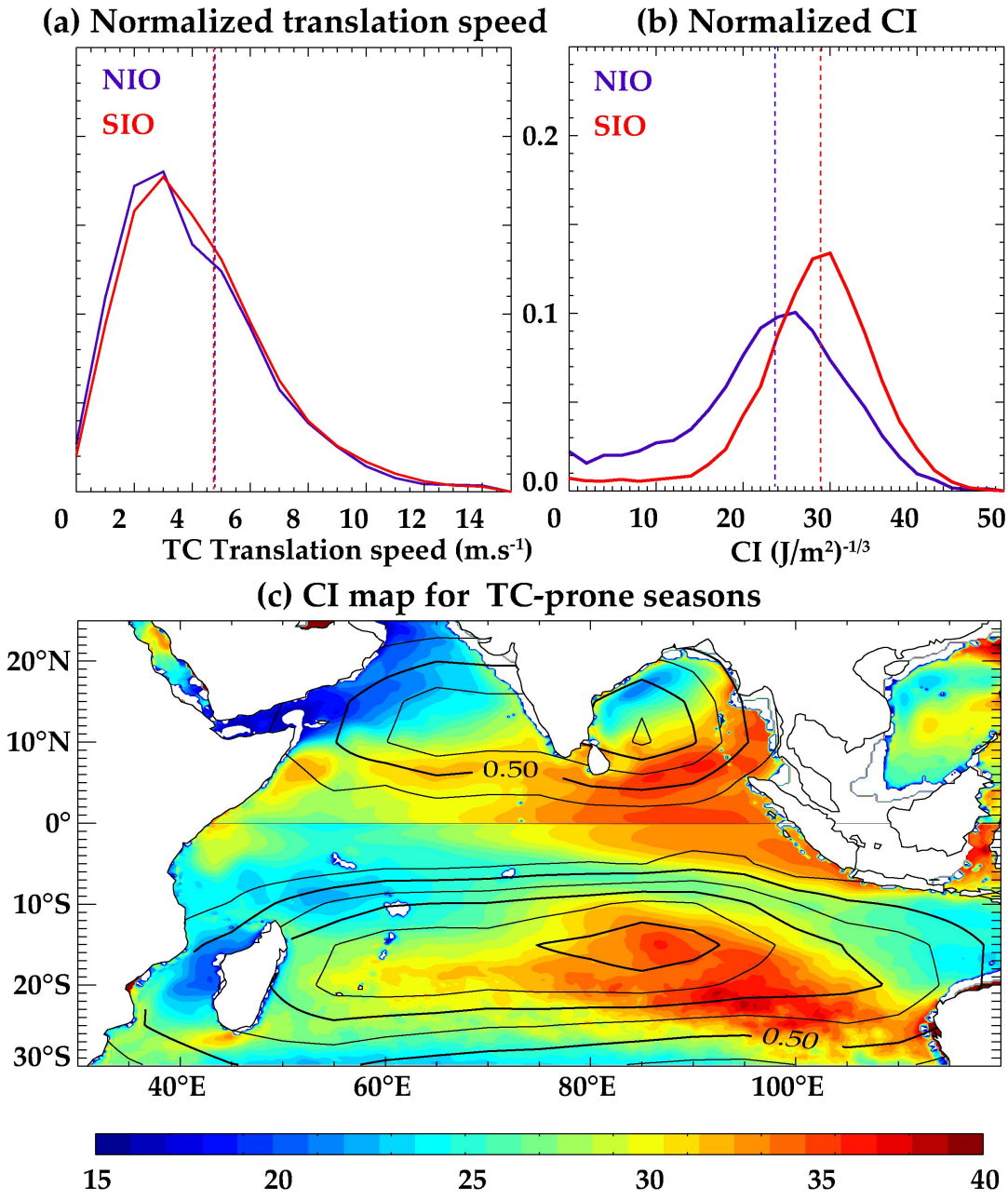

Figure 3.7: KF-CPL model normalized distribution of **(a)** TC translation speed and **(b)** cooling inhibition index (CI) under TCs for the NIO and SIO basins. **(c)** CI (color) and normalized TCs density (contour) climatological maps for extended cyclonic seasons (November to April for the Southern Hemisphere and April to December for the Northern Hemisphere).

The other plausible hypothesis relates to the differences in oceanic stratification between the two hemispheres. Those can indeed influence the amplitude of the TC-induced SST signature, as already acknowledged in past literature (e.g. Lloyd and Vecchi, 2011; Vincent et al., 2012b; Neetu et al., 2012). Vincent et al. (2012b) indeed showed that at the global scale the upper-ocean pre-cyclone stratification modulates the TC-induced cooling amplitude by up to an order of maginude for a given wind input to the ocean. Following Vincent et al., 2012b, we characterize the TC-induced surface cooling inhibition by the ocean background state by the Cooling Inhibition Index (CI). This index is defined as the cube root of the potential energy change necessary to induce a 2°C surface cooling via vertical mixing. CI is a physically relevant measure of this inhibition since it integrates two important parameters for the cooling amplitude: the MLD before the cyclone passage, and the strength of the stratification underneath this mixed layer. As illustrated on Figure 3.7b, the CI distribution underneath TCs is different between the two hemispheres, with generally weaker upper ocean stratification in the northern IO (average CI of 23 $(J/m^2)^{-1/3}$) compared to the southern hemisphere (average CI of 29 $(J/m^2)^{-1/3}$). Figure 3.7c displays the IO CI spatial distribution during the cyclonic season of each hemisphere. In the northern IO, the western BoB and AS, over which most TCs travel, are characterized by relatively low CI, ranging from 20 to 30 $(J/m^2)^{-1/3}$. In the southern IO, the core of the TC-prone region (between 10°S and 25°S) is characterized by larger CI, exceeding 30 $(J/m^2)^{-1/3}$. In this region, southeasterly trade winds regime prevail although the year, resulting in downward Ekman pumping and a deep thermocline. Weaker CI are however found in the thermocline ridge region of southwestern tropical IO, characterized by a climatologically shallow thermocline in the 5°S–10°S latitudinal band (e.g. Xie et al., 2002; Vialard et al., 2009; Jayakumar et al., 2011; Praveen Kumar et al., 2014). This low CI region is due to a shallow

thermocline, which results from Ekman pumping associated with the confluence of the southeasterly trades and equatorial westerlies. It is however located at the very northwestern end of the south IO TC-prone region (Figure 3.7c) where only a small fraction of the southern IO TCs occur. Similarly, the eastern and southern BoB exhibits considerably larger CI because of deeper thermocline than in the Nortwestern BoB there, in response to donwnwelling coastal Kelvin waves excited by the remote influence of equatorial westerlies during the intermonsoon seasons (e.g. Rao et al., 2010). Here, again, BoB TCs spend most of their time further Northwest (Figure 3.2c, where the thermocline is shallower and CI is lower).

Figure 3.8 provides a southern hemisphere composite of wind speed, SST and latent heat flux at the air-sea interface under a TC, for KF-CPL and KF-FOR. This composite is built by averaging composites performed for a given maximum wind (5 $m.s^{-1}$ wide bins), so that differences reflect the impact of air-sea coupling and not the different TC wind distributions (i.e. stronger TCs in KF-FOR than in KF-CPL). TC wind composites exhibit very similar wind speeds in both simulations, indicating that our compositing strategy smoothes out TC intensity differences between the two simulations (Figure 3.8abc). The 10-m wind speed composite features a clear cyclone eye with weaker winds and asymmetric eye wall for both simulations (Figure 3.8ab). Tangential winds are stronger on the storm's left-hand side because TC translation speed adds up on the left-hand side and subtracts on the right-hand side. The SST beneath TCs are warmer on the lower quadrant and cooler on the upper quadrant in KF-FOR (Figure 3.8e), due to

the tendency of southern IO TCs to

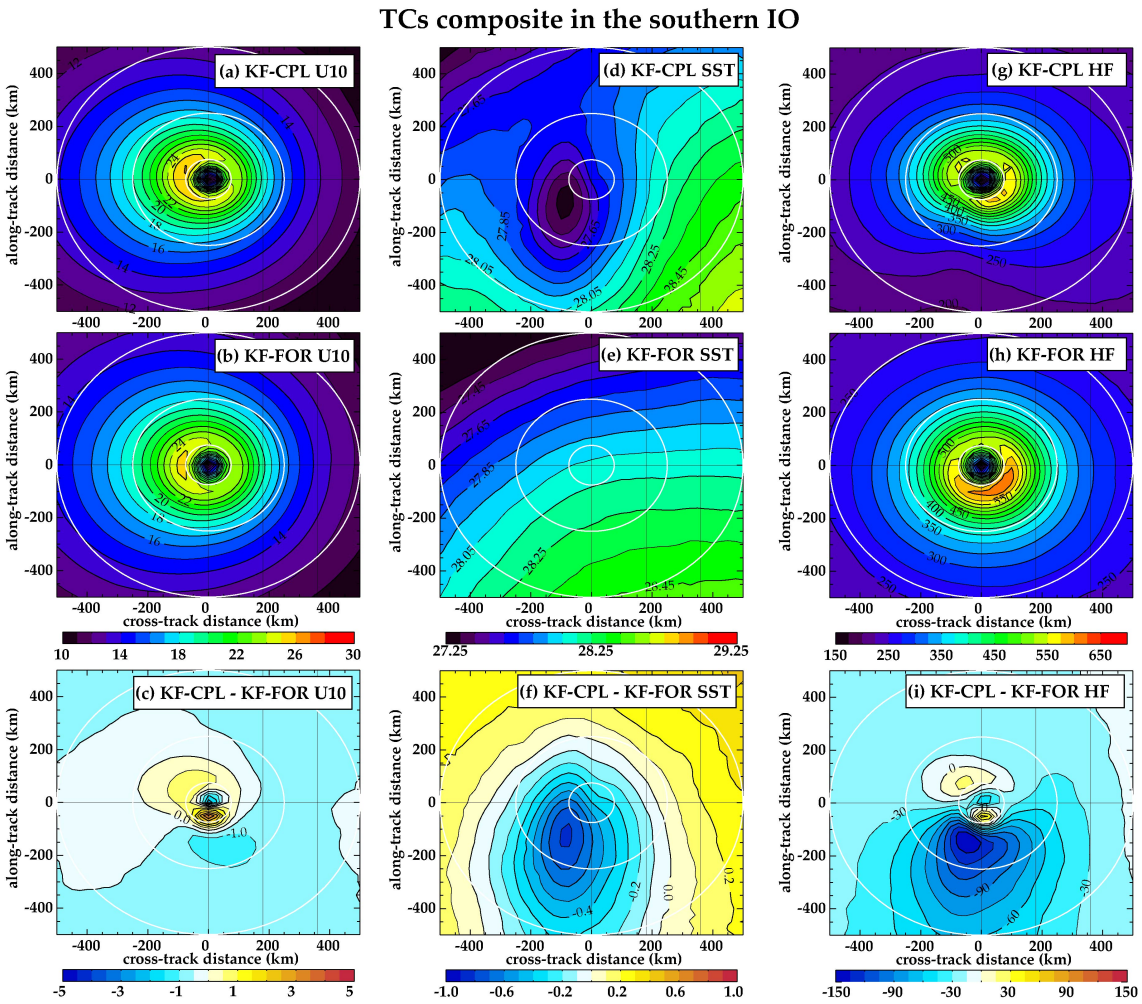

Figure 3.8: Southern IO composite of surface conditions under TCs: (left) wind speed, (middle) SST and (right) upward surface enthalpy flux for (top) KF-CPL experiment, (middle) KFFOR experiment and (bottom) KF-CPL minus KF-FOR. Storms are rotated so that the upper direction indicates the direction of propagation. The smallest circle represents the radius of maximum winds, the intermediate circle represents the 250 km radius and the biggest circle represent the 500 km radius**.**

move poleward from warm tropical SSTs to cold subtropical SSTs. The SST beneath TCs is very different in KF-CPL, with an additional strong cooling towards the rear-left of the TC track (Figure 3.8d). The TC cold wake exhibits a clear asymmetrical structure (Figure 3.8d, 3.8f), with a one Radius of Maximum Wind shift to the left-hand side of the TC in agreement with observations (Shay and Brewster, 2010; Vincent et al., 2012a).

This asymmetry is the result of the wind-current resonance at near-inertial periods (Shay et al., 1989; Jullien et al., 2012; Vincent et al., 2012a). In the southern hemisphere the TC winds and the inertial currents rotate in the same direction, leading to increase in the energy transfer to the inertial currents (Price, 1981). The strong inertial oscillations and resulting vertical shear in the southern hemisphere are generated to the left of the TC tracks. The radial structure of the enthalpy fluxes from the ocean to the atmosphere, that are largely dominated by latent heat fluxes, resembles that of the wind structure, with stronger latent heat release in regions of larger winds for both KF-FOR and KF-CPL experiments. These fluxes are rather weak in the eye region, reach a maximum within the eye wall and then slowly reduce outside the eye wall (Figure 3.8gh). Regarding the asymmetrical features, the enthalpy flux structure in KF-FOR is larger in the lower right quadrant (Figure 3.8h), most likely because of the tendency for the SST to be higher there compared to other quadrants (see Figure 3.8e). This is expected from the Clausius-Clapeyron relation, which results in upward latent heat fluxes that grow exponentially with SST when relative humidity and air-sea temperature differences are assumed to be constant:

$$L = A * u_{10} * \exp(\beta * SST) \qquad (3.1)$$

where A and b are positive constants characteristic of the Clausius-Clapeyron relation and u_{10} is the 10-m wind speed. Despite the slightly larger wind speeds in the left quadrant (see Figure 3.8b), the radial structure of the enthalpy flux is dominated by its exponential dependence to SST, resulting in larger latent heat release in the lower right quadrant where SST are warmer. This feature is not as clear in KF-FOR, because of the strong TC-induced cooling in this quadrant. In addition to these spatial structure differences, the TC-induced oceanic cooling reduces the amplitude of this enthalpy flux (Figure 3.8i). As expected, this reduction is maximum under the maximum TC-induced

cooling, in the lower left quadrant of the TC (~120W.m^{-2} reduction, i.e ~20% of the maximum enthalpy flux). The average enthalpy reduction within 200 km of the TC center is ~40W.m^{-2}, representing a 6% reduction of the total enthalpy flux fuelling the TC. This is consistent with previous literature analysing the TC-induced air-sea coupling processes in other TC-prone basins (Bender et al., 1993; Wu et al., 2004; Liu et al., 2011).

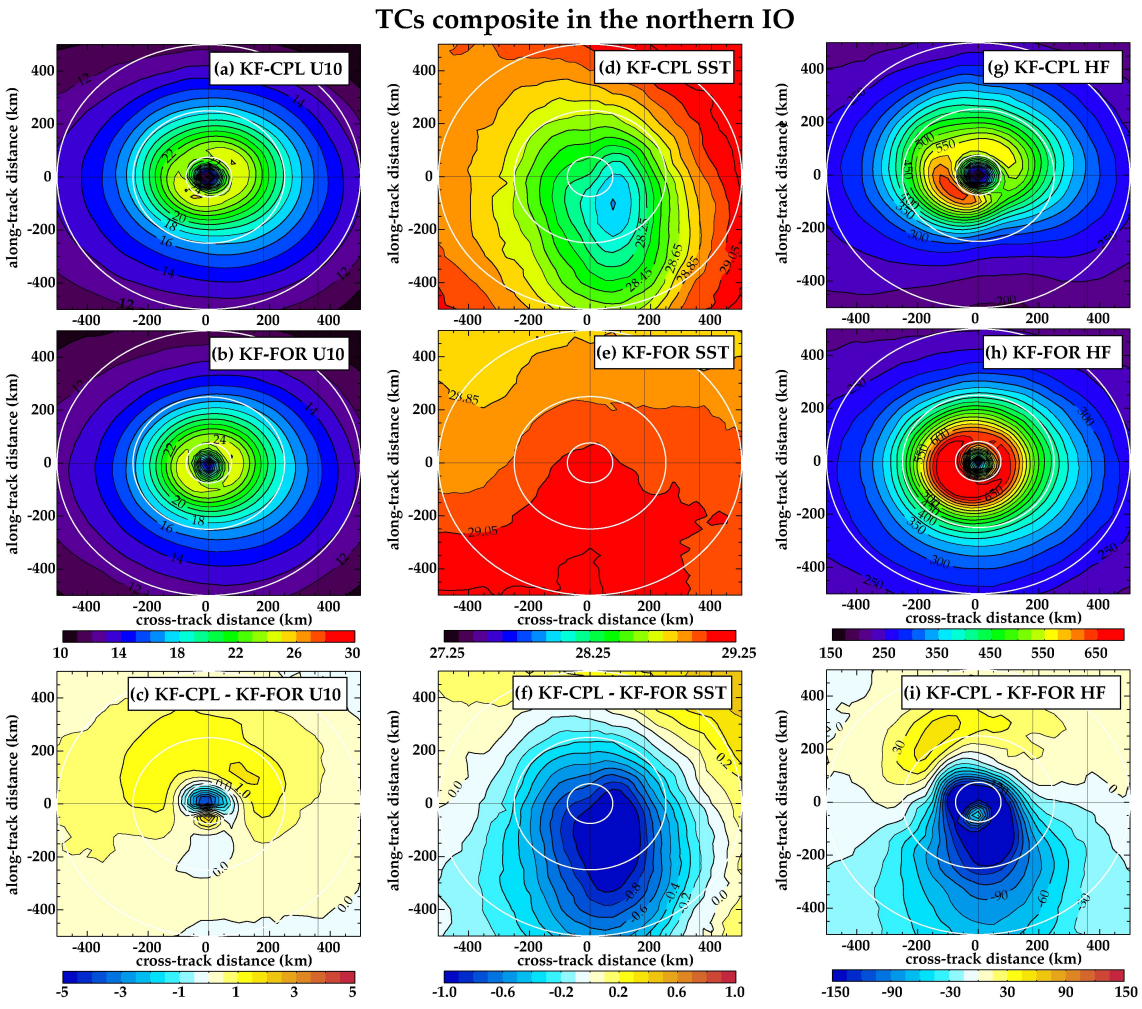

Figure 3.9: Same as Figure 3.8 for the northern IO.

Figure 3.9 provides a similar picture for northern hemisphere TCs. As for southern hemisphere TCs, northern IO TCs wind composites are very similar for the KF-CPL

and KF-FOR experiments (Figure 3.9a-c), implying that our compositing methods has removed the effect of different wind speed distributions and focusses on the effect of air-sea coupling. The KF-FOR SST beneath the TC (Figure 3.9d) is generally warmer in the northern than in the southern IO (Figure 3.8d; 29°C compared to 28°C) and is rather homogeneous spatially (BoB is uniformly warm during the cyclonic seasons). The slightly warmer SSTs at the rear of the TC are due to the poleward decrease of SST (TC form close to the equator and move poleward). KF-CPL exhibits a strong cooling at the rear of the TC on its right hand side, as the resonance between inertial oscillations and wind vector rotation occurs to the right of the track in the northern hemisphere (e.g., Price, 1981). As expected from Figure 3.6bc, the cooling is larger in the northern (Figure 3.9f) than in the southern IO (Figure 3.8f), reaching up to 1.4°C. As for the southern IO, KF-FOR enthalpy fluxes are generally larger on the lower left quadrant where SST is slightly warmer (Figure 3.9e and h). The maximum enthalpy flux reduction due to coupling with the ocean is approximately twice larger in the northern than in the southern IO (~230 $W.m^{-2}$): this is probably a result of the combined effect of the larger TC-induced cooling and warmer SST in the Northern hemisphere. While this reduction is mainly localized at the rear of the TC in southern IO (Figure 3.8i), this reduction is also prominent right under the TC in the northern IO. This results in a considerably larger upward latent heat flux reduction within 200km of the TC centre (~63$W.m^{-2}$, representing a 10% reduction of the total enthalpy flux fuelling the TC against 6% in the Southern IO).

We further investigate the dependency of the TC-related heat flux, intensification rate and SST to the TC wind intensity. To that end, Figure 3.10 displays the amplitude of the heat flux, intensification rate and SST as a function of wind intensity for KF-FOR. As

expected from eqn. (3.1), the amplitude of the enthalpy flux fuelling the TC increases with TC intensity for both hemispheres (Figure 3.10a). For a given TC wind intensity, the enthalpy flux fuelling the TC is however systematically larger in the northern compared to the southern IO in KF-FOR experiment. It is for instance 850W.m^{-2} for 45-50 m.s^{-1} TCs in the southern IO, but 1050W.m^{-2} in the northern IO. This difference can be attributed to the systematically ~1°C warmer SSTs in the northern IO (Figure 3.10c), which lead to higher enthalpy fluxes as indicated by eqn. (3.1). Consistently with those larger enthalpy fluxes, the intensification rate of intensifying TCs are generally larger in the northern than in the southern IO for the KF-For experiment, especially for maximum wind speeds above 35 m.s^{-1} (Figure 3.10b). It must however be noted that these differences may also partly be driven by the different large-scale environmental parameters that are also different in the two basins (Figure 3.4).

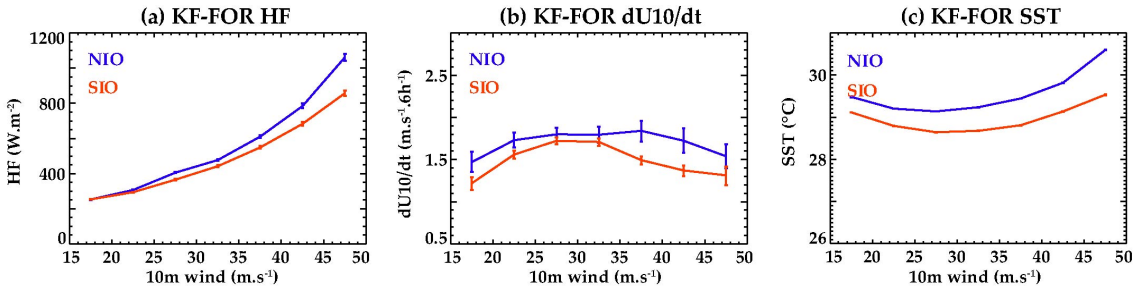

Figure 3.10: Mean (a) inner-core (i.e. within 200 km of the TC centre) upward surface enthalpy flux, (b) time rate of maximum wind speed change and (c) inner-core (i.e. within 200 km of the TC centre) SST as a function of the wind speed in the KF-FOR experiment for intensifying TCs in the (blue) northern and (red) southern IO. This figure was performed by averaging with 5 ms^{-1} bins.

Figure 3.11 further compares the impact of air-sea coupling on TCs intensification between the southern and northern IO. This is done by showing the KF-CPL minus KF-

FOR enthalpy fluxes (Figure 3.11a) and intensification rates (Figure 3.11c) for intensifying TCs as a function of the TC wind intensity. For the southern IO, air-sea coupling reduces the enthalpy flux by ~10% for a given storm strength, from ~20 $W.m^{-2}$ for weak storms to $60W.m^{-2}$ for the strongest TCs. This translates into a reduction of the intensification rate mainly for storms of intermediate strength: this reduction is indeed maximum for 30 to $40m.s^{-1}$ TCs, where it reaches ~0.2 $m.s^{-1}$ per 6h (i.e. a 10% reduction compared to the uncoupled simulation). This picture is quantitatively very different for the northern IO. In this region, air-sea coupling reduces the enthalpy flux from $30W.m^{-2}$ for weak storms to up to 210 $W.m^{-2}$ for the strongest TCs. This reduction for strongest TCs in the northern IO is hence 3 to 4 times larger than for the southern IO. This translates into a considerably larger reduction of the intensification rate of strongest TCs that reaches 0.8 $m.s^{-1}$ per 6h for the strongest storms (i.e a 50% reduction). This reduction is ~ 20-30% for storms of intermediate intensity (i.e. 35 to 45 $m.s^{-1}$). The different background SST allows understanding the larger sensitivity of NIO TCs to air-sea coupling. Based on eqn. (3.1), the air-sea coupling influence on the latent heat flux under TCs can be approximated as:

$$\Delta L_{CPL-FOR} = A * u_{10} * \exp(\beta * SST_{FOR}) * (\exp(\beta * \Delta SST_{CPL-FOR}) - 1) \qquad (3.2)$$

where $DL_{CPL-FOR}$ is the KF-CPL minus KF-FOR upward latent heat flux for a given wind storm intensity u_{10} , SST_{FOR} is the ambient SST under the TC (i.e. the KF-FOR SST, which does not account for air-sea coupling) and $DSST_{CPL-FOR}$ is the TC-induced cooling under the storm track. From this equation, two factors can contribute to the larger impact of air-sea coupling on the heat flux. First, as displayed on Figure 3.6bc, $DSST_{CPL-FOR}$ is larger in the NIO than in the SIO for a given storm intensity, arguably because of the difference in the ocean stratification in these two basins. Second, the ambient SST_{FOR} is also larger in the NIO than in the SIO (Figure 3.10b). These two

factors contribute to a larger upward latent heat flux reduction due to coupling in the Northern Hemisphere, and hence a larger impact on the cyclone growth rate.

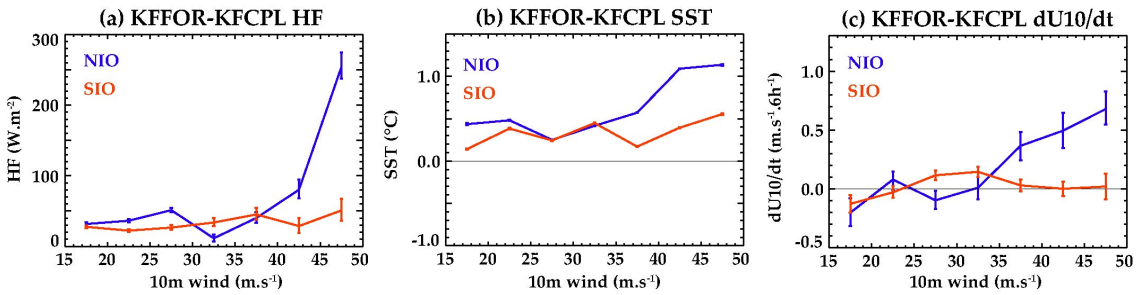

Figure 3.11: Mean KF-FOR minus KF-CPL (a) inner-core (i.e. within 200 km of the TC centre) upward surface enthalpy flux (b) inner-core (i.e. within 200 km of the TC centre) SST and (c) time rate of maximum wind speed change as a function of the wind speed for intensifying TCs in the (blue) northern and (red) southern IO.

3.5. Specific case of pre- and post-monsoon TCs characteristics in the BoB

In sections 3.3 and 3.4, we have investigated how air-sea coupling acts to reduce TC intensities in the IO, and investigated why this process is more efficient in the Northern than in the Southern IO. But previous studies (Sengupta et al., 2008) have also suggested that the change in oceanic stratification associated with the massive freshwater input in the BoB may affect the efficiency of the negative feedback on TCs due to coupling with the ocean. We will investigate this possibility in this section.

To that end, we compare the characteristics of TCs before and after the June-July period where TCs are nearly absent in observations (Figure 3.12a). In observation, all strong TCs (category 2 and above) occur during April-May and October-November (Figure 3.12b). Most of the simulated category 2 and above TCs occur in April-May during the pre-monsoon season and September to December period during the post-monsoon

(Figure 3.12b). In the following, April–May is considered as the pre-monsoon and September to December as the post-monsoon. Here, the pre-monsoon period is chosen differently than in chapter 1 (May-June as pre-monsoon), where we use forced ocean model to quantify the respective contribution of temperature and salinity stratification to the TC-induced cooling amplitude. This is because we now specifically focus on the BoB rather than the entire NIO and also because we focus on strongest TCs (category 2 and above), for which the negative feedback associated with air-sea interaction is generally stronger. It should however be noted that we have defined those periods based on cyclonic seasons rather than traditional monsoon (the months of June and September being usually encompassed within the monsoon period: Wang et al., 2009).

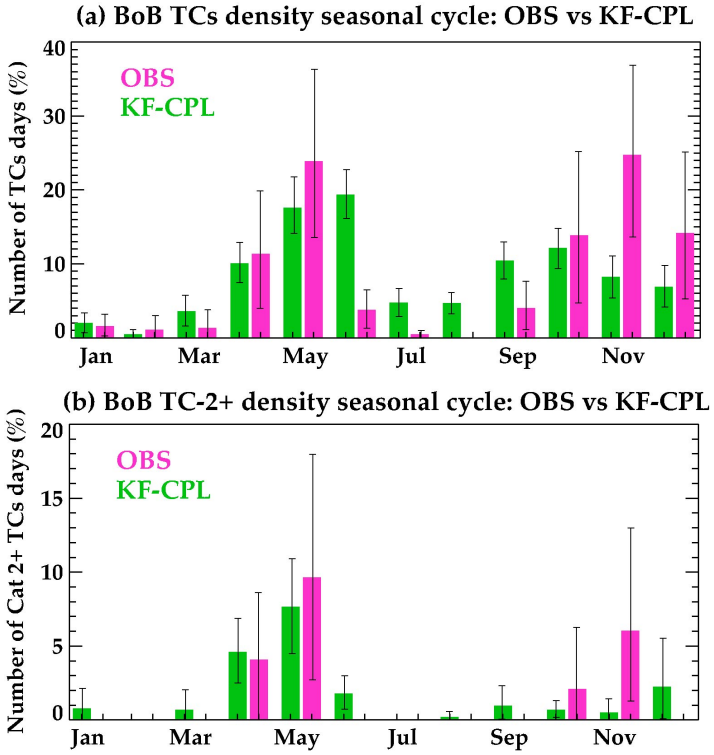

Figure 3.12. Monthly distribution of the (a) number of cyclone-days (in %) and (b) number of Cat-2 and above cyclone-days (in %) for observations and KF-CPL simulation with 90% significance level confidence intervals.

The pre and post-monsoon TCs intensity distributions are displayed on Figure 3.13 for observations, KF-CPL and KF-FOR simulations. A larger proportion of strong TCs (Category 2 and more) were observed during the pre-monsoon (see Figure 3.13a; 17% against 8%). Due to the limited sample size, this difference is however not significant at the 90% level (see the overlapping percentile of the bootstrap error bars of Figure 3.13a). Results from the coupled simulation are qualitatively similar to observations (Figure 3.13b against Figure 3.13a), with more strong TCs during the pre- (8%) than during the post-monsoon (2%). The larger model TCs sample size (due to the overestimated annual-rate of TCs) makes this difference significant at the 90% level. As stated earlier, there is however an obvious caveat in the simulated TCs: compared to observations, the model is not able to simulate cyclones above the category 2, most likely because of the insufficient horizontal atmospheric resolution (1/4°). Despite this caveat, observations and the coupled simulation both suggest that a larger proportion of strong (Cat-2 and above) TCs during the pre- than during the post-monsoon. Previous studies have shown that a stronger upper ocean stratification reduces the surface cooling under TCs during the post-monsoon (Sengupta et al., 2008; Neetu et al. ,2012), leading to hypothesize that the reduced negative air-sea coupling feedback should translate into stronger tropical storms during the post-monsoon (Sengupta et al., 2008). In contrast, our observational and model analyses indicate that TCs are stronger during the pre-monsoon. Li et al. (2013) also reported more super cyclones (category 4 and above) during the pre-monsoon, which they attributed to the stronger intraseasonal oscillations during the monsoon onset favouring TCs intensification.

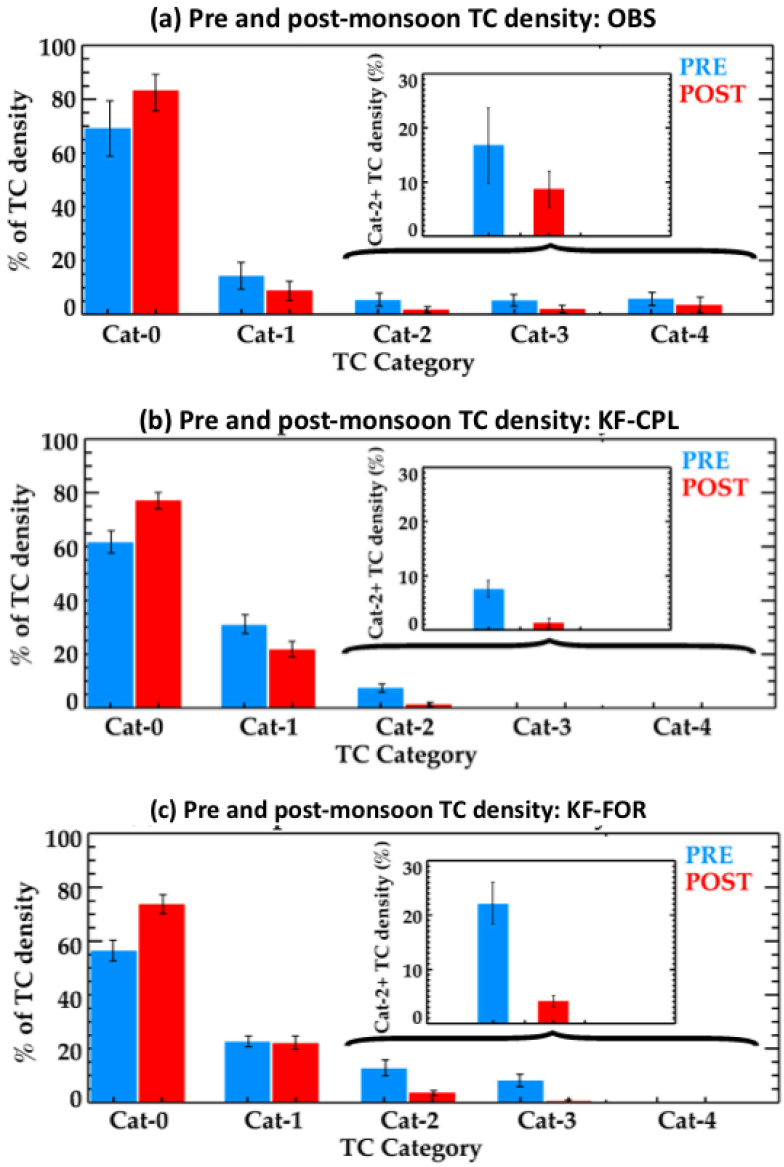

Figure 3.13. Histogram of BoB TC intensity based on maximum winds (m/s) during pre and post monsoon in (a) observations (b) KFCPL and (c) KFFOR simulations. The inset indicates the percentage of pre and post monsoon intense TCs (Cat-2 and above). The whiskers display the 90% confidence interval.

We explore the possible role of background atmospheric parameters in favouring stronger pre-monsoon TCs by comparing the coupled and forced simulations TCs intensity distributions during both cyclonic seasons (Figure 3.13b and Figure 3.13c). The forced and coupled simulations both exhibit stronger TCs during pre-monsoon,

indicating that air-sea coupling is not essential for explaining that feature. This suggests that the atmospheric background state is the main factor controlling the pre-monsoon/post-monsoon TC intensity change.

The pre/post monsoon changes in the most important atmospheric background parameters affecting TCs intensification (MPI, relative humidity and vertical wind shear) are further analysed on Figure 3.14. Large MPI and relative humidity and weak vertical wind shear are favourable conditions for stronger TCs. MPI (~ +10% in both observation and model) and vertical wind shear (~ -8% in observation, ~ -15% model) are both more favourable to stronger TCs during the pre-monsoon. On the other hand, relative humidity (~ -5% in observations and -10% in the model) is less favourable to stronger TCs during the pre-monsoon. Overall, increased MPI and weaker vertical wind shear tend to favour more intense cyclones during the pre-monsoon, with humidity changes contributing negatively.

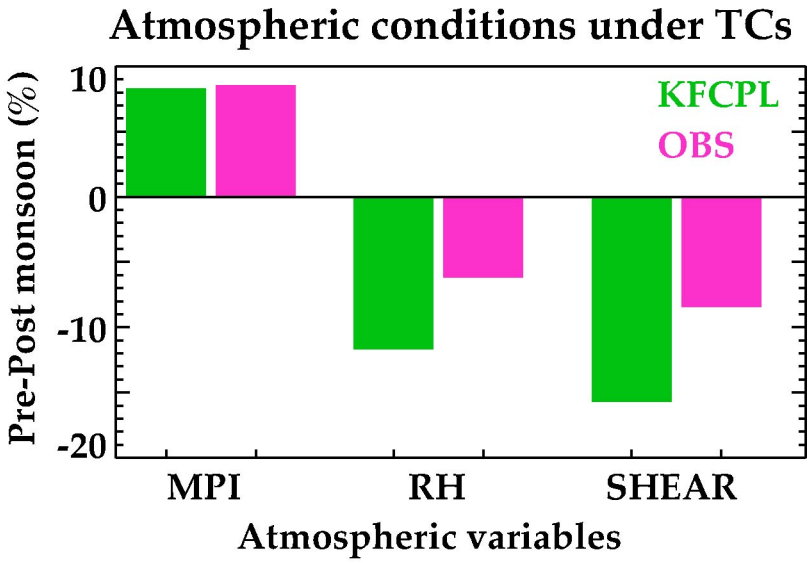

Figure 3.14. Pre-monsoon minus post-monsoon differences (%) of MPI, relative humidity at 600hPa and vertical wind shear within 200 km of all BoB TC-tracks for observations and the KFCPL simulation.

Figure 3.15ab displays the amplitude of TC-induced cooling in observations and KF-CPL simulation during the pre- and post-monsoon. In agreement with previous results (Sengupta et al., 2008; Neetu et al., 2012), the observed BoB TC-induced cooling is two to three times larger before (up to -0.7°C; Figure 3.15a) than after the monsoon (up to -0.3°C; Figure 3.15b). The KF-CPL simulation captures the timing of and seasonal contrast in the SST response to TCs, with a weaker cooling during the post- (up to -0.5°C) than during the pre-monsoon (up to -1.3°C). The simulated cooling under TCs is however overestimated during the pre-monsoon.

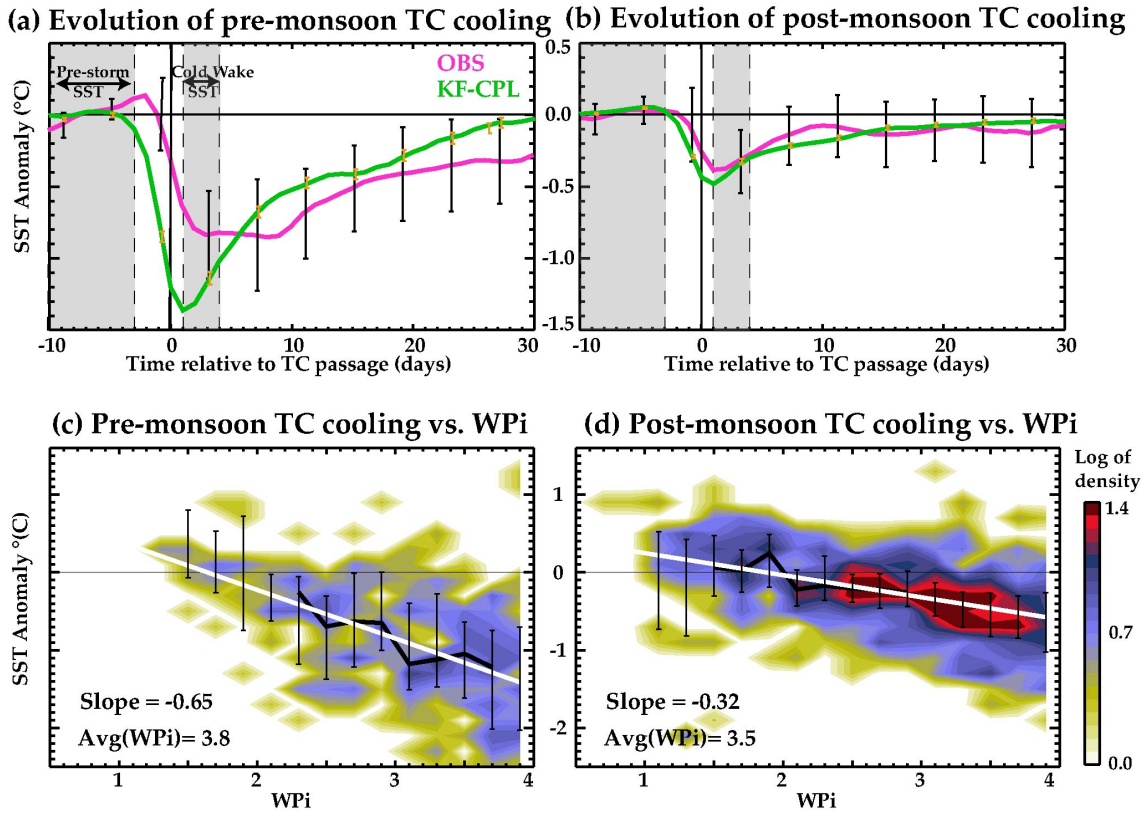

Figure 3.15. Composite evolution of BoB TC-induced SST cooling (°C) within 200 km of all TC-tracks during the (a) pre-monsoon and (b) post-monsoon for observations (black) and KF-CPL experiment (green). Whiskers indicate the 90% confidence level from a bootstrap method. Histograms of the KF-CPL TC-induced SST cooling (°C) as a function of WPi (dimensionless, no units) during the (c) pre-monsoon and (d) post-monsoon. The thick black line indicates the average cooling and the whiskers the upper and lower quartiles of the cooling distribution for a given WPi; the white line is a linear fit of the black line. The slope of this linear fit is indicated on each panel.

Figure 3.15cd exhibits the histograms of KF-CPL TC-induced SST cooling as a function of WPi for the pre- and post-monsoon. The amplitude of the cooling increases relatively linearly with WPi during both seasons. The regression slope of TC induced cooling against WPi is considerably weaker before (0.31°C) than after the monsoon (0.65°C). This indicates that, for a given wind power input, the resulting cooling is on average two to three times smaller after the monsoon. Similar results were obtained in an ocean model forced using observed TC tracks and wind speeds over the 1978–2007 period (see Chapter 2, Figure 2.8). This implies that the difference in pre vs. post-monsoon cooling intensity cannot be attributed to differences in the TC wind forcing but rather to changes in oceanic stratification. As discussed in section 1.3.2 and in chapter 2, the CI is a good metric of the influence of oceanic background conditions on the cooling amplitude. This index is shown in Figure 3.16 for observations and KF-CPL model. As shown by Neetu et al. (2012), the BoB stratification is relatively homogeneous during the pre-monsoon (Figure 3.16ad), but displays a very strong east/west contrast during the post-monsoon (Figure 3.16be). The eastern BoB (and east coast of India) indeed display CI of ~15% more than during the pre-monsoon (Figure 3.16cf). This increase is related to the formation of thick barrier layers in these regions (contours), in response to the strong freshwater input into the Bay during and shortly after the monsoon. As shown by Neetu et al. (2012), this seasonal stratification change is related to both a stronger near-surface haline stratification and a deeper thermocline after the monsoon, both of which favour a reduced SST cooling under TCs. Overall, we have hence shown that the cooling under TCs is weaker during the post-monsoon in both observations and our model, due to a deeper thermocline and strong near surface salinity stratification during that season. In the absence of changes in background

atmospheric characteristics, the air-sea feedback on TCs should hence lead to weaker TCs during that season.

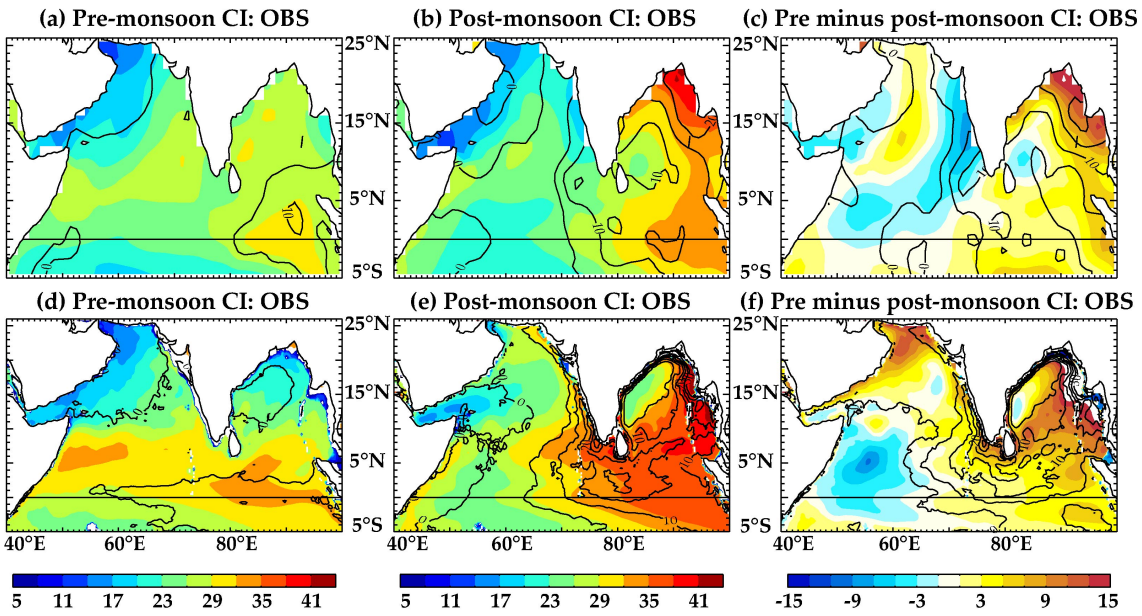

Figure 3.16. Climatological cooling inhibition (CI) index (shading; $(J.m^{-2})^{-1/3}$) and barrier layer thickness (contour; m) during the (a and d) pre-monsoon and (b and e) post-monsoon, and (c and f) their difference in (top) observations and (bottom) the KF-CPL simulation.

This is confirmed by Figure 3.17, which indicates a much larger shift towards weaker cyclone categories in the coupled simulation before (~15%) than after (~ 3%) the monsoon; i.e. a stronger negative feedback of air-sea coupling before the monsoon. The effect of air-sea coupling is hence to reduce the intensity of pre-monsoon cyclones, as hypothesized by Sengupta et al. (2008). This effect is however offset by the stronger impact of changes in MPI and vertical shear, which both tend to induce stronger pre-monsoon cyclones. But overall, air–sea coupling effects are not negligible and should be accounted for: neglecting it would result in a ~15% overestimation of strong cyclones before the monsoon.

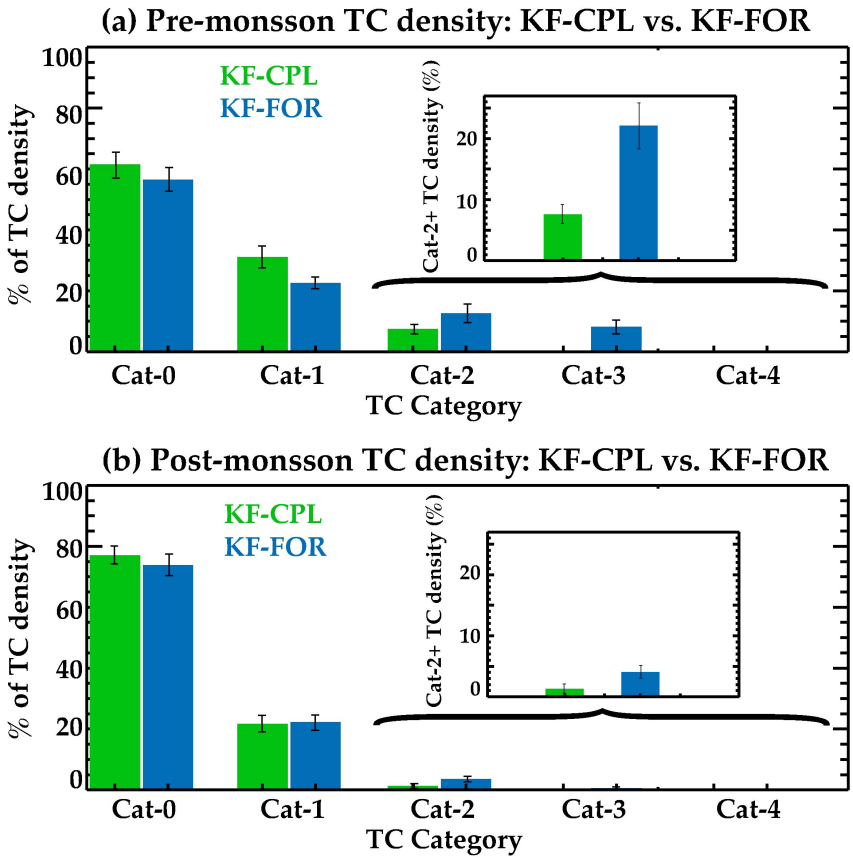

Figure 3.17. Histogram of KF-CPL and KF-FOR BoB TC occurrence (% of cyclone-days) as a function of the TC intensity based on maximum winds during the (a) pre-monsoon and (b) post-monsoon. The inset indicates the percentage of intense TCs (Cat-2 and above). The whiskers display the 90% confidence interval.

3.6 Sensitivity of the results to the atmospheric convective scheme

Deep atmospheric convection is the central process that allows the growth of TCs. It is hence possible that our results could be sensitive to the convective parameterization. We performed an additional set of experiments with the Bett-Miller-Janjic (BMJ) cumulus parameterization instead of that of Kain-Fritsch (BMJ-CPL and BMJ-FOR).

As KF-CPL, BMJ-CPL successfully captures the observed cyclogenesis and TCs density spatial patterns both for the northern and southern IO (Figure 3.18ab). However,

this simulation yields a far more realistic number of IO TCs (Figure 3.18d), in contrast to KF-CPL that produces three times more TCs as in observations (see Figure 3.2d). As in KF, air-sea coupling does not significantly impact the IO cyclogenesis and TC tracks spatial patterns (Figure 3.18bc). As in KF, the ocean feedback considerably decreases the number of TCs developing in both hemispheres in the IO (Figure 3.18d), with an even larger decrease in BMJ (~50%) than in KF experiments (~20%).

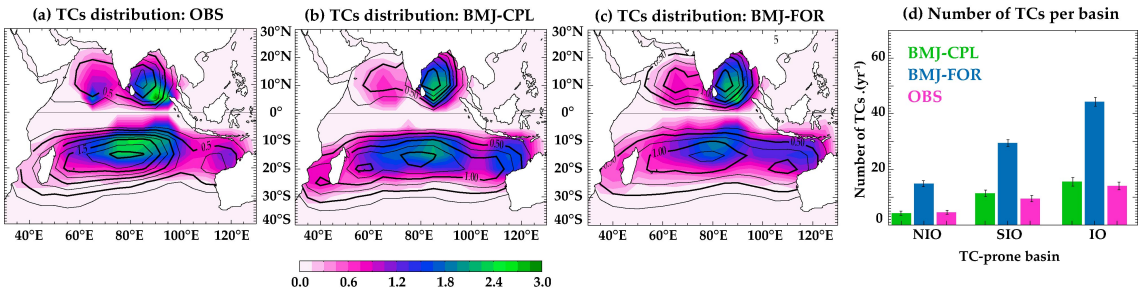

Figure 3.18: Same as Figure 3.2 but for BMJ experiments.

The seasonal evolution of TCs statistics in the IO is generally well captured by BMJ-CPL, with a maximum TC activity during austral summer in the southern IO (Figure 3.19b), a bimodal TCs distribution in the northern IO (Figure 3.19f), with TCs preferentially occurring the pre and post-monsoon. The observed absence of TCs during the core of the summer monsoon (July-August) is even better captured by BMJ-CPL (Figure 3.19f) than by KF-CPL (Figure 3.3f). Another noticeable improvement of BMJ-CPL is the better seasonal phasing of TCs occurrence during the post-monsoon season (October-November; Figure 3.19ef). The seasonal evolution of the large-scale atmospheric parameters driving the TCs seasonal evolution are also well captured by BMJ-CPL for both hemispheres (not shown). Although of different magnitude, the impact of air-sea coupling on seasonal changes in TCs number in BMJ (Figure 3.19dh)

is very similar to that of KF (Figure 3.3dh), with a larger decrease during non-cyclonic seasons as compared to cyclonic seasons.

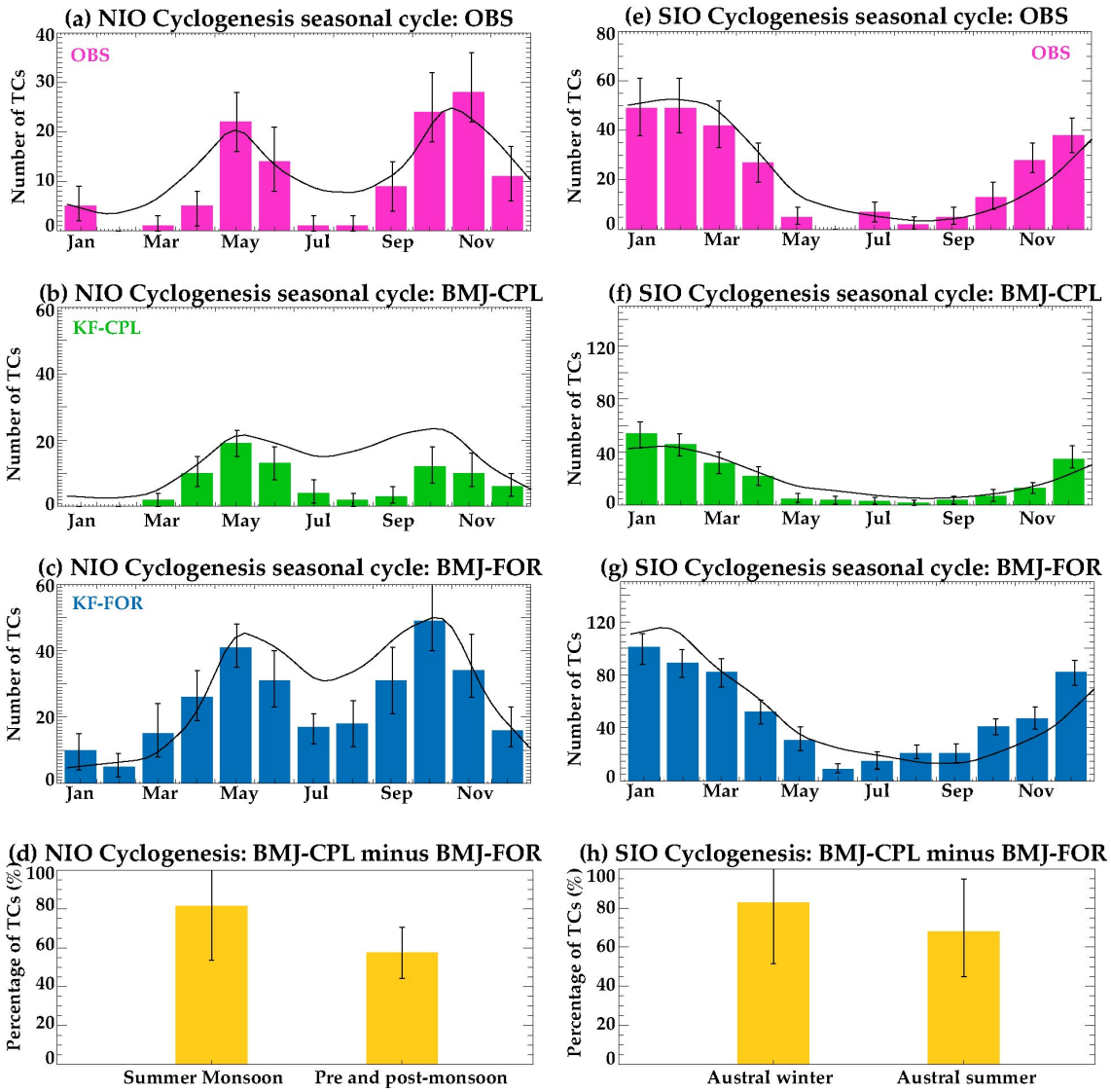

Figure 3.19: Same as Figure 3.3 but for BMJ-CPL and BMJ-FOR.

BMJ-CPL underestimates the proportion of strongest cyclones even more than KF-CPL. While KF-CPL is able to simulate TCs relatively intense tropical cyclones (up to Cat-3, the most intense simulated TC reaching a surface maximum wind speed of 56 m s^{-1}), BMJ-CPL never experiences TCs above Cat-1 (the most intense simulated TC reaching

a surface maximum wind speed of 40 m s^{-1}). In addition, KF-CPL experiment generally simulates a smaller, more realistic radius of maximum wind speed (~75 km) compared to the BMJ-CPL experiment (~100 km; see Samson et al., 2014). Despite these biases, the oceanic feedback onto the TCs intensity distribution acts in a similar way: coupling shifts the TC intensity distribution towards weaker cyclones (Figure 3.20). BMJ-FOR is for example able to simulate Cat-2, while it is not the case in BMJ-CPL. As for KF, there is no significant change in the spatial distribution of strongest TCs neither in the northern or southern IO (not shown).

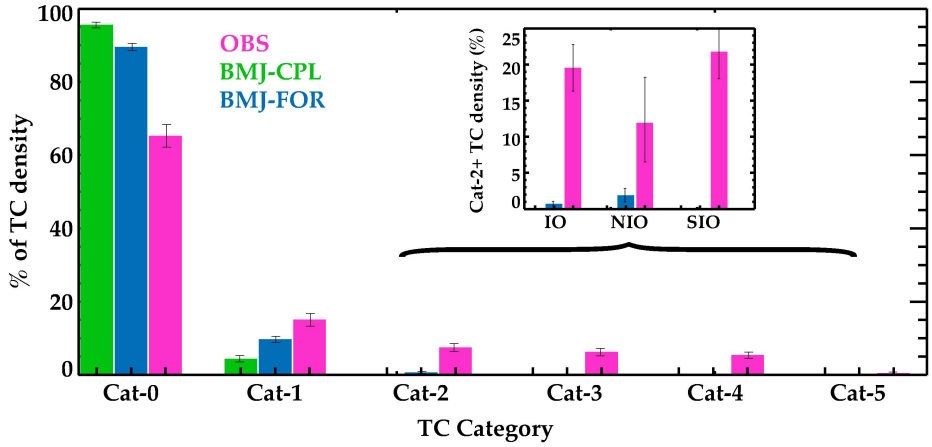

Figure 3.20. Same as Figure 3.5 but for BMJ-CPL and BMJ-FOR.

Compared to KF (Figure 3.6a), BMJ-CPL largely overestimates the amplitude of the maximum TC-induced cooling (Figure 3.21a; -0.6°C in observations vs -1°C in BMJ-CPL). This is probably related to the overestimated TC size in BMJ, which results in a longer influence of strong TC-winds at a given oceanic point. The TC)-induced cooling is larger in the Northern than in the Southern IO for a given TC amplitude (Figure

3.21bc). This can be attributed to an ocean stratification that favours more intense SST cooling in the Northern IO, as for KF-CPL.

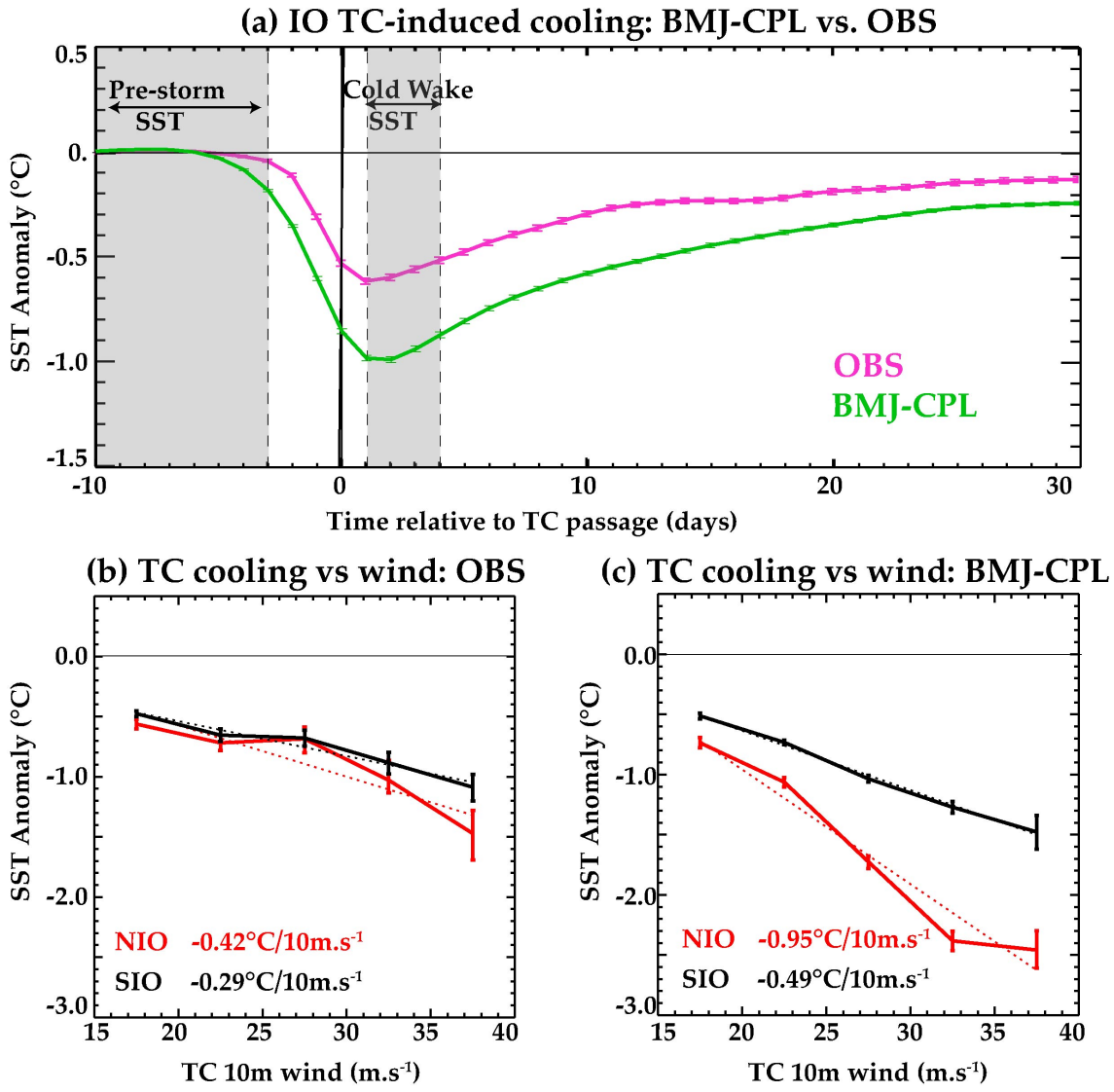

Figure 3.21. Same as Figure 3.6 but for BMJ-CPL and BMJ-FOR.

BMJ TC composites for both hemispheres give qualitatively similar results to those of Figure 3.8 and 3.9 for KF (not shown). BMJ-FOR also yields larger intensification rates for northern IO intensifying TCs than for the southern IO (Figure 3.22a), consistent with a warmer SST leading to larger upward enthalpy fluxes (not shown). TC-induced

cooling also acts to reduce the intensification rate in both hemispheres, by up to 0.4 $m.s^{-1}.6h^{-1}$ in the 30 to 35 $m.s^{-1}$ TC wind intensity (Figure 3.22b), (against only 0 to 0.2 $m.s^{-1}.6h^{-1}$ for KF). The larger effect of coupling on northern than on southern IO strong TCs intensification rates however cannot be confirmed in BMJ simulations, due to the absence of strong TCs (Cat2 and more) in those simulations.

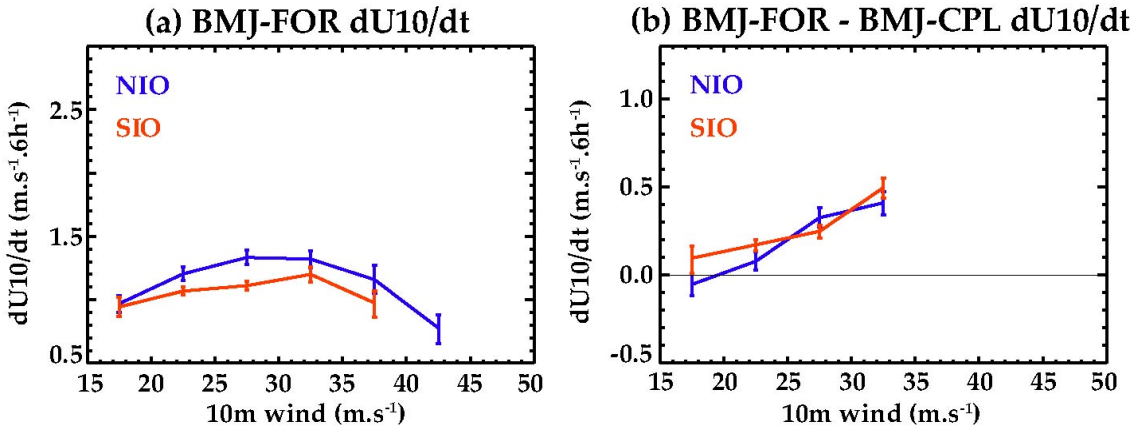

Figure 3.22. Same as Figure 3.10b and 3.11c but for BMJ-CPL and BMJ-FOR.

3.7 Summary and conclusions

In this study, we analyse a long-term simulations (20 years) of a ¼° regional Indian Ocean coupled ocean-atmosphere model to assess the impact of the negative oceanic feedback on TCs. This model simulates the TCs spatial and seasonal distributions and the TC-induced cooling reasonably well in both hemispheres. It however overestimates the number of TCs and fails to reproduce the strongest observed cyclone categories (Cat-3 and more). We compare storms statistics from the coupled simulation with those from an uncoupled simulation forced by the same SST (from which the storms cold wakes have been smoothed out). This allows to assess the impact of air-sea coupling under TCs on their TC characteristics.

Our results reveal that the spatial distribution of cyclogenesis in the IO is not affected by air-sea coupling. This result may partly be related to the fact that large-scale environmental parameters controlling cyclogenesis such as vertical wind shear or relative humidity are not sensitive to ocean-atmosphere coupling in our modelling framework. However, our results demonstrate that air-sea coupling reduces the number of Tcs by ~30%. It also influences the TCs seasonal distribution: while the forced simulation considerably underestimate the bimodal character of TCs seasonal distribution in the NIO, this bimodality is better represented in the coupled run, as a consequence of a larger TC reduction during the summer monsoon (50%) than during the pre and post-monsoon (20%). In addition, air-sea coupling also shifts the TC distribution toward weaker TCs (7% of Cat 2 and above TCs in the forced simulation vs. 2% in the coupled one). Because large-scale TC-prone atmospheric parameters do not change between the forced and coupled simulations, these changes can be confidently attributed to the local feedback of air-sea interactions below the storm.

The inner-core upward enthalpy fluxes that fuel the TCs are reduced in the coupled simulation in response to storm induced ocean cooling. This reduction is larger in the Northern IO (up to ~200W.m^{-2} for the most intense simulated TCs corresponding to a 20-30% reduction) than in the Southern IO (up to ~60W.m^{-2} for the most intense simulated TCs corresponding to a 10% reduction). This larger upward enthalpy flux reduction results in a larger reduction of the TCs intensification rate in the NIO. The northern IO intensifying strongest TCs growth rate is indeed twice larger in the coupled than in the forced simulation, against ~15% and only for moderate TCs in the Southern

IO. This constrast in the air-sea coupling impact on TCs can be attributed to the higher ambient SST and larger TC-induced cooling for a given storm intensity in the NIO.

Previous studies (Sengupta et al., 2008; Neetu et al., 2012) have shown that the BoB TC-induced cooling is larger during the pre-monsoon season. It is reduced to about one-third of its pre-monsoon value after the monsoon owing to changes in oceanic stratification. Since the cooling is negatively related to the TC intensity, this is expected to induce stronger cyclones during the post-monsoon season. TCs however tend to be stronger during the pre-monsoon in both the model and observations. Our study suggests that this is because the seasonal change in atmospheric background dominates the contrasts in TC intensity distribution between the two seasons. Reduced vertical wind shear and increased MPI both favour more intense cyclones during the pre-monsoon season. Air-sea coupling however acts in the opposite direction, and reduces the seasonal contrast in the TCs intensity distribution. Air-sea coupling hence needs to be accounted for to reproduce the observed density distribution, especially before the monsoon where its negative impact on TCs is largest.

The robustness of these results are further assessed by studying another set of 20-years long twin experiments which uses a different parameterization of deep atmospheric convection. This new configuration also realistically simulate the spatial and seasonal distributions of TCs. Compared to the initial configuration, it yields a more realistic number of TCs but with weaker wind amplitude (up to 40m.s^{-1}) and overestimated TC-induced cooling (probably because of the overestimated radius of maximum winds). The impact of air-sea coupling is qualitatively similar in that new set of experiments. Air-sea coupling does not affect the TCs spatio-temporal distribution, but considerably

reduces the number of TCs, especially during the non-cyclonic season leading to a more realistic bimodal seasonal TCs distribution in the northern IO. This reduction is however considerably larger in this new configuration (~50%) than in the earlier one (~20%). Finally, the percentage of strongest simulated TCs also decreases when air-sea coupling is included, with similar mechanisms. The lack of intense TCs (Cat-2 and more) in this configuration however prevents assessing the inter-hemispheric differences in air-coupling impact on TCs.

Chapter 4 A global statistical approach of TCs intensity forecast

4.1 Introduction

There are six major tropical cyclogenesis areas in the world (Figure 4.1): the North Western Pacific (NWP) is the most active cyclone region (~31% of the total number of cyclones at the global scale) followed by the North Atlantic (ATL; ~22%), the North Eastern Pacific (NEP; ~17%), the Southern Indian Ocean (SIO; ~13%) and South Western Pacific (SWP; ~10%). The North Indian Ocean (NIO) is least active cyclone region (~6%) but is the basin where TCs cause largest casualties (Longshore 2008).

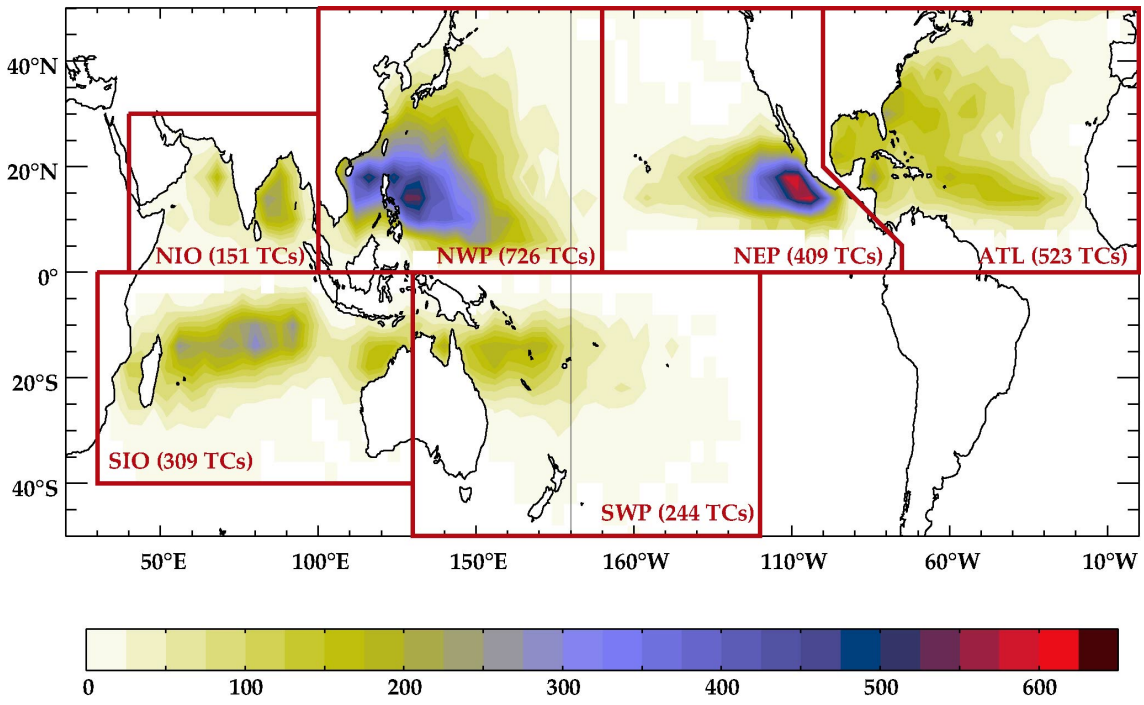

Figure 1: Tropical Cyclones (TCs) climatological density (per 4°x4° bin) global map. The six red frames indicate the TC-prone regions for which individual statistical TCs intensity prediction models are build (NWP: North Western Pacific, NEP: North Eastern Pacific, SWP: Southwestern Pacific, ATL: Atlantic, SIO: Southern Indian Ocean, NIO: Northern Indian Ocean). The numbers in parenthesis indicate the total number of TCs considered for each region over the 1979-2012 period.

Along with dynamical models, the so-called "statistical-dynamical models" are routinely used for predicting TC tracks and intensity. In a similar way to the early TCs intensity statistical forecast schemes (e.g. Neumann, 1972; Jarvinen and Neumann, 1979; Merrill, 1980; Chu, 1994; Aberson, 1998), these statistical-dynamical models use linear statistical regression techniques to predict intensity changes from predictors derived from climatology and persistence of TCs characteristics such as their current intensity and their time-derivative but they also include large-scale environmental parameters along the cyclone track as additional predictors. The environmental parameters along the cyclone tracks are usually obtained from a dynamical model forecast, hence the "statistical-dynamical" name. Historically, different operational statistical-dynamical prediction schemes have been developed separately for each basin and are discussed in section 1.2.4.

Several large-scale environmental parameters are commonly used as predictors in these statistical-dynamical schemes, as they are known to influence the TC intensification. These parameters include the MPI that a TC can reach, which increases with SST (Merrill, 1988; DeMaria and Kaplan, 1994b*;* Webster et al., 2005), the mid-tropospheric relative humidity that favours TC intensification through its influence on convective buoyancy through entrainment of sub-saturated air (Emmanuel et al., 2004) or the vertical wind shear that can inhibit TC intensification (Gray, 1968; DeMaria, 1996). Other environmental predictors in these statistical-dynamical models also include, amongst others, low-level vorticity and equivalent potential temperature as well as upper-level air temperature (Emanuel, 2007; Knaff et al., 2005; DeMaria et al., 2005). Because the current statistical-dynamical models have been developed individually for each basin, the selected large-scale environmental parameters used as predictors and the

database from which these variables are extracted generally differ from one basin to another. It is also important to mention that, in real-time application, these environmental predictors are affected by errors in the forecasted location (DeMaria, 2010; Tien et al., 2013).

Very few studies attempted to compare the predictive skill of statistical-dynamical forecast models across different TC-prone regions. A recent study (DeMaria et al., 2014) provided a comparison of the intensity error of these models over the recent period as a function of the basin and offered an update to DeMaria et al. (2007). Their results indicate that these errors are generally larger for the NWP and southern hemisphere TCs (~12kt at 24h lead-time and ~25kt at 120h lead-time) than for ATL and NEP TCs (~10kt at 24h lead-time and ~15kt at 120h lead-time). But the reasons behind this basin-wise skill dependency are currently unknown. They could indeed be of several distinct origins. First, these differences may be related to the different TCs intensity distribution in each of the basin: more intense TCs in the NWP may for instance explain the larger errors in this basin. It may however well be that the differences in the predictors and in datasets used in each of regional statistical schemes could contribute to this basin-wise skill dependency. Finally, this dependency could also simply be explained by differences in intrinsic TC intensity predictability in each basin.

Little is also known about the relative TC intensity statistical-dynamical hindcasts skill yielded by various predictors. Several studies (DeMaria and Kaplan, 1994a, 1999; Knaff et al., 2005; Knaff et al., 2009; DeMaria et al., 2014; Lee et al., 2015) acknowledged the key contribution arising from the storm climatology and persistence

predictors in most basin-wise prediction schemes, the inclusion of large-scale environmental parameters generally resulting in a modest skill improvement when compared to climatology and persistence-based models. Only a few studies provide a quantitative assessment of the respective influence of the various large-scale environmental predictors. A recent study discussing the case of the ATL basin (Lee et al., 2015) demonstrated that the initial TC intensity change is the most important predictor at short-time lead (<24h) but that MPI is the environmental parameter that yields most improvement at longer lead-times. In contrast, Sharma et al. (2013) show that the initial storm intensity is the most important parameter while the initial intensity time-derivative is not an important predictor for the NWP basin. Results for these two basins are however very difficult to compare, as the statistical model architecture, considered period and environmental datasets and predictors all differ.

Aside the relative importance of predictors, very little is also known about the TC intensity statistical-dynamical hindcasts skill as a function of the TCs characteristics, including their intensity. This assessment may however be very useful as it would allow to better identify at which TCs stage these models are less efficient and hence where a dedicated effort needs to be undertaken to improve the skill of these models.

Objectives and structure of the chapter. A thorough comparison of TC intensity statistical hindcasts, basin-wise skill and relative importance of predictors is hence still lacking. Therefore, the objective of this chapter is to identify the most important predictors in TC intensity statistical models at global-scale as well as to assess the sensitivity of the model skill to TCs strength. This endeavour requires a common framework for a meaningful comparison of the results between each basin. As detailed

in section 4.2, statistical-dynamical TC intensity hindcast schemes is developed for each basin using consistent predictors derived from a single atmospheric dataset over the same period. The basin-wise skill differences and the respective influences of the predictors on the model skill is discussed is section 4.3. The impact of environmental predictors calculated along the forecast track versus those calculated using climatology as well as stratify model performance by initial intensities are also discussed. A summary will finally be provided in Section 4.4.

4.2 Basin-wise statistical intensity forecast models

4.2.1 Datasets

The observed datasets used in the present study are listed in Table 4.1. Tropical cyclones location and wind intensity are derived from IBTrACS dataset (Knapp et al., 2010). IBTrACS combines the best track data from many agencies into one common format. We use the Joint Typhoon Warning Center (JTWC) data as our main database as it uses a consistent methodology for data preparation in every region (NWP, NEP, SWP, NIO and SIO basins), except in the ATL where JTWC does not operate. For this region, we use the National Hurricane Center (NHC) data. Both JTWC and NHC use 1-min average for sustained wind speed. As acknowledged in the literature (e.g. DeMaria and Kaplan, 1994; Knaff et al., 2005), the statistical properties of storms over land are different from those over the ocean and specific empirical inland decay models are used for predicting the intensity change for TCs after landfall. Here, we only consider TC located over the ocean (i.e. TCs are excluded from the present analysis for all points over land). It is likely that the inclusion of a specific ad-hoc parameterisation of the land effects would reduce the intensity errors, as it has been shown to be the case for the Atlantic and east Pacific for shorter-range forecasts by DeMaria et al. (2005). One

caveat of these best track data is that their intensity is generally derived using satellite-based methods, such as the Dvorak technique (Dvorak, 1984). The intensity archived in these datasets are estimated to the nearest 5 kt at 6-h intervals. For this reason, model formulation as well as any discussion of intensity in this chapter will be discussed knots rather than in meters per second.

We extract synoptic atmospheric conditions along the cyclone best tracks from the European Centre for Medium-range Weather Forecasts (ECMWF) Interim Re-Analysis (ERA-Interim; Dee et al., 2011) dataset. We use 34 years (1979-2012 period) of 6-hourly atmospheric ERA-I reanalysis fields at 0.75^{o}x0.75^{o} horizontal resolution.

S. No.	Parameter	Description
1	Tropical cyclone position and intensity	IBTrACS dataset (Knapp et al., 2010).
2	Atmospheric parameters	ERA-Interim atmospheric reanalysis (Dee et al., 2011).

Table 4.1: Data used in the study.

4.2.2 Model development

Table 4.2 lists the predictors used in our TCs intensity statistical hindcast schemes. These parameters are adapted from Knaff et al. (2005, 2009) and Sharma et al. (2013). Three variables account for the TC characteristics at the beginning of the forecast: the intensity (VMAX), the intensity squared ($VMAX^2$) and the intensity change over the previous 12-hours also referred as persistence (PER). We have constructed a first set of basin-wise hindcast models that only uses those predictors (i.e. predictors 1-3 from Table 4.1: the initial intensity, its square, and the intensity change 12 hours prior to the start of the forecast), which we will refer to as the "baseline" models (Table 4.3). But

we have also constructed models that also take the effects of environmental parameters along the cyclone tracks into account, referred to Atm models (Table 4.3).

S. No.	Predictor	Description
1	VMAX	Initial intensity
2	$VMAX^2$	Initial intensity squared
3	PER	Intensity change during previous 12 hour
4	MPI#	Maximum potential intensity
5	MPI^2#	Maximum potential intensity squared
6	SHRD*#	200 to 850 hpa Wind shear magnitude
7	USHR*#	200 to 850 hpa Zonal wind shear magnitude
8	RHHI*#	500 to 300 hpa Average relative humidity
9	T200*#	200 hpa Temperature
10	E925*#	925 hpa Equivalent potential temperature
11	Z850**#	850 hpa Vorticity
12	*VMXS*	*VMAX*SHRD*
13	*VMXM*	*VMAX*MPI*

Table 4.2: List of the predictors used in the present study. The predicted variable is DELV, i.e. the intensity change since the forecast start, at 12, 24, … , 120 hours into the forecast. The variables marked with a * are estimated from an area-average within 200 to 800 km of the cyclone track. The variables marked with a ** are estimated from an area-average within 1000 km of the cyclone track. The variables marked with a # are time-averaged from the initial to the forecast time. The variables in black (No 1 to 11) are used in the Atm reference model presented throughout the paper. The variables in *italics* (No 12 and 13; i.e. the cross-terms) are commonly used in statistical-dynamical forecasts but are discarded from the final list of predictors in the present study to allow a proper assessment of the relative importance of each of the predictors.

Name	Predictors used
Atm	Regional models build with predictors 1-11 in each basin
Atm+Cross	Regional models build with predictors 1-13 (Table 4.2) in each basin
Baseline	Regional models build with predictors 1-3 in each basin
Atm-VarN	As Atm, without predictor N; For Vmax and MPI, both the term and its square are removed from the predictors list
Atm_Clim	As Atm model but atmospheric predictors (4-11) are calculated from climatological fields
Glob	Single global model build with predictors 1-11

Table 4.3: List of different sensitivity experiments performed and related predictors used. The numbering of the predictors used refers to the parameters listed in Table 4.2.

Basin	MPI Equation	Reference
NWP	$A+Be^{C(T-T_0)}$, A=38.21 kt, B=170.72 kt C=0.1909 $^oC^{-1}$, T_0=30.0 ^oC	Knaff et al., *Wea. Forecasting*, 2005
NEP	A+BT, A=-79.17262 m s^{-1}, B=5.361814 m s^{-1} $^oC^{-1}$	DeMaria et al., *Wea. Forecasting*, 2005
SWP, SIO	$A+Be^{C(T-T_0)}$, A=-42.1 kt, B=220.58 kt C=0.0792 $^oC^{-1}$, T_0=30.0 ^oC	Knaff et al., *Aust. Met. Oceanogr. J.*, 2009
NIO	A+BT, A=-889.64 m s^{-1}, B=35.714 m s^{-1} $^oC^{-1}$	Kotal, et al., *Meteorol. Appl.*, 2009
ATL	$A+Be^{C(T-T_0)}$, A=28.2 m s^{-1}, B=55.8 m s^{-1} C=0.1813 $^oC^{-1}$, T_0=30.0 ^oC	DeMaria et al., *Wea. Forecasting*, 2005

Table 4.4: Empirical formulation of the Maximum Potential Intensity (MPI) for each TC-prone basin and related references.

The selected large-scale environmental parameters are commonly used in the statistical-dynamical models and are derived from the parameters list proposed by Sharma et al. (2013) for the NWP region and by Knaff et al. (2009) for the southern hemisphere. They have been computed using the 6-hourly ERA-Interim dataset and averaged in time along the TC track from the initial time till the forecast hour. They include the maximum potential intensity (MPI), a theoretical upper bound for the cyclone intensity that increases with sea surface temperature (Merrill, 1987; Miller, 1958; DeMaria and Kaplan, 1994b*;* Emanuel, 1988; Emanuel and Nolan, 2004; Holland, 1997; Webster et al., 2005). We have used empirical formulae to estimate the MPI in each basin. MPI is parameterized using an exponential function of sea surface temperature in the NWP, SWP, SIO and ATL regions, and a linear relationship in the NEP and NIO basins (DeMaria et al., 2005; Knaff et al., 2005; Knaff et al., 2009; Kotal et al., 2009). These empirical relationships and the corresponding references are listed in Table 4.4. The MPI is computed using 6-hourly sea surface temperature fields from ERA-Interim dataset and its maximum value set to 185kt. MPI and MPI^2 are both used as predictors in our model as it is the case in most other statistical-dynamical forecast models (see

Table 4.2). The 200-850 hPa wind shear magnitude (SHRD) and 200-850 hPa zonal wind shear magnitude (USHR) are used to account for the destructive effect of vertical shear on TCs. These variables (SHRD and USHR) are averaged over an annular region within 200 to 800 km from the center of the storm. Mid-tropospheric (i.e. average 300-500 hPa) relative humidity, temperature at 200 hPa (T200), and low-level (925 hPa) equivalent potential temperature (E925), all averaged within 200-800 km of the TC, are also used as predictors (see Table 4.1). Low-level relative vorticity (at 850 hPa, Z850) is also used as a predictor, but area-averaged within 1000 km from the center of the storm following Knaff et al. (2005, 2009).

Two more predictors VMAX multiplied by MPI (VMXM) and VMAX multiplied by SHRD (VMXS) are also been tested. In line with Sharma et al. (2013) but in contrast to Knaff et al. (2005, 2009), the storm translation speed and pressure of the initial steering motion of the wind are not included, as it resulted in marginal improvement of our forecasts (less than 1% skill improvement). We do not use any oceanic-derived metric as predictor in the model development because the short length over which oceanic datasets are available and/or reliable (daily ocean-reanalysis dataset are only available from 1993 onwards) would result in a considerable reduction of our training period. The primary aim of this work is indeed not to build an improved version of the existing statistical models, but rather to evaluate the importance of key predictors and regional skill variations, using a common framework. It must however be noticed that the inclusion of additional predictors does not affect the general conclusions derived from the present study.

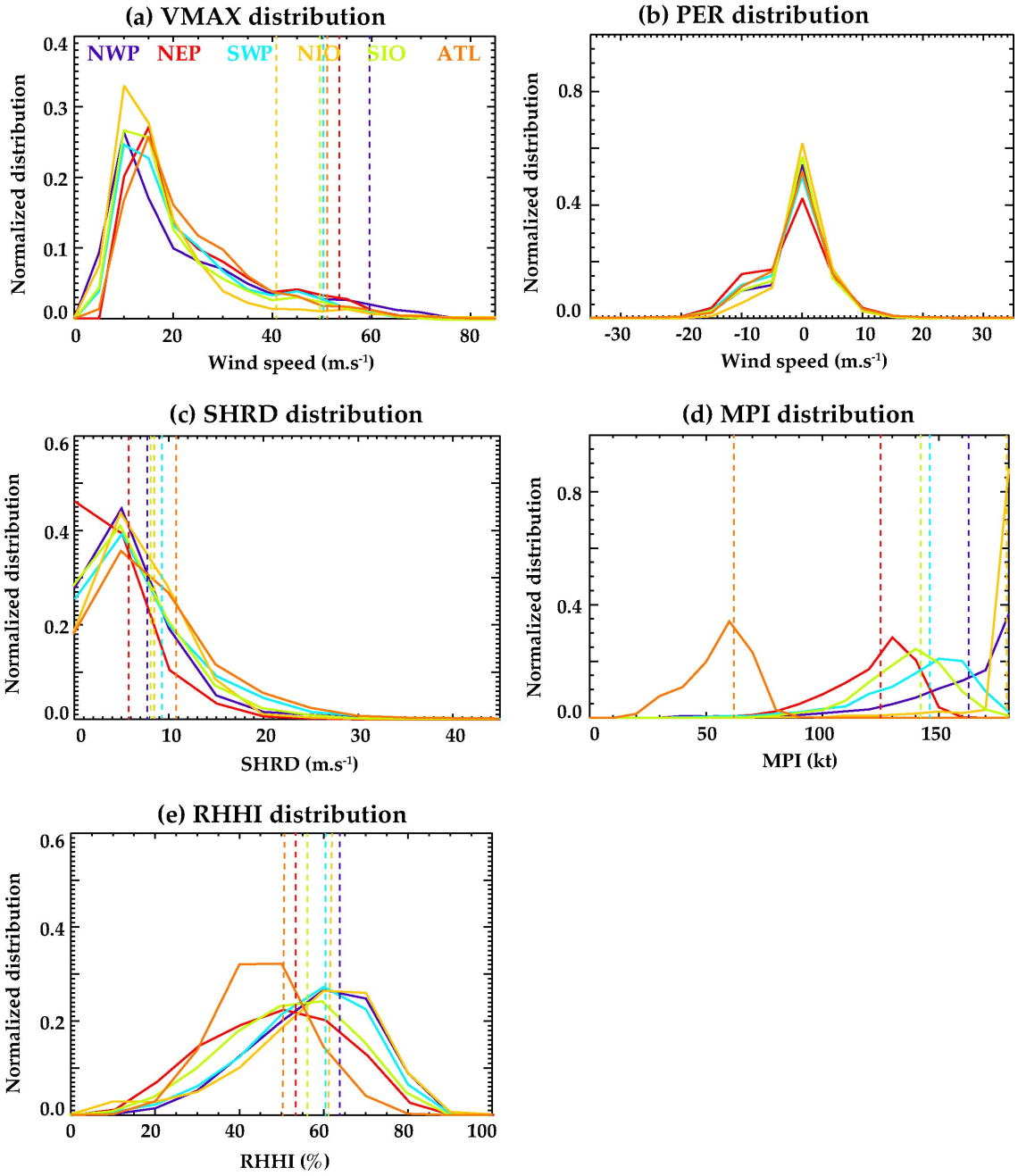

Figure 4.2: (a) Normalized distribution of TC intensity for each basin. Vertical dashed lines indicate the mean of the upper tenth percentile of the distribution for each basin. Normalized distribution of **(b)** SHRD, **(c)** MPI and **(d)** RHHI at 12h lead-time for each basin. Vertical dashed lines indicate the mean of the distribution for each basin.

The distributions of five of the main predictors used in the present study are shown on Figure 4.2 as a function of the TC-prone basin considered. The variables that account for the TC characteristics at the beginning of the forecast (VMAX and PER; Figure

4.2ab) share a rather similar distribution in each of the TC-prone basin. The NWP region is however the region showing the most intense TCs (with an averaged of 61 $m.s^{-1}$ for the highest tenth percentile in this basin; see dashed vertical lines on Figure 4.2a). In contrast, the NIO displays the weakest TCs. The four other basins (NEP, SWP, SIO and ATL) generally share similar TC intensity distribution (Figure 4.2a). In contrast to the TCs characteristics, the distribution of the environmental parameters can be far more different from one basin to another. For instance, the MPI distribution (Figure 4.2d) exhibits its largest values in basins where the warmest surface temperature are found (NIO and NWP where their averaged MPI value exceed 150 kt; see dashed vertical lines on Figure 4.2d). In contrast, MPI values are far weaker in the ATL basin, where its distribution hardly overlaps those in the NIO and NWP basin, with an averaged value lying around 60 kt. While these distributions are more similar for SHRD and RHHI environmental parameters (Figure 4.2c,e), they significantly differ from one basin to another, RHHI being for instance generally lower for the ATL basin and larger for the NWP, SWP and NIO basins.

	VMAX	**PER**	**MPI**	**SHRD**	**USHR**	**RHHI**	**T200**	**E925**	**Z850**	**VMAX²**	**MPI²**
VMAX	**1.00**	0.14	-0.20	0.03	0.21	-0.23	0.23	-0.09	0.08	**0.96**	-0.23
PER		**1.00**	0.12	-0.19	-0.11	0.19	0.00	0.18	0.02	0.13	0.13
MPI			**1.00**	-0.32	**-0.53**	**0.50**	0.44	**0.72**	0.09	-0.12	**0.99**
SHRD				**1.00**	0.45	-0.18	-0.05	-0.42	0.02	0.00	-0.29
USHR					**1.00**	-0.48	-0.17	**-0.50**	-0.09	0.17	**-0.52**
RHHI						**1.00**	0.21	**0.52**	0.14	-0.17	**0.52**
T200							**1.00**	0.46	0.15	0.24	0.42
E925								**1.00**	0.04	-0.04	**0.70**
Z850									**1.00**	0.10	0.16
VMAX²										**1.00**	-0.15
MPI²											**1.00**

Table 4.5: Correlation table between predictors at 60h at global scale. Performing these correlations per basin provides similar qualitative results.

A proper interpretation of the regression coefficients arising from these statistical models and a proper assessment of the relative importance of each predictor require investigating the correlations existing between the different predictors. Table 4.5 displays such a cross-correlation matrix for all predictors taken at 60h (considering another lead do not change qualitatively the results discussed). VMAX and PER are generally only weakly correlated with other predictors, indicating that these parameters are relatively independent (except for VMAX and $VMAX^2$ which are obviously correlated). Amongst the environmental predictors, it appears that MPI, USHR, RHHI, E925 and MPI2 are generally correlated with each other, with correlations exceeding +/- 0.5. In contrast, SHRD, T200 and Z850 appear to be more independent. This result implies that the interpretation of the regression coefficients and relative importance of correlated predictors has to be taken with cautious.

In our statistical scheme, the dependent variable or the predictand is the change in intensity (DELV) between the start of the forecast and the considered lead-time (for lead times up to 120 hours, at 12 hours intervals). The predictors are the TCs initial characteristics (predictors 1-3 in Table 4.2) and large-scale environmental parameters (predictors 4-11 in Table 4.2) described in the previous section. We then construct a statistical model using a multiple linear regression (MLR) technique for each TC-prone basin. A MLR model is built separately for each of the forecast lead-time, 12, 24, …, 120 hr. 80% of the TCs are used for building the model (training dataset) and the remaining 20% are used for testing the model performance. The training and testing datasets are chosen randomly but for entire TCs tracks (i.e. all the values along a TC track are either included in the training or in the testing dataset). This careful selection allows to avoid overfitting that could result from using data from the same TC in both

the training and testing datasets. For more reliable results, and to better approximate the generalization performance of the hindcast, each regional model fit was estimated 50 times for each forecast lead-time, using 50 different randomly-selected training and testing sets. The reported values were averaged over the 50 realizations. The confidence intervals on the value derived from this average are estimated using a bootstrap technique. To do so, we randomly select 50 values from the 50 realizations of each regional model. Overlapping selection is allowed, meaning that result from one realization can be selected more than once. We then re-calculate the average from these selected 50 values. By repeating this process 1,000 times, we obtain 1,000 estimated mean values. The upper and lower uncertainty on the mean is then considered to be the 5% and 95% percentile of the probability distribution function of the averaged value. This procedure is applied separately for each TC basin (NWP, NEP, SWP, NIO, SIP and ATL), using the same predictors and datasets (except for ATL and NEP TCs characteristics for which NHC TC characteristics are used in place of JTWC), allowing a fair comparison of results across TC-prone basins.

We choose commonly used metrics to evaluate the model performance in order to compare our model skill with previously published results. These metrics include the mean absolute error (MAE; Lee et al., 2015; Knaff et al., 2005; Knaff et al., 2009; Sharma et al., 2013) and the percentage of skill improvement compared to a given reference model (DeMaria et al., 2007). The MAE is defined as the mean of absolute values of the difference between predicted and observed TC intensity at each forecast hour. Consistently with DeMaria et al. (2007), the skill improvement is computed as follows,:

$$\text{Skill (\%)} = 100 * (MAE_{ref} - MAE_{Model)} / MAE_{ref},$$

where MAE_{ref} is the MAE derived from a reference model and MAE_{Model} is the MAE from the model being evaluated. In this chapter, we will use different choice for the reference model. For example, we can use a reference model that neglects a given environmental predictor to assess its importance (Atm-VarN sensitivity experiments summarized in Table 4.3 and detailed later in the chapter). We can also use "persistence" as a baseline model (where persistence is the simplest model of all, that simply assumes that DELV won't change from its value at the forecast time).

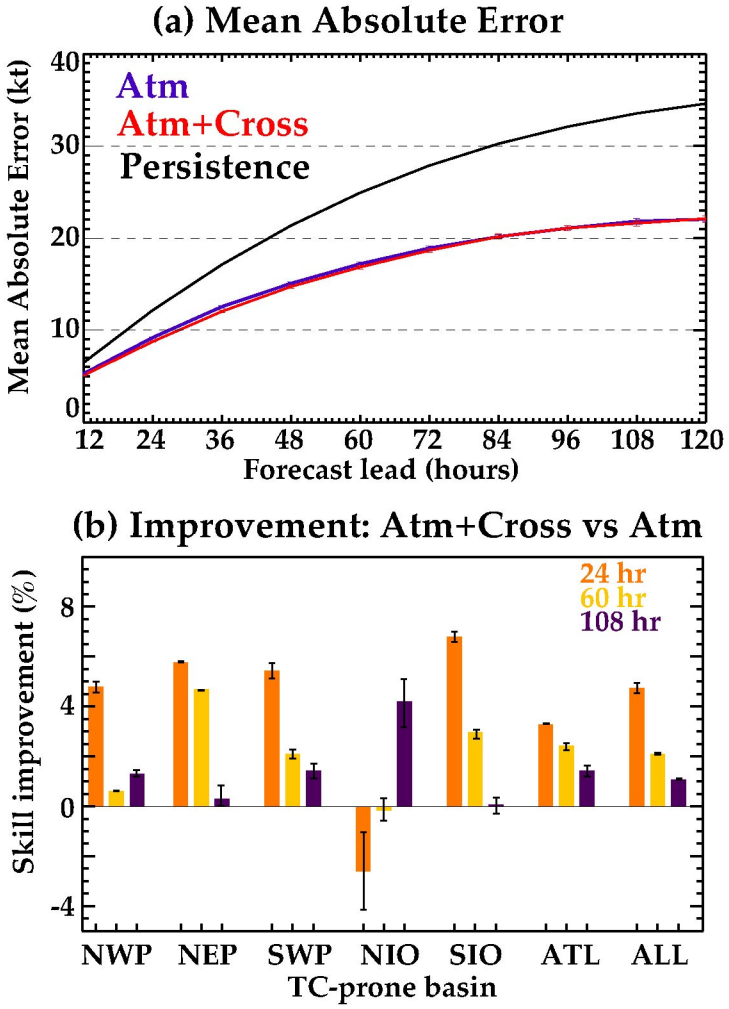

Figure 4.3: (a) MAE as a function of lead-time, averaged over all basins for persistence (black line), Atm model (blue line) and Atm+Cross model (red line). **(b)** Percentage of Atm+Cross improvement relative to Atm at 24h, 60h and 108h lead-times, for each basin and globally. Atm+Cross model is similar to Atm model, except that the two cross terms (VMXS and VMXM) are included in the predictors list. Error bars give the 95% confidence interval estimated from a bootstrap technique detailed in section 4.2.2.

In addition to the parameters used in our scheme, Knaff et al. (2005) also used two cross terms, namely VMXS and VMXM (also listed in Table 4.2). These terms make the assessment of the respective importance of the predictors involved in the cross-terms more complicated. To investigate whether they can be ignored, a sensitivity experiment was conducted to ascertain the importance of these terms. This model (referred to as Atm+Cross, see Table 4.3) is similar to our reference Atm model except that the two cross terms (VMXS and VMXM) are included in the predictors list. The statistics shown on Figure 4.3 (MAE and skill improvement of Atm+Cross relative to Atm, computed as in Eqn. (1)) and in the following analyses are calculated on the testing dataset of each experiment. As it will be illustrated later in Figure 4.5, performing the same diagnostics separately on the testing or training datasets generally leads to similar results. In agreement with past literature, Figure 4.3a first illustrates that the MAE generally increase with forecast lead-time: this increase is largest for forecast lead times between 12hr to 96hr and reduces beyond 96hr. When averaging results globally, the MAE of Atm experiments ranges from 5kt at 12h to 22kt at 120h (Figure 4.3a, blue curve). As expected, the Atm models are systematically more skilful than persistence (Figure 4.3a, black curve). The inclusion of cross-terms leads to a modest improvement of the model performance as measured by the MAE (Figure 4.3a): this improvement is indeed marginal for long lead-times and slightly larger for shorter lead times (~1kt improvement between 24h to 48h). The percentage of skill improvement of Atm+Cross as compared to Atm is further provided on Figure 4.3b at three lead-time (24h, 60h and 120h) for each TC-prone basin and globally. It indicates that including these cross terms results in a 5% skill improvement at 24h, 2% at 60h and 1% 120h globally. The relative influence of these terms however varies from one basin to another, being slightly larger

in the southern hemisphere and in the NEP and smaller in the NIO and NWP. Despite their non-negligible skill gain, we decided not to include VMXS and VMXM as predictors in our model as these cross terms prevent a simple quantitative assessment of the relative importance of the predictors involved in these cross-terms.

4.2.3 Model Performance

The Atm models skill is first evaluated by comparing basin-wise MAE of this model with similar results reported in the literature for the NWP (Knaff et al., 2005; their Table 6) and the combined results for the SWP and SIO (Knaff et al., 2009; their Table 5) for the training dataset and for the ATL on the testing dataset (Lee et al., 2015; their Figure 5). Such error estimates are not available for NEP and NIO in the peer-reviewed literature. As displayed on Figure 4.4, model skill generally compares favourably with previously published results. For the NWP region, this model is slightly less skilful than the STIPS model initially developed by Knaff et al. (2005), especially for lead-times > 48h, for which our MAE is larger by ~1-2kt (Figure 4.4a). The model performs slightly better for the SIO and SWP regions as compared to the SH-STIPS model proposed by Knaff and Sampson (2009), with a MAE reduction up to ~2-3kt for long lead-time (Figure 4.4b). Finally, our model performs very similarly to the recent model proposed by Lee et al. (2015) for the ATL region, our MAE being slightly weaker by 1-2kt for mid-range lead-times (Figure 4.4c). The modest differences between the skill of the model proposed in the present study and the skill from the models detailed in the past literature demonstrate that our model includes the most important predictors for an accurate TC prediction in each basin, giving us confidence in the robustness of the results discussed in the next section. These modest differences could arise from different sources: the choice of predictors, the source of the atmospheric data and TC

database as well as the different training/testing periods. The sensitivity to the choice of the period is further discussed below.

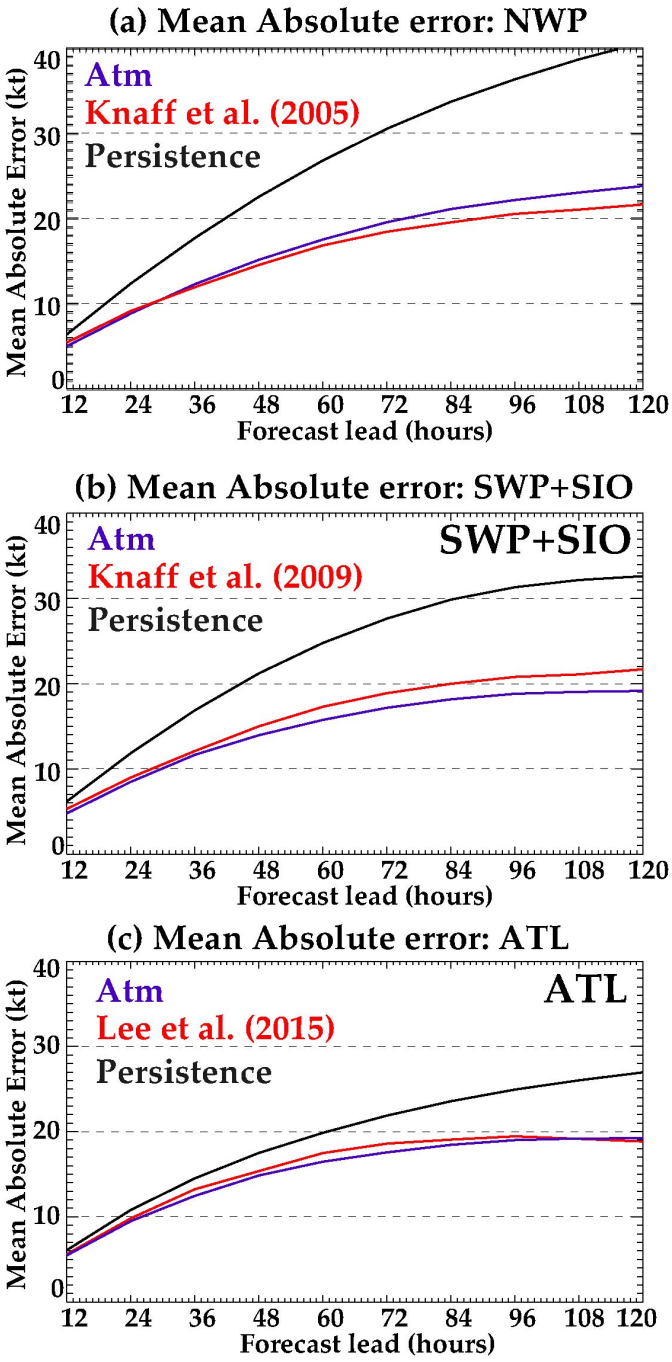

Figure 4.4: MAE as a function of lead-time for persistence (black line), Atm model (blue line) and previously published results (red line) in **(a)** the NWP for the training dataset (compared to Knaff et al. 2005; their Table 6), **(b)** in the southern hemisphere (SWP+SIO) for the training dataset (compared to Knaff et al. 2009; their Table 5) and **(c)** the ATL for the testing dataset (compared to Lee et al. 2015; their Figure 5).

Statistical-dynamical models presented by Knaff et al. (2005, 2009) are built on a rather short period (~7 years) as compared to our Atm experiment that is built from a dataset spanning 34 years. These may partly explain the skill differences seen on Figure 4.4ab. To investigate this further, Figure 4.5 compares the performance of statistical hindcast scheme built based on a 34 years long period (27 years for training and 7 years for testing; right panels on Figure 4.5) to that obtained when using a 7 years period (~5.5 years for training and ~1.5 years for testing; left panels on Figure 4.5). Using a 7 years dataset results in far weaker training errors than testing errors, especially in the southern hemisphere and ATL basin (~5kt for SWP+SIO basin, and ~3kt for ATL at long lead-time and only ~1kt for WP). In contrast, models built over a longer 34 years period exhibit far weaker skill differences between the training and testing datasets (less than 1kt in all the basins). These differences can be attributed to the tendency of models trained with relatively small datasets to overfit the data, which leads to accurate training skill but degraded testing skill. When using a 7 years dataset, the training performance indeed diverge more from the testing performance for basins with a lower TCs density (e.g. SIO+SWP and ATL) relative to the most active TC-prone basin (NWP), for which the larger number of cyclone yields a larger training sample. As Knaff et al. (2005, 2009) provided the MAE from their training dataset of ~5 years long, a fair comparison with our scheme would be to compare these results with our training results for the shorter training period (blue curves on the left panels of Figure 4.5). Doing so, although still slightly less accurate, our results comes closer to Knaff et al. (2005) for the NWP basin and outperforms the results of Knaff et al. (2009) for the southern hemisphere even more than on Figure 4.4b.

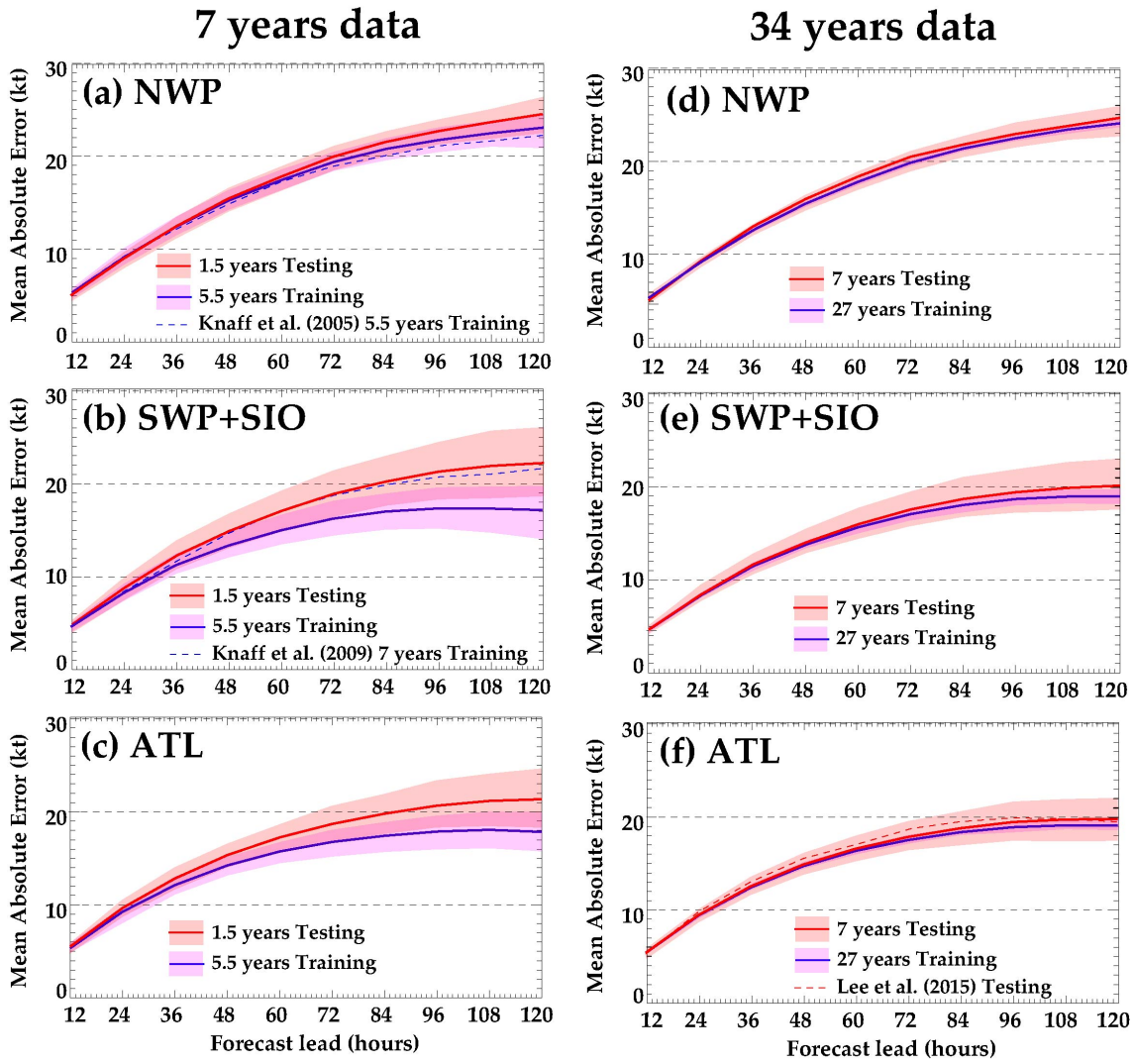

Figure 4.5: (Left panels) MAE as a function of lead-time of the training dataset (blue line) and testing dataset (red line) for the Atm model built from a 7 year period in the **(a**) NWP, **(b)** SWP+SIO and **(c)** ATL. MAEs from already published results are also shown as dashed lines. **(Right panels)** Same as left panels but for a model build over a 34 years period. Thick lines indicate MAE resulting from averaging results from 1000 simulations with different randomly selected training/testing datasets while shading indicate the 5% lower and 95% higher bound of the ensemble distribution.

The data length also considerably influences the stability of the skill: using a smaller dataset systematically leads to a larger spread of the model performance between the 50 models built based on random selections of the training/testing datasets (shadings of the left panels of Figure 4.5) relative to bigger datasets (shadings of the left panels of Figure 4.5). For the southern hemisphere, the MAE on the testing dataset at 120 h forecast

lead-time ranges between ~19kt and ~26kt when the model is built on a 7 years period while it ranges between ~19kt and ~23kt when the model is built for 34 years. These results illustrate the strong sensitivity of the model skill to the period used to build the model, demonstrating that building a model with larger datasets using a cross validation method will systematically result in more reliable and robust estimate of the skill. In the following sections, we will hence calculate the metrics used in the present study (MAE and skill improvement) for the entire 34 years on the testing average of the 50 randomly-selected realisations of the model. Since best track locations are used in these evaluations, the results are not influenced by track errors that occur with real-time applications of these models (DeMaria, 2010, Tien et al., 2013).

4.3 Results

4.3.1 Basin-wise performance

As discussed in the introduction, DeMaria et al. (2014; their Figure 4) provides a recent basin-wise evaluation of the statistical-dynamical models performances. They show that models developed for NWP and the southern hemisphere (~12kt at 24h lead-time and ~25kt at 120h lead-time) generally exhibit larger MAE than those developed for the ATL and NEP basins (~10kt at 24h lead-time and ~15kt at 120h lead-time). These differences may however be partly due to the different training/testing periods, predictors and atmospheric datasets used to derive the large-scale environmental parameters. Our common framework allows addressing the basin-wise skill differences more thoroughly. In contrast to DeMaria et al. (2014), Figure 4.6a indicates that the MAE derived our common modelling framework only modestly differs from a basin to

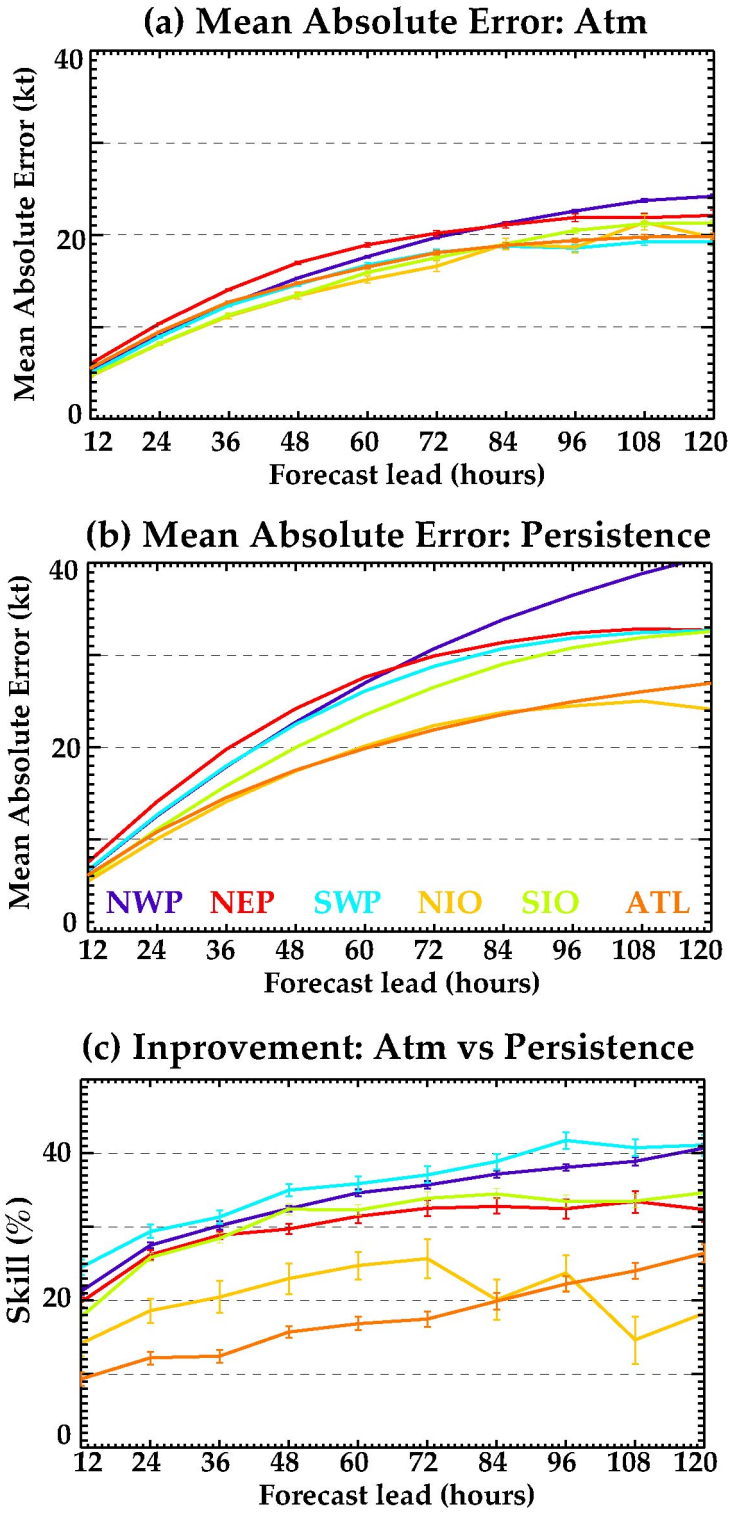

Figure 4.6: MAE as a function of lead-time for **(a)** Atm model and **(b)** persistence for each basin (i.e. NWP, NEP, SWP, ATL, SIO, NIO). **(c)** Percentage of skill improvement of these models relative to persistence as a function of lead-time for each basin. See section 2.2 for a definition of persistence metric and the skill metrics shown on panel c. Error bars on panels a and c give the 95% confidence interval estimated from a bootstrap technique detailed in section 4.2.2.

another: they systematically range between 8 and 11kt at 24h and between 20 and 24kt at 120h. The MAE are however slightly larger for the NEP region at short time-lead and for the NWP region at long time-lead. In contrast, they are weaker for the NIO and SIO regions at short time-lead and for SWP at long time-lead. While results from DeMaria et al. (2014) indicate that errors are generally far larger for southern hemisphere TCs than for ATL and NEP TCs, it is not the case in our analysis, implying that the differences discussed in DeMaria et al. (2014) are hence likely attributable to the differences in the modelling framework (the LGEM model used for ATL and EP regions includes the same inputs as SHIPS but utilizes a more sophisticated prediction equation; see DeMaria et al., 2009) rather than to the inherent predictability of TCs in these basins. In contrast, the larger MAE in the NWP region as compared to ATL basin, also noticeable in DeMaria et al. (2014), cannot be explained by differences in the model architecture and are hence likely to arise from the specific TCs characteristics in this basin (e.g., the fact that this basin hosts generally stronger TCs) or to the inherent predictability in this region.

Comparing the basin-wise models performances based on the percentage of improvement compared to simple persistence (Figure 4.6c) provide a different picture from the comparison based on the MAE (Figure 4.6a). Based on this metric, four basins (NWP, SWP, SIO and NEP) exhibit similarly high percentages of improvement relative to persistence, ranging from ~20 to 40% depending on the lead-time considered. In contrast, the skill improvement compared to persistence is considerably weaker in the ATL and to a lesser extent in the NIO basin, where it ranges ranging between 10 and 25%. While the ATL model exhibit one of the weakest MAE, it also exhibits one of the weakest relative improvement compared to persistence (along with NIO). This apparent

discrepancy can be explained by the performance of the persistence model in each basin. Figure 4.6b indeed shows that MAE from persistence is actually weaker for both the ATL and NIO basins, illustrating that TCs in these basins show smaller intensity changes as compared to the other basins. Similarly, while the NWP model exhibits one of the strongest MAE, it also shows one of the largest relative improvements compared to persistence (along with SWP). NWP persistence model shows one largest MAE (Figure 4.6b) and can hence explain the larger MAE for the NWP model (Figure 4.6c), despite the fact that the model developed for this basin shows one of the largest improvements relative to persistence amongst all basins (Figure 4.6a). The larger MAE derived from the persistence model in the NWP is likely to arise from the fact that this exhibits the most intense TCs (see Figure 4.2a) and hence the larger errors. Similarly, the weaker MAE derived from the persistence model in the NIO is likely to arise from the fact that this exhibits the weakest TCs (see Figure 4.2a). This interpretation does not however hold for the ATL basin where TCs intensity distribution is similar to that in the NEP and SIO basins (see Figure 4.2a) but its persistence skill is larger than in these basins. It implies that, for similar TCs intensity, TCs in this basin appears to exhibit more steady intensity variations compared to other basins.

We further investigate differences in the basin-wise models architecture by comparing the coefficients of the multiple linear regression at 60h lead for each basin for some key predictors in Figure 4.7. This figure first reveals that these regression coefficients are generally significant (see error bars on Figure 4.7) and exhibit consistent signs and order of magnitude across basins, suggesting qualitatively similar influences of each predictor. For instance, PER regression coefficients are systematically positive, illustrating that an intensifying TC is likely to further intensify in the near future.

Similarly, regression coefficients for RHHI are systematically positive, demonstrating the favourable impact of large mid-tropospheric humidity on TC intensification. In contrast, regression coefficients for SHRD are systematically negative, highlighting that

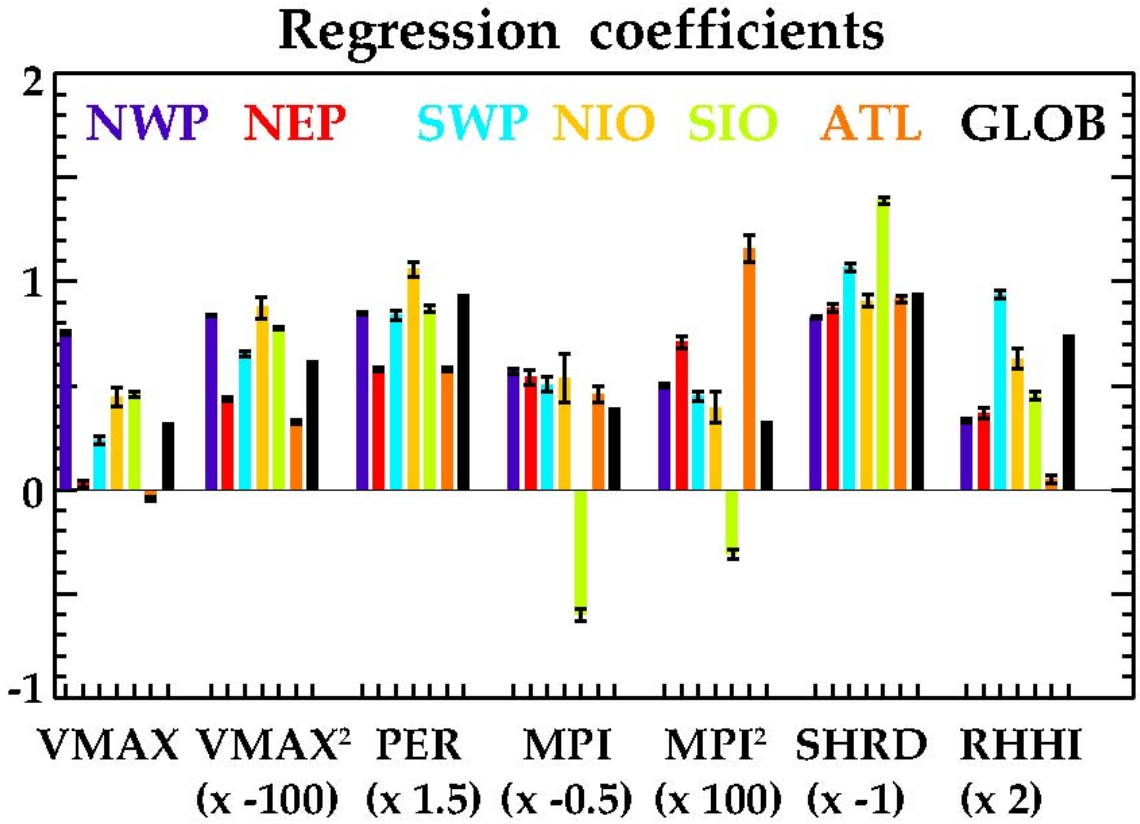

Figure 4.7: (a) Regression coefficients for the key predictors used in the Atm model at 60h for each basin. Error bars give the 95% confidence interval estimated from a bootstrap technique detailed in section 4.2.2. These regression coefficients have been multiplied by 100, 1.5, -0.5, 100, -1 and 2 for VMAX2, PER, MPI, MPI2, SHRD and RHHI respectively for a better readability.

a strong vertical shear is detrimental to TC intensification in all basins. Results related to MPI are more difficult to interpret as they involve two predictors (MPI and MPI^2) that are strongly correlated (see Table 4.5). Regression coefficients are generally negative for MPI, and positive for MPI^2, except for SIO where these two signs reversed. This change of sign could result from the strong correlation existing between these two

parameters (MPI and MPI^2; see Table 4.5) that could result in coefficient estimates that may drastically change from one basin to another. Because VMAX and $VMAX^2$ are also strongly correlated, their regression coefficients are also more difficult to interpret. Despite this overall consistency of the regression coefficients amongst the basins, the exact values of these coefficients are shown to significantly vary from one basin to another. While SHRD and PER regression values are rather close to each other in most basins, it is not the case for instance for RHHI whose regression coefficients can vary by an order of magnitude from one basin to another. As shown on Figure 4.2d, the rather different distribution of this parameter amongst the basins could explain the basin-wise differences in the regression coefficients, i.e. the influence of a given environmental parameter may differ depending the range of this parameter variation in each basin.

Figure 4.7 clearly indicates that the linear regression coefficients can vary from a basin to another, suggesting that it is better to construct TC intensity statistical hindcast schemes regionally than globally. To quantify this, we constructed a hindcast scheme that was trained collectively on all the basins (Glob model; see Table 4.3). The performance of the regional models relative to that of a global model is shown on Figure 4.8. As expected from the basin-wise disparity for some of the regression coefficients, regional models generally outperform the global model. However, when comparing these skills at global scale, the improvement arising from a regional training compared to a global one is rather modest, reaching respectively 2%, 3% and 1% at 24h, 60h and 108h (Figure 4.8), suggesting that it may be possible to build an efficient statistical model for TCs intensity forecast at global-scale. These relative improvements however strongly vary from one basin to another: some regions such as SIO and SWP

exhibit very similar skills when trained regionally or globally while the improvement gained from a regional training is larger for the ATL and NIO basins (up to 5%). As expected, the regression coefficients for each predictor derived from the global model generally falls within the range of those derived for the regional ones (Figure 4.7).

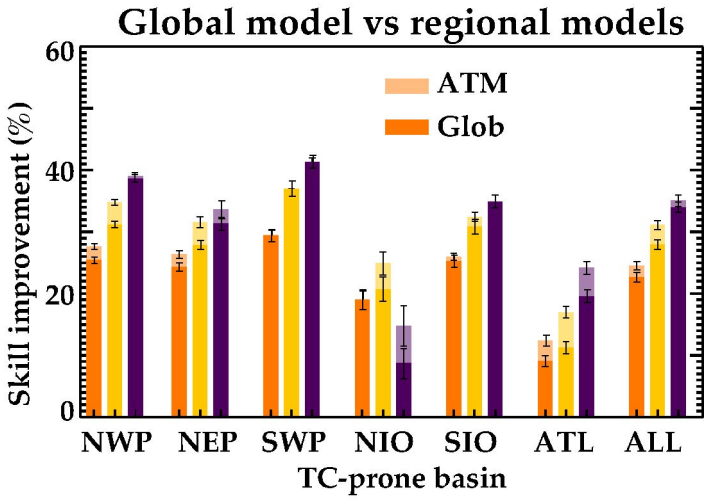

Figure 4.8: Percentage of model skill improvement relative to persistence for basin-wise trained Atm models (light colors; see Table 4.3) and the globally-trained Glob model (plain colors; see Table 4.3) at 24h, 60h and 108h, as a function of the basin. Error bars give the 95% confidence interval estimated from a bootstrap technique detailed in section 4.2.2.

4.3.2 Relative importance of predictors

Following this basin-wise performance assessment, our next objective is to compare the respective contribution of each predictor to the overall skill of these models. We first assess the contribution of the TC characteristics at the beginning of the hindcast, since they strongly contribute to the model skill (e.g. DeMaria and Kaplan 1994a, 1999; Knaff et al. 2005, 2009; Lee et al. 2015). In Figure 4.9, we compare the skill of the "Atm" models with all environmental predictors to that of "baseline" models (Table 4.3) built by only accounting for the TC initial characteristics (predictors 1, 2 and 3 from Table 4.2). This Figure reveals that TCs characteristics (i.e., the baseline models)

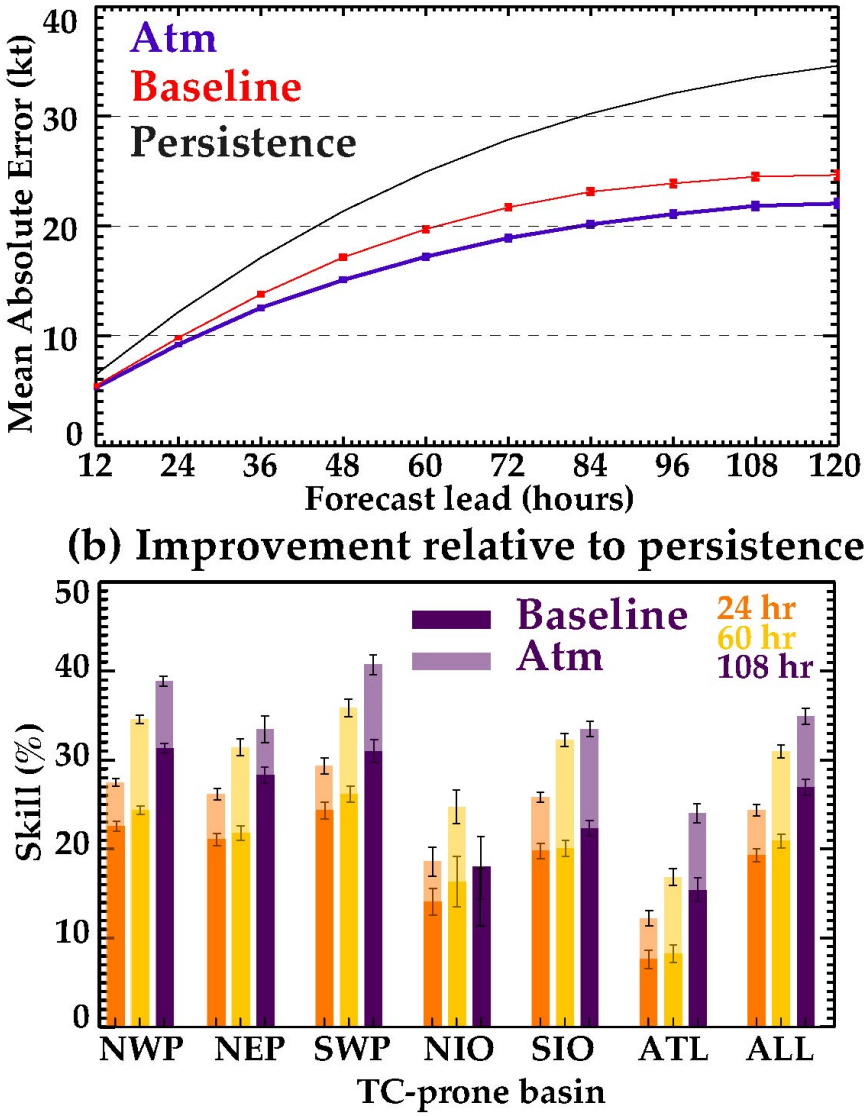

Figure 4.9: (a) MAE as a function of lead-time, averaged over all basins, for persistence (black curve), Atm model (blue curve) and baseline model (red curve). **(b)** Percentage of skill improvement of baseline (plain colors) and Atm models (light colors) relative to persistence at 24h, 60h and 108h lead for each basin and globally. Only the TC initial characteristics (predictors 1 to 3 in Table 4.2) are used as predictors in the baseline model (cf table 4.3). Error bars give the 95% confidence interval estimated from a bootstrap technique detailed in section 4.2.2.

explain a large fraction of the MAE decrease when compared to persistence (Figure 4.9a): the average MAE at 60 h averaged over all basins decreases by 6 kt (25 kt to 19

kt) from persistence to baseline model and by only further 2.5kt (to 16.5 kt) for the Atm model. When averaged over all basins, the relative improvements compared to persistence range from 19% for 24hr lead to 27% for 108-h lead time for the baseline model, while they reach 24% for 24-h lead time to 36% for 108-h lead time for the Atm model (Figure 4.9b). The inclusion of the large-scale environmental parameters in the predictors hence results in an additional skill improvement relative to the baseline model ranging from ~5% at 24hr to ~9% at 108hr. That is, accounting for environmental parameters accounts for 20 to 40% of the Atm model performance. The improvement brought by the inclusion of environmental parameters is qualitatively similar from one basin to another (Figure 4.9b). As a summary, Figure 4.9 generally illustrates that the TC initial characteristics account for a large fraction of the TCs hindcasts skill of the statistical-dynamical linear models in all TC basins, in agreement to previously published literature.

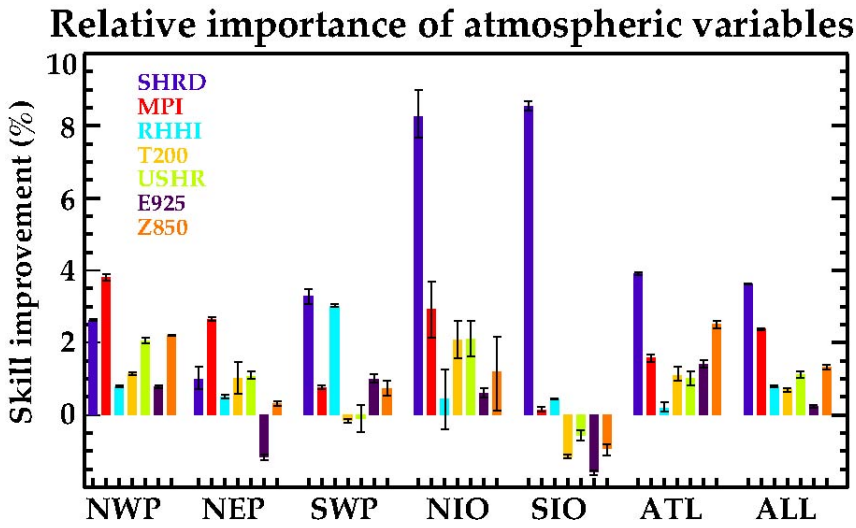

Figure 4.10: Percentage of skill improvement of Atm relative to Atm-VarN (see table 4.3) at 60h for each basin and globally. This is a measure of the respective contributions of the SHRD, MPI, PHHI, T200, USHR, E925 and Z850 predictors to the overall skill. Error bars give the 95% confidence interval estimated from a bootstrap technique detailed in section 4.2.2.

To further quantify the relative contribution of each large-scale environmental parameter listed in Table 4.2 (predictors 4 to 11), a series of experiments excluding each of these environmental parameters is carried out (Atm-VarN experiments in Table 4.3). The contribution of each large-scale environmental parameter is assessed by calculating the percentage of skill improvement of the Atm model relative to Atm-VarN, using Eq. (1). For VMAX and MPI parameters, both the term and its square are removed from the predictors list when carrying out the Atm-MPI and Atm-VMAX experiments. Figure 4.10 displays this result for a particular lead-time (60 h) in each of the basins but results are qualitatively similar at all forecast lead times (not shown). When averaged over all basins, SHRD is the most important environmental parameter, yielding to a ~4% skill improvement. The most important parameters are then MPI (~2.5%) followed by Z850, USHR, RHHI and T200 (~1%). Finally, E925 contributes very weakly to the skill improvement at global-scale (~0.25%). When looking at these contributions basin-wise, the skill improvement is also generally dominated by a subset of environmental parameters. As it is the case at global scale, SHRD is generally the most important environmental parameter in all TC-prone basins, except in the NEP and NWP where the improvement brought by MPI is larger. Its contribution is particularly large in the Indian Ocean basin (NIO and SIO) where it yields to ~8% of skill improvement versus 2 to 4% improvement in other basins. While the MPI contribution is the second largest when assessed at global scale, its contribution considerably vary from one basin to another: it is relatively large in the NWP, NEP and NIO (~3 to 4% improvement) but far weaker in SWP, SIO (less than 1%) and ATL (less than 2%). Finally, some parameters yields to negligible improvements in most basins but are skilful for some specific basin: it is for instance the case for RHHI which does not contribute much in most basins, while this parameter is amongst the two most important (with SHRD) for the SWP

basin. This probably translates some differences in the relative importance of processes that control the TC intensity between various basins as well as the basin-wide climatology and variability of these quantities.

4.3.3 Real-time vs climatological environmental parameters

The environmental parameters used as predictors in the present and previously published TC intensity statistical-dynamical hindcast models are systematically calculated based on data at the lead-time of the forecast (and at previous lead-times, since there is an average from the forecast time to the lead time). These daily data hence include seasonal variations but also perturbations at other timescales, ranging from synoptic features to large-scale interannual anomalies associated with climate modes such as the El Niño Southern Oscillation. In this section, we evaluate the relative contribution of the mean climatological seasonal cycle and non-seasonal variability to the performance of the model. To reach that goal, we perform additional regional experiments in which the climatological environmental parameters are used in place of the actual environmental parameters at the time of the hindcast (Atm_Clim experiment; see Table 4.3). In the case of Atm_Clim experiments, the parameters have been computed along the TCs track from a 6-hourly ERA-Interim climatological dataset. As for the Atm model, these parameters are then averaged in time along the TC track from the initial time till the forecast hour. Comparing Atm_Clim with Atm experiments hence allows assessing the added value of considering the environmental parameters actual values instead of considering those derived from a climatological environment for each basin. Figure 4.11a illustrates the model using a climatological seasonal cycle for environmental predictors (Atm_Clim) yields a very similar skill compared that using actual values (Atm): the globally-averaged MAE is nearly identical for lead-times

greater than 84 h, where errors tend to saturate, and only slightly reduced for shorter lead-times. Figure 4.9b allows a basin-wise quantification of that feature. At global scale, using real-time

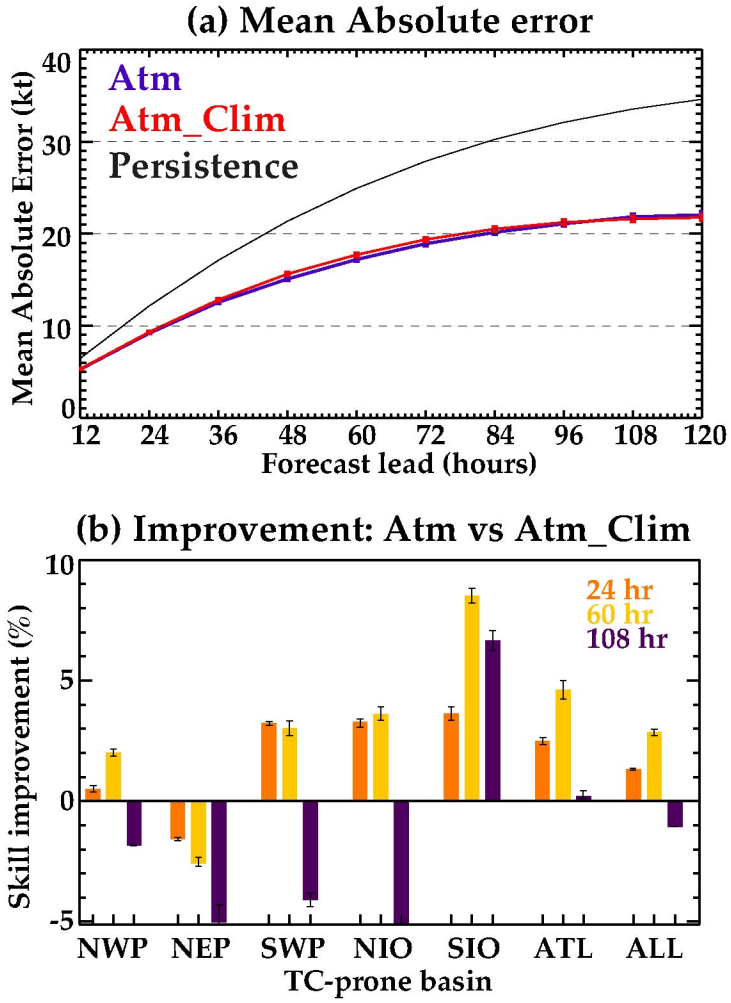

Figure 4.11: (a) MAE as a function of lead-time, averaged over all basins, for persistence (black curve), Atm model (blue curve) and Atm_Clim model (red curve). **(b)** Percentage of skill improvement of Atm relative to Atm_Clim at 24h, 60h and 108h lead-times for each basin and globally. In Atm_Clim, the environmental parameters are calculated from their climatology, rather than on their actual value at the forecast time (cf. Table 4.3). Error bars give the 95% confidence interval estimated from a bootstrap technique detailed in section 4.2.2.

predictors do not improve the model skill at long lead-time but modestly improve it at short to mid-range lead-time (1 to 3%). The added value of using daily parameters in

place of climatological parameters varies from one basin to another: it does not improve the skill for NWP and NEP and marginally for the ATL basin (~2%). In contrast, the use of daily parameters leads to a larger improvement for the southern hemisphere TCs, especially in the SIO basin where this improvement reaches ~8% for medium to long lead-time. The good performance of the Atm_Clim hindcast scheme suggests that TCs intensity change are far more constrained by the seasonal variations of environmental predictors rather than by their non-seasonal component related to synoptic signals and large-scale climate modes, especially for the northern hemisphere.

4.3.4 Skill as a function of TC intensity

We finally evaluate the model skill as a function of the TCs intensity. For this purpose, the predictands are divided into two subsets based on the TCs intensity. The TCs up to category 2 (<96 kt) are considered as "weak" (~60% of the dataset) and those under category 3-5 (≥96 kt) are considered as "strong" (~40% of the dataset). Rather surprisingly, Figure 4.12 indicates that the model skill strongly depends on the TC intensity, with considerably weaker skill for weak relative to strong TCs. The global skill improvement relative to persistence indeed reaches ~35% to 45% for strongest TCs (Figure 4.12a) but only ~10% to 20% for weak TCs (Figure 4.12b). That is, the TC hindcast model is about three to four times more skilful for strong than for weak TCs. This result holds for all basins but is particularly striking for ATL where the model skill is marginal for weak TCs. We further checked that results related to the basin-wise performance of the model (Figure 4.6), the importance of TC initial characteristics (Figure 4.9), the relative environmental parameters (Figure 4.10) and the good performance of Atm_Clim compared to Atm (Figure 4.11) obtained for the entire TCs database holds true for the strongest TCs (not shown).

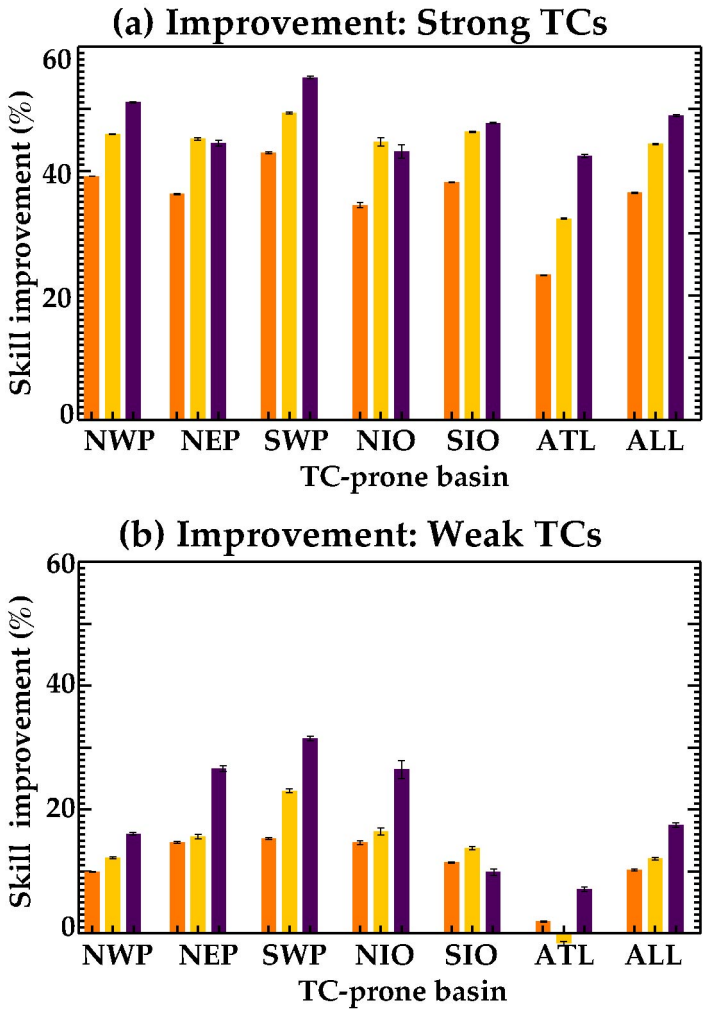

Figure 4.12: Percentage of Atm model skill improvement relative to persistence for **(a)** strong and **(b)** weak TCs at 24h, 60h and 108h, as a function of the basin. Here, TCs up to category 2 (< 96 kt) are considered as "weak" and those under category 3-5 (≥ 96 kt) are considered as "strong". Error bars give the 95% confidence interval estimated from a bootstrap technique detailed in section 4.2.2.

4.4 Summary and conclusions

The prediction of tropical cyclone intensity is still a challenging problem. Along with dynamical models, TC intensity prediction relies on statistical-dynamical linear models that use linear statistical regression techniques to predict intensity changes from predictors derived from initial TCs characteristics and from large-scale environmental

parameters along the TC track. Given the tremendous consequences of TCs worldwide, it is a must to better assess the performance of these regional models. However, it is difficult to compare these models across TC basins, as these models have generally been developed independently, using different predictors, atmospheric datasets and training periods. In this chapter, we develop statistical-dynamical linear hindcast models for each TC-prone basin using the same set of predictors, atmospheric dataset and extended training/validation period (1979-2012). It is to our knowledge the first time that TC intensity statistical-dynamical linear hindcast models are built consistently for all TC-prone basins. This common framework allows us to confidently compare basin-wise variations of the models skill, most skilful predictors and sensitivity of the skill to the TC strength. The models in this study display similar skills to those previously published, giving confidence in the conclusions drawn from this analysis. We have shown that the long period that we consider in the present study ensures a better robustness of the results. Re-conducting analyses in this chapter over 1990-2012, during which intensity records (e.g. Kossin et al., 2013) and tracks (Velden et al., 2006; Knapp and Kossin, 2007) are more reliable, does not change the overall conclusions of the present study (not shown).

Our results first reveal that the mean absolute errors derived from these regional models is rather similar amongst the different TC-prone basins. However, the relative skill improvement brought by using this multi-linear statistical framework as compared to simple persistence is larger for northwest and northeast Pacific, the southwest Pacific and the southern Indian Ocean compared to the Atlantic and Northern Indian Ocean basins. Because the models developed in this study share the same environmental parameters, source of atmospheric data and are built over the same period, we also show

that this relative skill difference can confidently be attributed to weaker errors for simple persistence in the Atlantic and Northern Indian Ocean basins, i.e. that these basins exhibit more steady intensity variations compared to others. We further show that that the regression coefficients for each predictor of these models generally exhibit consistent signs and order of magnitude across basins, suggesting qualitatively similar influences of each predictor. Comparing results from models trained for each TC-prone regions to those from a model trained over the entire globe demonstrates that the improvement arising from a regional training compared to a global one is rather modest, reaching respectively 2%, 3% and 1% at 24h, 60h and 108h, suggesting that it may be possible to build an efficient statistical model for TCs intensity forecast at global-scale.

Several studies already mentioned that, amongst all predictors, the storm characteristics at the beginning of the forecast (intensity and its time-derivative) are dominant contributors to these models performance. Our results confirm those findings and quantifies them more precisely: TC initial characteristics contributes to ~ 60 to 80% to the model skill improvement relative to persistence in all TC-prone basins, with large-scale environmental predictors accounting for the rest (~20 to 40 %). At global scale, we find that the most important environmental predictor is the vertical shear, followed by the maximum potential intensity. In contrast, the other environmental parameters contribute to the skill improvement to a lesser extent. Despite the key role played by vertical shear in most TC-prone basins, the relative contribution of each environmental parameter however varies considerably from a basin to another. We find that the vertical shear has a very large impact in the Indian Ocean, contributing to ~8% of the skill increase relative to persistence. Our result for the northwest Pacific broadly agrees with the STIPS model result that also showed that the vertical shear and the maximum

potential intensity are the most important predictors (Knaff et al., 2005). Lee et al. (2015) do not use the 850hPa vorticity as a predictor in their model, which is the second most important predictor in our model for the Atlantic. However, in the absence of this parameter in their model, vertical shear and a form of maximum potential intensity are the two most important atmospheric predictors, which are first and third most important parameters in our analysis for this basin. A more quantitative comparison with earlier studies is however not possible due to various differences arising from the choice of predictors, data source and period.

One of the key results of the present study could lead to a considerable simplification of the implementation of current statistical forecast of TCs intensity. Our results indeed reveal that a model built from environmental parameters calculated from the climatological evolution along the TC-track yields nearly the same predictive skill as a model built from real-time values. The improvement of using daily environmental parameters is marginal for the northern hemisphere TCs (less than 2%), while larger for the southern hemisphere TCs (up to 9% in the SIO). This result echoes Lee et al. (2015) who demonstrated that its statistical hindcast model has a comparable skill when using environmental predictors derived from monthly rather than daily environmental data for the case of the Atlantic. In agreement with our results, this suggests that subseasonal variations of environmental parameters only marginally contribute the skill improvement of the model. Our results further demonstrate that the same conclusion holds for interannual anomalies, such as those associated with large-scale climate modes such as the El Niño Southern Oscillation. This result is potentially interesting for statistical operational forecasting of TC intensity. For implementation purposes, it is indeed far simpler to use atmospheric predictors calculated from their seasonal

climatology than to retrieve the real-time forecasted values of those predictors along the forecasted TC track. This strategy may however not be adapted to the southern hemisphere, where our results suggest the largest skill gains when accounting for real-time environmental parameter variations.

Finally, our analysis also demonstrates that these forecasting schemes are skilful to predict intensity changes for strongest TCs (Cat 3 to 5), while it is hardly the case for weaker TCs: the skill improvement relative to persistence is indeed three to four times weaker for weak than for the strong TCs. It is plausible that the strength of the control of a given environmental parameter is varying as a function of the TC intensity, a non-linear behaviour that our linear scheme is not able to capture. It will be interesting to investigate whether non-linear statistical prediction schemes are able to improve the hindcasts for weaker cyclones. The use of non-linear schemes such as Artificial Neural Networks (Fine, 1999) or Support Vector Machines (Cortes and Vapnik, 1995) may be beneficial to further improve the performance of these statistical TCs intensity models.

In real-time applications of these methods it is important to note that both uncertainties in TC location and intensity and the use of a forecast track will result in additional sources of errors. Nonetheless, results of this study will still be valid.

Chapter 5 Assessment of air-sea coupling on statistical prediction of TCs intensity

5.1 Introduction

As illustrated in Chapter 3, the ocean feedbacks negatively on the TC intensity, because the cold wake under the TC track reduces the upward enthalpy flux that feeds the cyclone. Recent modelling studies have shown that the upper ocean stratification ahead of the TC strongly modulates the TC-induced cooling amplitude and hence potentially its intensification rate (e.g. Jullien et al., 2014; Ogata et al., 2015; Chapter 3 of this thesis). Very few studies have however attempted to quantify the improvement yielded by including oceanic metrics in TC intensity statistical forecast models. TC heat potential (referred as to OHC in the following) is the commonly-used oceanic metric to account for air-sea interactions under TCs in these statistical models. OHC is the heat content between the sea surface and the depth of the 26°C isotherm (e.g. Goni and Trinanes, 2003; described in section 1.4.3), and is generally estimated by combing an ocean climatology, oceanic re-analysis and satellite data (Mainelli et al., 2008). Including OHC as an additional input parameter to the SHIPS statistical model in the Atlantic over the 2002-2003 period however resulted in very modest improvement at initial to mid forecast leads and no improvement at longer forecast leads (DeMaria et al., 2005). Mainelli et al. (2008) however showed that the inclusion of OHC in SHIPS over the 2003-2005 period resulted in a 5% skill improvement of Category 5 TCs (with up to 20% for individual category 5 TCs, especially at long forecast leads; Mainelli et al., 2008). Mainelli et al. (2008) also reported that OHC behaves non-linearly with respect to TCs intensification rate, only yielding a significant improvement when its value exceeds a certain threshold. These results however relied on a very limited sample, as

only five Category 5 TCs occured over the short analysed period (three cyclonic seasons). Finally, Lin et al. (2013) and Goni et al. (2009) respectively further demonstrated that including OHC in SHIPS over 2004-2007 in the Atlantic and in STIPS for 63 TCs in North western Pacific yielded up to ~3% improvement at long forecast lead-times.

These contrasted results may arise from the choice of the OHC metric, used by DeMaria et al. (2005), Goni et al. (2009), Lin et al. (2013) and Mainelli et al. (2008). In a review paper, Goni et al. (2009) underlined the need to quantify the skill improvement brought by oceanic metrics of air-sea interactions under TCs. As suggested by Cione and Uhlhorn (2003), the upper-ocean heat content is at least an order of magnitude larger than the energy extracted by the storm, suggesting that the OHC may not be the most appropriate parameter to account for the upper-ocean effect on TC intensity. Recent studies hence proposed alternative metrics to quantify the effect of the oceanic background state on TCs intensification. Price (2009) proposed a metric based on the vertically-averaged temperature over the upper 100m (T100), the typical mixing depth of a strong TC. This metric may indeed be more relevant than the OHC, as it better reflects the way TCs interact with the ocean. Lloyd and Vecchi (2011) further proposed a metric that reflects the near-surface stratification: the depth at which ocean temperature is 2°C below the surface temperature (h2). Finally, Vincent et al. (2012b) proposed another physically-based metric, i.e. the cooling inhibition index (CI), a proxy of the potential energy change associated with vertical mixing of the water column. An added advantage of CI over the other proposed metrics is to account for the effect of salinity stratification, which is likely to play a strong role in the Bay of Bengal, as demonstrated in Chapter 2.

Vincent et al. (2012b) compared the ability of these metrics to estimate the cold wake amplitude based on a large TCs sample (more than 3,000 TCs over the last 30 years) simulated by an ocean model. While OHC is the most popular index of oceanic control of air-sea interactions below TCs, Vincent et al. (2012b) showed that it does not perform well for predicting the TC-induced cooling, as well as other metrics based on a fixed threshold and/or absolute temperature such as T100. In contrast, they show that metrics that account for the mixed layer depth and the steepness of the thermal stratification at its base (e.g., CI, h2, SST-T100) perform much better at estimating the cold wake amplitude. The SST effect on the cyclone can be split into two distinct contributions: the ambient SSTs ahead of the storm (cyclones form and intensify above surface temperatures of 26°C or more) and the SST cooling induced by the storm under the eyewall. Previous studies suggest that the cooling under the storm has the largest impact on its short-term intensity evolution (Schade, 2000). In addition, satellite observations accurately capture the ambient SST ahead of the storm, while they do not provide reliable estimates of inner-core SST due to intense rainfall under TCs (Brennan et al., 2009). To be useful in terms of forecasting, metrics of the oceanic influence on TCs should therefore be able to quantify the amplitude of the storm-induced cooling, since it is through this cooling that air-sea interactions impact the storm intensity. Including a metric of the amplitude of the TC-induced cooling (i.e. based on steepness of the ocean stratification) in TC intensity statistical forecast schemes is thus likely to yield a larger skill improvement than a metric based on absolute temperature, as this information is already included in commonly used atmospheric parameters such as the maximum potential intensity. Based on this reasoning, Vincent et al. (2012b) hence proposed that such metrics, which properly captures the ocean propensity to modulate

TC-induced surface cooling (and hence the storm growth rate), should be tested in TC intensity forecast schemes.

The objective of the present chapter is to test the added value of such metrics, relative to the commonly-used OHC. Most TC intensity statistical forecast uses linear schemes to the forecast, i.e. they assume a linear relationship between the predictor and the surface cooling and/or TC intensity. Potential nonlinearities are thus usually dealt with using an ad-hoc scaling of the OHC, e.g. using the square root of OHC as a predictor (13 predictor version of STIPS model, https://www.godae.org/; Sharma et al., 2013). Here, our aim is to test several oceanic metrics of air-sea interactions below TCs, which may not have the same non-linear influence on the TC intensification. It would be difficult and time-consuming to test all possible scaling for each parameter in a linear statistical scheme. Another option is to use statistical schemes that are designed to capture the non-linear relationships between variables, without applying any ad-hoc scaling on the input parameters. Artificial Neural Networks (ANN; Bishop, 1995; Ripley, 1996; Fine, 1999) and Support Vector Machines (SVM; Cortes and Vapnik, 1995; Vapnik, 1999; Vapnik, 2000) are such popular statistical non-linear modelling tools for non-parametric predictions purpose in many fields and more specifically for oceanographic, climatic and impact studies (e.g. Ali et al., 2004, 2007, 2012; Hennon, 2005; Tolman et al., 2005; Chen et al., 2005, 2006; Swain et al., 2006; Lee, 2009; Elshorbagy and Parasuraman, 2008; Liu et al., 2010; Chaudhary and Middey, 2011; Roy and Kovordányi, 2012 for ANN and Mahjoobi and Mosabbeb, 2009; Elbisy, 2015; Wei, 2012; Aguilar-Martinez and Hsieh, 2009 for SVM). Regarding TCs, both ANN (Chen, 2005) and SVM (Lin et al., 2009; Wei, 2012) have for instance been used to predict rainfall under TCs. For this specific application, Lin et al. (2009) argued that SVM-

based models are more skilful than ANN-based models in predicting TC-induced rainfall. ANNs have also been used to predict TC-induced storm surges (Lee, 2009), tropical cyclogenesis (Hennon et al., 2005) and TC tracks prediction (Ali et al., 2007; Roy and Kovordányi, 2012).

A couple of studies have already used non-linear statistical tools to forecast TC intensity in the northwest Pacific using either SVM (Lin et al., 2013) or ANN (Sharma et al., 2013). Lin et al. (2013) showed that their non-linear SVM scheme improved the TC intensity forecast by about 5-10% relative to the operational forecast based on linear modelling, especially the long-lead times. Using the same parameters as in the linear STIPS model (Knaff et al., 2005), Sharma et al. (2013) showed that their non-linear ANN scheme yielded a 3-11% skill improvement, with larger improvement for long-lead times. They further found that OHC was the fourth most skillful predictor of their non-linear scheme, after the squared initial TC intensity, MPI and initial intensity times MPI. Chaudhari et al. (2015) is the only study that attempted to use non-linear statistical tools to predict the TC intensity in the northern IO. They developed an ANN-based approach for short lead-times only (6, 12 and 24 hours). The parameters for their short-range model were significantly different from the ones used in mid to long range statistical-dynamical forecasts (12-120 hours forecast period), being mainly based on cloud properties (e.g. cloud cover, cloud top temperature) along with TCs initial intensity and central pressure drop. They show that this model improves the TC intensity prediction over the 2002-2010 period, relative to IMD operational forecasts at 12 and 24 hours lead-time.

The general objective of this chapter is to quantify the TC intensity prediction skill improvement yielded by including oceanic subsurface metrics that account for the cooling under TCs. For this purpose, the linear scheme used in the previous chapter (MLR) as well as two non-linear schemes (ANN and SVM) will be used. This will allow assessing the added value of accounting for the oceanic stratification in TC intensity forecasts and whether a non-linear scheme is needed for that purpose. Section 5.2 provides a description of the architecture of each of The ANN and SVM schemes. Section 5.3 compares the performance of these non-linear models to that of the linear model discussed in chapter 4. Section 5.4 discusses the skill improvement yielded when including different oceanic parameters in each of those forecast schemes. The final section provides a summary of the results.

5.2 Development of non-linear statistical models for TC intensity forecast

5.2.1 SVM and ANN general principles

ANN and SVM both are supervised learning tools that require training in order to link a given set of input parameters to an output. Neural networks are biologically-inspired distributed parallel processors, which can approximate any continuous function when a sufficient number of hidden nodes are used (Barron, 1993; Hornik et al., 1989). These supervised networks are particularly suited for predicting and forecasting, because of their ability to model nonlinear and non-gaussian processes like those encountered in the context of extreme events. ANNs consist of number processing neurons, linked by synaptic connections and arranged in layers. The network is fed through the input layer and inputs are delivered to the first hidden layer, after applying synaptic weights and biases. In the hidden neurons, the weighted sum of inputs is transformed by a nonlinear

activation function, usually the logistic function or a hyperbolic tangent. The same process is repeated in each of the following hidden layers, until the outcomes reach the output nodes. The weights and biases contain all the information about the network. The objective is therefore to train the network (on the basis of a "training dataset") to obtain a combination of weights and biases that minimize the error between the neural network output and the observed output. The most commonly used criterion is to minimize the mean squares error between the simulated output and the observed output.

The ANN models I use in this chapter are made up of three neural layers: the input, output, and a middle 'hidden' layer. The input layer contains of as many neurons as there are inputs parameters (i.e. predictors) while the output layer consists of a single neuron that predicts the TC intensification rate at a given lead-time. To train the network, we used a back-propagation procedure (Reed et al., 1999) that adjusts the weights and biases to minimize the error function. This adjustment is performed in the steepest descent direction. One of the problems with this method is that the error function is nonlinear and usually has several local minimums, where the model solution can be trapped. Another problem of neural networks is overfitting, i.e. when the network performs almost perfectly on the training dataset, but is unable to generalize to new situations. To avoid overfitting, we use a technique called early stopping. For this, ANN requires three disjoint datasets for training, validation and testing. The training subset is used to obtain the weights and biases of the network. The validation subset is used to stop the training when the error on the validation set begins to rise (i.e. when the network starts overfitting the training data). The testing subset is not used to build the ANN model, but only to assess the performance of the trained model on a completely independent dataset.

SVM basically is a kernel-based supervised learning method that stems from Statistical Learning Theory (Vapnik, 2000). SVMs were initially developed for classification purposes in the early1990s, and then extended for regression by Vapnik (1995). The concept of SVM is to design a function, which correctly classifies all of the objects of the training dataset. Two major differences between SVMs and ANNs are the optimization algorithm and the minimizing norms. For a given training dataset, SVM maps the input vector onto a higher dimensional space, where the training dataset become linearly separable. It uses an appropriate kernel function in the optimization process. One of the main advantages of SVM is hence to transform the problem into a linear optimization problem without the multiple minima issue. While the architecture and weights of ANNs are respectively determined by a trial and error procedure and an iterative process (the back-propagation procedure), which are both very time consuming, the SVMs architecture and weights are the solution of a quadratic optimization problem, which has both a unique minima and can rapidly be solved using a standard algorithm. It also uses a more robust error norm based on the principle of structural risk minimization, where error rates and model complexity are minimized simultaneously, while only the error rate is minimized once the model architecture has been designed for ANNs. This yields a better generalization ability of SVMs. Finally, The SVM model however has several "hyperparameters", which need to be determined by the user.

The SVM schemes I will use in this chapter use the same inputs as the ANN and MLR (i.e. the set of predictors used to forecast the TC intensity change at a given lead time). SVM only requires two disjoint sets of data for training and testing. The training dataset

is used for the development of the model while the testing dataset allows assessing the model performance on an independent dataset.

5.2.2 Development of SVM and ANN schemes for TC intensity forecasts

The non-linear models developed in this chapter use the same predictors (listed in Table 4.2) and datasets as those used for the multi-linear model discussed in Chapter 4 and referred to as 'Atm' experiment. We have also included the latitude, longitude, translation speed and the pressure level of the mean wind flow that matches the initial storm wind steering motion as additional input parameters. We did include these extra predictors, which are used in some linear statistical models (e.g. Knaff et al., 2009, 2010; Lee et al., 2015), as the present chapter focuses on building the most skilful model for TC intensity prediction and not on analysing of the respective contribution of the major parameters as was the case in the previous chapter. The only difference in input parameters between the linear and non-linear schemes is that the two squared terms $VMAX^2$ and MPI^2 are not included in the non-linear schemes, since these schemes are supposed to naturally capture non-linear dependencies between predictors and the predictand. All models are evaluated using the same MAE and skill (in %) metrics as those in the previous chapter (with confidence intervals computed in the same manner).

In section 5.4, the added value of adding oceanic predictors to the above statistical schemes will be discussed. These predictors are meant to account for the influence of oceanic stratification on the cooling below the TC, and on the evolution of its intensity. As mentioned in the introduction, the focus is on the following parameters:

1. The TC heat potential (OHC) calculated as the heat content between the ocean surface and the 26^{o}C isotherm
2. The mixing depth corresponding to 2^{o}C surface cooling produced by a heat-conserving vertical mixing (HMIX)
3. The Cooling inhibition index (CI) calculated as the cubic root of the change in potential energy necessary to cause the mixing to the depth HMIX
4. The SST minus the average temperature of the upper 100m of oceanic layer (dT100)
5. The depth of the isotherm corresponding to the mixed layer temperature minus 2^{o}C (H2)

Details about the calculation of these variables can be found in Vincent et al. (2012b). These variables are computed from the Global Ocean Reanalysis and Simulation (GLORYS) dataset (Ferry et al., 2012; Jourdain et al., 2013, 2014). This dataset is derived from an eddy-permitting (1/4^{o}) version of the NEMO ocean model (Madec, 2008), in which in-situ and satellite altimetry measurements are assimilated. Its temperature and salinity structure is in good agreement with observations, especially in the upper hundred meters, where the interaction with TCs takes place (Ferry et al., 2012). This dataset is available from 1993 onward, and data over the 1993-2012 period is used in the present chapter.

As mentioned above, the ANN scheme requires the input dataset to be separated into three parts. In the following, 80% of the TCs (60% for training and 20% for validation) are used to build the model and the remaining 20% are used for testing the model performance. As explained in chapter 4, the training and testing datasets are chosen randomly but for entire TC tracks. To minimize the problem of being trapped in a local

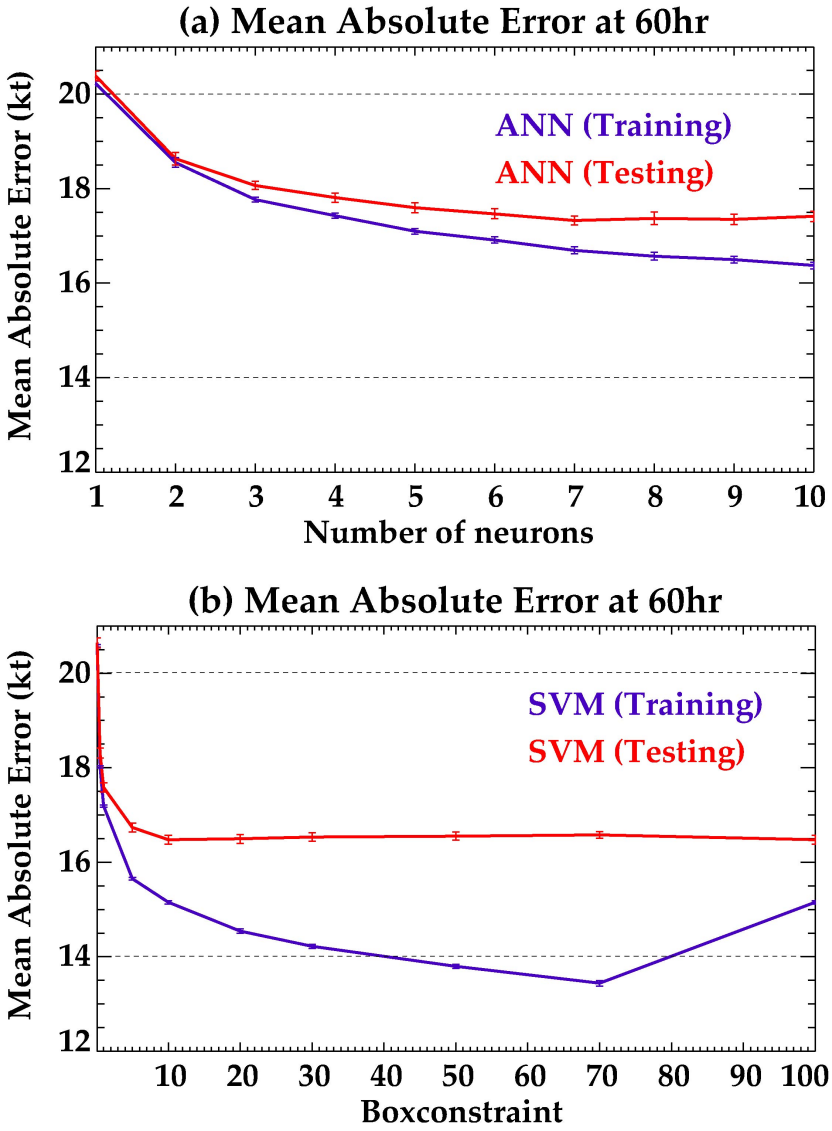

Figure 5.1: Globally-averaged MAE (see section 4.2.2) (kt) for training (blue) and testing (red) datasets at 60 hr forecast lead as function of **(a)** number of ANN neurons and **(b)** value of the SVM optimization parameter. MAE was estimated as an average of 50 independent runs. Error bars give the 95% confidence interval estimated from a bootstrap technique detailed in section 4.2.2. On the basis of this figure, the ANN used in the rest of this chapter uses five neurons in the hidden layer and SVM uses an optimisation parameter of 10.

minimum and avoid overfitting, each experiment was repeated 50 times with different initial weights, training, validation and testing sets. The ANN parameter values were averaged over the 50 independent runs. To determine the optimum number of neurons to be used in the ANN hidden layer, the MAE was computed for a hidden layer

including 1 to 10 neurons. Generally speaking, the more neurons in the hidden layer, the better the network performance on the training dataset. A large number of neurons however increases the risk of over-fitting, which leads to poorer predictions. This is illustrated by Figure 5.1a, which displays the average training and testing MAE over the 50 runs for the dataset, as a function of the number of hidden neurons. While the training dataset MAE monotonically decreases with the increasing number of neurons, it reaches a plateau or even slightly increases beyond about five to seven neurons for the testing dataset. The ANN architecture from structural learning is therefore chosen to be five nodes in the hidden layer.

In contrast to ANN, the SVM scheme only requires the input dataset to be separated into two parts. In that case, 80% and 20% of the TCs are used as training and testing datasets. As ANN, SVM models were constructed separately for each TC-prone basin using 50 randomly selected datasets and the reported performance was averaged over these 50 runs. In the following, the kernel function was chosen to be a radial basis function because of its advantages over other kernel functions, including a limited number of hyperparameters (three) to be set into the SVM regression formulation. SVM performance depends on the choice of these three hyperparameters. To illustrate this aspect, Figure 5.1b shows the sensitivity of the SVM predictive skill for different values of the most sensitive hyperparameter, i.e. the one controlling the width of the kernel function for values ranging from 0 and 100. While the MAE monotonically decreases with an increase of this hyperparameter for the training dataset, it only decreases up to 10 for the testing dataset. Further increasing the value of this parameter results in a marginal MAE increase for testing, which deviate from the MAE for training, indicating that there is overfitting in this range. This parameter was therefore fixed to 10. The

SVM predictive skills are much less sensitive to the choice of the two other hyperparameters (not shown).

5.3 Performance of non-linear statistical TC models

5.3.1. Regionally vs globally trained models

To decide whether to use globally or regionally-trained models in this chapter, the performance of these models is compared using the same predictors (i.e. TC characteristics plus large-scale atmospheric parameters listed above), as it was done in Figure 4.8 for MLR. Figure 5.2 illustrates the improvement of regional models relative to global models for each of the three considered schemes. As already mentioned in Chapter 4, regionally-trained MLR models slightly outperform globally-trained MLR models, when averaged over all the basins (up to 3%; Figure 5.2a). This improvement is seen in all northern hemisphere TC-prone basins, but not for southern hemisphere TCs. This improvement is particularly large for the NIO at long leads (20%) but this result may not be very reliable given the small dataset used to validate the MLR regional model at these extended range.

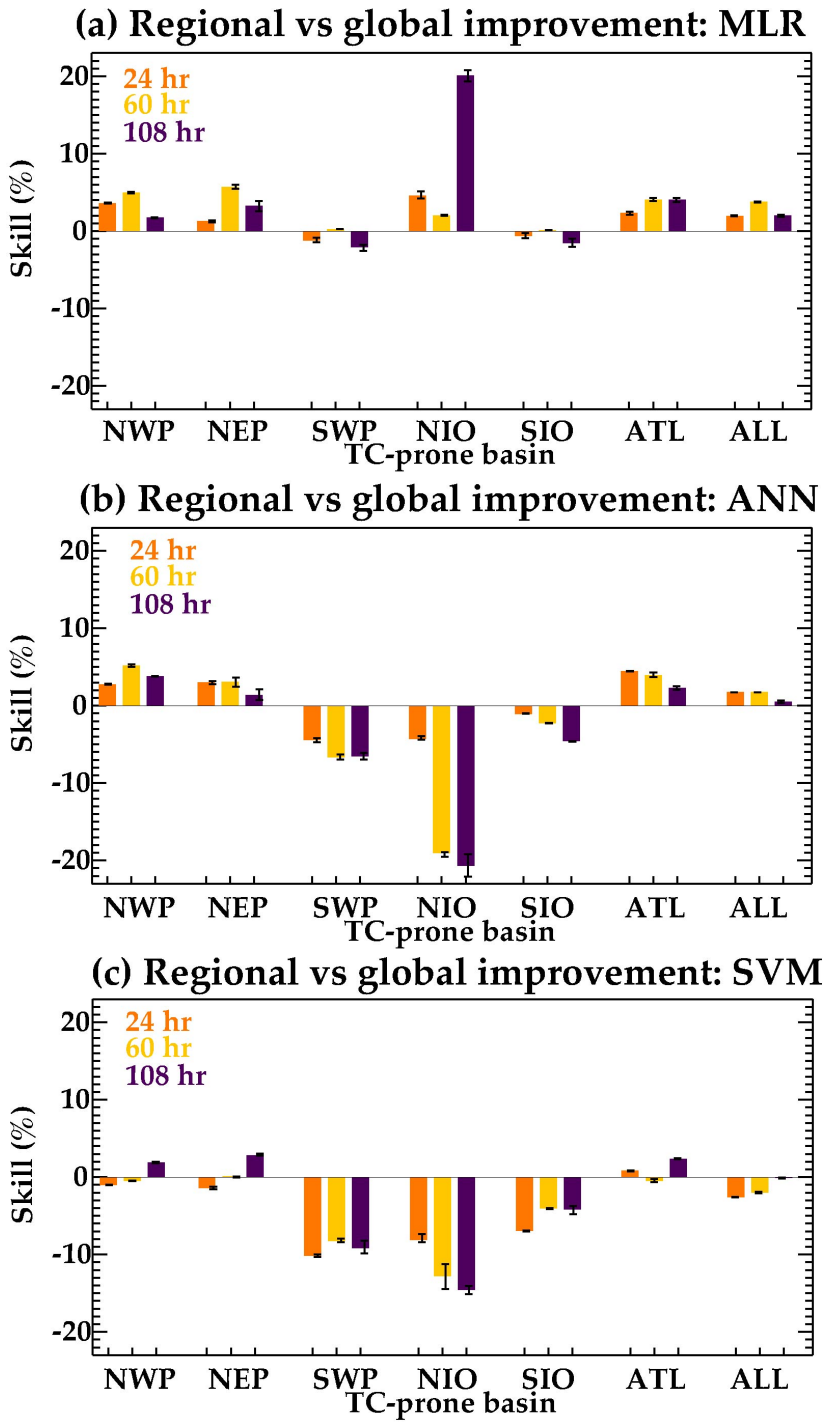

Figure 5.2: Percentage of skill improvement of regionally-trained over globally-trained models using **(a)** MLR, **(b)** ANN and **(c)** SVM schemes at 24h, 60h and 108h lead-times, for each basin and globally-averaged. See section 4.2.2 for a definition of the skill metric. Error bars give the 95% confidence interval estimated from a bootstrap technique detailed in section 4.2.2.

This superior performance of regionally-trained models does not hold for non-linear schemes. It is only ~1% at global scale for ANN (Figure 5.2b), with strong regional contrast: while this improvement is still obvious for NWP, NEP and ATL basins (2 to 5%), the globally-trained model overcome the regionally-trained models for southern hemisphere TCs (1 to 6%) and even more in the NIO basin (5 to 20%). For SVM, the globally-trained model overcomes the regionally-trained ones at global scale (up to 3%, Figure 5.2c). Regionally, skills are similar for the two types of models for the NWP, NEP and ATL, while the improvement of a globally-trained model is obvious for SWP (~10%), SIO (5%) and NIO basin (~5 to 15%). Non-linear models (and more specifically SVM) are thus able to benefit from the larger global training database to improve the skill relative to regionally-trained models. This justifies the use of globally-trained rather than regionally-trained non-linear models in the following. Conducting all the analyses below using regionally-trained models however does not change the overall conclusions of this Chapter, except for the inclusion of oceanic parameters for which results are more stable and the improvement is larger when using globally-trained models (not shown).

5.3.2. Performance of linear vs. non-linear models

In Chapter 4, we have seen that regionally-trained MLR models outperform persistence by a similar amount in most basins (see Figure 4.6c; 20 to 40% of skill improvement), except in the ATL and NIO, where the skill gain is weaker (10 to 25%). Figure 5.3 provide a similar basin-wise skill assessment as in Figure 4.6c but for globally-trained MLR, ANN and SVM models. Comparing Figure 5.3a with Figure 4.6c demonstrates that the conclusions derived from regionally-trained MLR models hold for globally-trained MLR models: the relative skill improvement

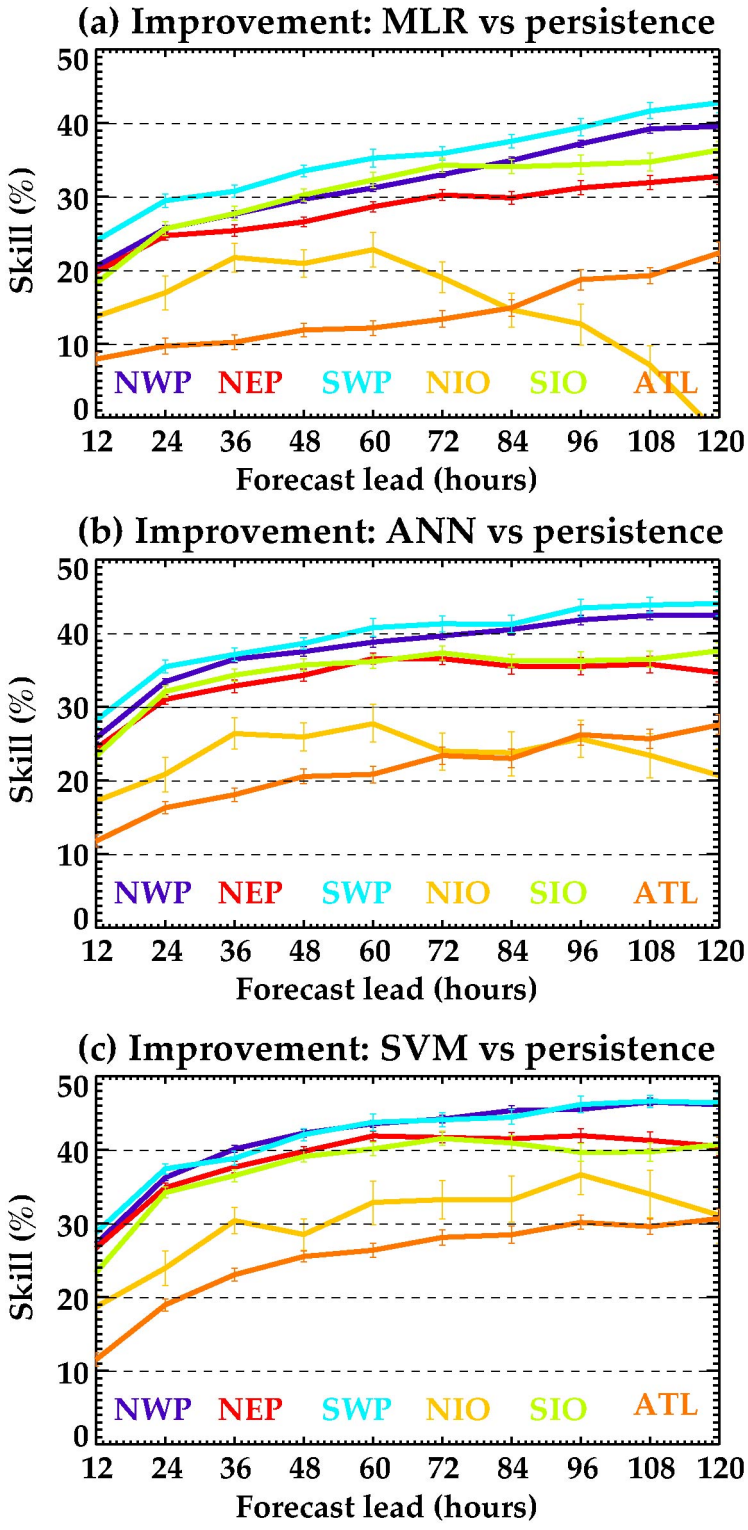

Figure 5.3: Basin-wise percentage of skill improvement of globally-trained **(a)** MLR, **(b)** ANN and **(c)** SVM models relative to persistence as a function of lead-time. See section 4.2.2 for a definition of the skill metric. Error bars give the 95% confidence interval estimated from a bootstrap technique detailed in section 4.2.2.

compared to persistence is generally similar in four basins (NWP, SWP, SIO and NEP) where there is a ~20 to 40% (depending on the lead-time) improvement relative to persistence. In contrast, the skill improvement relative to persistence is considerably weaker in the ATL and NIO basins, where it ranges between 10 and 25%. A careful comparison of these two panels however reveals some differences between regionally- and globally-trained MLR models. First, consistently with Figure 5.2a, this skill improvement is generally slightly larger especially for mid range time-lead in all basins for regionally-trained compared to globally trained models (2 to 5%). Second, the improvement for NIO at long lead-time is considerably larger for regionally-trained models (10% to 20% improvement) as also evidenced in Figure 5.2a. Turning to non-linear schemes (Figure 5.3bc), it appears that the ranking of the skill improvement as a function of the basin remains very similar to the one obtained for linear models, with a similar skill improvement in most basins (Figure 5.3bc; 25 to 45% of skill improvement), except in the ATL and NIO, where the skill gain is weaker (10 to 35% depending on the scheme and lead-time). Non-linear schemes also generally outperform linear schemes in all basins. This aspect is further detailed in the next paragraph.

The added value of using non-linear models is further evaluated by computing the relative skill improvement of ANN and SVM models relative to the MLR model for each basin (light colour bars on Figure 5.4). As can be seen on Figure 5.4, using ANN or SVM improves the skill relative to the MLR at all lead-times and in all basins. Comparing light colour bars on Figure 5.4a and 5.4b also indicates that this improvement is systematically larger for SVM than for ANN. When averaged over all the basins, the skill improvement over MLR is about 5-10% for ANN (light colour bars on Figure 5.4a) and about 12-17% for SVM (light colour bars on Figure 5.4b). The

additional skill yielded by nonlinear schemes is similar in each basin (light colour bars on Figure 5.4bc), except for the NIO where the additional skill is much larger at long-leads (18% for ANN and 29% for SVM), a result that has again to be taken cautiously given the small TC sample that is used to compare these extended-range skills in the NIO, where TCs lasting more than 4 days are rare.

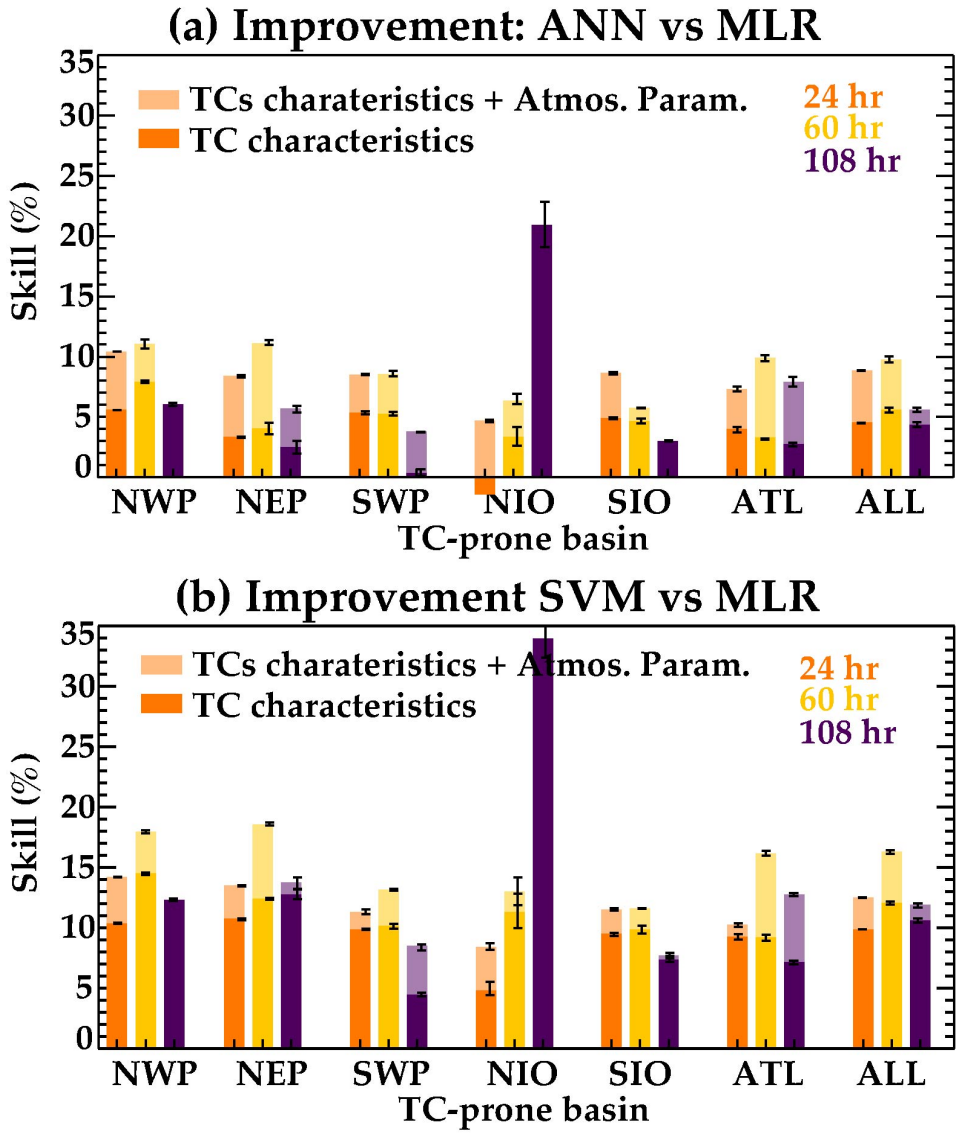

Figure 5.4: Percentage of **(a)** ANN and **(b)** SVM skill improvement relative to MLR for baseline models (i.e. only TC initial characteristics, plain bars) and full models (i.e. also environmental parameters along the TC track, light colour bars) at 24h, 60h and 108h lead-times, for each basin and globally-averaged. Error bars give the 95% confidence interval estimated from a bootstrap technique.

5.3.3. Relative importance of input parameters

Now it is tested whether the major conclusions drawn from MLR models in Chapter 4 hold for non-linear models. First, are TC initial characteristics major contributors to the skill in non-linear models as they were for MLR? To explore this, ANN and SVM hindcasts with TC initial characteristics as only input parameters were performed. As for MLR models, TC initial characteristics contribute to about 60 to 80% of the skill improvement relative to persistence for non-linear schemes (not shown). It is however interesting to analyse which input parameters contribute most to the skill improvement of non-linear models relative to linear ones (see light colour bars on Figure 5.4 and related discussion above). Plain bars on Figure 5.4 compare the skill improvement of non-linear baseline (i.e. only TC characteristics as predictors) models relative to the linear baseline models. Comparing plain colour and light colour bars on Figure 5.4a reveals that the overall skill improvement brought by ANN equally arises from both from a better handling of TC characteristics and environmental parameters (~5% of globally-averaged improvement when accounting only for TC initial characteristics and ~10% improvement when accounting for both TC initial characteristics and environmental parameters). In contrast, comparing plain and light bars on Figure 5.4b reveals that the overall SVM models skill improvement predominantly arises from a better handling of TC characteristics (~10% improvement), with a weaker contribution of environmental parameters (~3 to 5% additional improvement).

Another important result obtained with MLR models was that a model built from climatological environmental parameters along the TC-track yields nearly the same predictive skill as a model built

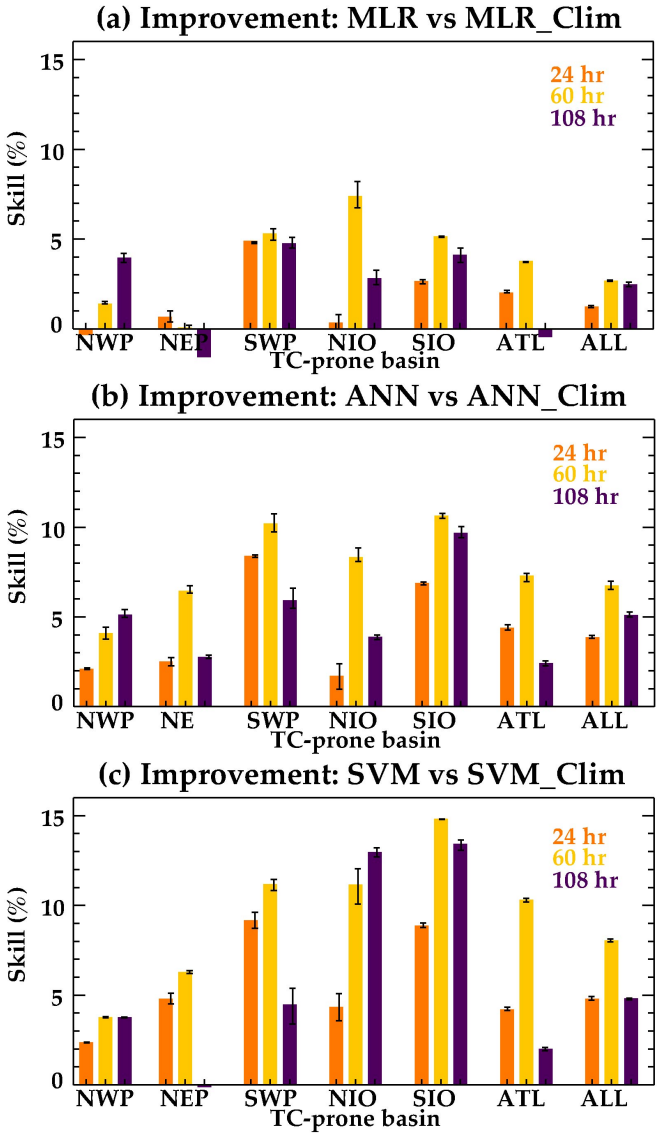

Figure 5.5: Percentage of (a) MLR, (b) ANN and (c) SVM models skill improvement yielded by using real-time rather than climatological environmental atmospheric parameters, at 24h, 60h and 108h lead-times, for each basin and globally-averaged. Error bars give the 95% confidence interval estimated from a bootstrap technique.

from real-time values (Figure 5.5a). Along the same lines, experiments trained with climatologically-derived atmospheric predictors were performed for both ANN and SVM. Figure 5.5 illustrates that, in non-linear models, the use of real-time predictors systematically improves the skill relative to climatological (Figure 5.5bc). The globally-averaged skill improvement ranges between 4% and 7% for ANN (Figure 5.5b) and

between 5 and 8% for SVM (Figure 5.5c), against less than 3% for MLR (with even some negative values at long-lead times). This suggests that ANN and SVM are able to better capture the influence of the non-seasonal variations of atmospheric parameters onto TCs intensification rate. This result holds for each individual basin, with a larger improvement in the southern hemisphere for both non-linear schemes (Figure 5.5bc) and the northern IO for SVM (Figure 5.5c). The basin-wise dependency of the improvement brought by real-time environmental parameters is quite similar to that of MLR, but it is generally larger (Figure 5.5bc vs. 5.5a).

5.3.4. Skill as a function of TC intensity

I have shown that MLR hindcasts are 3 to 4 times more skilful for strongest TCs (Cat 3 to 5) relative to weaker TCs (up to Cat 2). Figure 5.6 hence compares the skill of the linear and non-linear models as a function of TCs intensity. As for MLR (Figure 5.6a), non-linear models are systematically more skilful for predicting intensity changes of strongest TCs relative to weaker ones (Figure 5.6bc). There are however noticeable differences between the three schemes. Relative to MLR (Figure 5.6a), ANN marginally improves the skill for both strong TCs and weak TCs (2-5% improvement in both cases), resulting in a ANN model that is still 3 times more skilful for strongest as compared to weak TCs (Figure 5.6b). In the case of SVM scheme, the skill improvement over MLR is significant for strong TCs (~10%) but even larger for weak TCs (~20%), resulting in a near-doubling of the forecast skill for these TCs categories. This results in a SVM skill improvement relative to persistence reaching 50% to 60% for strong TCs and 30% to 40% for weak TCs (Figure 5.6c). The skill improvement between weak and strong TCs is hence reduced in the case of the SVM scheme as compared to both MLR and ANN schemes (Figure 5.6).

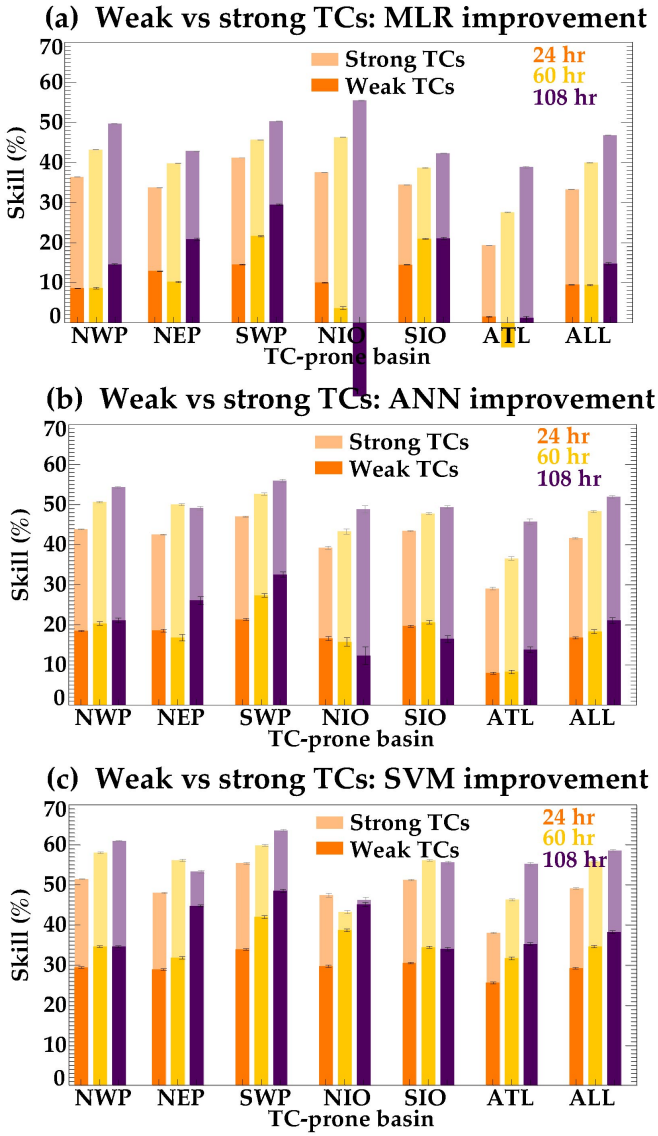

Figure 5.6: Percentage of skill improvement relative to persistence for weak (i.e. < 96 kt: cat 2 and below, plain bars) and strong (i.e. > 96 kt: Cat. 3 or more, light colour bars) TCs for **(a)** MLR, **(b)** ANN and **(c)** SVM models at 24h, 60h and 108h, as a function of the basin and globally-averaged. Error bars give the 95% confidence interval estimated from a bootstrap technique.

5.4 Accounting for air-sea coupling in TCs intensity forecast

The ocean feedbacks on TCs intensification rate by reducing SST and evaporation under their track. In this section we assess the impact of accounting for this variable cooling in global TCs intensity statistical forecasts.

5.4.1. Sensitivity of the results to the data length

The aim of this section is to quantify the skill improvement brought by including suitable oceanic predictors (metrics of the control of the cooling under the TC by the oceanic stratification) in these statistical schemes. Unlike the atmospheric dataset, which is derived from an atmospheric reanalysis (ERAI) that provides data starting in 1979, the oceanic reanalysis used to calculate the oceanic parameters provides data from 1993 only. The results discussed above, which use only TC characteristics and large-scale environmental predictors and do not include oceanic parameters, use a rather long period (1979-2012, i.e. 34 years). The limited time-span over which oceanic variables are available (1993-2012) implies that the influence of oceanic predictors can only be tested with models built over a shorter 20 years period. This reduced dataset size may impact the models performance. In this subsection, first the skill of global models built from a 34 years database is compared against those built from a 20 years database. The inclusion of oceanic variables will be discussed in the next section.

As shown on Figure 5.7, reducing the data length to 20 years degrades the skill of the all models: 2% to 3% for MLR, 3% to 5% for ANN and 5% to 7% for SVM globally. This skill degradation is particularly large for the NIO (5%-10% for MLR, 5%-15% for ANN, 8%-18% for SVM) and the NEP (3%-10% for MLR, 8%-12% for ANN, 10%-17% for SVM) and SWP (5%-10% for ANN and SVM both) while it is negligible for the NWP most likely because this region accounts for a large percentage of global TCs (and a 20 years period may hence contain a sufficient number of NWP cyclones to properly train the model for that region).

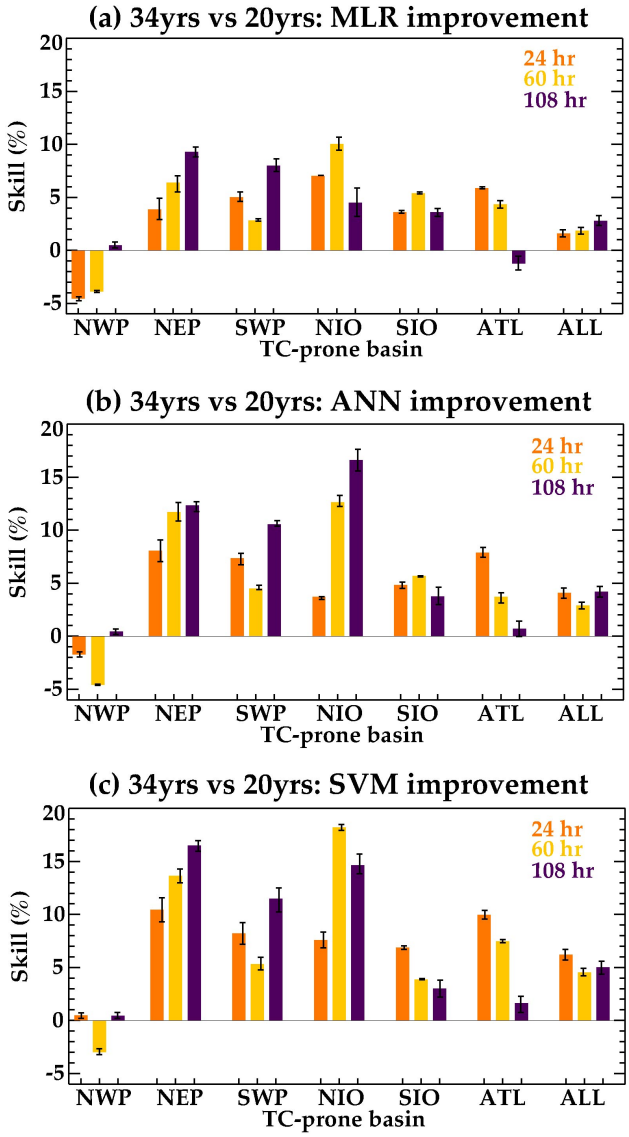

Figure 5.7: Percentage of skill improvement brought by training the model over a 34 years rather than a 20 years period for **(a)** MLR, **(b)** ANN and **(c)** SVM models at 24h, 60h and 108h lead-times, for each basin and globally-averaged. Error bars give the 95% confidence interval estimated from a bootstrap technique.

5.4.2 Inclusion of oceanic predictors

The oceanic parameters listed in section 5.2 are included sequentially in the globally-trained statistical models. The skill improvement brought by the inclusion of a particular oceanic parameter (relative to a forecast that does not account for ocean subsurface information) is then presented on Figure 5.8. Figure 5.8 first indicates that non-linear methods generally yield a larger global skill improvement (up to 2%)

compared to the linear method (up to 0.7%), which may be explained by the non-linear nature of the relationship between the TC intensification rate and the oceanic stratification. The recently proposed CI metric (Vincent et al. 2012b) generally yields the most systematic and consistent improvement when using non-linear schemes. In particular, it systematically outperforms the results obtained with OHC that does not bring any improvement or even degrades the results in

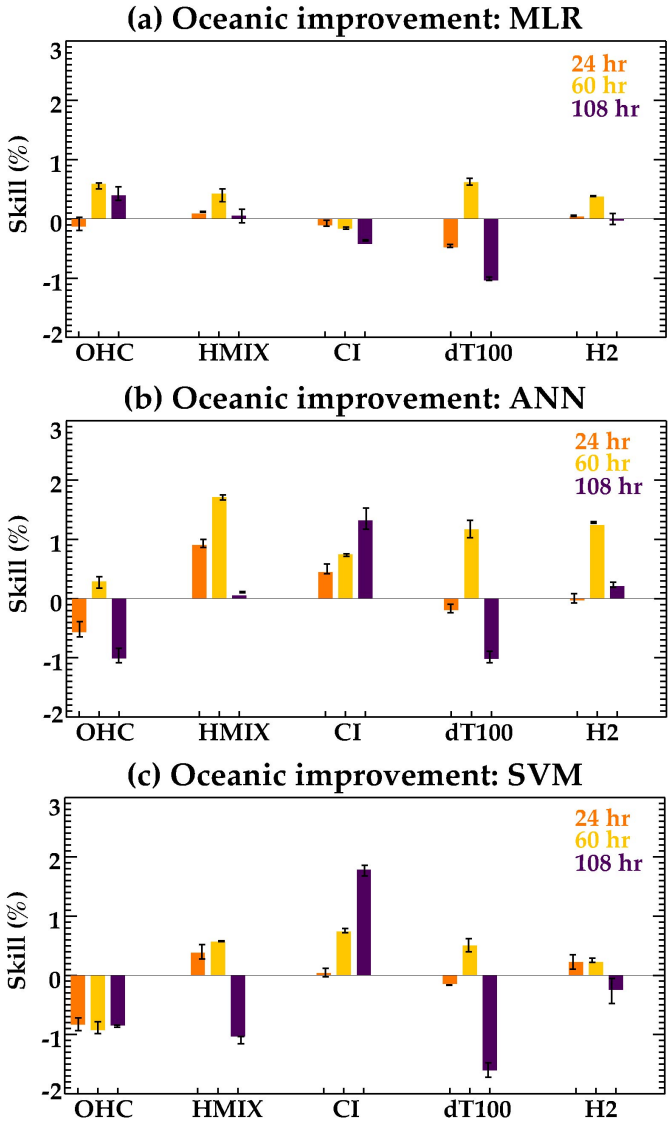

Figure 5.8: Percentage of skill improvement brought by including different oceanic predictors (OHC, HMIX, CI, dT100 and H2: see section 5.2) over the 1993-2012 period in **(a)** MLR, **(b)** ANN and **(c)** SVM models at 24h, 60h and 108h lead-times globally-averaged. Error bars give the 95% confidence interval estimated from a bootstrap technique.

non-linear schemes (Figure 5.8bc). The contribution from the other tested oceanic metrics (HMIX, dT100, H2) is more variable, depending on the lead-time and non-linear scheme. For instance, while dT100 improves the skill at 60h lead-time, it degrades it at shorter and longer forecast ranges. Similarly, while Hmix and H2 generally improve the ANN model skill, results are less compelling when using an SVM scheme. Since CI is the metric that brings a consistent TC intensity forecast improvement for both non-linear schemes, I therefore focus on this metric in the following, as being representative of the impact of air-sea coupling. When averaged at global scale, the improvement due to the inclusion of this metric is however modest, ranging from less than 0.5% at short lead-time to 2% at long lead-time (Figure 5.8bc).

However, Figure 5.9 clearly illustrates that the improvement due to the inclusion of CI strongly depends on the basin. Including CI yields a large improvement in the NIO (up to 5% for ANN and 3% for SVM) and the NEP (up to 4% for ANN and ~7% for SVM) followed by the NWP (~1-2% in both ANN and SVM) (Figure 5.9bc). Other basins show either a small improvement or even degradation due to CI inclusion. Though the CI inclusion does not improve the model skill at global scale when using MLR scheme, basin-wise results are however consistent with the non-linear schemes, with a larger improvement in NIO (~3-4%) and NEP (~2%) than in other basins (Figure 5.9a).

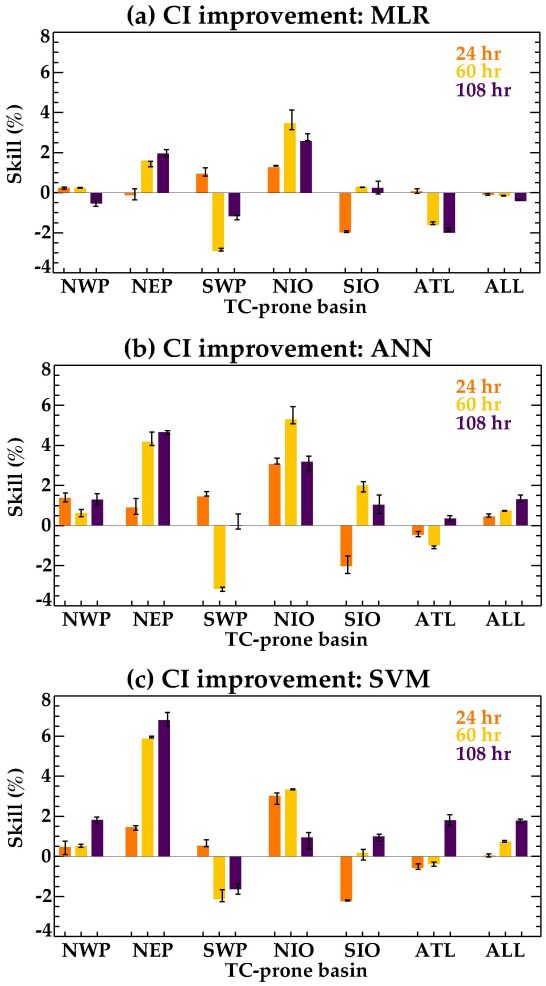

Figure 5.9: Percentage of skill improvement brought by adding CI to the environmental parameters set in (a) MLR (b) ANN and (c) SVM models at 24h, 60h and 108h lead-times, for each basin and globally-averaged. Error bars give the 95% confidence interval estimated from a bootstrap technique.

To put these results in a broader context, finally the skill yielded by CI is compared with that of the three most skilful atmospheric predictors: SHRD, MPI and RHHI. SHRD is undoubtedly the most skillful large-scale environmental predictor for all schemes, with a ~4%, 8% and 4% improvement, respectively, when using MLR, ANN and SVM schemes (Figure 5.10). However, the next most important environmental parameter is CI (~2%) for the ANN scheme. For the SVM scheme, CI is of similar importance to MPI or RHHI (Figure 5.10).

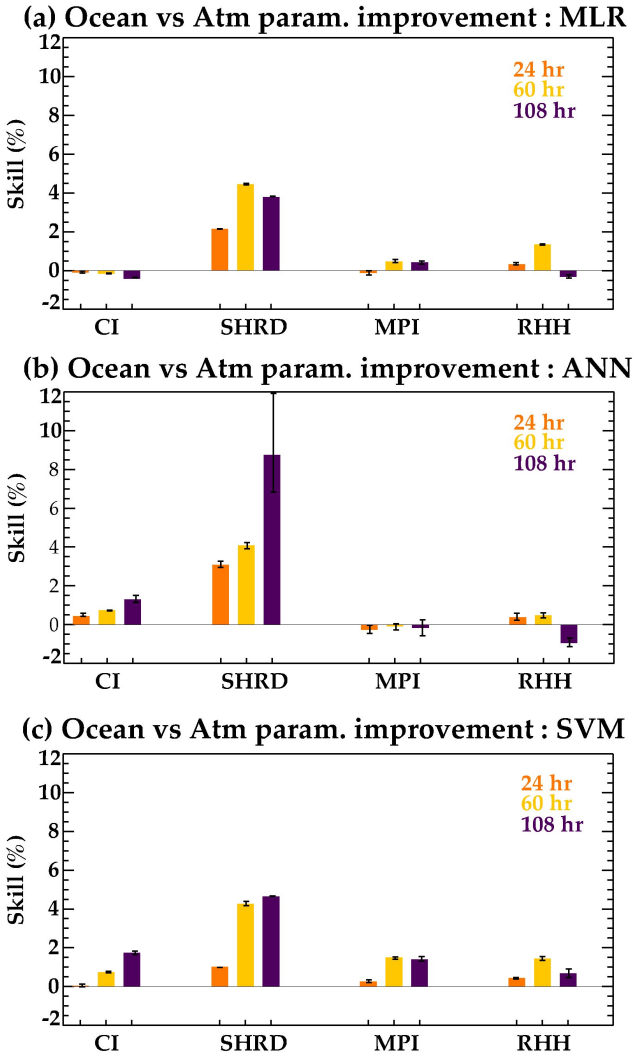

Figure 5.10: Globally-averaged percentage of skill improvement brought by including CI and the three most skillful large-scale atmospheric predictors (SHRD, MPI, RHHI) in **(a)** MLR, **(b)** ANN and **(c)** SVM models at 24h, 60h and 108h lead-times. Error bars give the 95% confidence interval estimated from a bootstrap technique.

5.4 Summary and conclusions

The goal of this chapter was two-fold: (1) to assess the added value of using non-linear statistical models over the commonly used linear ones, and (2) to assess the added value of including physically-based metrics of sub-surface oceanic stratification in predicting the TC intensity globally. The first objective is a must before tackling the second one due to probable non-linearities in the relation between the TC intensity growth rate and oceanic subsurface stratification.

The results first indicate that globally-trained non-linear models have a very similar performance to those trained regionally (Figure 5.2). Non-linear models yield more skill than the widely-used MLR models in all TC-prone basins. The additional skill relative to MLR is as large as ~10% for ANN and ~15% for SVM. My results hence clearly demonstrate that accounting for the non-linear relationship between input parameters and the TC intensity change greatly improves the skill (and that SVM is particularly efficient at capturing this non-linearity). This result echoes the two studies that compared the performance of linear and non-linear schemes in the northwest Pacific using either SVM (Lin et al., 2013) or ANN (Sharma et al., 2013). Lin et al. (2013) found an improvement of 5-10% when comparing their non-linear SVM scheme to operational MLR forecasts. Our results for the Northwest Pacific indicate an even larger improvement (12 to 23%; see Figure 5.4b), but, contrary to our study, they did not use the same set of input parameters as the operational forecast, which makes the two studies difficult to compare. Our ANN results for the Northwest Pacific can however be compared with those of Sharma et al. (2013) who used the same parameters as the linear STIPS model (Knaff et al., 2005) and showed that their non-linear ANN scheme improved forecasts by 3-11% at all lead-times. This is quite consistent with the present study.

As for linear models, a large fraction (~60%-80%) of non-linear models skill arises from initial TC characteristics. Accounting for non-linearities between the TC intensity change and TC initial characteristics/ environmental parameters equally contribute to the additional ANN skill relative to MLR. The larger SVM model skill improvement relative to MLR is dominated by the inclusion of non-linear dependencies to the TC

initial characteristics (~11%) rather than to atmospheric parameters (4%). Using a climatological seasonal cycle of environmental predictors (rather than real-time data) yields a global skill degradation of about 4%-7% for ANN and about 5%-8% for SVM, i.e. clearly larger than for the MLR model (~1%-3%). Non-linear models are hence able to extract much more information from real-time environmental parameters than linear ones, for which the technically simpler accounting for climatological atmospheric background characteristics along the TCs tracks suffices.

As already discussed in Chapter 4, the MLR model performs poorly to predict intensity changes of category 2 and below TCs, while they are 2 to 4 times more skilful for the strongest TCs (Cat3 and more). This is also true of ANN, which also yields little skill for TCs of category 2 and less. In contrast, the SVM model considerably improves the skill for weak TCs relative to using MLR (2 to 3 times more skilful) while this improvement is weaker for stronger TCs. This results in a skill difference between weak and strong TCs that is considerably smaller for SVM than for MLR and ANN. The good SVM performance for predicting weaker TCs (cat. 2 and less) intensification makes it the most suitable tool for TC intensity prediction.

Adding oceanic predictors to MLR TC intensity forecasts only yields a marginal skill improvement. The improvement is considerably larger for non-linear schemes. CI is the oceanic predictor that brings the largest and most consistent improvement (~1%-2% globally for both MLR and ANN), while the commonly-used OHC in operational forecasts does not improve the non-linear models skill. This demonstrates the advantage of using a physically-based oceanic metric for improving TCs intensity prediction. In addition, my results demonstrate that the improvement brought by this oceanic metric

varies considerably depending on the basin. While oceanic predictors yield a negligible skill improvement in the southern hemisphere, the improvement is far larger in the NIO (3%-5%) and NEP basins (2%-7%) for both non-linear schemes. Finally, I show that including a suitable representation of the oceanic stratification yields as much additional skill as maximum potential intensity (MPI), which is the second most important large-scale atmospheric parameter.

Overall, my results demonstrate that using non-linear schemes with a relevant oceanic parameter considerably improves the forecast skill in all basins relative to the widely-used linear models using TC heat potential (OHC). It must however be noted that the skill improvement arising from the use of non-linear models (10 to 15% globally) is far larger than the one arising from the inclusion of a suitable oceanic metric (up to 2% globally). This Chapter hence clearly demonstrates that operational TCs forecast centres should replace their commonly-used linear statistical prediction schemes with non-linear statistical prediction schemes, with the SVM scheme displaying at this stage the largest promise for skill improvement. Although the inclusion of a suitable oceanic metric only modestly improves the non-linear model skill, this inclusion generally requires the model to be trained over a shorter period (1993-onward vs. 1979-onward) as oceanic stratification is generally more reliable over the satellite era (1993 onwards) in oceanic reanalyses. This reduction of the dataset length results in a degradation of the performance of non-linear models (~5%), which generally overcomes the improvement brought by including oceanic parameters (up to 2%). At this stage, it may hence be more efficient to use non-linear models trained over a long period using only TCs characteristics and environmental atmospheric parameters as input, rather than using use non-linear models trained over a shorter period and including an additional oceanic

parameter. While we expect a skill degradation for operational application due to use of forecasted rather than reanalysed fields of environmental parameters along the TC track, the TCs intensity skill improvement expected from the present results are sufficiently large to motivate a trial in operational mode.

Chapter 6 Thesis Summary and Perspectives

TCs are one of the deadliest natural hazards in coastal areas, causing huge lives and property losses. India has more than 64 millions people living in coastal regions (Neumann et al., 2015). As a result, the Indian sub-continent is one of the most heavily TCs-affected regions in the world. The BoB is home to about four named TCs each year, which only accounts for ~5% of TCs globally (Alam et al, 2003). BoB TCs may be neither the most intense nor the most numerous, but they have catastrophic impacts. Of the top twenty deadliest TCs in the world history, fourteen were generated in the BoB (Longshore, 2008). The high population density distributed along low-lying coastal areas and the poor disaster management strategies largely explain this very strong vulnerability of the countries surrounding the BoB to natural disasters. The Nargis TC in May 2008 is a dramatic example: it reached Category 4 and caused the worst natural disaster in Myanmar history, with more than 140,000 lives lost, one million homeless people and over $10 billion of economic losses (Webster et al., 2008). However, while TC tracks forecasts have considerably improved over the last 20 years, TCs intensity forecast are still far from reliable (DeMaria et al., 2014). It is therefore of utter practical importance to identify the key factors that control TCs intensity, in particular in the BoB. Air-sea interactions under TCs have been identified as one of the key processes affecting TC intensity evolution, aside internal dynamics and large-scale atmospheric environmental forcing (e.g. Wang and Wu, 2004). TCs cool the ocean below them through vertical mixing (e.g. V12a). The cooling below TCs reduces their intensification rate by reducing upward enthalpy fluxes that fuel its growth (e.g. Cione and Ulhorn, 2003). The cooling below the TC not only depends on its properties (intensity, propagation speed, radius) but also on the subsurface oceanic stratification.

This thesis hence aims at investigating the influence of ocean-atmosphere coupling on TCs characteristics, with a specific focus on the Bay of Bengal through the use of both statistical and dynamical modelling. How should oceanic predictors that account for the oceanic cooling feedback on the TC intensity be included in statistical TC intensity forecasts?

6.1 Summary

NIO TCs generally develop before (pre-monsoon) and after (post-monsoon) the summer monsoon and are more frequent in the BoB than in the Arabian Sea. Several TC case studies suggest that the surface cooling under BoB cyclones is larger during the pre-monsoon (about 2-3^{o} C) than during the post-monsoon. Aside its very warm waters, the BoB is rather unique amongst other TCs-prone regions, due to the large quantity of fresh water it receives through rainfall and river discharge during the summer monsoon. This results in a strong near-surface salinity stratification after the monsoon, which inhibits vertical mixing, the main source of surface cooling under TCs. This weak cooling could hence favour the development of intense TCs in the BoB after the monsoon. While several statistical and dynamical studies have already addressed the influence of ocean-atmosphere coupling on TCs characteristics in the Atlantic and Pacific, this topic has not been much investigated in the NIO. The tremendous human and socio-economical consequences of these extreme events as well as the specificity of the hydrography of the Bay, with very strong salinity stratification during the post-monsoon, plead for an in-depth investigation of the influence of ocean-atmosphere coupling on TCs characteristics in this region.

The first objective of this thesis was to investigate the processes responsible for the smaller amplitude TC-induced surface cooling in the BoB before than after the monsoon. A case study of eight TCs suggested that the weak observed surface cooling after the monsoon in the BoB is due to haline stratification (Sengupta et al., 2008). This small sample however prevented a quantitative estimate of the respective influences of haline and thermal stratification and TCs winds intensity on the amplitude of the surface ocean response to TCs. To address this question using a much larger sample, observations as well as ½° global ocean model simulation forced by realistic TC winds derived from an analytic shape adjusted to observed TC tracks and magnitude over the 1978-2007 period were used. This approach samples the ocean response to 135 BoB TCs over this 30-year period. It is demonstrated that this simulation accurately captures the seasonal cycle of salinity, temperature, and barrier layer in this region, with fresher waters, deeper upper-ocean stratification, and thicker barrier layers after the monsoon. As a result, this simulation also reproduces the three times larger TC-induced cooling before than after the monsoon. The results demonstrate that this difference in TC-induced cooling amplitude is essentially related to seasonal changes in oceanic stratification rather than to differences in TC wind energy input. After the monsoon, the enhanced haline and deeper thermal stratification combine to inhibit vertical mixing underneath TCs, and the resulting cooling. On average, the thermal stratification changes account for ~60% of the TCs-induced cooling reduction during the post-monsoon, while haline stratification accounts for the remaining ~40%. The respective contributions of thermal and haline stratification however vary strongly within the BoB: haline stratification explains most of the TC-induced cooling inhibition in the northern BoB (offshore of Bangladesh-Myanmar-east coast of India), where seasonal changes in salinity are the strongest, while thermal stratification explains most of the cooling

inhibition in the southwestern BoB. This major influence of salinity in the northern BoB advocates for an improved representation of upper-ocean salinity and temperature effects in statistical and dynamical TCs forecasts, which could ultimately lead to significant improvements of TC intensity forecasts in dynamical models.

The second objective of the thesis was to quantify and understand the feedback of this TC-induced cooling on IO TC characteristics, an assessment that has been performed in other basins but not yet in the IO. To attain that goal, a long-term simulation (20 years) with a ¼° regional IO coupled ocean-atmosphere model (NEMO ocean model coupled to WRF atmospheric model) has been used. This simulation simulates the IO spatial and seasonal TCs distributions and the TC-induced cooling reasonably well. It however overestimates the number of TCs and fails to reproduce the strongest observed cyclones (Cat-3 and more). To isolate the impact of the oceanic feedback onto TCs characteristics, TCs statistics from this reference coupled simulation was compared to a uncoupled atmospheric experiment forced by the SST of the coupled experiment (from which cyclone colds wakes have been filtered out). This experiment effectively suppresses air-sea interactions, a strategy that allows a reliable statistical assessment of the air-sea coupling impact on IO TCs. The results reveal that the IO cyclogenesis spatial distribution is not affected by air-sea coupling, but that coupling reduces the number of TCs by ~30% in both hemispheres. It also influences the TCs seasonal distribution with a much better resolved bimodal character of northern IO TCs seasonal distribution in the coupled run. Air-sea coupling also reduces the percentage of intense TCs (Category 2 and more) in the two basins, from 7% in the forced simulation to 2% in the coupled one. This impact of air-sea coupling on strongest TCs can be traced back to a 15% reduction of inner-core upward enthalpy fluxes in the coupled simulation, as a

direct response to the TC-induced ocean cooling. The results also demonstrate that BoB TCs tend to be stronger before the monsoon in the model and observations, because of a more favourable atmospheric environment (less vertical shear, warmer SST). The effect of air-sea coupling is weaker, but far from negligible, and contributes to diminish the contrast between pre- and post-monsoon BoB TCs amplitude distribution. Overall, results from this chapter demonstrated the key role of air-sea interactions on TCs intensification in the northern IO.

Along with dynamical models, TC intensity prediction relies on statistical-dynamical linear models that use linear statistical regression techniques that relate TCs intensity changes to predictors combining the TCs initial characteristics and large-scale environmental parameters along its track. In operational centres, most of those models are developed for a single or two TC basins. Before testing the influence of oceanic parameters on TCs intensity forecasts, the characteristics of linear statistical models developed for TCs intensity prediction at global-scale was assessed. To that end, multi-linear regression (MLR) models were developed separately for each TC-prone basin, but based on the same set of predictors and datasets, in order to allow comparing skill for the northern IO to that in other basins. First, it is demonstrated that these models display comparable skill to previously-described similar operational schemes in hindcast mode. The skill improvement relative to persistence is similar in most basins (20%-40%), except in the north Atlantic and northern Indian Ocean where it is weaker (10%-20%). A large fraction (60 to 80%) of this skill improvement arises from accounting for initial (i.e. at the beginning of the hindcast) TC characteristics in all basins. The atmospheric environmental parameters that yield most skill globally are vertical wind shear followed by maximum potential intensity, but with individual

contributions that strongly depend on the basin. It is also demonstrated that statistical TC intensity forecasts perform poorly to predict intensity changes of weak TCs in all basins, and are 2 to 4 times more skilful for strongest TCs (Category 3 and more). This suggests that these linear models do not properly capture the processes controlling TCs intensification during their initial stages. Finally, the results reveal that hindcast models built from climatological environmental predictors perform almost as well as those using real-time values. For example, in the northern IO, using real-time predictors only modestly improves the skill at short to mid-range lead-time (~3%). This result is important, as it has the potential to considerably simplify the implementation of operational forecasts using such linear statistical models.

The third and the last objective of this thesis was to quantify of the skill improvement brought by including oceanic subsurface metrics into the statistical intensity hindcast schemes. The relationship between these oceanic metrics and the TC intensification rate being likely non-linear, I also developed and tested non-linear statistical TC intensity prediction schemes based on two different approaches (artificial neural network -ANN- and support vector machine –SVM-). I first show that, while regionally-trained linear models generally slightly overcome the skill of a globally-trained linear model, it is not the case for non-linear models. For instance, a globally-trained non-linear model performs considerably better (~10%) than a regionally-trained model for northern IO TCs, probably because the small TC sample does not allow a proper training in that basin. Both non-linear approaches also considerably improve the prediction skill relative to the linear model in all TC-prone basins, with a larger improvement for SVM (~13% vs. ~7% for ANN). Non-linear models are better able than linear ones to capture the influence of atmospheric parameters non-seasonal variations on TCs intensification

rate, with real-time predictors systematically improving the prediction skill (~4-7% for ANN and ~5-8% for SVM). Then the skill improvement brought by various oceanic metrics that account for air-sea interactions under TCs was evaluated. Non-linear schemes yield a much larger TC intensity hindcast improvement than linear schemes when including oceanic metrics, most likely because of the non-linear relation between the TC intensification and these oceanic parameters. The analysis also indicates that the widely-used OHC parameter (i.e. the heat content between the 26°C isotherm and the surface) yields a negligible skill improvement. Recently proposed physically-based oceanic metrics perform far better than the TC heat potential, with the cooling inhibition index bringing the largest ~2% global improvement. It is also demonstrated that the improvement yielded by oceanic parameters is strongly basin-dependent. Oceanic subsurface information helps most in the northeast Pacific and northern IO (up to 6%). Oceanic metrics yield as much skill as maximum potential intensity, which is the second most important large-scale atmospheric parameter. Overall, using non-linear schemes with a relevant oceanic parameter considerably improves the forecast skill in all basins relative to the widely-used linear models using OHC. These results could hence greatly benefit the agencies responsible for operational TCs forecast, especially in the northern IO.

Overall, this thesis has allowed several steps forward in understanding the ocean response to TCs and air-sea coupling feedback to TCs, with a particular focus on the north IO. The main achievements of this thesis are:

- A quantification of the impact of the BoB salinity stratification on TCs-induced cooling

- A quantification of the impact of air-sea coupling on TC characteristics in the Indian Ocean
- The setup of a consistent statistical scheme for global TCs intensity forecasts
- The improvement of state-of-the-art TCs intensity statistical schemes by using a non-linear scheme and including oceanic parameters

6.2 Limitations and perspectives

6.2.1 Oceanic response to TCs

Chapter 2 of this thesis demonstrates that the post-monsoon BoB haline stratification induces an average 40% reduction of TC-induced cooling, and potentially much more locally in the northern and eastern rim of the Bay. The rather coarse ocean resolution model used in the chapter 2 simulates rather accurately the contrasted TC-induced cooling amplitude between pre- and post-monsoon, suggesting that the 1/2° resolution is sufficient to capture the TC-induced mixing, a dominant process in the cold wake formation. Refined resolution in the BoB within our global model (Biastoch et al., 2008) or the use of high-resolution regional models (Diansky et al., 2006; Benshila et al., 2014) may however be required to better represent the TC-induced Ekman suction that shoals the thermocline near the eye, increasing the cooling efficiency of vertical mixing (Yablonsky and Ginis, 2009; Jullien et al., 2012). Although presumably of secondary importance (Jacob and Koblinsky, 2007; Jourdain et al., 2013), a realistic parametrization of the TCs-related precipitation may as well improve the TC-induced ocean response, by accounting for their stabilizing effect on the water column. As shown by Jourdain et al. (2013), this stabilizing effect may reduce the cooling amplitude by 5 to 10% in the Bay, hence reducing the model TC-induced cooling overestimation (Figure 2.6).

A significant increase in the horizontal and vertical resolutions of the model together with an improved representation of river discharge and precipitation patterns within the Bay (Papa et al., 2010) may also allow a better representation of the mixed layer and the offshore export of coastal freshwaters. The model underestimation of the freshening in the northern BoB during the post-monsoon season indeed probably results in an underestimation of the salinity influence on the TC-induced surface cooling. Estimates derived from the observed climatology however suggest that at least 50% of the reduction in TC-induced cooling amplitude may be related to thermal changes (Figure 2.10). The exact quantification of the influence of salinity may require a more exhaustive and in-depth analysis of oceanic controls on TC-induced cooling within the Bay using observations. The Argo program (Gould et al., 2004) provides a unique opportunity to investigate this issue: started in 2002, this program has reached its targeted density in late 2006. The availability of both temperature and salinity profiles in the upper ocean with reasonable temporal and spatial coverage may allow quantifying the respective contributions of salinity and temperature stratification on TC-induced cooling inhibition from in-situ observations over the recent period.

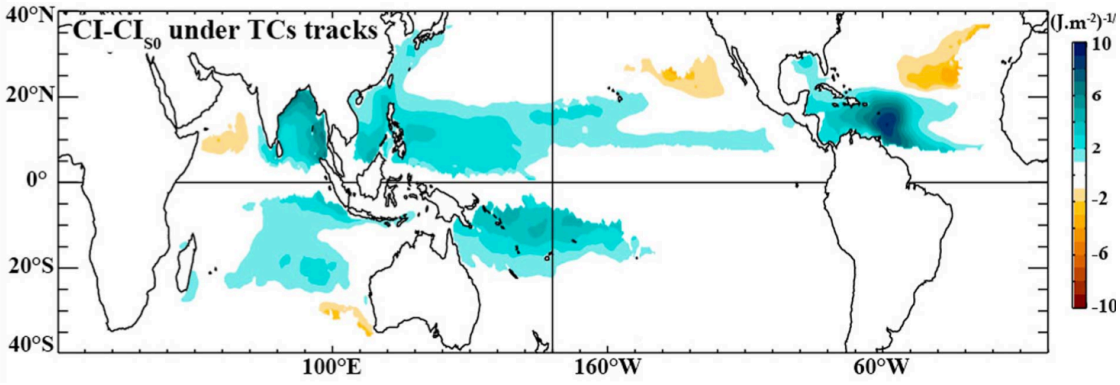

Figure 6.1: Spatial distribution of the difference between average standard CI underneath TCs tracks (in $(J.m^{-2})^{-1/3}$) minus CI_{S0} calculated over the 1978-2007 period. Both quantities are estimated from the weekly average stratification model outputs, within 200km and between 10 days and 3 days before each cyclone eye passage location. This plot indicates where salinity stratification inhibits (blue shades) or enhances (red shades) TC-induced cooling.

Chapter 2 brings further evidence of the haline stratification impact on TC-induced surface cooling. Neglecting haline stratification indeed results in a 50% overestimation of the TC-induced cooling during the post-monsoon season in the BoB. Figure 6.1 shows the spatial distribution of the long-term average impact of salinity stratification on the pre-cyclone cooling inhibition. Figure 6.1 hence provides a global view of regions where salinity stratification may significantly influence the TC-induced SST cooling. Since TCs mostly develop in deep atmospheric convection regions, the associated climatological rainfall results in a stable haline stratification that inhibits TC-induced cooling, explaining the dominance of negative values in Figure 6.1. While the BoB, studied in this work, is associated with a rather strong influence of haline stratification on TC-induced cooling, there is also a moderate influence of haline stratification in the western Pacific and South Indian Ocean TC basins. But there is a very clear influence of haline stratification on TC-induced cooling in the low-salinity region due to the discharge from the Amazon and Orinoco rivers whose waters are advected northwestward by the North Brazilian and Guyana Currents (Muller-Karger et al., 1995; Hellweger and Gordon, 2002). Given that TC that transit over this area can hit densely populated regions of Mexico and Southeastern United States (Weinkle et al., 2012), this region probably deserves a dedicated study.

Vertical mixing and upwelling generated by TCs in the BoB also trigger a very intense biological response in the western part of the Bay, giving rise to phytoplankton blooms by bringing nutrients such as nitrate and phosphate in the upper layers (Nayak et al., 2001; Madhu et al., 2002 ; Vinayachadran and Mathew, 2003; Reddy et al., 2008 ; Nagamani et al., 2011), the offshore extent and the intensity of the bloom strongly varying from one storm to another (Vinayachadran and Mathew, 2003). Maneesha et al.

(2011) further suggested that the impact of TCs is also noticed up to the fishery productions, with a 40% increase of the fish catches during the 2007 post-monsoon relative to 2006, in response to cyclone Sidr that considerably increased phytoplankton biomass and hence food availability. The phytoplankton bloom reported in these studies may have a considerable importance, as the BoB is a region of very low productivity compared to the Arabian Sea. However, the restricted number of TCs investigated by these authors prevents them from providing a quantitative estimate of the respective influence of haline and thermal stratification and TCs winds intensity on the amplitude of the TC-induced bloom. It could be interesting to repeat the numerical strategy proposed in Chapter 2 but using a regional model that couples a physical model such as NEMO to a biogeochemical component such as PISCES (Aumont and Bopp, 2006). Such a simulation should allow assessing the surface chlorophyll response to TCs forcing in this region and to quantify the importance of changes in subsurface oceanic stratification on the diversity of surface chlorophyll response observed in the wake of TCs. These TCs-related phytoplankton bloom may also have a considerable importance on the productivity in the BoB, a region of relatively low productivity compared to the Arabian Sea. This simulation can further be used to quantify the impact of TCs on the seasonal productivity in the Bay.

6.2.2 Influence of air-sea coupling on BoB TCs

Results from our $1/4^{o}$ regional coupled model discussed in Chapter 3 indicate that the impact of air-sea coupling is largest for the strongest simulated TCs developing in the BoB. Because of the very warm SST in the BoB, the TC-induced ocean cooling translates into a stronger reduction of inner-core upward enthalpy fluxes (~200W.m^{-2} for Category 2 TCs) due to Clausius-Clapeyron, and hence a large impact on the TC

intensification rate. As for other modelling studies on air-sea coupling impact on TCs statistics (Jullien et al., 2014; Ogata et al., 2015), the rather coarse resolution of our model (1/4°) does not allow to simulate the strongest TCs (Category 3 and above) that have the most devastating impact.

The ability of a model to simulate a realistic TC intensity distribution (including the strongest observed TCs) relies on the model horizontal resolution, and also on the choice of the convective parmeterization used. Convective rainfall in atmospheric models is simulated through implicit convective parameterization scheme and explicit microphysics scheme. A realistic simulation of TCs rainfall and related winds is complex for mesoscale atmospheric models with a grid resolution of a few tens of kilometres, as the one used in the present study, as it depends on a precise balance between implicit and explicit convective schemes that work simultaneously. As suggested by Samson et al. (2014), a rather coarse resolution model can simulate strong TCs intensity but for wrong reasons. That the Kain-Fritsch convective scheme allows simulating stronger TCs compared to the Bett-Miller-Janjic scheme is a resultant of the fact that this paramerization is over reactive to the environmental forcing in a destabilized atmospheric column. This could explain the overestimation of the number of tropical convective disturbances, as the case with KF-CPL simulation. Thus the better performance of the KF scheme in simulating the strong TCs as compared to BMJ is likely due to its overactive nature rather than the convective parameterization being better.

Whatever the convective parameterization, our 25km model resolution is not sufficient enough to realistically simulate the strongest TCs. At this resolution, the sharp eyewall

tangential winds structure is too smooth and the strongest eyewall updrafts and compensating subsidences, which contribute to the hydrostatic reduction of pressure within the eye, are underestimated (Gentry and Lackmann, 2010). Numerous studies using similar horizontal resolution in their atmospheric models reported similar findings (e.g. Zhao et al., 2009; Murakami et al., 2012). Increasing resolution leads to improved simulation of intense TCs (e.g. Murakami et al., 2012; Manganello et al., 2012). This is evident from the study of Manganello et al. (2012) that the 10-km resolution ECMWF Integrated Forecast System simulates more realistically the global TC frequency and TC intensity distribution. To obtain more realistic extreme TC distribution, recent studies hence suggest that an atmospheric model with finer resolution of ~10km is needed to assess the impact of air-sea coupling on strongest TCs (Jung et al., 2012; Manganello et al., 2012; Satoh et al., 2012; Murakami et al., 2015).

A 10 km-resolution version of the current IO regional coupled model would currently be computationally too expensive to allow performing long experiments. Increasing the model resolution hence also requires reducing the model domain to obtain a reasonable computational cost. As a next step, it is planned to develop a 10km resolution regional air-sea coupled model using the same oceanic and atmospheric components focused over the BoB. This would allow simulating the most intense TCs observed over the BoB, where they are known to have catastrophic impacts. With this higher-resolution coupled model, it is then planned to apply a similar strategy as in our coupled model study to analyse the impact of air-sea coupling on strongest TCs in the BoB. This configuration can also be used to perform ensemble of coupled and forced sensitivity experiments for selected case studies to better understand the coupled mechanisms at stake in the TCs intensification in this region. Cases corresponding to strong cyclones

with landfall other India can be selected in order to investigate their predictability, and how air-sea coupling influences them. At 1/10° resolution, the ocean component will also resolve the intense mesoscale eddy variability in the BoB, which will allow to specifically address the impact of warm oceanic eddies on TC intensification and its evolution by adding/removing warm subsurface anomalies in the pre-storm ocean initial conditions. Another perspective will also be to address the specific impact of salinity stratification by shutting down the impact of salinity in the ocean mixing parametrisation.

6.2.3 Towards improved operational statistical models for TCs intensity prediction

Chapter 5 demonstrated that using non-linear schemes with a relevant oceanic parameter considerably improves the forecast skill relative to the widely-used linear models using TC heat potential in all basins. It must however be noted that the skill improvement arising from the use of non-linear models (10 to 15% globally) is far larger than the one arising from the inclusion of a suitable oceanic metric (up to 2% globally). Chapter 5 hence clearly demonstrates that operational TCs forecast centres should replace their commonly-used linear statistical prediction schemes with non-linear statistical prediction schemes. Our preliminary results suggest that the SVM non-linear scheme yields the largest skill improvement. Although the inclusion of a suitable oceanic metric generally modestly improve non-linear models skill, this inclusion requires the models to be trained over a shorter period, as oceanic reanalyses are generally more reliable over the satellite era (1993 onwards) thanks to sea-level assimilation and more reliable satellite-derived wind stress forcing. This reduction of the dataset length results in a ~5% degradation of the non-linear models performance, which generally overcome the ~2% improvement yielded by including oceanic

parameters. At this stage, it may hence be more efficient to use non-linear models trained over a long period using only TCs characteristics and environmental atmospheric parameters as input, rather than using use non-linear models trained over a shorter period and including an additional oceanic parameter. In principle, however, our results demonstrate the potential added value from using oceanic predictors. Research to take advantage of the longer training period of atmospheric parameters, but to add oceanic parameters during a second training over a shorter period may hence provide a way for further improvements.

While our results strongly suggest that using the SVM scheme discussed in Chapter 5 has the potential to improve operational statistical forecasts skill, but further significant improvements to the current model version can still be obtained. First, a very crude tuning of the optimization parameters of the SVM scheme was performed and exploring the full parameter space should allow to further improve the model performance. Second, since the initial TC characteristic parameters explain a major part of the model skill, additional TC characteristic predictors proposed in the literature (DeMaria et al., 2005; Lee et al., 2015) could also be tested, including initial maximum winds times previous 12 hr intensity change and rate of change of maximum winds in the previous 12 hr etc. I should also test the added value of including other large-scale atmospheric predictors recently proposed in the literature (Lee et al. 2015) but not considered in our model architecture, such as the divergence at 200hPa. Once these steps completed, a thorough assessment of the model skill in real forecast mode should be performed by testing the model using predictors derived from forecasted TC tracks and large-scale environmental parameters predicted from atmospheric forecast models. These skills should hence be compared to the skill of the current operational system used in the

different basins. As a final step, this new scheme should be implemented operationally in the centres responsible for the TCs prediction, especially to the Indian Meteorological Department for the Northern Indian Ocean.

References

Aberson SD (1998), Five-day tropical cyclone track forecasting in the North Atlantic Basin, *Wea. Forecasting,* 13, 1005-15.

Aguilar-Martinez S and WW Hsieh (2009), Forecasts of tropical pacific sea surface temperatures by neural networks and support vector regression. *International Journal of Oceanography*, 13, http://dx.doi.org/10.1155/2009/167239.

Akhil VP, F Durand, M Lengaigne, J Vialard, MG Keerthi, VV Gopalakrishna, C Deltel, F Papa and C de Boyer Montégut (2014), A modeling study of the processes of surface salinity seasonal cycle in the Bay of Bengal, *J. Geophys. Res. Oceans*, 119, 3926–3947, doi:10.1002/2013JC009632.

Alam MM, MA Hossain, and S Shafee (2003), Frequency of Bay of Bengal cyclonic storms and depressions crossing different coastal zones, *Int. J. Climatol.*, 23, 1119–1125.

Ali MM, CM Kishtawal and J Sarika (2007), Predicting cyclone tracks in the north Indian Ocean: An artificial neural network approach, *Geophys. Res. Lett.*, 34, doi:10.1029/2006GL028353.

Ali MM, D Swain, RA Weller (2004), Estimation of ocean sub- surface thermal structure from surface parameters: a neural net- work approach, *Geophys. Res. Lett.,* 31, L20308, doi: 10.1029/2004GL021192.

Ali MM, PSV Jagadeesh, II Lin, JY Hsu (2012), A neural network approach to estimate tropical cyclone heat potential in the Indian Ocean, IEEE *Geoscience and Remote Sensing Letters*, 9, 1114–1117, doi: 10.1109/LGRS.2012.2190491.

Ali MM, PSV Jagadeesh, S Jain (2007), Effects of eddies on Bay of Bengal cyclone intensity, *Eos Trans*., 88, 93-95.

Antonov JI, D Seidov, TP Boyer, RA Locarnini, AV Mishonov, HE Garcia, OK Baranova, MM Zweng, and DR Johnson (2010), World Ocean Atlas 2009, Volume 2: Salinity. S. Levitus, Ed. NOAA Atlas NESDIS 69, U.S. Government Printing Office, Washington, D.C., 184 pp.

Antonov JI, RA Locarnini, TP Boyer, AV Mishonov and HE Garcia (2006), World Ocean Atlas 2005, Volume 2: Salinity. S. Levitus, Ed. NOAA Atlas NESDIS 62, U.S. Government Printing Office, Washington, D.C., 182 pp.

Anwar A (1999), Climate change impacts and adaptation assessment in Bangladesh. *Climate Res*., 12, 109-16.

Aumont O and L Bopp (2006), Globalizing results from ocean in situ iron fertilization studies, *Glob. Biogeochem. Cy.*, 20, GB2017, doi:10.1029/2005GB002591.

Axell LB (2002), Wind-driven internal waves and langmuir circulations in a numerical ocean model of the southern baltic sea, *J. Geophys. Res.,* 107, doi:10.1029/2001JC000922.

Balaguru K (2016), Global warming-induced upper-ocean freshening and the intensification of super typhoons, *Nat. Commun.,* 7, 13670 doi: 10.1038/ncomms13670.

Balaguru K, P Chang, R Saravanan, LR Leung, Z Xu, M Li *and* J-S Hsieh *(*2012*),* Ocean barrier layers' effect on tropical cyclone intensification*, PNAS,* 109*, 36,* 14343–14347*, doi:10.1073/pnas.1201364109.*

Balaguru K, S Taraphdar, LR Leung and GR Foltz (2014), Increase in the intensity of postmonsoon Bay of Bengal tropical cyclones, *Geophys. Res. Lett*., 41, 3594–3601, doi:10.1002/2014GL060197.

Bao JW, JM Wilczak, JK Choi, and LH Kantha (2000), Numerical simulations of air-sea interaction under high wind conditions using a coupled model: A study of hurricane development, *Mon. Wea. Rev*., 128, 7, 2190-2210.

Behera SK, AA.Deo and PS Salvekar (1998), Investigation of mixed layer response to Bay of Bengal cyclone using a simple ocean model, *Meteorol. Atmos. Phys*., 65, 77–91.

Bender MA and I Ginis (2000), Real-case simulations of hurricane-ocean interaction using a high-resolution coupled model: Effects on hurricane intensity, *Mon. Wea. Rev.,* 128, 917-946.

Bender MA, I Ginis and Y Kurihara (1993), Numerical simulations of tropical cyclone-ocean interaction with a high-resolution coupled model. *J. Geophys. Res. (Atmos)*, 98, D12, 23245– 23263.

Bender MA, I Ginis, R Tuleya, B Thomas, T Marchok (2007), The operational GFDL coupled hurricane–ocean prediction system and a summary of its performance, *Mon. Wea. Rev.*, 135, 3965–3989.

Benshila R, F Durand, S Masson, R Bourdalle-Badie, C De Boyer Montegut, F Papa and G Madec (2014), The upper Bay of Bengal salinity structure in a high-resolution model, *Ocean Modelling*, 74, 36-52.

Barron AR (1993), Universal approximation bounds for superpositions of a sigmoidal function, *IEEE Transactions on Information Theory*, 39, 3, 930-945, doi: 10.1109/18.256500.

Biastoch A, CW Boning, J Getzlaff, J–M. Molines and G Madec (2008), Causes of interannual-decadal variability in the meridional overturning circulation of the midlatitude North Atlantic ocean, *J. Clim.*, 21, 6599-6615, doi:10.1175/2008JCLI2404.1.

Bishop CM (1995), Neural Networks for Pattern Recognition. Oxford University Press, Inc., New York, NY, 500p.

Blanke B, and P Delecluse (1993), Variability of the tropical Atlantic ocean simulated by a general circulation model with two different mixed layer physics, *J. Phys. Oceanogr.*, 23, 1363-1388.

Brennan MJ, CC Hennon and RD Knabb (2009), The operational use of QuikSCAT ocean surface vector winds at the National Hurricane Center, *Wea. Forecasting*, 24, 3, 621–645, doi:10.1175/ 2008WAF2222188.1.

Brodeau L, B Barnier, A-M Treguier, T Penduff and S Gulev (2010), An ERA40-based atmospheric forcing for global ocean circulation models, *Ocean Modelling*, 31, 3-4, 88-104, doi:10.1016/j.ocemod.2009.10.005.

Buarque SR, C Vanroyen and C Agier (2009), Tropical cyclone heat potential index revisited, *Mercator Ocean Q. Newsl*., 33, 24–30.

Burchard H (2002), Energy-conserving discretisation of turbulent shear and buoyancy production, *Ocean Modelling,* 4, 347–361, doi:10.1016/S1463-5003(02)00009-4.

Byju P, SP Kumar (2011), Physical and biological response of the Arabian Sea to tropical cyclone Phyan and its implications, *Mar. Environ. Res*., 71, 325−330.

Camargo SJ, AH Sobel, AG Barnston, KA Emanuel (2007b), Tropical cyclone genesis potential index in climate models, *Tellus*, 59A, 428–443.

Camargo SJ, KA Emanuel, AH Sobel (2007a), Use of a genesis potential index to diagnose ENSO effects on tropical cyclone genesis, *J. Clim.,* 20, 4819–4834.

Camargo SJ, MC Wheeler, AH Sobel (2009), Diagnosis of the MJO modulation of tropical cyclogenesis using an empirical index, *J. Atmos. Sci.*, 66, 3061–3074.

Cangialosi JP and JL Franklin (2014), 2013 National Hurricane Center Forecast Verification Report, NOAA/NWS/NCEP/National Hurricane Center. [Available online at www.nhc.noaa.gov/verification/pdfs/Verification_2013.pdf].

Chaitanya VS, M Lengaigne, J Vialard, VV Gopalakrishna, F Durand, C KranthiKumar, S Amritash, V Suneel, F Papa and M Ravichandran (2014), Salinity Measurements Collected by Fishermen Reveal a "River in the Sea" Flowing Along the Eastern Coast of India, *Bull. Amer. Meteoro. Soc*., 95, 1897-1908, doi:10.1175/BAMS-D-12-00243.1.

Chang SW and RA Anthes (1979), Mutual response of the tropical cyclone and the ocean. *Journal of Physical Oceanography*, 9, 1, 128–135.

Charney JG and A Eliassen (1964), On the growth of the hurricane depression, *J. Atmos. Sci.*, 21, 68–75.

Chatterjee A, D Shankar, SSC Shenoi, GV Reddy, GS Michael, M Ravichandran, VV Gopalkrishna, EP Rama Rao, TVS Udaya Bhaskar and VN Sanjeevan (2012), A New Atlas of Temperature and Salinity for the North Indian Ocean, *J. Earth Syst. Sci*., 121, 3, 559-593.

Chaudhuri S and A Middey (2011), Adaptive neuro-fuzzy inference system to forecast peak gust speed during thunderstorms. *Meteorol. Atmos. Phys*., 114, 139-149.

Chaudhuri S, D Dutta, S Goswami and A Middey (2015), Track and intensity forecast of tropical cyclones over the North Indian Ocean with multilayer feed forward neural nets, *Meteorol. Appl*., doi:10.1002/met.1488.

Chen F, K Mitchell, J Schaake, Y Xue, H-L Pan, V Koren, QY Duan, M Ek and A Betts (1996), Modeling of land surface evaporation by four schemes and comparison with FIFE observations, *J. Geophys. Res.*, 101, D3, 7251-7268, doi:10.1029/95JD02165.

Chen G and CY Tam (2010), Different impacts of two kinds of Pacific Ocean warming on tropical cyclone frequency over the western North Pacific, *Geophys. Res. Lett.,* 37, L01803, doi:10.1029/2009GL041708.

Chen JY and BJ Adams (2006), Integration of artificial neural networks with conceptual models in rainfall-runoff modelling, *J. Hydrol.,* 318, 232–249.

Chen X, JL Wu and L Wang (2005), Prediction of climate change impacts on streamflow of lake bosten using artificial neural network model (in Chinese), *J. Lake Sci*., 17, 207–212.

Chiang TL, CR Wu and LY Oey (2011), Typhoon Kai-Tak: An ocean's perfect storm, *J. Phys. Oceanogr.,* 41, 221–233, doi:10.1175/ 2010JPO4518.1.

Chinthalu GR, P Seetaramayya, M Ravindran and PN Mahajan (2001), Response of the Bay of Bengal to Gopalpur and Paradip Super Cyclones during 15–31 October, 1999, *Curr. Sci.*, 81, 283–291.

Chou M and M Suarez (1999), A solar radiation parameterization for atmospheric studies, Tech Rep NASA/TM-1999-104606, NASA/GSFC.

Chu J-H (1994), A regression model for the western North Pacific tropical cyclone intensity forecasts, NRL Memo. Rep, 7541-94-7215, Naval Research Laboratory, 33 pp. [Available from Naval Research Laboratory, 7 Grace Hopper Avenue, Monterey, CA 93943-5502]

Cione JJ (2015), The relative roles of the ocean and atmosphere as revealed by buoy air-sea observations in hurricanes, *Mon. Wea. Rev*., 143, 3, 904-912, doi:10.1175/MWR-D-13-00380.1.

Cione JJ and EW Uhlhorn (2003), Sea surface temperature variability in hurricanes: Implications with respect to intensity change. *Mon. Wea. Rev., 131*, 1783–1796.

Cione JJ, PG Black and SH Houston (2000), Surface Observations in the Hurricane Environment, *Mon. Wea. Rev.,* 128, 1550–1561.

Clifford SF, B Subrahmanyam, VSN Murty (2013), ENSO-modulated cyclogenesis over Bay of Bengal, *J. Clim*., 26, 9806–9818.

Cortes C, V Vapnik (1995), Support-vector networks. Machine Learning, 20, 3, 273–297. doi: 10.1007/BF00994018.

Cuypers Y, XLe Vaillant, P Bouruet-Aubertot, J Vialard, M McPhaden (2013), Tropical storm-induced near inertial internal waves during the Cirene experiment: energy fluxes and impact on vertical mixing, *J. Geophys. Res.,* 118**,** 358-380**.**

D'Asaro EA (2003), The ocean boundary layer below Hurricane Dennis, *J. Phys. Oceanogr.,* 33, 561–579.

D'Asaro EA, TB Sanford, PP Niiler and EJ Terrill (2007), Cold wake of Hurricane Frances, *Geophys. Res. Lett.,* 34, L15609, doi:10.1029/2007GL030160.

Dai A and KE Trenberth (2002), Estimates of freshwater discharge from continents: Latitudinal and seasonal variations. *J. Hydrometeorol.*, 3, 660-687

Dare RA and JL McBride (2011), Sea surface temperature response to tropical cyclones. *Mon. Wea. Rev.,* 139, 3798–3808.

Das Y, UC Mohanty, I Jain, M Subba Rao and ASN. Murty (2014), Modeling on the Aspects of Thermal Response of Bay of Bengal to Tropical Cyclone TC05B 1999 using Princeton Ocean Model (POM): Preliminary Results, *American Journal of Modeling and Optimization*, 2, 2, 47-59, doi: 10.12691/ajmo-2-2-2.

De Boyer Montégut C, G Madec, AS Fischer, A Lazar, and D Iudicone (2004), Mixed layer depth over the global ocean: an examination of profile data and a profile-based climatology, *J. Geophys. Res.,* 109, C12003. doi:10.1029/2004JC002378.

De Boyer Montégut C, J Mignot, A Lazar and S Cravatte (2007b), Control of salinity on the mixed layer depth in the world ocean. Part I: general description, *J. Geophys. Res.*, 112, C06011, doi:10.1029/2006JC003953.

De Boyer Montégut C, J Vialard, SSC Shenoi, D Shankar, F Durand, C Ethé and G Madec (2007a), Simulated Seasonal and Interannual Variability of the Mixed Layer Heat Budget in the Northern Indian Ocean, *J. Clim.,* 20, 3249-3268.

Dee DP, SM Uppala, AJ Simmons et al. (2011), The ERA-Interim reanalysis: Configuration and performance of the data assimilation system, *Q. J. Roy. Meteorol. Soc.*, 137, 656, 553–597.

Delcroix T, A Dessier, Y Gouriou and M McPhaden (2005), Time and space scales for sea surface salinity in the tropical oceans. *Deep Sea. Res.*, *52*, 787–813.

DeMaria M (1996), The effect of vertical shear on tropical cyclone intensity change, *J. Atmos. Sci.,* 53, 2076–2087.

DeMaria M (2009), A simplified dynamical system for tropical cyclone intensity prediction, *Mon. Wea. Rev*., 137, 68-82.

DeMaria M (2010), Tropical cyclone intensity change predictability estimates using a statistical-dynamical model, 29th AMS conference on hurricanes and tropical meteorology, Tucson, AZ. 5 pp. (Available on-line at https://ams.confex.com/ams/pdfpapers/167916.pdf)

DeMaria M and J Kaplan (1994a), A statistical hurricane intensity prediction scheme (SHIPS) for the Atlantic basin, *Wea. Forecasting*, 9, 209 220.

DeMaria M and J Kaplan (1994b), Sea surface temperature and the maximum intensity of Atlantic tropical cyclones, *J. Climate*, 7, 1324–1334.

DeMaria M and J Kaplan (1999), An updated statistical hurricane intensity prediction scheme (SHIPS) for the Atlantic and eastern north Pacific basins, *Wea. Forecasting*, 14, 326-337.

DeMaria M, CR Sampson, JA Knaff, KD Musgrave (2014), Is tropical cyclone intensity guidance improving? *Bull. Amer. Meteor. Soc*., 95, 387-398.

DeMaria M, JA Knaff and CR Sampson (2007), Evaluation of long-term trend in tropical cyclone intensity forecasts, *Meteor. Atmos Phy*., 97, 19-28.

DeMaria M, M Mainelli, LK Shay, JA Knaff and J Kaplan (2005), Further Improvements in the Statistical Hurricane Intensity Prediction Scheme (SHIPS), *Wea. Forecasting*, 20, 531-543.

Deo AA, DW Ganer and PS Salvekar (2006a), Sensitivity of oceanic mixed layer to different model resolutions in response to Indian Ocean cyclone, *J. Ind. Geophys. Union*, 10, 2, 87–100.

Deo AA, DW Ganer and PS Salvekar (2006b), Oceanic mixed layer variation during the movement of cyclone along symmetric tracks in the Indian Ocean, *Indian J. Mar. Sci.,* 35, 2, 111–122.

Deo AA, DW Ganer and PS Salvekar (2012), Simulation of ocean upper layer response to moving Indian Ocean cyclone using reduced gravity ocean model, *Mar. Geod*., 35, 121–140.

Diansky NA, VB Zalesny, SN Moshonkin and AS Rusakov (2006), High resolution modeling of the monsoon circulation in the Indian Ocean, *Oceanology*, 46, 608–628.

Dickey TD and JJ Simpson (1983), The sensitivity of the upper ocean structure to time varying wind direction, *Geophy. Res. Lett*., 10, 2, 133-136.

Donelan MA, BK Haus, N Reul, WJ Plant, M Stiassnie, HC Graber, OB Brown and ES Saltzman (2004), On the limiting aerodynamic roughness of the ocean in very strong winds, *Geophys. Res. Lett.,* 31, L18306, doi:10.1029/2004GL019460.

Drévillon M et al. (2008), The GODAE/Mercator-Ocean global ocean forecasting system: results, applications and prospects, *Journal of Operational Oceanography*, 1, 51-57.

Dunion JP and CS Velden (2004), The impact of the Saharan air layer on Atlantic tropical cyclone activity, *Bull. Amer. Meteor. Soc.*, 85, 3, 353-365, doi:10.1175/BAMS-85-3-353.

Durand F, D Shankar, F Birol, SSC Shenoi (2009), Spatio-temporal structure of the East India Coastal current from satellite altimetry, *J. Geophys. Res.,* 114, C02013.

Dvorak VF (1975), Tropical cyclone intensity analysis and forecasting from satellite imagery, *Mariners Weather Log*., 19, 4, 199–206.

Dvorak VF (1984), Tropical cyclone intensity analysis using satellite data, NOAA Tech. Rep. 11, 45 pp.

Elbisy MS (2015), Sea Wave Parameters Prediction by Support Vector Machine Using a Genetic Algorithm, *Journal of Coastal Research*, 31, 4, 892 –899.

Elshorbagy A and K Parasuraman (2008), On the relevance of using artificial neural networks for estimating soil moisture content, *J. Hydrol*. 362, 1-18.

Elsner JB, JP Kossin and TH Jagger (2008), The increasing intensity of the strongest tropical cyclones. *Nature*, 455, 92–95.

Emanuel K (2003), Tropical cyclones, *Annu. Rev. Earth Planet. Sci.,* 31, 75-104.

Emanuel K (2007), Environmental factors affecting tropical cyclone power dissipation, *J. Climate*, 20, 5497-5509.

Emanuel KA (1986), An air-sea interaction theory for tropical cyclones. Part 1 : Steady-state maintenance, *J. Atmos. Sci*., 43, 6, 585–604.

Emanuel KA (1988), The maximum intensity of hurricanes, *J. Atmos. Sci*., 45, 1143–1155.

Emanuel KA, JD Neelin and CS Bretherton (1994), On large-scale circu- lations in convecting atmospheres, *Quarterly Journal of the Royal Meteorological Society*, 120, 519, 1111–1143.

Emanuel KA (1995), Sensitivity of tropical cyclones to surface exchange coeffi- cients and a revised steady-state model incorporating eye dynamics, *J. Atmos. Sci*., 52, 3969–3976.

Emanuel KA (1999), Thermodynamic control of hurricane intensity, *Nature*, 401, 665-669 .

Emanuel KA (2005), Increasing destructiveness of tropical cyclones over the past 30 years, *Nature,* 436, 686–688.

Emanuel KA (2006), Climate and tropical cyclone activity : A new model downscaling approach, *Journal of Climate*, 19, 19, 4797–4802.

Emanuel KA, C DesAutels, C Holloway, R Korty (2004), Environmental control of tropical cyclone intensity, *J. Atmos. Sci*., 61, 843–858.

Emanuel KA, DS Nolan (2004), Tropical cyclone activity and global climate, *26th Conf. on Hurricanes and Tropical Meteorology*, Miami, FL, Amer. Meteor. Soc., 240–241.

Evan AT and SJ Camargo (2011), A climatology of Arabian Sea cyclonic storms. *J. Clim.*, 24, 140-158, doi: 10.1175/2010JCLI3611.1.

Evan AT, JP Kossin, C Chung and V Ramanathan (2011), Arabian Sea tropical cyclones intensified by emissions of black carbon and other aerosols. *Nature*, 479, 94-97.

Fekete BM, CJ Vörösmarty and W Grabs (1999), Global Composite Runoff Fields Based on Observed River Discharge and Simulated Water Balances, Tech. Rep. 22, Global Runoff Data Cent., Koblenz, Germany.

Ferry N, L Parent, G Garric, C Bricaud, CE Testut, OLe Galloudec, JM Lellouche, M Drévillon, E Greiner, B Barnier, JM Molines, N Jourdain, S Guinehut, C Cabanes and L Zawadzki (2012), Reanalysis of the Altimetric Era (1993-2009) at Meso Scale, Mercator Ocean Quarterly Newsletter, 44.

Fine TL (1999), Feedforward neural network methodology. Springer-Verlag, New York; 356p.

Frank WA and EA Ritchie (2001), Effects of vertical wind shear on the intensity and structure of numerically simulated hurricanes, *Mon. Wea. Rev*., 129, 2249–2269.

Frank WA and EA Ritchie EA (1999), Effects of environmental flow upon tropical cyclone structure, *Mon. Wea. Rev*., 127, 2044-2061.

Gadgil S, PV Joseph, NV Joshi (1984), Ocean atmosphere coupling over monsoon regions, *Nature*, 312, 141145.

Gentry MS and G Lackmann (2010), Sensitivity of simulated tropical cyclone structure and intensity to horizontal resolution. *Mon. Wea. Rev.,* 138, 688–704.

Girishkumar MS and M Ravichandran (2012), The influences of ENSO on tropical cyclone activity in the Bay of Bengal during October–December, *Geophys. Res. Lett*., 117, C02033, doi: 10.1029/2011JC007417.

Girishkumar MS, K Suprit, J Chiranjivi, TVS Udaya Bhaskar, M Ravichandran, R Venkat Shesu and E Pattabhi Rama Rao (2014), Observed Oceanic response to tropical cyclone Jal from a moored buoy in the south-western Bay of Bengal, *Ocean Dyn.,* 64, 325-335, doi:10.1007/s10236-014-0689-6.

Girishkumar MS, VPT Prakash, M Ravichandran (2015), Influence of Pacific Decadal Oscillation on the relationship between ENSO and tropical cyclone activity in the Bay of Bengal during October-December, *Clim. Dyn.,* 44, 3469–3479.

Goni G et al. (2009), Applications of satellite-derived ocean measurements to tropical cyclone intensity forecasting, *Oceanography*, 22, 190-197.

Goni GJ and JA Trinanes (2003), Ocean thermal structure monitoring could aid in the intensity forecast of tropical cyclones. *EOS, Trans. Amer. Geophys. Union,* 84, 573-580.

Gopalakrishna VV, VSN Murty, MSS Sarma and JS Sastry (1993), Thermal response of upper layers of Bay of Bengal to forcing of a severe cyclonic storm: A case study, *Indian J. Mar. Sci.*, 22, 8-11.

Gould J et al. (2004), Argo profiling floats bring new era of in situ ocean observations, *Eos Trans. AGU*, 85, doi:10.1029/2004EO190002.

Gray W and Emanuel K (2010), Introduction to tropical meteorology, chapter 8, *Tropical Cyclones*, COMET® Website at http:// meted.ucar.edu of the University Corporation for Atmospheric Research (UCAR).

Gray WM (1968), A global view of the origin of tropical disturbances and storms. *Mon. Wea. Rev.* 96, 669-700.

Gray WM (1975), Tropical cyclone genesis, Atmospheric Science Paper, 234, Colorado State University, Ft. Collins, CO, 121 pp.

Gray WM (1979), Hurricanes: Their formation, structure and likely role in the tropical circulation. Meteorology over Tropical Oceans, D. B. Shaw, Ed., Royal Meteorological Society, 155–218.

Griffies S et al. (2009), Coordinated ocean-ice reference experiments (COREs), *Ocean Modelling,* 26, 1–46, doi:10.1016/j.ocemod.2008.08.007.

Halliwell GR, LK Shay, J Brewster and WJ Teague (2011), Evaluation and sensitivity analysis to an ocean model response to hurricane Ivan, *Mon. Wea. Rev*., 139, 921-945.

Halliwell GR, S Gopalakrishnan, F Marks, D Willey (2015), Idealized study of ocean impacts on tropical cyclone intensity forecasts *Mon. Wea. Rev*. 143, 1142-1165, doi: 10.1175/MWR-D-14-00022.1.

Harenduprakash LL and AK Mitra (1988), Vertical turbulent mass flux below the sea surface and air-sea interaction: monsoon region of the Indian ocean, *Deep Sea Res.*, 43, 8, 1423-1451.

Hawkins HF and SM Imbembo (1976), The Structure of a Small, Intense Hurricane-Inez 1966, *Monthly Weather Review*, 104, 418.

Hellweger FL and AL Gordon, (2002), Tracing Amazon River Water into the Caribbean Sea, *Journal of Marine Research*, 60, 4, 537-549.

Hennon CC, C Marzban, JS Hobgood (2005), Improving tropical cyclogenesis statistical model forecasts through the application of a neural network classifier. *Wea. Forecasting*, 20, 1073–1083.

Holland GJ (1980), An analytic model of the wind and pressure profiles in hurricanes, *Mon. Wea. Rev*., 108, 1212–1218

Holland GJ (1997), The maximum potential intensity of tropical cyclones, *J. Atmos. Sci*., 54, 2519-2541.

Hong S-Y and J-OJ Lim (2006), The WRF Single-Moment 6-Class Microphysics Scheme (WSM6), Asia-Pacific, *J. Atmos. Sci.,* 42, 2, 129–151.

Hong X, SW Chang, S Raman, LK Shay and R Hodur (2000), The interaction between Hurricane Opal (1995) and a warm core eddy in the Gulf of Mexico, *Mon. Wea. Rev.,* 128, 5, 1347-1365.

Hornik K, M Stinchcombe and H White (1989), Multilayer feedforward networks are universal approximators, *Neural Networks*, 2, 359–366.

Islam T and RE Peterson (2009), Climatology of land falling tropical cyclones in Bangladesh 1877–2003, *Nat. Hazard*, 48, 1, 115–135.

Ito K, T Kuroda and K Saito (2015), Forecasting a large number of tropical cyclone intensities around Japan using a high-resolution atmosphere-ocean coupled model, *Wea. Forecasting*, 30, 793–808, doi:10.1175/WAF-D-14-00034.1.

Jacob S and C Koblinsky (2007), Effects of precipitation on the upper-ocean response to a hurricane, *Mon. Wea. Rev.*, 135 (6), 2207–2225.

Jacob SD and LK Shay (2003), The role of oceanic mesoscale features on the tropical cyclone-induced mixed layer response: A case study, *J. Phys. Oceanogr.,* 33, 649–676.

Jacob SD, LK Shay, AJ Mariano and PG Black (2000), The 3D oceanic mixed layer response to Hurricane Gilbert, *J. Phys. Oceanogr.,* 30, 1407–1429, doi:10.1175/1520-0485(2000)030<1407:TOMLRT>2.0. CO;2.

Jaimes B and LK Shay (2009), Mixed layer cooling in mesoscale oceanic eddies during hurricanes katrina and rita. *Mon. Wea. Rev.*, 137(12): 4188–4207.

Janjic´ Z I (1994), The step-mountain Eta coordinate model: Further developments of the convection, viscous sublayer, and turbulence closure schemes, *Mon. Wea. Rev.,* 122, 5, 927–945, doi:10.1175/1520-0493(1994)122<0927:TSMECM>2.0.CO;2.

Jarvinen BR and CJ Neumann (1979), Statistical forecasts of tropical cyclone intensity for the North Atlantic basin, NOAA Tech. Memo, NWS NHC–10, 22 pp. [Available from NTIS, Technology Administration, U.S. Dept. of Commerce, Springfield, VA 22161]

Jayakumar A, J Vialard, M Lengaigne, C Gnanaseelan, JP McCreary and Praveen Kumar B (2011), Processes controlling the surface temperature signature of the Madden-Julian Oscillation in the thermocline ridge of the Indian Ocean. *Clim Dyn*. doi:10.1007/s00382-010-0953-5.

Jin, F-F, J Boucharel and II Lin (2014), Eastern Pacific tropical cyclones intensified by El Niño delivery of subsurface ocean heat, *Nature*, 516, 82–85.

Jourdain NC, B Barnier, N Ferry, J Vialard, CE Menkes, M Lengaigne and L Parent (2014), Tropical cyclones in two atmospheric (re)analyses and their response in two oceanic reanalyses, *Ocean Modell*ing, 73, 108–122, doi:10.1016/j.ocemod.2013.10.007.

Jourdain NC, M Lengaigne, J Vialard, G Madec, CE Menkes, EM Vincent, S Jullien, and B Barnier (2013), Observation-based estimates of surface cooling inhibition by heavy rainfall under tropical cyclones, *J. Phys. Oceanogr*., 43, 1, 205–221, doi:10.1175/JPO-D-12-085.1.

Jourdain NC, P Marchesiello, CE Menkes et al. (2011), Mesoscale Simulation of Tropical Cyclones in the South Pacific: Climatology and Interannual Variability, *J. Climate*, 24, 3–25, doi: 10.1175/2010JCLI3559.1

Jullien S, CE Menkes, P Marchesiello, NC Jourdain, M Lengaigne, A Koch-Larrouy, J Lefèvre, EM Vincent and V Faure (2012), Impact of tropical cyclones on the heat budget of the South Pacific Ocean. *J. Phys. Oceanogr.*, early online release , doi :10.1175/JPO-D-11-0133.1.

Jullien S, P Marchesiello, CE Menkes, J Lefèvre, NC Jourdain, G Samson and M Lengaigne (2014), Ocean feedback to tropical cyclones: Climatology and processes, *Clim. Dyn.,* 43, 9–10, 2831–2854.

Jung T and Coauthors (2012), High-resolution global climate simulations with the ECMWF model in Project Athena: Experimental design, model climate, and seasonal forecast skill, *J. Climate,* 25**,** 3155–3172.

Kain JS (2004), The Kain-Fritsch convective parameterization: An update, *J. Appl. Meteorol*, 43, 1, 170-181, doi:10.1175/1520-0450(2004)043<0170:TKCPAU>2.0.CO;2.

Kalsi SR and KB Srivastava (2006), Characteristic features of Orissa super cyclone of 29th October, 1999 as observed through CDR Paradip, *Mausam*, 57, 21-30.

Kaplan J, M DeMaria (2003), Large-scale characteristics of rapidly intensifying tropical cyclones in the North Atlantic basin, *Wea. Forecasting*, 18, 1093–1108.

Keerthi MG, M Lengaigne, J Vialard, C de Boyer Montegut and PM Muraleedharan (2013) Interannual variability of the Tropical Indian Ocean mixed layer depth, *Clim. Dyn.*, 40, 743-759, doi:10.1007/s00382-012-1295-2.

Kikuchi K, B Wang and H Fudeyasu (2009), Genesis of tropical cyclone Nargis revealed by multiple satellite observations, *Geophys. Res. Lett*., 36, L068, doi:10.1029/2009GL037296.

Kim HS, GA Vecchi, TR Knutson, WG Anderson, TL Delworth, A Rosati, F Zeng and M Zhao (2014), Tropical cyclone simulation and response to CO2 doubling in the GFDL CM2.5 high-resolution coupled climate model. *J. Clim.*, 27, 8034–8054, doi: 10.1175/jcli-d-13-00475.1.

Knaff JA and CR Sampson (2009), Southern Hemisphere tropical cyclone intensity forecast methods used at the Joint Typhoon Warning Center Part II: Statistical–dynamical forecasts, *Aust. Meteor. Oceanogr. J.,* 58, 9–18.

Knaff JA, CR Sampson and M DeMaria (2005), An operational Statistical Typhoon Intensity Prediction Scheme for the western North Pacific*, Wea. Forecasting*, 20, 688–699.

Knaff JA, M DeMaria, CR Sampson and JM Gross (2003), Statistical, five-day tropical cyclone intensity forecasts derived from climatology and persistence, *Wea. Forecasting*, 18, 80-92.

Knapp KR, JP Kossin (2007), New global tropical cyclone data set from ISCCP B1 geostationary satellite observations*, J. Appl. Remote Sens*., 1, 013505, doi: 10.1117/1.2712816.

Knapp KR, MC Kruk, DH Levinson, HJ Diamond and CJ Neumann (2010), The International Best Track Archive for Climate Stewardship (IBTrACS): Unifying Tropical Cyclone Data, *Bull. Amer. Meteor. Soc.,* 10, doi:10.1175/2009BAMS2755.1.

Knutson T et al. (2010), Tropical cyclones and climate change, *Nat. Geosci.,* 3, 157-163.

Kossin JP, KR Knapp, DJ Vimont, RJ Murnane and BA Harper (2007), A globally consistent reanalysis of hurricane variability and trends, *Geophys. Res. Lett*., 34, L04815. doi: 10.1029/ 2006GL028836.

Kossin JP, TL Olander , KR Knapp (2013), Trend analysis with a new global record of tropical cyclone intensity, *J. Climate*., 26, 9960–9976. doi: 10.1175/JCLI-D-13-00262.1.

Kotal SD, SK Roy Bhowmik, PK Kundu and AK Das (2008), A Statistical Cyclone Intensity Prediction (SCIP) Model for Bay of Bengal, *J. Earth Sys. Sci*., 117, 157-168.

Kotal SD, PK Kundu and SK Roy Bhowmik (2009), *Nat. Hazards*, 50, 389, https://doi.org/10.1007/s11069-009-9348-5.

Kucas ME (2010), Challenges of forecasting tropical cyclone intensity change at the Joint Typhoon Warning Center, Preprints, 29th Conf. on Hurricanes and Tropical Meteorology, Tucson, AZ, Amer. Meteor. Soc., 9C.6. [Available online at https://ams.confex.com/ams/pdfpapers/168732.pdf.]

Kurihara Y, RE Tuleya and MA Bender (1998), The GFDL hurricane prediction system and its performance in the 1995 hurricane season, *Mon. Wea. Rev.,*126**,** 1306–1322.

Large W and S Yeager (2009), The global climatology of an interannually varying air–sea flux data set, *Clim. Dyn.,* 33, 341–364.

Lee CY, MK Tippett, SJ Camargo, AH Sobel (2015), Probabilistic Multiple Linear Regression Modeling for Tropical Cyclone Intensity, *Mon. Wea. Rev.,* 143, 933–954. doi: http://dx.doi.org/10.1175/MWR-D-14-00171.1

Lee TL (2009), Prediction of typhoon storm surge using artificial neural network. Adv. Eng. Softw. 40, 1200–1206.

Leipper D and D Vogenau (1972), Hurricane heat potential of the Gulf of Mexico, *J. Phys. Oceanogr.*, 2, 218-224.

Leipper DF (1967), Observed Ocean Conditions and Hurricane Hilda, 1964, *J. Atmos. Sci.,* 24, 182–186, doi: 10.1175/1520-0469.

Lengaigne M, G Madec, CE Menkes and G Alory (2003), Impact of isopycnal mixing on the tropical ocean circulation, *J. Geophys. Res.*, 108, C11, 3345, doi:10.1029/2002JC001704.

Lengaigne M, U Haussmann, G Madec, C Menkes, J Vialard, JM Molines (2012) Mechanisms controlling warm water volume interannual variations in the equatorial Pacific: diabatic versus adiabatic processes, *Clim. Dyn.*, 38, 5, 1031-1046, doi 10.1007/s00382-011-1051-z.

Li Z, T Li, W Yu, K Li and Y Liu (2016), What controls the interannual variation of tropical cyclone genesis frequency over Bay of Bengal in the post monsoon peak season?, *Atmos. Sci. Lett.,*17,148-154.

Li Z, W Yu, T Li, VSN Murty and F Tangang (2013), Bimodal character of cyclone climatology in Bay of Bengal modulated by monsoon seasonal cycle. *J. Clim.,* 26, 1033-1046.

Lin GF, GR Chen, MC Wu and YC Chou (2009), Effective forecasting of hourly typhoon rainfall using support vector machines, *Water Resour. Res*., 45, W08440, doi:10.1029/2009WR007911.

Lin GF, PK Huang and HY Lin (2013), Forecasting tropical cyclone intensity change in the western North Pacific, *Journal of Hydroinformatics*, 15, 3, 952–966.

Lin II et al. (2003), New evidence for enhanced primary production triggered by tropical cyclone. *Geophys. Res. Lett*., 30, 1718, doi:10.1029/2003GL017141.

Lin II, CC Wu, IF Pun and DS Ko (2008), Upper-ocean thermal structure and the western North Pacific category-5 typhoons. Part I: Ocean features and category-5 typhoon's intensification, *Mon. Weather Rev.*, 136, 3288–3306, doi:10.1175/2008MWR2277.1.

Lin II, CC Wu, KA Emanuel, IH Lee, CR Wu and IF Pun (2005) The interaction of Supertyphoon Maemi (2003) with a warm ocean eddy, *Mon. Wea. Rev.*, 133, 2635–2649.

Lin II, CH Chen, IF Pun, WT Liu and CC Wu (2009b), Warm ocean anomaly, air sea fluxes, and the rapid intensification of tropical cyclone Nargis (2008), *Geophys. Res. Lett.*, 36, L03817, doi:10.1029/ 2008GL035815.

Lin II, GJ Goni, J Knaff, C Forbes and MM Ali (2013), Ocean heat content for tropical cyclone intensity forecasting and its impact on storm surge, *Nat. Hazards*, 66, 3, 1481-1500.

Lin II, IF Pun and CC Lien (2014), "Category-6" supertyphoon Haiyan in global warming hiatus: Contribution from subsurface ocean warming, *Geophys. Res. Lett.*, 41, 8547–8553, doi:10.1002/2014GL061281.

Lin II, IF Pun and CC Wu (2009a), Upper-ocean thermal structure and the western North Pacific category-5 typhoons. Part II: Dependence on translation speed, *Mon. Wea. Rev.*, 137, 3744–3757, doi:10.1175/ 2009MWR2713.1.

Lin II, P Black, JF Price, CY Yang, SS Chen, CC Lien, P Harr, NH Chi, CC Wu and EA D'Asaro (2013), An ocean coupling potential intensity index for tropical cyclones, *Geophys. Res. Lett*., 40, 1878–1882, doi:10.1002/grl.50091.

Liu B, H Liu, L Xie, C Guan and D Zhao (2011), A coupled atmosphere-wave-ocean modeling system: Simulation of the intensity of an idealized tropical cyclone, *Mon. Wea. Rev*., 139, 132-152.

Liu ZL, CH Peng, WH Xiang et al. (2010), Application of artificial neural networks in global climate change and ecological research: An overview, *Chinese Sci. Bull.*, 55, 3853-3863, doi: 10.1007/s11434-010-4183-3.

Lloyd ID and GA Vecchi (2011), Observational evidence of oceanic controls on hurricane intensity, *J. Clim*., 24, 1138–1153.

Locarnini RA, AV Mishonov, JI Antonov, TP Boyer and HE Garcia (2006), World Ocean Atlas 2005, Volume 1: Temperature. S. Levitus, Ed. NOAA Atlas NESDIS 61, U.S. Government Printing Office, Washington, D.C., 182 pp.

Locarnini RA, AV Mishonov, JI Antonov, TP Boyer, HE Garcia, OK Baranova, MM Zweng and DR Johnson (2010), World Ocean Atlas 2009, Volume 1: Temperature. S. Levitus, Ed. NOAA Atlas NESDIS 68, U.S. Government Printing Office, Washington, D.C., 184 pp.

Longshore D (2008), Encyclopedia of Hurricanes, Typhoons, and Cyclones. Checkmark books, 468 pp, ISBN 978-0-8160-7409-9.

Lukas R and E Lindstrom (1991), The mixed layer of the western equatorial Pacific, *J. Geophys. Res.*, 96, 3343–3357.

Ma Z, J Fei, L Liu, X Huang and X Cheng (2013), Effects of the cold core eddy on tropical cyclone intensity and structure under idealized air-sea interaction conditions, *Mon. Weather Rev*., 141, 1285-1303.

Madec G (2008), NEMO ocean engine, Note du Pôle de modélisation, Institut Pierre-Simon Laplace (IPSL), France, 27, ISSN No 1288-1619.

Madhu NV, PA Maheswaran, R Jyothibabu, V Sunil, C Revichandran, T Balasubramanian, TC Gopalakrishnan and KKC Nair (2002), Enhanced biological production off Chennai triggered by October 1999 super cyclone (Orissa), *Curr. Sci.*, 82, 1472–1479.

Mahala BK, BK Nayak, PK Mohanty (2015), Impacts of ENSO and IOD on tropical cyclone activity in the Bay of Bengal, *Nat. Hazards*, 75, 1105–1125.

Mahjoobi J and EA Mosabbeb (2009), Prediction of significant wave height using regressive support vector machines. *J. Ocean Engineering*, 36(5), 339-347.

Mainelli M, M DeMaria, LK Shay and G Goni (2008), Application of oceanic heat content estimation to operational forecasting of recent Atlantic category 5 hurricanes. *Wea. Forecasting* 23, 3-16.

Malkus JS and H Riehl (1960), On the dynamics and energy transformations in steady state hurricanes, *Tellus*, 12, 1–20.

Maneesha K, V Sarma, P Reddy, Y Sadhuram, TVR Murty, VV Sarma, MD Kumar (2011), Meso-scale atmosphere events promote phytoplankton blooms in the coastal Bay of Bengal, *J. Earth Syst. Sci*., 120, 4, 773–782.

Maneesha K, Y Sadhuram and KVSR Prasad (2015), Role of upper ocean parameters in the genesis, intensification and tracks of cyclones over the Bay of Bengal, *Journal of Operational Oceanography*, 8, 2, 133-146.

Manganello JV and Coauthors (2012), Tropical cyclone climatology in a 10-km global atmospheric GCM: Toward weather-resolving climate modeling. *J. Climate*, 25, 3867-3893.

Marks FD, and LK Shay (1998), Landfalling tropical cyclones: Forecast problems and associated research opportunities, *Bull. Amer. Meteor. Soc.*, 79, 305–323.

Marsaleix P, F Auclair, JW Floor, MJ Herrmann, C Estournel, I Pairaud and C Ulses (2008), Energy conservation issues in sigma-coordinate free-surface ocean models, *Ocean Modelling,* 20, 61–89, doi:10.1016/j.ocemod.2007.07.005.

Mavume AF, L Rydberg, M Rouault, JRE Lutjeharms (2009), Climatology and landfall of tropical cyclones in the south-west Indian Ocean, *Western Indian Ocean Journal of Marine Science*, 8, 15-36.

McCreary JP, W Han, D Shankar, SR Shetye (1996), Dynamics of the east India coastal current 2. Numerical solutions, *J. Geophys. Res*., 101, 13993-14010.

McPhaden MJ, GR Foltz, T Lee, VSN Murty, M Ravichandran, GA Vecchi, J Vialard, JD Wiggert and L Yu (2009), Ocean-atmosphere interactions during cyclone Nargis. *Eos, Trans. Amer. Geophys. Union*, 90, 53-54, doi:10.1029/2009EO070001.

Mei W and C Pasquero (2013), Spatial and temporal characterization of sea surface temperature response to tropical cyclones, *J. Clim*., 26, 3745–3765, doi:10.1175/JCLI-D-12-00125.1.

Mei W, C Pasquero and F Primeau (2012), The effect of translation speed upon the intensity of tropical cyclones over the tropical ocean. *Geophy. Res. Lett*., 39, L07801, doi:10.1029/2011GL050765.

Mei W, S-P Xie, F Primeau, JC McWilliams and C Pasquero (2015), Northwestern Pacific typhoon intensity controlled by changes in ocean temperatures. *Sci. Adv*. 1, e1500014.

Mellor G and A Blumberg (2004), Wave breaking and ocean surface layer thermal response, *J. Phys. Oceanogr.*, 34(3), 693–698, doi:10.1175/2517.1.

Merrill RT (1988), Environmental influence of hurricane intensification, *J. Atmos. Sci.,* 45, 1678–1687.

Menkes CE, M Lengaigne, P Marchesiello, N Jourdain, EM Vincent, J Lefèvre, F Chauvin, J-F Royer (2012), Comparison of tropical cyclogenesis indices on seasonal to interannual timescales, *Clim. Dyn.,* doi 10.1007/s00382-011-1126-x.

Merrill RT (1980), A statistical tropical cyclone motion forecasting system for the Gulf of Mexico, NOAA Tech. Memo. NWS NHC 14, 21 pp. [Available from NTIS, Technology Administration, U.S. Dept. of Commerce, Springfield, VA 22161]

Merrill RT (1987), An experiment in statistical prediction of tropical cyclone intensity change, NOAA Tech. Memo., NWS NHC 34, 34 pp. [Available from the National Technical Information Ser- vice, U.S. Department of Commerce, 5285 Port Royal Rd., Springfield, VA 22151.]

Merrill RT (1988), Environmental influence of hurricane intensification, *J. Atmos. Sci*., 45, 1678–1687.

Miller BI (1958), On the maximum intensity of hurricanes, *J. Meteor*., 15, 184–195.

Mlawer EJ, SJ Taubman, PD Brown, MJ Iacono and SA Clough (1997), Radiative transfer for inhomogeneous atmospheres: RRTM, a validated correlated-k model for the longwave, *J. Geophys. Res.,* 102, D14, 16, 663–16, 682, doi:10.1029/97JD00237.

Mohapatra M, BK Bandyopadhyay and DP Nayak (2013), Evaluation of operational tropical cyclone intensity forecasts over north Indian Ocean issued by India Meteorological Department, *Nat. Hazards*, 68, 433–451.

Muller-Karger FE, PL Richardson and D McGillicuddy (1995), On the offshore dispersal of the Amazon's plume in the North Atlantic, *Deep Sea Res I*, 42, 2127– 2137.

Murakami H, M Sugi and A Kitoh (2012), Future changes in tropical cyclone activity in the North Indian Ocean projected by high-resolution MRI-AGCMs. *Clim. Dyn*. 40, 1949–1968.

Murakami H and Coauthors (2015), Simulation and prediction of category 4 and 5 hurricanes in the high-resolution GFDL HiFLOR coupled climate model, J. Climate, 28, 9058–9079, doi:10.1175/JCLI-D-15-0216.1.

Murty VSN, DP Rao and JS Sastry (1983), The lowering of sea surface temperature in the east central Arabian Sea associated with a cyclone, *Mahasagar, Bull. Natl. Inst. Oceanogr.*, 16, 67-71.

Nagamani PV, R Shikhakolli and P Chauhan (2011), Phytoplankton Variability in the Bay of Bengal During Winter Monsoon Using Oceansat-1 Ocean Colour Monitor Data, *J Indian Soc. Remote Sens.*, 39, 1, 117–126 doi: 10.1007/s12524-010-0056-0.

Nayak SR, RK Sarangi and AS Rajawat (2001), Applications of IRS-P4 OCM data to study the impact of cyclone on coastal environment of Orissa, *Curr. Sci*., 80, 1208-1213.

Neetu S, M Lengaigne, E Vincent, J Vialard, G Madec, G Samson, S Masson, F Durand (2012), Influence of upper ocean stratification on tropical cyclones surface cooling in the Bay of Bengal, *J. Geophys. Res.*, 117, doi:10.1029/2012JC008433.

Neumann CJ (1972), An alternate to the HURAN (hurricane analog) tropical cyclone forecasting system, NOAA Tech Memo., NWS SR 62, 23 pp. [Available from NTIS, Technology Administration, U.S. Dept. of Commerce, Springfield, VA 22161].

Neumann CJ (1993), Global overview, Chapter 1, Global guide to tropical cyclone forecasting. WMO, Geneva.

Neumann B, AT Vafeidis, J Zimmermann, RJ Nicholls (2015), Future coastal population growth and exposure to sea-level rise and coastal flooding-a global assessment, *PLoS One*, 10, 3, e0118571. doi:10.1371/journal.pone.0118571.

Ng EKW and JCL Chan (2012), Interannual variations of tropical cyclone activity over the north Indian Ocean. *Int. J. Climatol.*, 32, 819–830, doi:10.1002/joc.2304.

Nidheesh AG, M Lengaigne, J Vialard, AS Unnikrishnan and H Dayan (2013), Decadal variability in the tropical Indo-Pacific region, *Clim. Dyn*., 41, 381-402.

Noh Y, WG Cheon, SY Hong and S Raasch (2003), Improvement of the K-profile model for the planetary boundary layer based on large eddy simulation data, *Boundary Layer Meteorol.*, 107, 2, 401-427, doi:10.1023/A:1022146015946.

Ogata T, R Mizuta, Y Adachi, H Murakami and T Ose (2015), Effect of air-sea coupling on the frequency distribution of intense tropical cyclones over the northwestern Pacific, *Geophys. Res. Lett*., 42, 10,415–10,421, doi:10.1002/ 2015GL066774.

Papa F, F Durand, WB Rossow, A Rahman and S Bala (2010), Satellite altimeter-derived monthly discharge of the Ganga-Brahmaputra River and its seasonal to interannual variations from 1993 to 2008. *J. Geophys. Res.*, 115, C12013, doi:10.1029/2009JC006075.

Papa F, SK Bala, RK Pandey, F Durand, VV Gopalakrishna, A Rahman, WB Rossow (2012), Ganga-Brahmaputra river discharge from Jason-2 radar altimetry: an update to the long-term satellite-derived estimates of continental freshwater forcing flux into the Bay of Bengal. *J. Geophys. Res.*, 117, C11021, http://dx.doi.org/10.1029/2012JC008158.

Penduff T, M Juza, L Brodeau, GC Smith, B Barnier, J-M Molines, A-M Treguier, and G Madec (2010), Impact of global ocean model resolution on sea-level variability with emphasis on interannual time scales, *Ocean Sci.*, 6, 269–284.

Powell MD and TA Reinhold (2007), Tropical cyclone destructive potential by integrated kinetic energy, *Bull. Amer. Meteor. Soc*., 88, 4, 513–526, 2007.

Powell MD, PJ Vickery and TA Reinhold (2003), Reduced drag coefficient for high wind speeds in tropical cyclones, *Nature*, 422, 279–283

Prasad TG (1997), Annual and seasonal mean buoyancy fluxes for the tropical Indian Ocean. *Curr. Sci.,* 73, 8, 667-674.

Prasad TG (2004), A comparison of mixed-layer dynamics between the Arabian Sea and Bay of Bengal: One-dimensional model results, *J. Geophys. Res.,* 109, C03035, doi:10.1029/2003JC002000.

PrasannaKumar S, P M Muraleedharan, T G Prasad, M Gauns, N Ramaiah, SN deSouza, S Sardesai and M Madhupratap (2002), Why is the Bay of Bengal less productive during summer monsoon compared to the Arabian Sea?, *Geophys. Res. Lett.*, 29, 24, 2235, doi:10.1029/2002GL016013.

Praveen Kumar B, J Vialard, M Lengaigne, VSN Murty, GR Foltz, MJ McPhaden, S Pous and C de Boyer Montegut (2014), Processes of interannual mixed layer temperature variability in the thermocline ridge of the Indian Ocean, *Clim. Dyn*., doi:10.1007/s00382-014-2059-y.

Price JF (1981), Upper ocean response to a Hurricane, *J. Phys. Oceanogr*., 11, 153-175.

Price JF (2009), Metrics of hurricane-ocean interaction: Vertically-integrated or vertically-averaged ocean temperature?, *Ocean Sci*., 5, 351–368.

Price JF, J Morzel and PP Niiler (2008), Warming of SST in the cool wake of a moving hurricane, *J. Geophys. Res*., 113, C07010, doi:10.1029/2007JC004393.

Price JF, TB Sanford and GZ Forristall (1994), Forced stage response to a moving hurricane, *J. Phys. Oceanogr*., 24, 233–260, doi:10.1175/1520-0485(1994)024<0233:FSRTAM>2.0.CO;2.

Rao RR (1987), Further analysis on the thermal response of the upper Bay of Bengal to the forcing of the pre-monsoon cyclonic storm and summer monsoonal onset during MONEX-79, *Mausam*, 38, 2, 147-156.

Rao RR and R Sivakumar (2002), Seasonal variability of sea surface salinity and salt budget of the mixed layer of the north Indian Ocean. *J. Geophys. Res.*, 108. Doi: 10.1029/2001JC00907.

Rao RR, MS GirishKumar, M Ravichandran, AR Rao, VV Gopalakrishna and P Thadathil (2010), Interannual variability of Kelvin wave propagation in the wave guides

of the equatorial Indian Ocean, the coastal Bay of Bengal and the southeastern Arabian Sea during 1993–2006, *Deep Sea Res.,* Part I, 57, 1-13, doi:10.1016/j.dsr.2009.10.008.

Reddy PRC, PS Salvekar, S Nayak (2008), Super Cyclone Induces a Mesoscale Phytoplankton Bloom in the Bay of Bengal, *Geoscience and Remote sensing letters*, 5, doi: 10.1109/LGRS.2008.2000650.

Reed RD and RJ Marks (1999), Neural Smithing: Supervised Learning in Feedforward Artificial Neural Networks, The MIT Press, Cambridge, MA. 346p.

Riehl H (1950), A model of hurricane formation, *J. of Applied Physics,* 21, 917–925.

Ripley BD (1976), The second-order analysis of stationary point processes, *Journal of Applied Probability*, 13, 255–266.

Roy C and R Kovordanyi (2012), Tropical cyclone track forecasting techniques: A review, Atmospheric research, 104-105, 40-69, http://dx.doi.org/10.1016/j.atmosres.2011.09.012.

Royer J-F, F Chauvin, B Timbal, P Araspin, D Grimal (1998), AGCM study of the impact of greenhouse gas increase on the frequency of occurrence of tropical cyclones, *Clim. Chang.* 38, 307-343

Sadhuram Y, K Maneesha, TWR Murty (2012), Intensification of Aila (May 2009) due to a warm core eddy in the North Bay of Bengal, *Nat. Hazards,* 63, 1515-1525.

Samson G, H Giordani, G Caniaux and F Roux (2009), Numerical investi- gation of an oceanic resonant regime induced by hurricane winds, *Ocean Dynamics*, 59, 4, 565–586.

Samson G, S Masson, M Lengaigne, MG Keerthi, J Vialard, S Pous, G Madec, NC Jourdain, S Jullien, C Menkes, P Marchesiello (2014), The NOW regional coupled model: application to the Tropical Indian ocean climate and tropical cyclone activity, *J. Adv. Mod. Earth Sys.*, 6, 3, 700-722, doi:10.1002/2014MS000324.

Sandery PA, GB Brassington, A Craig and T Pugh (2010), Impacts of ocean-atmosphere coupling on tropical cyclone intensity change and ocean prediction in the aus- tralian region. *Mon. Wea. Rev.*, 138, 6, 2074–2091.

Sanford TB, JF Price, JB Girton and DC Webb (2007), Highly resolved observations and simulations of the ocean response to a hurricane, *Geophys. Res. Lett*., 34, L13604, doi:10.1029/2007GL029679.

Satoh M, K Oouchi K, T Nasuno and Coauthors (2012), Intra-seasonal oscillation and its control of tropical cyclones simulated by high-resolution global atmospheric models, *Clim. Dyn.*, 39, 2185, doi:10.1007/s00382-011-1235-6.

Schade LR (2000) Tropical cyclone intensity and sea surface temperature, *J. Atmos. Sci.,* 57, 3122–3130.

Schade LR (2000), Tropical cyclone intensity and sea surface temperature, *J. Atmos. Sci.,* 57, 3122–3130.

Schade LR and KA Emanuel (1999), The ocean's effect on the inten- sity of tropical cyclones: Results from a simple coupled atmosphere– ocean model, *J. Atmos. Sci.,* 56, 642–651, doi:10.1175/1520-0469 (1999)056<0642:TOSEOT>2.0.CO;2.

Schott F and JP McCreary (2001), The monsoon circulation of the Indian Ocean, *Prog. Oceanogr*., 51, 1–123.

Sengupta D, GN Bharath Raj and SSC Shenoi (2006), Surface freshwater from Bay of Bengal runoff and Indonesian throughflow in the tropical Indian Ocean, *Geophys. Res. Lett.,* 33, L22609, doi: 10.1029/2006GL027573.

Sengupta D, RG Bharath, DS Anitha (2008), Cyclone-induced mixing does not cool SST in the post-monsoon north Bay of Bengal, *Atmos. Sci. Lett*., 9, 1-6.

Shankar D, JP McCreary, W Han and SR Shetye (1996), Dynamics of the East India Coastal Current 1. Analytic solutions forced by interior Ekman pumping and local alongshore winds, *J. Geophys. Res.,* 101, 13, 975–13, 991, doi:10.1029/96JC00559.

Sharma N, MM Ali, JA Knaff and P Chand (2013), A soft-computing cyclone intensity prediction scheme for the Western North Pacific Ocean, *Atmosph. Sci. Lett*., 14, 187–192. doi: 10.1002/asl2.438

Shay L, R Elsberry and P Black (1989), Vertical structure of the ocean current response to a hurricane. *J. Phys. Oceanogr.* 19, 5, 649–669. doi:10.1175/1520-0485(1989)019<0649:VSOTOC>2.0.CO;2

Shay LK and JK Brewster (2010), Oceanic Heat Content Variability in the Eastern Pacific Ocean for Hurricane Intensity Forecasting, *Mon. Wea. Rev.,* 238, 2110–2131.

Shay LK, G Goni and PG Black (2000), Effects of a warm oceanic feature on Hurricane Opal, *Mon. Wea. Rev.,* 128, 1366–1383.

Shay LK, P Black, A Mariano, J Hawkins and R Elsberry (1992), Upper ocean response to hurricane Gilbert, *J. Geophys. Res.*, 97, 20, 227–248.

Shay LK, PG Black, JD Hawkins, RL Elsberry and AJ Mariano (1991), Sea surface temperature response to Hurricane Gilbert. Preprints, 19th Conf. on Hurricanes and Tropical Meteorology, Miami, FL, Amer. Meteor. Soc., 574–578.

Shenoi SSC, D Shankar and SR Shetye (2002), Differences in heat budgets of the near-surface Arabian Sea and Bay of Bengal: Implications for the summer monsoon, *J. Geophys. Res.*, 107(C6), 3052, doi:10.1029/2000JC000679.

Shetye SR, AD Gouveia AD, D Shankar, SSC Shenoi, PN Vinayachandran, D Sundar, GS Michael, G Nampoothiri (1996), Hydrography and circulation in the western Bay of Bengal during the northeast monsoon. *J. Geophys. Res.*, 101, 14011–14025.

Singh OP, TM Ali Khan and MS Rahman (2001), Probable reasons for enhanced cyclogenesis in the Bay of Bengal during July-August of ENSO years. *Global Planet. Change*, 29, 135–147.

Singh OP, TMA Khan and MS Rahman (2000), Changes in the frequency of tropical cyclones over the North Indian Ocean, *Meteorol. Atmos. Phys.,* 75, 11-20, doi:10.1007/s007030070011.

Skamarock WC and JB Klemp (2008), A time-split nonhydrostatic atmospheric model for weather research and forecasting applications, *J. Comput. Phys*., 227, 7, 3465-3485, doi:10.1016/j.jcp.2007.01.037.

Smitha A, KH Rao and D Sengupta (2006), Effect of May 2003 tropical cyclone on physical and biological processes in the Bay of Bengal, *International J. Remote Sensing*, 27, 5301-5314.

Sprintall J, and M Tomczak (1992), Evidence of barrier layer in the surface layer of tropics. *J. Geophys. Res.*, 97, 7305–7316.

Srinivas CV, D Hariprasad, DV Bhaskar Rao, Y Anjaneyulu, R Baskaran and B Venkatraman (2013a), Simulation of the Indian summer monsoon regional climate using advanced research WRF model, *Int. J. Climatol*., 33, 5, 1195–1210, doi:10.1002/joc.3505.

Srinivas CV, DV Bhaskar Rao, V Yesubabu, R Baskaran, and B Venkatraman (2013b), Tropical cyclone predictions over the Bay of Bengal using the high-resolution Advanced Research Weather Research and Forecasting (ARW) model, *Q. J. R. Meteorol. Soc*., 139, 676, 1810– 1825, doi:10.1002/qj.2064.

Subrahmanyam B, VSN Murty, RJ Sharp, JJ O'Brien (2005), Air-sea coupling during the Tropical Cyclones in the Indian Ocean: a case study using satellite observations, *Pure and Applied Geophysics,* 162, 1643–1672.

Sumesh KG, MR RameshKumar (2013), Tropical cyclones over north Indian Ocean during El Nino modoki years, *Nat. Hazards*, 68, 1057–1074.

Sutyrin GG (1979), Energetics of a stratified ocean under a stationary tropical cyclone, *Izvestiya Akademii Nauk Sssr Fizika Atmosfery I Okeana*, 15, 10, 1076–1083.

Sutyrin GG and AP Khain (1984), The influence of the ocean-atmosphere interaction on the intensity of moving tropical cylones, *Izvestiya Akademii Nauk Sssr Fizika Atmosfery I Okeana*, 20, 9, 787–794.

Swain D, MM Ali, RA Weller (2006), Estimation of mixed-layer depth from surface parameters, *Journal of Marine Research*, 64, 745-758.

Tallapragada V, CQ Kieu, YC Kwon, SG Trahan, Q-F Liu, Z Zhang and I-H Kwon (2014), Evaluation of Storm Structure from the Operational HWRF Model during 2012 Implementation, *Mon. Wea. Rev.*, 142, 4308-4325. doi: http://dx.doi.org/10.1175/MWR-D-13-00010.1.

Tang B and K Emanuel (2010), Midlevel ventilation's constraint on tropical cyclone intensity, *J. Atmos. Sci.*, 67, 1817–1830.

Thadathil P, PM Muraleedharan, RR Rao, YK Somayajulu, GV Reddy and C Revichandra (2007), Observed seasonal variability of barrier layer in the Bay of Bengal, *J. Geophys. Res.,* 112, C02009, doi:10.1029/2006JC003651.

Tien DD, T Ngo-Duc, HT Mai, C Kieu (2013), A study of the connection between tropical cyclone track and intensity errors in the WRF model, *Meteorol. Atmos. Phys.,* 122, 55–64. doi: 10.1007/s00703-013-0278-0

Tippett MK, SJ Camargo and AH Sobel (2011), A Poisson regression index for tropical cyclone genesis and the role of large-scale vorticity in genesis. *J. Climate*, 24, 2335–2357. http://journals.ametsoc.org/doi/10.1175/2010JCLI3811.1.

Tolman HL, VM Krasnopolsky, DV Chalikov (2005), Neural network approximations for nonlinear interactions in wind wave spectra: direct mapping for wind seas in deep water. *Ocean Modelling*, 8, 253-278.

Valcke S *(*2013*),* The OASIS3 coupler: A European climate modelling community software*, Geosci. Model Dev., 6(2),* 373–388*, doi:10.5194/gmd-6-373-2013.*

Vapnik V (1995), The Nature of Statistical Learning Theory. Springer, New York.

Vapnik VN (1999), An overview of statistical learning theory. IEEE Transactions on Neural Networks, 10, pp. 988–999.

Vapnik VN (2000), The Nature of Statistical Learning Theory (New York: Springer-Verlag).

Vecchi GA and TR Knutson (2008), On estimates of historical North Atlantic tropical cyclone activity, *J. Climate*, 21, 3580–3600.

Velden C, D Herndon, J Kossin, J Hawkins, M DeMaria (2006), Consensus estimates of tropical cyclone intensity using integrated multispectral (IR and MW) satellite observations, Preprints, 26th AMS Conf. on Hurr. and Trop. Meteor., Monterey, CA, Amer. Meteor. Soc.

Venkatesan R, S Mathew, J Vimala , G Latha, MM Arul, S Ramasundaram, R Sundar, R Lavanya, MA A (2014), Signatures of very severe cyclonic storm Phailin in met–ocean parameters observed by moored buoy network in the Bay of Bengal, *Curr. Sci*., 107, 4, 589-595.

Vialard J et al. (2009), Cirene: Air sea interactions in the Seychelles-Chagos thermocline ridge region, *Bull. Am. Meteorol. Soc.,* 90, 45–61, doi:10.1175/2008BAMS2499.1.

Vinayachandran PN and S Mathew (2003), Phytoplankton bloom in the Bay of Bengal during the northeast monsoon and its intensification by cyclones, *Geophys. Res. Lett.,* 30, 11, 1572, doi:10.1029/2002GL016717.

Vinayachandran PN, CP Neema, S Mathew and R Remya (2012), Mechanisms of summer intraseasonal sea surface temperature oscillations in the Bay of Bengal, *J. Geophys. Res.*, 117, C01005, doi:10.1029/2011JC007433.

Vinayachandran PN, T Kagimoto, Y Masumoto, P Chauhan, SR Nayak , T Yamagata (2005), Bifurcation of the East India Coastal Current east of Sri Lanka. *Geophys Res Lett,* 32. doi: 10.1029/2005GL022864.

Vinayachandran PN, VSN Murty and VR Babu (2002), Observations of barrier layer formation in the Bay of Bengal during summer monsoon. *J. Geophys. Res.*, 107, 8018, doi:10.1029/2001JC000831.

Vincent EM, G Madec, M Lengaigne, A Koch-Larrouy, J Vialard (2012c), Influence of Tropical Cyclones on sea surface temperature seasonal cycle and ocean heat transport, *Clim. Dyn*., 41, 2019-2038, doi:10.1007/s00382-012-1556-0.

Vincent EM, M Lengaigne, CE Menkes, NC Jourdain, P Marchesiello and G Madec (2009), Interannual variability of the South Pacific Convergence Zone and implications for tropical cyclone genesis, *Clim. Dyn*., 36, 1881–1896.

Vincent EM, M Lengaigne, G Madec, J Vialard, G Samson, N Jourdain, CE Menkes, S Jullien (2012a), Processes setting the characteristics of sea surface cooling induced by tropical cyclones, *J. Geophys. Res.,* 117, C02020, doi:10.1029/2011JC007396.

Vincent EM, M Lengaigne, J Vialard, G Madec, N Jourdain, S Masson (2012b), Assessing the Oceanic Control on the Amplitude of sea Surface Cooling induced by Tropical Cyclones, *J. Geophys. Res.,* 117, C05023, doi:10.1029/2011JC007705.

Vissa NK, ANV Satyanarayana and B Prasad Kumar (2013a), Intensity of tropical cyclones during pre- and post-monsoon seasons in relation to accumulated tropical cyclone heat potential over Bay of Bengal, *Nat. Hazards*, 68, 351, doi:10.1007/s11069-013-0625-y.

Vissa NK, ANV Satyanarayana and B Prasad Kumar (2013b), Response of upper ocean and impact of barrier layer on Sidr cyclone induced sea surface cooling, *Ocean Sci. J*., 48, 279, doi:10.1007/s12601-013-0026-x.

Walker ND, RR Leben and S Balasubramanian (2005), Hurricane-forced upwelling and chlorophyll a enhancement within cold-core cyclones in the Gulf of Mexico, *Geophys. Res. Lett.*, 32, L18610, doi:10.1029/2005GL023716.

Walker ND, RR Leben, CT Pilley, M Shannon, D Herndon, I-F Pun, I-I Lin and CL Gentemann (2014), Slow translation speed causes rapid collapse of northeast Pacific Hurricane Kenneth over cold core eddy, *Geophys. Res. Lett.,* 41, 7595–7601, doi:10.1002/ 2014GL061584.

Wang B, Q Ding and PV Joseph (2009), Objective Definition of the Indian Summer Monsoon Onset. *J. Climate*, 22, 3303–3316, doi: http://dx.doi.org/10.1175/2008JCLI2675.1.

Wang J-W and W Han (2014), The Bay of Bengal upper-ocean response to tropical cyclone forcing during 1999, *J. Geophys. Res.,* Oceans, 119, 98–120, doi:10.1002/2013JC008965.

Wang J-W, W Han and RL Sriver (2012a), Impact of tropical cyclones on the ocean heat budget in the Bay of Bengal during 1999: 1. Model configuration and evaluation, *J. Geophys. Res.,* 117, C09020, doi:10.1029/2012JC008372.

Wang J-W, W Han *and* RL Sriver *(*2012b*),* Impact of tropical cyclones on the ocean heat budget in the Bay of Bengal during 1999. Part II: Processes and interpretations*, J. Geophys. Res.,* 117*, C09021, doi:10.1029/2012JC008373.*

Wang S-Y, BM Buckley, JH Yoon and BO Fosu (2013), Intensification of premonsoon tropical cyclones in the Bay of Bengal and its impacts on Myanmar, *J. Geophys. Res. Atmos.*, 118, 4373–4384, doi:10.1002/jgrd.50396.

Wang Y and CC Wu (2004), Current understanding of tropical cyclone structure and intensity changes—A review. *Meteor. Atmos. Phys.*, 87, 257–278. doi:10.1007/s00703-003-0055-6.

Webster PJ (2008) Myanmar's deadly "daffodil." *Nat. Geosci.*, 1, 488–490.

Webster PJ, GJ Holland, JA Curry, H-R Chang (2005), Changes in tropical cyclone number, duration, and intensity in a warming environment, *Science*, 309, 1844-1846.

Wei CC (2012), Wavelet support vector machines for forecasting precipitations in tropical cyclones: Comparisons with GSVM, regressions, and numerical MM5 model, *Wea. Forecasting*, 27, 438-450.

Weinkle J, R Maue and R Pielke (2012), Historical global tropical landfalls, *J. Climate*, 25, 4729-4735, doi: http://dx.doi.org/10.1175/JCLI-D-11-00719.1

Wentz FJ, C Gentemann, D Smith, and D Chelton (2000), Satellite measurements of sea surface temperature through clouds, *Science,* 288, 847–850.

Willoughby HE and ME Rahn (2004), Parametric representation of the primary hurricane vortex Part I: Observations and evalua- tion of the Holland (1980) model, *Mon. Wea. Rev.,* 132, 3033– 3048.

Willoughby HE, RWR Darling and ME Rahn (2006), Parametric representation of the primary hurricane vortex. Part II: A new family of sectionally continuous profiles, *Mon. Wea. Rev.,* 134, 1102–1120.

Wu C-C, C-Y Lee and I-I Lin (2007), The effect of the ocean eddy on tropical cyclone intensity, *J. Atmos. Sci*., 64, 3562–3578.

Wu L and H Zhao (2012), Dynamically derived tropical cyclone intensity changes over the western North Pacific, *J. Clim*., 25, 89–98.

Wu L and X Chen (2016), Revisiting the steering principal of tropical cyclone motion in a numerical experiment, *Atmos. Chem. Phys*., 16, 14925-14936, doi:10.5194/acp-16-14925-2016.

Wu MC, WL Chang and WM Leung (2004), Impacts of El Niño-Southern oscillation events on tropical cyclone landfalling activity in the western North Pacific*, J. Climate*, 17, 1419-1428.

Xie S-P, H Annamalai, FA Schott and JP McCreary Jr. (2002), Structure and mechanisms of south Indian Ocean climate variability, *J. Clim.,* 15, 8, 864–878.

Xing W and F Huang (2013), Influence of summer monsoon on asymmetric bimodal pattern of tropical cyclogenesis frequency over the Bay of Bengal, *Journal of Ocean University of China*, 12, 2, doi: 10.1007/s11802-013-2219-4.

Yablonsky RM, and I Ginis (2009), Limitation of one-dimensional ocean models for coupled hurricane-ocean model forecasts, *Mon. Weather Rev.*, 137, 4410–4419, doi:10.1175/2009MWR2863.1.

Yanase W, M Satoh, H Taniguchi and H. Fujinami (2012), Seasonal and intraseasonal modulation of tropical cyclogenesis environment over the Bay of Bengal during the extended summer monsoon. *J. Climate*, 25, 2914–2930.

Yu L and MJ McPhaden (2011), Ocean Preconditioning of Cyclone Nargis in the Bay of Bengal: Interaction between Rossby Waves, Surface Fresh Waters, and Sea Surface Temperatures. *J. Phys. Oceanogr.*, 41, 1741–1755. doi: 10.1175/2011JPO4437.1

Yuan JP and J Cao (2013), North Indian Ocean tropical cyclone activities influenced by the Indian Ocean Dipole mode, *Science China Earth Sciences*, 56, 855–865.

Zedler SE (2009), Simulations of the ocean response to a hurricane: Nonlinear processes, *J. Phys. Oceanogr*., 39, 2618–2634.

Zeng Z, L-S Chen and Y Wang (2008), An observational study of environmental dynamical control of tropical cyclone intensity in the North Atlantic. *Mon. Wea. Rev.*, 136, 3307–3322, doi:10.1175/2008MWR2388.1.

Zeng Z, Y Wang, CC Wu (2007), Environmental dynamical control of tropical cyclone intensity - an observational study, *Mon. Wea. Rev*., 135, 38 –59

Zhao M, IM Held, S-J Lin and GA Vecchi (2009), Simulations of global hurricane climatology, interannual variability and response to global warming using a 50 km resolution GCM, *J. Clim*., 22, 6653–6678.

Zheng Z-W, C-R Ho, Q Zheng, Y-T Lo, N-J Kuo and G Gopalakrishnan (2010), Effects of preexisting cyclonic eddies on upper ocean responses to category 5 typhoons in the western north pacific. *J. Geophy. Res.,* 115, C9, 1978-2012.

Zhu H, U Wolfgang and SK Roger (2004), Ocean effects on tropical cyclone intensification and inner-core asymmetries, *J. Atmos. Sci*., 61, 1245-1258.

Zhu T and D-L Zhang (2006), The impact of the storm-induced SST cooling on hurricane intensity, *Adv. Atmos. Sci*., 23, 14–22.